Suprathermal electron studies in Tokamak plasmas by means of diagnostic measurements and modeling

THÈSE N^{O} 6523 (2015)

PRÉSENTÉE LE 27 FÉVRIER 2015

À LA FACULTÉ DES SCIENCES DE BASE
CRPP - PHYSIQUE DU TOKAMAK TCV
PROGRAMME DOCTORAL EN PHYSIQUE

ÉCOLE POLYTECHNIQUE FÉDÉRALE DE LAUSANNE

POUR L'OBTENTION DU GRADE DE DOCTEUR ÈS SCIENCES

PAR

Josef KAMLEITNER

acceptée sur proposition du jury:

Prof. R. Houdré, président du jury
Dr S. Coda, directeur de thèse
Dr D. Farina, rapporteuse
Prof. C. Forest, rapporteur
Dr J. Graves, rapporteur

ÉCOLE POLYTECHNIQUE FÉDÉRALE DE LAUSANNE

Suisse
2015

Abstract

To achieve reactor-relevant conditions in a tokamak plasma, auxiliary heating systems are required and can be realized by waves injected in the plasma that heat ions or electrons under certain conditions. Electron cyclotron resonant heating (ECRH) is a very flexible and robust technique featuring localized power deposition and current drive (CD) capabilities. Its fundamental principles such as damping on the cyclotron resonance are well understood and the application of ECRH is a proven and established tool; electron cyclotron current drive (ECCD) is regularly used to develop advanced scenarios and control magnetohydrodynamics (MHD) instabilities in the plasma by tailoring the current profile.

There remain important open questions, such as the phase space dynamics, the observed radial broadening of the suprathermal electron distribution function (e.d.f.) and discrepancies in predicted and experimental CD efficiency. These are addressed in this thesis. One of its main goals is indeed to improve the understanding of wave-particle interaction in plasmas and current drive mechanisms. This was accomplished by combined experimental and numerical studies, strongly based on the conjunction of hard X-ray (HXR) bremsstrahlung measurements and Fokker-Planck modeling, characterizing the suprathermal electron population.

The hard X-ray tomographic spectrometer (HXRS) diagnostic [1] was purposely developed to perform these studies, in particular by investigating spatial HXR emission asymmetries in the co- and counter-current directions and within the poloidal plane. The system uses cadmium-telluride ($CdTe$) detectors and digital acquisition to store the complete time history of incoming photon pulses. An extensive study of digital pulse processing algorithms was performed [2] and its consequent application allows the HXRS to handle high count rates in a noisy tokamak environment. Numerous other numerical tools were developed in the course of this thesis, among others to improve the time resolution by conditional averaging and to obtain local information with the general tomographic inversion (GTI) package.

The interfaces of the comparatively new LUKE code and well-established CQL3D Fokker-Planck code to the Tokamak à Configuration Variable (TCV) data were refurbished and a detailed benchmarking of these two codes was performed for the first time. Indeed, the theory-predicted toroidal and poloidal emission asymmetries could be consistently verified by experiment and modeling in many cases, including scans of a variety of plasma and wave parameters. The effects of suprathermal electron diffusion and radio frequency (RF) wave scattering, both resulting in a radial broadening of the HXR emission, were separated by a poloidal de-

position location angle scan. Furthermore, previous results [3] on anomalous diffusion and CD efficiency were reproduced with increased confidence arising from enhanced diagnostic specifications. The plasma response to electron cyclotron (EC) absorption and the role of quasi-linear effects were investigated using the coherent averaging capabilities of the HXRS.
Several MHD instabilities can occur in the plasma center and better understanding of these modes and events is indispensable for their mitigation in order to prevent their negative effects on confinement and stability. Sawtooth crashes are such a major instability and localized at the $q = 1$ surface. They can be described as the evolution of an internal $m = 1$ kink mode leading to magnetic reconnection and consequently enhanced transport; additionally, the crashes can trigger secondary deleterious instabilities. The electron acceleration in the magnetic reconnection process was studied as well as the impact on the suprathermal tail. While acceleration was not specifically observed, the efficient ejection of suprathermal electrons due to sawtooth crashes could be quantified. In low density discharges this rapid transport leads to bursts of energetic HXR thick-target bremsstrahlung from the limiter.
A $m/n = 1/1$ internal kink mode coupled to a $m/n = 2/1$ component and closely related to sawtooth crashes is regularly observed in the presence of ECRH/CD close to the $q = 1$ surface. It occurs in bursts, alternating with phases of one or more sawtooth crashes. The dynamics of this bursty mode, which generally affects confinement, turn out to be connected to suprathermal electrons that are efficiently reheated after the preceding sawtooth crash and then dragged by the mode.
Another mode investigated in this thesis is the electron fishbone instability, another $m/n = 1/1$ internal kink mode excited by resonant interaction with the drift reversal of precessing fast electrons, according to current understanding. There is as yet no complete picture of this instability. Significant differences in the observations on various tokamaks show the importance of a more systematic experimental study to advance the qualitative understanding and quantitative description of the instability. In particular, the presumed roles of barely trapped, barely passing and other specific regions of the e.d.f. in phase space were expected to be clarified by experiments on TCV using the HXRS as the main diagnostic. However, it proved more difficult than expected to destabilize this mode, and only preliminary, though promising results were obtained in the available time.

Keywords: Suprathermal electrons, fast electrons, electron distribution, Tokamak, plasma, hard X-ray, bremsstrahlung, diagnostic, CdTe, digital pulse processing, spectroscopy, tomography, GTI, ECRH, ECCD, Fokker-Planck, modeling, simulation, LUKE, CQL3D, TORAY, sawtooth, internal kink, electron fishbone, SVD, FEM, diffusion, magnetic reconnection, TCV, HXRS, TXDA, PMTX, PHAV, conditional averaging, coherent averaging

Kurzfassung

Zusatzheizungssysteme sind für das Erreichen von reaktorrelevanten Bedingungen in Tokamakplasmen unabdingbar und können durch ins Plasma eingespeiste Wellen realisiert werden, die die Ionen oder Elektronen unter gewissen Bedingungen heizen. Elektronzyklotronresonanzheizung (ECRH) ist eine sehr flexible und robuste Technik die lokalisierten Leistungseintrag und Stromtrieb ermöglicht. Das Verständnis ihrer zugrunde liegenden Gesetzmäßigkeiten, wie Dämpfung an der Zyklotronresonanz, ist gegeben, und auch die Anwendung von ECRH ist wohl erprobt und etabliert. Stromtrieb (CD) mit ECRH (ECCD) wird routinemäßig per Stromprofiladjustierung zur Entwicklung fortgeschrittener Szenarien und zur Kontrolle von magnetohydrodynamischen (MHD) Instabilitäten im Plasma verwendet.

Etliche wichtige Fragestellungen, wie die Dynamik im Phasenraum, die beobachtete radiale Verbreiterung der suprathermischen Elektronendichteverteilung und Abweichungen zwischen vorhergesagter und experimenteller Stromtriebeffizienz blieben bisher unbeantwortet und werden in dieser Dissertation abgehandelt. Ein besseres Verständnis der Wellen-Teilchen Wechselwirkung in Plasmen und der Stromtriebmechanismen stellen in der Tat eine der Hauptzielsetzungen dieser Arbeit dar und konnten durch kombinierte experimentelle und numerische Studien, basierend auf Messungen harter Bremsstrahlung und Fokker-Planck Simulationen, die gemeinsam die suprathermische Elektronenpopulation charakterisieren, erreicht werden.

Ein tomographisches Spektrometer für harte Röntgenstrahlung (HXRS) [1] wurde speziell für diese Studien entwickelt; im Besonderen zur Untersuchung von räumlichen Abstrahlungsasymmetrien im harten Röntgenbereich, sowohl in toroidaler Richtung (mit dem und entgegengesetzt zum Plasmastrom) als auch in der poloidalen Ebene. Das Messgerät verbaut Cadmiumtellurid ($CdTe$)-Detektoren und zeichnet den gesamten Zeitverlauf der eintreffenden Photonen digital auf. Eine umfassende Studie zu digitalen Impulsverarbeitungsalgorithmen [2] wurde durchgeführt um durch die konsequente Anwendung derselben dem Spektrometer die Verarbeitung hoher Zählraten auch im hohen Störsignalniveau eines Tokamakexperiments zu ermöglichen. Im Verlauf der Arbeit wurden zahlreiche weitere numerische Anwendungen entwickelt, unter anderem zur Verbesserung der Zeitauflösung durch bedingte Mittelung sowie Ortsinformation durch das GTI-Programmpaket für Tomographie.

Die Schnittstellen des vergleichsweise neuen LUKE Codes und des etablierten CQL3D Fokker-Planck Codes wurden erneuert und erstmalig wurde ein detaillierter Vergleich der beiden Codes durchgeführt. Die theoretisch vorhergesagten

toroidalen und poloidalen Abstrahlungsasymmetrien konnten in vielen Fällen konsistent durch Experiment und Simulationen verifiziert werden, wobei eine Vielzahl von Plasma- und Wellenparametern abgedeckt wurde. Die Effekte der Diffusion suprathermischer Elektronen und der Radiofreqeuenzwellenstreuung, welche beide in einer radialen Verbreiterung der harten Röntgenstrahlungsprofile resultieren, konnten durch die Abtastung des poloidalen Leistungseintragspositionswinkels getrennt werden. Weiters wurden vorhergehende Resultate [3] zu anomaler Diffusion und Stromtriebeffizienz mit den verbesserten Messsystemen reproduziert und dadurch besser abgesichert. Die Rückmeldung des Plasmas auf Elektronzyklotronabsorption und die Rolle von quasilinearen Effekten wurde mithilfe von kohärenter Mittelung der HXRS-Daten untersucht.
Im Zentrum des Plasmas können diverse MHD-Instabilitäten auftreten, wobei ein besseres Verständnis dieser Moden und Ereignisse für deren Unterdrückung unabdingbar ist um die damit einhergehenden negativen Effekte auf Einschluss und Stabilität zu verhindern. Eine der wichtigsten Instabilitäten ist die Sawtoothoszillation. Sie befinden sich auf der $q = 1$ Flussfläche und kann als die Entwicklung einer zu magnetischer Rekonnexion und folglich erhöhtem Transport führenden internen $m = 1$ Kinkmode beschrieben werden. Zusätzlich können diese Ereignisse weitere abträgliche Instabilitäten auslösen. Die Elektronenbeschleunigung im magnetischen Rekonnexionsprozess wurde genauso untersucht wie die Auswirkungen auf die vorher vorhandenen schnellen Elektronen. Während Beschleunigung nicht spezifisch beobachtet wurde, konnte der effektive Ausstoß der suprathermischen Elektronen aufgrund der Sawtoothcrashs quantifiziert werden. In Plasmaentladungen niedriger Dichte führt der schnelle Transport zu einer stoßhaften Ausstrahlung hochenergetischer Röntgenstrahlung vom Limiter.
In Gegenwart von ECRH/CD nahe der $q = 1$ Fläche wird eine interne Kinkmode ($m/n = 1/1$), die zu einer $m/n = 2/1$ Komponente koppelt und in engem Verhältnis zu Sawtoothcrashs steht, regelmäßig beobachtet. Sie hat allgemeine Auswirkungen auf den Einschluß und tritt in Stößen, abwechselnd mit Sawtoothcrashphasen, auf. Es stellt sich heraus, dass die Entwicklung dieser stoßhaften Mode mit suprathermischen Elektronen verbunden ist, welche nach dem vorhergehenden Sawtoothcrash effizient wiedererhitzt und sodann von der Mode mitgerissen werden.
Eine ebenfalls in dieser Dissertation untersuchte Mode ist die Elektronenfishboneinstabilität, eine weitere interne $m/n = 1/1$ Kinkmode, die laut derzeitigem Verständnis durch die resonante Wechselwirkung mit schnellen Elektronen in umgekehrter Präzessionsdrift angeregt wird. Bisher gibt es allerdings kein umfassendes Bild dieser Instabilität. Bedeutende Unterschiede in den Beobachtungen an verschiedenen Tokamakexperimenten zeigen die Wichtigkeit einer systematischeren Experimentalstudie auf, um das qualitative Verständnis voranzubringen und die Instabilität quantitativ zu beschreiben. Im Speziellen wurde erwartet, dass durch Experimente in TCV unter Einsatz des HXRS als Hauptmesssystem Klarheit über die mutmaßlichen Rollen der kaum gefangenen, gerade noch passierenden und weiteren spezifischen Regionen der Elektronendichteverteilung erlangt wird. Da sich die Destabilisierung der Mode allerdings als weitaus schwieriger herausstellte, konnten in der zur Verfügung stehenden Zeit nur vorläufige, wenngleich auch vielversprechende Resultate erzielt werden.

Schlüsselwörter: Suprathermische Elektronen, schnelle Elektronen, Elektronendichteverteilung, Tokamak, Plasma, harte Röntgenstrahlung, Bremsstrahlung, CdTe, Diagnostik, digitale Impulsverarbeitung, Spektroskopie, Tomographie, GTI, ECRH, ECCD, Fokker-Planck, Modellierung, Simulation, LUKE, CQL3D, TORAY, Sawtooth, Interne Kinkmode, Electronenfishbone, SVD, FEM, Diffusion, Magnetische Reconnexion, TCV, HXRS, TXDA, PMTX, PHAV, bedingte Mittelung, kohärente Mittelung

Résumé

Pour atteindre les conditions suffisantes pour faire fonctionner un réacteur de type tokamak, des systèmes de chauffage auxiliaire sont nécessaires. Une solution consiste à injection des ondes ondes radio-fréquence (RF) qui chauffent alors les ion ou les électrons. Le chauffage des électrons à la résonance cyclotronique (ECRH) est une technique très flexible et robuste qui permet de déposer de la puissance et de générer des courants localisés. Ses principes fondamentaux tels que l'absorption à la résonance cyclotronique sont bien compris, et le système ECRH est un outil éprouvé et établi. La génération de courant (CD) par ECRH (ECCD) est régulièrement utilisée pour ajuster le profil de courant ce qui permet de développer des scénarios avancés et contrôler les instabilités magnétohydrodynamiques (MHD) dans le plasma.

Des questions importantes, concernant la dynamique des électrons dans l'espace des phases, y compris l'élargissement radial du dépôt de courant, ainsi que les écarts entre les efficacités de génération de courant prédites et expérimentales, restent ouvertes. Celles-ci sont adressées dans cette thèse. L'amélioration de la compréhension de l'interaction entre les ondes et les particules dans les plasmas, et les mécanismes de génération de courant, sont en effet parmi les objectifs principaux de ce travail. Ce problème a été adressé par des études expérimentales et numériques, fortement basées sur la comparaison entre les mesures de rayons X durs et les modélisations Fokker-Planck correspondantes, caractérisant la population des électrons suprathermiques.

Le spectromètre tomographique de rayons X durs (HXRS) [1] a été développé délibérément pour ces études, en particulier en analysant les asymétries spatiales de l'émission des X durs dans la direction toroïdale (avec et contre le courant de plasma) ainsi que dans le plan poloïdal. Le dispositif utilise des détecteurs en tellurure de cadmium ($CdTe$) et une acquisition digitale pour stocker l'histoire complète des pulses de photons entrants. Une étude étoffée des algorithmes de traitement digital d'impulsions a été effectuée [2] afin de permettre au spectromètre de traiter des taux de comptage élevés malgré le bruit inhérent aux expériences tokamak. Au cours de la thèse, de nombreux outils numériques ont été développés, entre autres pour améliorer la résolution temporelle par le moyennage conditionnel, et pour obtenir de l'information locale avec le paquet d'inversion tomographique générale (GTI).

Les interfaces des codes Fokker-Planck LUKE (récent) et CQL3D (plus ancien) avec le Tokamak à Configuration Variable (TCV) ont été rénovées et une référenciation de ces deux codes a été effectuée pour la première fois. Les asymétries d'émission toroïdale et poloïdale, prédites par la théorie, ont pu être vérifiées de manière co-

hérente par des expériences et modélisations dans beaucoup de cas, couvrant une multitude de paramètres de plasma et d'onde. Les effets de diffusion des électrons suprathermiques et la diffusion des RF, deux effets produisant un élargissement radial de l'émission de rayons X durs, ont été séparés par un balayage de l'angle poloïdal du lieu de dépôt. De plus, des anciens résultats [3] sur la diffusion anormale et l'efficacité de génération de courant anormale ont été reproduites avec les dispositifs améliorés et, par conséquent, mieux assurées. La réaction du plasma à l'absorption d'ondes à la résonance cyclotronique des électrons et le rôle des effets quasi-linéaires ont été analysés en moyennant de manière cohérente des données de l'HXRS.

Au centre du plasma, plusieurs instabilités MHD peuvent apparaître, et une meilleure compréhension de ces modes et événements est indispensable afin de les atténuer pour prévenir leurs impacts négatifs sur le confinement et la stabilité du plasma. L'instabilité de dents de scie est une instabilité majeure localisée à la surface $q = 1$. Elle peut être décrite comme l'évolution d'un mode kink $m = 1$ interne induisant de la reconnexion magnétique et augmentant le transport par conséquent. Les chutes de dents de scie peuvent déclencher des instabilités secondaires nuisibles. L'accélération dans le processus de reconnexion magnétique a été étudiée de même que l'impact sur les électrons rapides. Tandis qu'aucune accélération n'était observée spécifiquement, l'éjection massive des électrons suprathermiques dû aux chutes de dents de scie a pu être quantifiée. Dans des décharges à basse densité, ce transport rapide cause des rafales de rayons X durs de freinage au niveau du limiteur.

Un mode kink interne $m/n = 1/1$, couplé à une composante $m/n = 2/1$ et étroitement lié aux chutes de dents de scie, est régulièrement observé en présence de ECRH/CD près de la surface $q = 1$. Il apparaît en rafales, alternant avec des phases d'une ou plusieurs chutes de dents de scie. Le déroulement de ce mode en rafale, qui dégrade généralement le confinement, se révèle être connecté aux électrons suprathermiques qui sont efficacement réchauffés après la chute de dents de scie précédente et ensuite entraînés dans le mode.

Un autre mode analysé dans cette thèse est l'instabilité fishbone électronique, un autre mode kink interne $m/n = 1/1$ excité par l'interaction résonante autorisée par le renversement de la dérive toroïdale des électron rapides. Jusqu'à présent il n'y a pas de description complète de cette instabilité. Des différences significatives entre les observations dans des tokamaks divers montrent l'importance d'une étude expérimentale plus systématique afin d'avancer la compréhension qualitative et la description quantitative de l'instabilité. En particulier, les rôles présumés des électrons faiblement piégés, faiblement passants et des autres régions spécifiques de la fonction de distribution des électrons dans l'espace de phases doivent être clarifiés par des expériences au TCV utilisant l'HXRS comme diagnostique principal. Cependant, il est plus difficile qu'anticipé de déstabiliser le mode, et seul des résultats préliminaires, pourtant prometteurs, ont été obtenus sur ces modes.

Mots clefs Électrons suprathermiques, électrons rapides, distribution des électrons, Tokamak, plasma, rayons X durs, rayonnement de freinage, diagnostique, CdTe, traitement digital de pulse, spectroscopie, tomographie, GTI, ECRH, ECCD, Fokker-Planck, modélisation, simulation, LUKE, CQL3D, TORAY, dent de scie, kink interne, fishbone électronique, SVD, FEM, diffusion, reconnexion magnétique, TCV, HXRS, TXDA, PMTX, PHAV, moyennage conditionnel, moyennage cohérent

Contents

Chapter 1

Introduction

1.1 Nuclear fusion

Nuclear fusion, in general, is a nuclear reaction in which two or more atomic nuclei join to form a new, heavier atomic nucleus. Additionally, other particles may be produced and energy may be consumed or released by the process. The most important example of nuclear fusion can be found in the sun, where fusion reactions release the energy that created and is required for life on earth. All existing power plants that are not based on nuclear fission or tides use this energy more (solar panels) or less (coal) directly to produce electricity.
Since all these renewable and conventional means of electricity production have quite serious drawbacks, humankind is always optimizing these and searching for new energy sources. One of these new energy sources could be realized by using fusion reactions directly on earth. There is a list of reactions of light atomic nuclei that are available on earth or can be produced continuously using reaction products, like tritium from lithium using neutrons. An analysis of this list results in the conclusion that the reaction of deuterium (^2D) and tritium (^3T)

$$^{2}\mathrm{D} + ^{3}\mathrm{T} \rightarrow ^{4}\mathrm{He}(3.5\,\mathrm{MeV}) + \mathrm{n}^{0}(14.1\,\mathrm{MeV}) \tag{1.1}$$

in a plasma confined at high temperature (thermonuclear fusion) is the most promising candidate [4, 5]. This is simply because it reaches ignition more easily under terrestrial conditions than all the other reactions, including those that take place in the sun. Ignition designates the condition in which the plasma does not require any external heating in order to sustain a constant fusion reaction rate with significant energy output. For a commercial reactor, ignition is not strictly necessary, it is sufficient that the reactor acts as an energy amplifier. The amplification factor (Q) is the fraction of the fusion power divided by the external heating power. $Q \approx 30$ is envisioned for a first demonstration reactor (DEMO). The current record for the highest Q is about ≈ 0.7 and has been achieved in 1997 in the Joint European Torus (JET) experiment [6]. ITER, a new tokamak experiment currently under construction, is planned to reach $Q = 10$ in the 2020s.
A simple condition for ignition based on power balance has been derived by Lawson [7]. The well-known Lawson criterion states that the product of density (n), temperature (T) and energy confinement time (τ_{E}), the so-called triple product,

has to exceed a certain value:

$$nT\tau_E \geq \frac{12k_B T}{\langle\sigma v\rangle \epsilon}. \tag{1.2}$$

The terms in the denominator of the right hand side (r.h.s.) are the reaction rate $\langle\sigma v\rangle$ and the energy of the α particles from fusion reactions $\epsilon = 3.5\,\mathrm{MeV}$. The minimal triple product for ignition lies at $T = 14\,\mathrm{keV}$ with the numerical value

$$nT\tau_E \geq 2.8 \times 10^{21}\,\mathrm{m}^{-3}\mathrm{keVs}. \tag{1.3}$$

This value [8] is corrected when additional effects and losses are included; a similar criterion can also be written for finite Q [4].
In order to attain such conditions, two main approaches are pursued: In magnetic confinement fusion (MCF) a relatively tenuous plasma is confined for a long time by magnetic fields, while in inertial confinement fusion (ICF) a dense plasma is compressed by beams and therefore confined by inertia for a short time. Both concepts have proven that they can reach a sufficient combination of density and confinement time to approach to $Q = 1$. Nonetheless, many (plasma) physics questions still remain open and those can also be addressed in experiments with $Q \ll 1$. Additionally, pure deuterium plasmas can be used instead of D-T, in order to retain the physics while avoiding the complexities and hazards of tritium handling.
With the plasmas approaching reactor conditions, more and more engineering and material limits are reached. Therefore, the newest experiments do not only explore the forefront of plasma physics, but also of remote handling, plant control, diagnostic systems, superconductors and material science in general.
In the following, the focus lies on plasma physics in MCF, the currently most promising approach for a reactor based on nuclear fusion.

1.2 The plasma state

The cross section for the fusion reaction (1.1) is, due to the high Coulomb well that has to be overcome, quite low. It can be shown easily that it is too low to build a commercial reactor based on accelerators because the particles do not collide often enough with the energy required [5]. In a hot plasma, however, ${}^2D$ and ${}^3T$ have high kinetic energies too, but additionally, they collide much more often before they leave the system. This allows, as stated in the Lawson criterion (1.2), the attainment of break-even and ignition in a confined plasma.
We shall therefore recapitulate a few basic properties of plasmas that are important in the course of this thesis.
The electron density (n_e) and the temperature of plasmas in MCF are around $n_e \approx 10^{20}\,\mathrm{m}^{-3}$ and $T \approx 10\,\mathrm{keV}$ and can be lower in smaller experiments. In any case they lie well inside the region that defines "ideal" plasmas [9], shown in Fig. 1.1. They are fully ionized, except for the boundary and sparse heavy impurities.

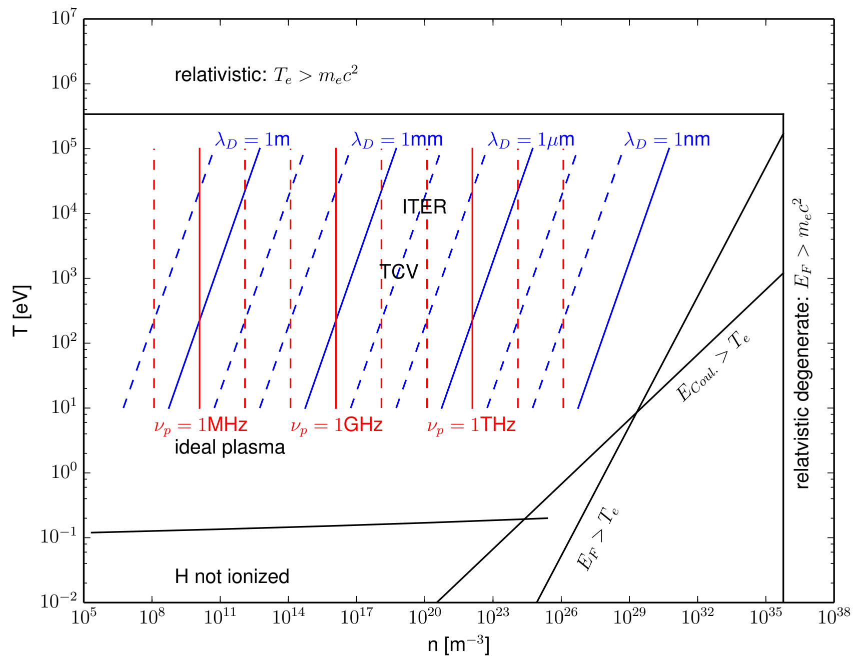

Figure 1.1: Ideal plasma range in the (n, T) space with Debye length (λ_D), plasma frequency (ν_p) and the region of plasmas in TCV and ITER.

The thermal energy dominates over the Coulomb and Fermi energies

$$E_{Coul.} = \frac{e^2}{4\pi\varepsilon_0} n^{1/3} \tag{1.4}$$

$$E_F = \frac{\hbar^2}{2m} \left(3\pi^2\right)^{2/3} n^{2/3}. \tag{1.5}$$

Relativistic effects are only important for high energy tails of the distribution function; the corresponding energy is $E_{rel,e} = m_e c^2 = 511\,\text{keV}$.
An important property is the quasi-neutrality

$$\frac{n_e - Z_i n_i}{n_e} \ll 1, \tag{1.6}$$

where Z_i and n_i are the ion charge and ion density, respectively. The value in (1.6) is typically 10^{-6} [9]. The perturbing effects of a charge (violation of quasi neutrality) are only felt to a distance of the order of the Debye length (λ_D)

$$\lambda_D = \sqrt{\frac{\epsilon_0 k_B}{\left(n_e/T_e + \sum_i Z_i^2 n_i/T_i\right) e^2}}. \tag{1.7}$$

Usually, the ion contribution is neglected and the Debye length is approximated by the electron Debye length:

$$\lambda_D \approx \lambda_{D,e} = \sqrt{\frac{\epsilon_0 k_B T_e}{n_e e^2}}. \tag{1.8}$$

The Debye number (N_D) is defined as the number of particles in a Debye sphere (a sphere with radius λ_D).

$$N_D = \frac{4}{3}\pi n_e \lambda_D^3 \tag{1.9}$$

For ideal plasmas this sphere is densely populated ($N_D \gg 1$). The plasma parameter (Λ), the maximum impact parameter divided by the classical distance of closest approach in Coulomb scattering, is closely related:

$$\Lambda = 4\pi n_e \lambda_D^3 \tag{1.10}$$

The Coulomb logarithm ($\ln\Lambda$) is the logarithm of the plasma parameter.
Due to their lower mass and therefore higher mobility, electrons dominate the dynamic shielding even more than the static shielding. The eigenfrequency of the electrons is the plasma frequency (ω_p)

$$\omega_p = \sqrt{\frac{n_e e^2}{m_e \epsilon_0}}, \tag{1.11}$$

$$\nu_p = \frac{\omega_p}{2\pi}. \tag{1.12}$$

Electromagnetic waves with lower frequencies cannot enter the plasma and are reflected while higher frequency waves can propagate in the plasma. [9]

1.3 Magnetic confinement fusion

1.3.1 Single particle motion

A charged particle in a magnetic field gyrates around a magnetic field line. The frequency of this gyration is called cyclotron frequency (ω_c) and depends on the magnetic field ($\mathbf{B}$) and the particle type:

$$\omega_{ce} = \frac{eB}{m_e}, \tag{1.13}$$

$$\omega_{ci} = \frac{ZeB}{m_i}, \tag{1.14}$$

for electrons and ions, respectively. For a typical magnetic field, $B = 1\,\mathrm{T}$, the numerical values are $\nu_{ce} = 28.0\,\mathrm{GHz}$ and $\nu_{cH^+} = 15.25\,\mathrm{MHz}$.
The radius of the gyration, called cyclotron or Larmor radius (r_L), depends also on the particle's velocity perpendicular to the magnetic field ($v_\perp$):

$$r_L = \frac{v_\perp}{\omega_c} = \frac{m v_\perp}{|q| B}. \tag{1.15}$$

Since this radius is usually much smaller than the plasma region, the particle is confined in the direction perpendicular to $\mathbf{B}$. However, the motion along the field line of an homogeneous magnetic field is unhindered (parallel velocity ($v_\parallel$)).
The motion of the particle can therefore be described as the sum of the gyration plus the motion of the guiding center, around which the particle gyrates. Due to

external forces, fields or magnetic field inhomogenities the guiding center is subject to drifts, most importantly the $\mathbf{E}\times\mathbf{B}$ (due to an electric field ($\mathbf{E}$)), gradient B, curvature and polarization drift [5]. Furthermore the particles undergo Coulomb collisions at frequencies ν_{kl}, with k and/or l being electrons e or ions of type i. Reasonable approximations yield [5]:

$$\nu_{ei} \approx \left(\frac{1}{4\pi}\frac{n_i e^4}{\varepsilon_0^2 m_e^2}\ln\Lambda\right)\frac{1}{v_e^3} \tag{1.16}$$

$$\nu_{ee} \approx \left(\frac{1}{2\pi}\frac{n_e e^4}{\varepsilon_0^2 m_e^2}\ln\Lambda\right)\frac{1}{v_e^3+1.3v_{T_e}^3} \propto \nu_{ei} \tag{1.17}$$

$$\nu_{ii} \approx \left(\frac{1}{2\pi}\frac{n_i e^4}{\varepsilon_0^2 m_i^2}\ln\Lambda\right)\frac{1}{v_i^3+1.3v_{T_i}^3} \propto \left(\frac{m_e}{m_i}\right)^{1/2}\left(\frac{T_e}{T_i}\right)^{3/2}\nu_{ei} \tag{1.18}$$

$$\nu_{ie} \approx \left(\frac{1}{4\pi}\frac{n_e e^4}{\varepsilon_0^2 m_e m_i}\ln\Lambda\right)\frac{1}{v_i^3+1.3v_{T_e}^3} \propto \left(\frac{m_e}{m_i}\right)\nu_{ei} \tag{1.19}$$

In magnetized fusion plasmas the drifts (τ_d) are slower than the gyro motion but faster than the Coulomb collision rate, which in turn is faster than fusion reactions, yielding the following ordering [5]

$$\omega_c \gg \omega_\mathrm{d} \gg \nu_\mathrm{Coul.} \gg \nu_\mathrm{fus.} \tag{1.20}$$

Magnetic mirror

If the magnetic field is constant or changes only slowly along the field line (as compared to r_L and ω_c), the magnetic moment (μ)

$$\mu = \frac{m v_\perp^2}{2B} \tag{1.21}$$

is an adiabatic invariant. Due to conservation of the particle's kinetic energy, parallel kinetic energy is transferred to perpendicular kinetic energy when the particle moves to a region of stronger magnetic field, in order to keep μ constant. At a point where $v_\parallel$ becomes zero, the particle cannot proceed any further and is therefore reflected. Therefore, such a magnetic field configuration is called a magnetic mirror. Still in the single particle picture, all particles whose fraction of $v_\parallel$ to perpendicular velocity ($v_\perp$) fulfills the condition

$$\frac{v_\parallel^2}{v_\perp^2} < \frac{B_\mathrm{max}}{B_\mathrm{min}} - 1 \tag{1.22}$$

at $B = B_\mathrm{min}$ are reflected before $B = B_\mathrm{max}$. All other particles can pass. In a configuration with two magnetic mirrors (one on each side of the minimum B), the particles fulfilling (1.22) are trapped. Introducing the pitch angle (θ) by

$$\tan\theta = \frac{\|v_\perp\|}{\|v_\parallel\|}, \quad \theta \in [0, \pi/2], \tag{1.23}$$

the trapped-passing boundary (θ_tp) can be expressed by

$$\sin^2\theta_\mathrm{tp} = \frac{B_\mathrm{min}}{B_\mathrm{max}}, \quad \theta_\mathrm{tp} \in [0, \pi/2]; \tag{1.24}$$

particles with $\theta < \theta_\mathrm{tp}$ are passing, and particles with $\theta > \theta_\mathrm{tp}$ are trapped.

1.3.2 Magnetohydrodynamics (MHD)

Since the charge and currents carried by the particles in the plasma affect the electric and magnetic field, the single particle approach lacks self-consistency. Due to the large number of particles in the electron and ion distribution functions, we can and have to average over particles. This allows one to derive a self-consistent two-fluid model and subsequently the single-fluid magnetohydrodynamics (MHD) model under certain assumptions [5, 10]. In this model, the equations of conservation of mass (1.25), momentum (1.26) and energy (1.28), the Ohm's law (1.27) and Maxwell's equations (1.29–1.31) relate the density (ρ), velocity ($\mathbf{v}$), current ($\mathbf{J}$), pressure (p), $\mathbf{E}$ and $\mathbf{B}$.

$$\frac{\mathrm{d}\rho}{\mathrm{d}t} + \rho\nabla\cdot\mathbf{v} = 0 \tag{1.25}$$

$$\rho\frac{\mathrm{d}\mathbf{v}}{\mathrm{d}t} = \mathbf{J}\times\mathbf{B} - \nabla p \tag{1.26}$$

$$\mathbf{E} + \mathbf{v}\times\mathbf{B} = \eta_\parallel\mathbf{J} \tag{1.27}$$

$$\frac{\mathrm{d}}{\mathrm{d}t}\left(\frac{p}{\rho^\gamma}\right) = 0 \tag{1.28}$$

$$\nabla\times\mathbf{E} = -\frac{\partial\mathbf{B}}{\partial t} \tag{1.29}$$

$$\nabla\times\mathbf{B} = \mu_0\mathbf{J} \tag{1.30}$$

$$\nabla\cdot\mathbf{B} = 0 \tag{1.31}$$

In ideal MHD the resistivity ($\eta_\parallel$) is neglected ($\eta_\parallel = 0$) while it is included in resistive MHD ($\eta_\parallel > 0$).

MHD equilibrium model

A further simplification of the MHD model arises from the restriction to plasma equilibria ($\partial/\partial t = 0$) without static flows ($\mathbf{v} = 0$). The only remaining non-trivial equations, being the same for ideal and resistive MHD, read

$$\mathbf{J}\times\mathbf{B} = \nabla p, \tag{1.32}$$

$$\nabla\times\mathbf{B} = \mu_0\mathbf{J}, \tag{1.33}$$

$$\nabla\cdot\mathbf{B} = 0. \tag{1.34}$$

Applying a dot product with $\mathbf{B}$ and $\mathbf{J}$, respectively, the momentum equation (1.32) yields

$$\mathbf{B}\cdot\nabla p = 0, \tag{1.35}$$

$$\mathbf{J}\cdot\nabla p = 0. \tag{1.36}$$

Equation (1.35) means that the magnetic field lines lie in surfaces of constant pressure. In a confined plasma these pressure contours coincide with flux contours; the surfaces are called flux surfaces. Furthermore, due to (1.36), the current lines lie on the flux surfaces too. [5]
The common approach is to assume that the plasma as is in a near-equilibrium state: that is, that the equilibrium equations apply to lowest order, with higher-order perturbations.

Magnetic pressure

Combining the momentum equation (1.32) and Ampère's law by eliminating **J** yields the pressure balance perpendicular to the magnetic field

$$\nabla_\perp \left(p + \frac{B^2}{2\mu_0} \right) - \frac{B^2}{\mu_0} \kappa = 0, \tag{1.37}$$

with the perpendicular component of the gradient operator $\nabla_\perp = \nabla - \mathbf{b}(\mathbf{b}\cdot\nabla)$, the curvature vector $\kappa = \mathbf{b}\cdot\nabla\mathbf{b}$ and the magnetic field direction $\mathbf{b} = \mathbf{B}/B$.
The term $B^2/2\mu_0$ is called magnetic pressure. The ratio of thermal to magnetic pressure is the normalized pressure factor (β)

$$\beta = \frac{\langle p \rangle}{B_0^2/2\mu_0}, \tag{1.38}$$

where $\langle p \rangle$ is the volume-averaged thermal pressure. [5]

1.3.3 Magnetic confinement fusion concepts

One of the oldest concepts in MCF is the mirror machine, a linear device with homogeneous magnetic field and a magnetic mirror on each of the two ends. However, particles with a small pitch angle escape through the mirrors and this passing region of the distribution function is refilled by scattering through the trapped-passing boundary. This constant rate of loss defines a confinement time, τ_E. Additional effects decrease τ_E even further. It soon became clear that break-even ($Q = 1$) cannot be reached with such a device. To remove the end-losses the magnetic field lines (or more generally flux surfaces) have to close onto themselves. This can be done by bending the linear device into a torus. All important MCF concepts that are pursued at the moment are indeed toroidal devices, namely, in order of increasing importance, reversed field pinch (RFP), stellarator and tokamak.
A simple torus with a magnetic field only in the toroidal direction is not viable: due to the $1/R$ dependence of **B**, there is a gradient B drift that leads to charge separation and a subsequent vertical **E**. The resulting $\mathbf{E}\times\mathbf{B}$ drift points radially outwards, so that the plasma is not confined. To obtain a stable equilibrium, an additional magnetic field component in the poloidal direction is required.

Stellarator

In a stellarator, the toroidal as well as the poloidal magnetic field are created by external coils. The required shape and/or configuration of the coils is extremely challenging from the engineering point of view. Already the design optimization requires, due to the lack of toroidal symmetry, powerful numerical tools that became available only in the end of the 20$^\text{th}$ century. The Stellarator Wendelstein 7-X, starting operation in 2015 is shown in Fig. 1.2 as an example.
In a stellarator, there is no induced plasma current, which allows, in principle, steady-state operation and, as an additional advantage, the stellarator lacks some of the instabilities that are inherent to tokamaks. However, since there is no

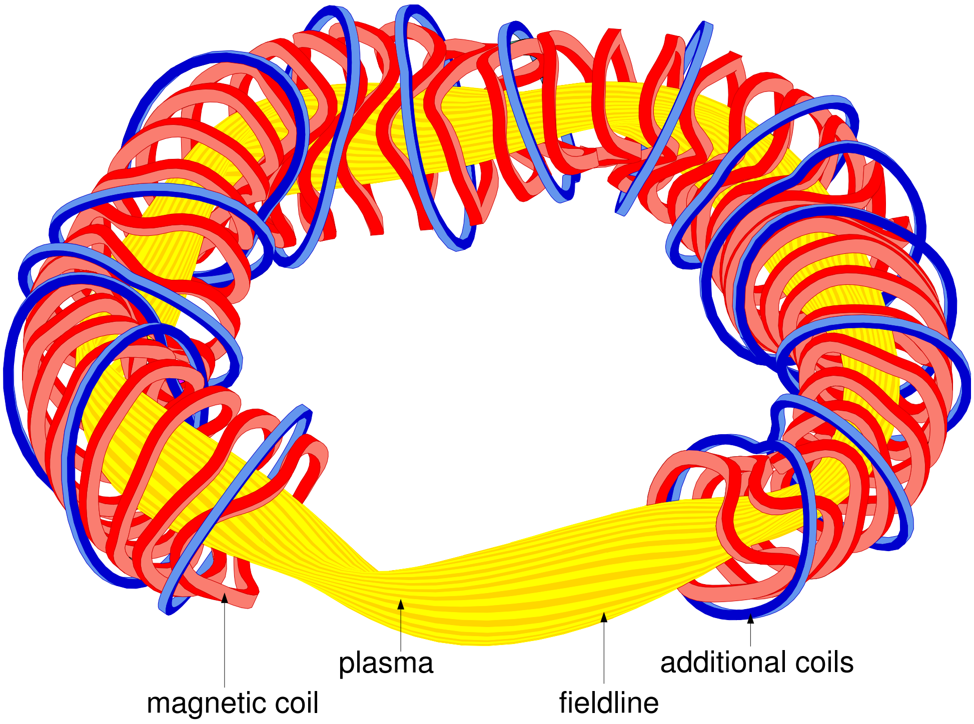

Figure 1.2: Schematics of the stellarator Wendelstein 7-X [11]

ohmic heating, all the thermal energy has to be provided by auxiliary heating systems. Furthermore, all currents in the plasma, such as Pfirsch-Schlüter currents, change the magnetic field, so they have to be minimized or taken into account directly in the design phase.

Tokamak

The tokamak is the currently most advanced MCF concept. It has reached the highest triple product coming close to $Q = 1$ in TFTR, JT-60 and JET. The next generation device ITER, that will enable studies on a burning plasma for the first time, is under construction. As this thesis addresses tokamak plasmas, they will be described in more detail in the following section.

1.3.4 Tokamak

In a tokamak the toroidal magnetic field (B_ϕ) is created by a set of equal toroidal field (TF) coils. The poloidal magnetic field (B_θ) is primarily created by a toroidal current in the plasma, although it is further adjusted by poloidal field (PF) coils for position and shape control. The plasma current (I_p) is induced by a transformer, the central solenoid, and provides an efficient way of heating plasma up to temperatures in the keV range. This ohmic heating is one of the main reasons for the success of the tokamak concept already in the early days of fusion research. The toroidal symmetry of the system simplifies measurements, data analysis and interpretation.

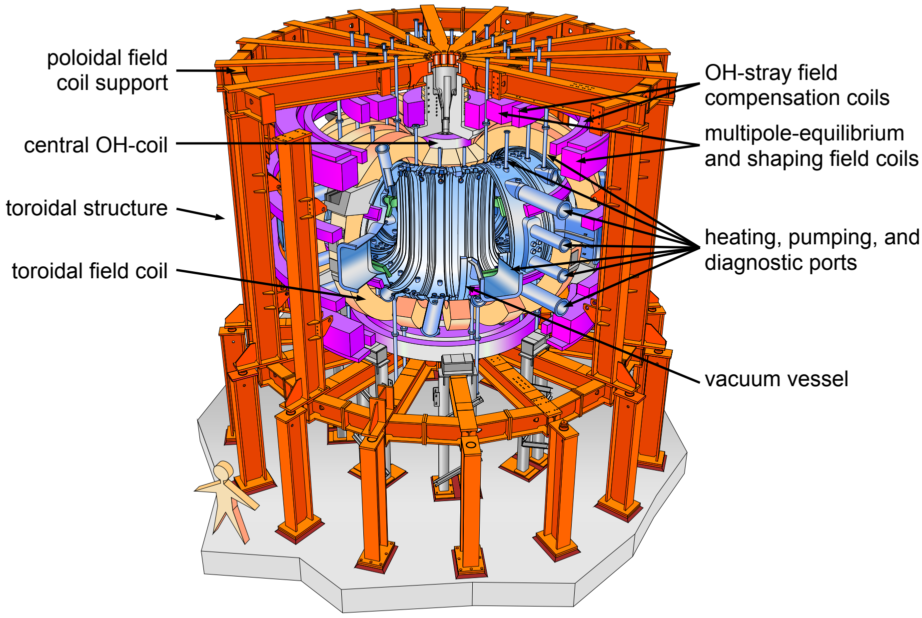

Figure 1.3: Schematic drawing of a typical tokamak: ASDEX Upgrade [11]

Usually, a tokamak can only be operated in pulsed mode since the current in the transformer has to be ramped. However, it has already been demonstrated that advanced scenarios allow the sustainment of the plasma current by bootstrap current and current drive only (fully non-inductively, without using the transformer)[12, 13, 14].

Another drawback of a plasma current is that it comes inherently with several plasma instabilities. Those can cause either reduced confinement or even a sudden loss of the plasma (disruption). Especially in the largest tokamaks the energy stored in the plasma, including the current, can cause serious damage during disruptions. This problem can be tackled by advanced plasma control techniques [15, 16].

Main parameters

The size of the plasma can be characterized by its major radius (R) and minor radius (a). The resulting inverse aspect ratio (ϵ) is defined as

$$\epsilon = \frac{a}{R} \tag{1.39}$$

Due to the superposition of the toroidal and poloidal magnetic fields, the magnetic field lines wind around the plasma center in nested flux surfaces. The number of toroidal turns a field line performs for one poloidal is defined as the safety factor (q). In standard scenarios q rises monotonically from the plasma center to the edge, while current research includes also advanced scenarios with negative magnetic shear (s) (logarithmic radial derivative of q) in the center.

The boundary of the plasma is defined by the last closed flux surface (LCFS) and surrounded by the scrape-off layer (SOL), which is unconfined as it is composed of open field lines. The LCFS can either touch the first wall at a so-called limiter (limited plasma) or be in a diverted configuration. In the divertor configuration the poloidal field vanishes at one or more points on the LCFS, the X-points. The LCFS shares these X-points with two or more divertor legs that intersect the wall. Since the confined plasma itself does not touch the wall in the divertor configuration the impurity transport from the wall into the plasma is usually highly reduced as compared to limited plasmas. This and several other advantages make the diverted configuration the favored one for a future fusion reactor. In current research however, both limited and diverted plasmas are investigated.
Usually, the shape of the poloidal cross section of the LCFS deviates from a circle. This deviation is described by the elongation (κ), triangularity (δ), squareness (ζ) and higher order corrections. The LCFS and the whole equilibrium can be computed by solving the so-called Grad-Shafranov equation. It is derived (in (R,Z) coordinates) from the ideal MHD model assuming toroidal asymmetry [10]. Defining the elliptic operator

$$\triangle^* := R^2\nabla\cdot\left(\frac{\nabla}{R^2}\right) = R\frac{\partial}{\partial R}\left(\frac{1}{R}\frac{\partial}{\partial R}\right)+\frac{\partial^2}{\partial Z^2} \tag{1.40}$$

it reads

$$\triangle^*\psi = -\mu_0 R^2\frac{dp}{d\psi} - F\frac{dF}{d\psi} \tag{1.41}$$

for the stream function (ψ). The poloidal flux (ψ_{pol}), $\mathbf{B}$ and $\mathbf{J}$ are obtained by

$$\psi_{\mathrm{pol}} = 2\pi\psi, \tag{1.42}$$

$$\mathbf{B} = \frac{1}{R}\nabla\psi\times\mathbf{e}_\phi + \frac{F}{R}\mathbf{e}_\phi, \tag{1.43}$$

$$\mu_0\mathbf{J} = \frac{1}{R}\frac{dF}{d\psi}\nabla\psi\times\mathbf{e}_\phi - \frac{1}{R}\triangle^*\psi\mathbf{e}_\phi. \tag{1.44}$$

The Grad-Shafranov equation is solved in practice under the constraints provided by the magnetic measurements and the known coil currents. The outward shift of the magnetic axis that is found from the solution of the Shafranov equation as compared to concentric flux surfaces is called Shafranov shift (Δ).
There are several flux surface labels that introduce a radial coordinate in the poloidal cross section (minor radius). The poloidal flux surface label (ρ_{pol}) is defined as

$$\rho_{\mathrm{pol}} = \sqrt{\frac{\psi_{\mathrm{pol}}-\psi_{\mathrm{pol,axis}}}{\psi_{\mathrm{pol,LCFS}}-\psi_{\mathrm{pol,axis}}}}. \tag{1.45}$$

and therefore ranges from 0 on the magnetic axis to 1 on the LCFS. In this thesis, mainly the toroidal flux surface label (ρ_{tor}) is used, defined in the same manner, but based on toroidal flux (ψ_{tor}) instead of ψ_{pol}. Another common coordinate, ρ_{vol}, is based on the normalized volume enclosed by a flux surface.
The deviation of the toroidal magnetic field from toroidal symmetry, due to the finite extent of the magnets, is the so-called "magnetic ripple". The ripple amplitude ($\delta B/B$) is typically in the range of $0.08-1.5\%$ [17].

1.4 Auxiliary heating

To reach break-even ($Q = 1$) a plasma temperature of $T \approx 5-7\,\mathrm{keV}$ is required. From this point on, alpha heating starts to dominate and even higher temperatures and Q can be reached. This however also means that external heating has to be supplied in order to reach $T \approx 5-7\,\mathrm{keV}$.
The resistivity of the plasma decreases with temperature:

$$\eta \propto \frac{1}{T_e^{3/2}}. \tag{1.46}$$

Therefore, ohmic heating becomes less efficient with increasing temperature and the current is limited by several constraints. The analysis for typical parameters of a tokamak shows that the maximum temperature that can be achieved with ohmic heating alone is about $T \lesssim 3\,\mathrm{keV}$. [5]
Therefore additional heating is required and this can be provided by auxiliary heating systems. Some of these heating systems include also the capability of driving current in the plasma, which can be used to extend the pulse length (towards steady-state) or to tailor the current profile.
Currently, there are 4 main types of auxiliary heating systems that are all extensively used and researched on several tokamaks and other MCF experiments: electron cyclotron resonant heating (ECRH) and electron cyclotron current drive (ECCD), ion cyclotron resonant heating (ICRH), lower hybrid (LH) heating and lower hybrid current drive (LHCD) and neutral beam heating (NBH). [18]
This thesis focuses on ECRH and ECCD, the most robust and flexible technique. Its basics are introduced in the following section 1.4.1.

1.4.1 ECRH and ECCD

The principle of ECRH is the resonant absorption of electromagnetic waves by electrons at the electron cyclotron frequency (ω_{ce})(1.13) and its harmonics. As shown in [19], there are cut-off densities limiting the propagation of the waves at the resonant frequencies. For ordinary mode (O-mode) polarization the density cut-off occurs at the density associated with the plasma frequency (ω_p)

$$\omega_p^2 \leq \omega_{ce}^2, \tag{1.47}$$

while for the extraordinary mode (X-mode) the cut-off lies at

$$\omega_p^2 \leq \ell\,(\ell-1)\,\omega_{ce}^2, \quad \ell \geq 2. \tag{1.48}$$

Most tokamaks use 1st harmonic O-mode (O1) and/or 2nd harmonic X-mode (X2) heating because of their good access and high absorption efficiency, whereas 1st harmonic X-mode (X1), 2nd harmonic O-mode (O2) and 3rd harmonic X-mode (X3) are rarely used. Due to the LH cut-off, X1 can only be launched from the high field side (HFS) which is technically challenging owing to space limitations. O2 and X3 are poorly absorbed. X3 is usually used in tokamaks with relatively low magnetic field to keep the cut-off density sufficiently high.
The frequencies lie typically in the range $28-170\,\mathrm{GHz}$, where high-power microwaves can be generated by gyrotrons. These devices are very reliable and can

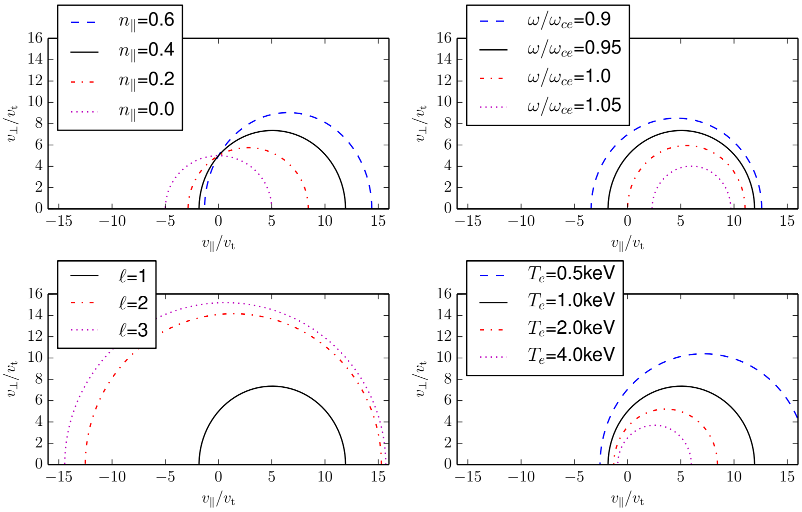

Figure 1.4: EC wave-particle resonance curves in velocity space. Based on $n_\parallel = 0.4$, $\omega/\omega_{ce} = 0.95$, $\ell = 1$ and $T_e = 1\,\mathrm{keV}$ (black line) one of these parameters is varied in each subplot as indicated in the legend. For $T_e = 1\,\mathrm{keV}$ the thermal velocity is $v_t = c/16$, so c coincides with the plot limits in this case.

deliver power in the MW range [20]. The gyrotrons can be far away from the harsh plasma environment [21], since the microwaves are transported in waveguides in vacuum or in air, where they propagate as narrow beams to the tokamak. There they are launched from mirrors and couple efficiently to the plasma, transferring their energy locally at the corresponding resonance layer. In state of the art tokamaks the injected power can be changed and steerable mirrors allow one to control the deposition location and current drive in real-time on the ms timescale. Therefore, the current profile can be effectively tailored by ECCD. In particular, the local and controllable power deposition can be used to develop internal transport barriers (ITBs), resulting in enhanced confinement and high bootstrap current fraction [22, 23]. This in turn may enable steady state operation of tokamak fusion reactors [12]. ECRH is also crucial for MHD instability mitigation, particularly by power deposition on magnetic islands [16, 24].
The basic physics of ECRH and ECCD is well understood [19] and introduced in the following, before presenting remaining open questions that will provide a motivation for the present research.

Wave-particle resonance

The Doppler-shifted relativistic resonance condition at the ℓ^{th} harmonic is [19]

$$\omega = \frac{\ell\omega_{ce}}{\gamma} + k_\parallel v_\parallel, \tag{1.49}$$

with the relativistic factor (γ)

$$\gamma = \frac{1}{\sqrt{1 - v^2/c^2}} \tag{1.50}$$

and the component of the wave vector (**k**) parallel to **B**

$$k_{\parallel} = \frac{\omega n_{\parallel}}{c}. \tag{1.51}$$

In the velocity space $\left(v_{\parallel}, v_{\perp}\right)$ the resonance condition describes an ellipse with the major axis at $v_{\perp} = 0$, reducing to a circle centered on the origin for $n_{\parallel} = 0$ [19]. Typical cases are illustrated in Fig. 1.4, where

$$v_t = \sqrt{\frac{2k_B T_e}{m_e}}, \tag{1.52}$$

is the most probable velocity of an electron in a Maxwell-Boltzmann distribution (Maxwellian). It should be noted that the definition of v_t in literature is not consistent, the factor 2 is often omitted.

Current drive

Electron cyclotron (EC) waves do not accelerate electrons (significantly) directly in the parallel direction. However, there are two principles of current drive (CD) by EC waves in a toroidal plasma, described first by Ohkawa [25] and Fisch and Boozer [26]. In both cases the parallel propagation component ($n_{\parallel}$) is non-zero, but the resulting current drive direction is opposite.

Fisch-Boozer CD This process increases $v_{\perp}$ of electrons on the resonance layer without them crossing the trapped-passing boundary. The collision rate at their previous location is higher than at their current one, decreasing as $1/v^3$ (1.16)–(1.17). The pitch angle scattering towards equilibration (and symmetrization) is therefore more efficient in the previous location, yielding a net current in the direction opposite to the $v_{\parallel}$ direction in which the resonant interaction takes place.

Ohkawa CD The process pointed out by Ohkawa can be efficient if the resonance lies close to the trapped-passing boundary in velocity space. In that situation, slow passing electrons are accelerated into the trapped area, which is an asymmetric process with respect to $v_{\parallel}$. This $v_{\parallel}$ asymmetry is lost on the bounce (τ_{b}) time scale in the trapped region, such that the slower collisional detrapping (τ_{dt}) process is symmetric. The net effect is a current in the $v_{\parallel}$ direction in which the resonant interaction takes place.

Motivation

An improvement in the understanding of wave-particle interaction in plasmas and of the current drive mechanisms is one of the main goals of this thesis. The radio frequency (RF) waves are absorbed by cyclotron damping and the current drive is described by the Fisch-Boozer and Ohkawa models [19]. As these two models produce currents in opposite directions and their balance depends on the

details of the distribution function (particularly the trapped particles), a better understanding of the fundamental wave-particle interaction phenomena must rely strongly on modeling and experimental measurements. These combined numerical and diagnostic studies aim generally at characterizing the suprathermal electron population in space, velocity space (pitch angle) and time with regard to their creation by and their interaction with EC waves.
In particular, the electron distribution is investigated for theoretically predicted spatial asymmetries in the poloidal plane and co-counter current asymmetries measuring the enhanced bremsstrahlung emission in the forward cone due to the relativistic effects. It should be noted that the potential for achieving new physics insight is substantial since the measurement capabilities (Sec. 1.7) have never been available anywhere in the world in the presence of ECRH/CD.

1.5 MHD instabilities

Tokamak plasmas are prone to several MHD instabilities that can be characterized by and differ in several parameters. They occur under certain conditions and appear at specific locations. They can yield a different state with persistent modes or magnetic islands, recur periodically or end the plasma in a disruption. Usually, the effects of instabilities are unwanted since they cause the plasma to deviate from the programmed scenario. Degradation of the plasma performance (confinement), triggering of other instabilities [24] or high peak heat fluxes at the first wall (due to edge localized modes (ELMs)) are only examples of such negative results.
In the frame of this work, instabilities and modes in the plasma center are important. There, a significant fraction of the electron distribution function (e.d.f.) can be suprathermal and may interact with the modes. Such modes are the internal kink mode around $q = 1$ that responsible for the sawtooth [27] and the (electron) fishbone [28] instabilities. In addition, neoclassical tearing modes (NTMs) at the $q = 3/2$ and $q = 2$ surfaces can also have a significant impact on the central plasma, including the suprathermal electron distribution.

1.5.1 Sawtooth instability

Sawtooth crashes are a major instability localized at the $q = 1$ surface. This instability and the subsequent relaxation, resulting in sawtooth-shaped core density and temperature time traces, can be partly explained by the Kadomtsev model [27, 29]. This model describes the evolution of an internal $m = 1$ kink mode leading to magnetic reconnection; this in turn results in enhanced bulk plasma transport and subsequently a flattened temperature profile. However, the predicted sawtooth period is not consistent with experiments and partial reconnection has been observed too [30].

Magnetic reconnection and particle acceleration

The magnetic reconnection itself is described by the Petschek model adding pairs of shocks to the Sweet-Parker diffusive layer in the MHD reconnection theory

[31, 32]. But the establishment and role of the anomalous resistivity in this model is not well understood. Recent advances in the topic were achieved with a model of collisionless reconnection that is no longer based on MHD but on a two-fluid or kinetic description [33, 34]. During the reconnection process electrons are accelerated to suprathermal energies, as observed in the T-10 and TCV tokamaks [35, 36]. Two main acceleration processes can be distinguished: direct acceleration by (mean) electric fields and stochastic acceleration (first proposed by Fermi) in a turbulent environment [37]. Direct acceleration occurs for instance at density cavities on the border of magnetic islands [38]. The shock-wave acceleration at the shocks described by the Petschek model can be divided into the (direct) drift acceleration, due to curvature and gradient drift, of particles crossing the shock [39] and the stochastic acceleration of particles bouncing between a pair of slow shocks [40] or undergoing Fermi acceleration at a fast shock [41].

Motivation

The observation of electrons accelerated in the current sheet during magnetic reconnection may be one of the keys to a fundamental understanding of the sawtooth instability and possibly to a mitigation of its negative effects, such as a reduction of energy and particle confinement and the triggering of secondary deleterious instabilities such as NTMs.

1.5.2 Electron fishbones

Fast ions can excite MHD instabilities near the $q = 1$ surface, that are, due to the characteristic bursty (and frequency chirping) signal on the Mirnov coils, called "fishbones". This phenomenon was first observed in the PDX tokamak during NBH, causing a 20 – 40% loss of beam heating power [42]. The result was also confirmed and studied on other tokamak experiments like JET [43, 44, 45]. The mode is identified as a $m/n = 1/1$ internal kink whose excitation can be explained by the resonant interaction of fast ions at the precession velocity corresponding to the phase velocity of the mode [28, 46].

Recently, similar modes were observed under conditions without ions fulfilling the resonance condition, but under the presence of strong ECRH and/or LHCD. Therefore, it is proposed that fast electrons excite these "electron fishbones", that were first seen in DIII-D [47] and subsequently in other tokamaks [48, 49, 50, 51], under certain conditions.

Up to now there is no complete picture of the electron fishbone instability. The experimental observations can be explained qualitatively quite well with an instability analysis based on the proposed underlying mechanisms [52, 53, 54, 55]. However, there are significant differences in the observations on the various tokamaks, revealing that a more systematic experimental study may strongly advance the qualitative description and possibly allow a quantitative description of the electron fishbone mode.

Experimental evidence

The first electron fishbone observations, on DIII-D during off-axis ECCD with the resonance layer on the HFS, close to the $q = 1$ surface, and NBH, are the only observations in non-circular plasmas that have been reported. The brief description in [47] was not followed by more detailed publications.
On the HL-1M tokamak the mode occurred (without the presence of energetic ions) during ECRH on the HFS near the $q = 1$ surface. Additional LHCD enhanced the mode but could not drive it alone [48]. LHCD alone, but at much higher power than on HL-1M, lead to the observation of the fishbone instability on Frascati Tokamak Upgrade (FTU). There, the redistribution of suprathermal electrons due to the mode is claimed to be observed too [49].
On HL-2A, fishbone-like observations were then reported during ECRH not only on the HFS at the $q = 1$ surface, but also on the low field side (LFS) at the $q = 1$ surface. Additionally, the resonance condition for the mode excitation was investigated more in detail, the fast electron hard X-ray bremsstrahlung emission was measured and the mode was compared to ion fishbones in the same machine [50, 56, 44]. Electron fishbones including transitions to higher multiples like $^2/_2$ and $^3/_3$ were observed on Tore Supra during LHCD discharges [51] and compared to the FTU results in [53]. Finally, fishbone-like modes are also reported from Alcator C-Mod [57], also during LHCD.

Current understanding

The current understanding is that the mode occurs close to the $q = 1$ surface, preferentially with low or reversed central shear, even with the minimal q ($q_{\min}$) being slightly above unity [55]. In the latter case there are no sawteeth, consistent with several observations [47, 53], whereas fishbones with intermittent sawteeth are also possible [48, 49, 57].
In any case, there is a significant dependence on the local magnetic shear, also via the impact on penetration of shaping [55], of the drift reversal of the precessing fast electrons driving the mode. Furthermore, an inverted spatial gradient of the suprathermal tail of the e.d.f. is required [52], usually accompanied by hollow central pressure profiles. In terms of plasma shape, circular plasmas are more prone to the instability than elongated plasmas [55]. Regarding phase space, a significant population of barely trapped energetic electrons is most likely to drive the instability. Barely passing electrons may also resonate with the mode, whereas the role of freely passing particles seems to be limited to the regulation of the pressure and current profiles [52].
The change of the radial position of the mode during a burst can be attributed to the evolution of the equilibrium (q-profile) [53]. The characteristic frequency chirping is connected to the evolution of the resonant electrons' energy and subsequent change in resonant condition. This is also accompanied by a radial displacement of the mode and is reproduced in simulations [58].

Motivation

The main relevance of electron fishbone studies lies in their parallels to ion fishbones in future burning fusion plasmas. While only a small number of fast ions with large radial excursions account for ion fishbone excitation in present-day devices, the situation in plasmas with significant alpha particle (α) heating is thought to be closer to the current electron fishbone observations. This is mainly because large fractions of the particle species are suprathermal, but still in small orbits.
Moreover, electron heating systems allow for greater flexibility (e.g. heating location and CD) and consequently to explore a much larger parameter space as compared to NBH systems that are quite limited in this respect. On the diagnostics side the situation is similar: the various suprathermal electron diagnostics (see Sec. 1.7) provide a much better spatial, energy and time resolution than the most advanced fast ion diagnostics such as neutron detectors [59].
Therefore the instability could be studied experimentally in much more detail in a tokamak with high electron heating power and state of the art suprathermal electron diagnostics. This would allow, on the one hand, to analyze the excitation model quantitatively, including the importance of the different regions in velocity space (barely/deeply trapped/passing), and also with respect to plasma shaping. On the other hand, experimental observation of suprathermal electron transport due to the mode is feasible with the newest diagnostics. Since fishbones could have a significant impact on transport in the plasma center of future reactors, the main goal is to characterize scenarios prone to fishbones and explore mitigation techniques, with focus on the planned advanced scenarios with low or reversed central shear.

1.6 Suprathermal electrons

The ensemble of electrons in a plasma can be described by a distribution function f defined in real and velocity space, as solution of the Boltzmann equation (1.62). In the limit of stationary thermal equilibrium, this is a Maxwellian

$$f(\mathbf{r},\mathbf{v}) = f_{T_e}(\mathbf{r},\mathbf{v}) = n_e(\mathbf{r})\left(\frac{m}{2\pi k T_e}\right)^{3/2}\exp\left(-\frac{m\,\|\mathbf{v}\|^2}{2kT_e}\right), \tag{1.53}$$

characterized by n_e and electron temperature (T_e). Its extension to relativistic temperatures, the Maxwell-Jüttner distribution [60, 61], is not required in tokamak plasmas since $kT \lesssim 50\,\mathrm{keV} \ll 511\,\mathrm{keV} = mc^2$.
However, in plasmas with significant electron heating and/or electron acceleration due to other effects such as magnetic reconnection, the e.d.f. deviates significantly from an equilibrium state and therefore from a Maxwellian. The difference lies mainly in the higher energy range. This part of the distribution function is called the suprathermal electrons, with energies (E) in the non-relativistic range

$$kT_e \ll E \leq 511\,\mathrm{keV} \tag{1.54}$$

and runaway electrons (Sec. 1.6.1) with (highly) relativistic energies in the MeV range.

Analytically, such e.d.f.s can sometimes be well approximated by the sum of two Maxwellians. This so-called Bi-Maxwellian is composed of a thermal bulk (T_e) and a suprathermal tail, where the smaller fraction of the e.d.f. resides at a higher temperature, the suprathermal electron temperature ($T_{e,2}$). Bi-Maxwellians are a reasonably good and simple approximation for EC heated plasmas [62].
A generalization of Maxwellians are Kappa-distributions and Bi-Kappa distributions, where the latter are characterized by differing temperatures in the parallel and the perpendicular directions. These e.d.f.s are widely used in astrophysical plasmas. More details about analytical e.d.f.s can be found in appendix A.
In the scope of ECCD, usually a numerical treatment of the e.d.f. is necessary, in order to describe the suprathermal electrons, i.e. to capture the complicated dynamics in velocity space, correctly. But even in this case a large fraction of the electrons remains in the thermal bulk. Thus, the modeled distribution function consists often of a Maxwellian (f_{T_e}) and a numerical correction (δf)

$$f = f_{T_e} + \delta f. \tag{1.55}$$

The modeling of e.d.f.s is discussed in more detail in Sec. 1.8.

Motivation

Although the fraction of suprathermal electrons is usually smaller than the thermal bulk of the e.d.f., they are of significant importance. Their dynamics in real and velocity space govern the physics of electron heating and current drive by EC and LH waves. While ECRH/CD and LHCD are well-established and robust tools for heating and current drive, there remain open questions on the suprathermal electron distribution, especially concerning transport and quasilinear effects. An assessment of the role of the detailed phase-space dynamics in determining the properties of ECRH and ECCD is of special interest regarding its more and more sophisticated usage as a practical fusion plasma control tool.
Separate from the creation of suprathermal electrons by auxiliary heating or MHD events, the characteristics and dynamic behavior of these fast electrons in the plasma form an additional, fundamental area of research. Several competing processes are at play in velocity space, including collisional pitch-angle scattering and slowing down, quasilinear RF diffusion and anomalous turbulence-driven transport; collisional and turbulent effects are also involved in the spatial transport [3]. Additionally, the interaction of pre-existing suprathermals with magnetic islands and reconnection events is a key issue. Therefore, the ultimate goal is to quantify and characterize the transport of the suprathermal electrons individually for each of the relevant phenomena, especially by studying the time scales and the relevant parametric dependencies with the aid of dedicated experiments and modeling.

1.6.1 Runaway electrons

For fast electrons the Coulomb collision frequency (1.16)–(1.17) decreases rapidly with velocity ($\sim \frac{1}{v_e^3}$), enabling a part of the electron distribution to gain more energy through acceleration by the electric field of the tokamak (though relatively weak) than they lose in the rare collisions. This situation is unstable and the electrons at these highly relativistic energies ($\gg 511\,\text{keV}$), called “runaways”, eventually escape the plasma and hit the first wall. As they carry a substantial amount of energy, this phenomenon reduces the plasma energy; in addition, the escaping runaway electrons can, focused in beams, cause serious damage to the first wall. Fortunately their numbers are only significant if the electric field exceeds a critical parameter, the Dreicer field (E_D) [63, 64, 65, 66]. It is defined as

$$E_D = \frac{m_e \nu_{ei} v_t}{e}, \tag{1.56}$$

where electron-ion collision frequency (ν_{ei}) and v_t were defined in (1.17) and (1.52), respectively. Since E_D is proportional to n_e, the number of runaway electrons is strongly reduced in plasmas with densities of 10^{20}m^{-3} or more as is the case in most current experiments as well as in fusion reactors [5]. Nevertheless, even when these conditions are satisfied in the flat-top phase, runaway electrons can still play an important role during the start-up phase and especially during disruptions [35, 67].

Motivation

Advances in the understanding of particle acceleration during magnetic reconnection may be applied to mitigate runaways in these regimes. Moreover, the measurement and study of runaway electrons can contribute to the mitigation of plasma disruptions, which is one of the main concerns for future tokamak experiments and fusion reactors.

1.7 Suprathermal electron diagnostics

There are two main diagnostic techniques to study suprathermal electron dynamics in tokamak plasmas: the measurement of hard X-ray (HXR) bremsstrahlung radiation ($5\,\text{keV} - 1\,\text{MeV}$) that is emitted when suprathermal electrons collide with plasma ions, and the electrons' cyclotron emission (ECE) [68]. Both techniques provide only indirect information about the e.d.f., convolved with other quantities, as can be seen in the following, more detailed discussion.

1.7.1 Electron cyclotron emission (ECE)

Due to gyro motion of charged particles in magnetized plasmas, which is an accelerated motion, the electrons emit electron cyclotron radiation. Its frequency is expressed in (1.49) [68] and can be rewritten as [69]

$$\frac{\omega}{\ell \omega_{ce}} = \frac{1}{\gamma} \frac{1}{1 - \beta_{\parallel} \cos\theta}, \tag{1.57}$$

with terms from (1.49), the normalized velocity $\beta := v/c$, its parallel component $\beta_{\parallel} := v_{\parallel}/c$ and the angle of the wave vector to the magnetic field (θ). The emission occurs in both polarizations (O- and X-mode) at all ℓ^{th} harmonics.
The first term on the r.h.s. of (1.57) causes a relativistic frequency downshift,

whereas the second one yields, for high forward parallel velocities in the case $k_\parallel \neq 0$, a Doppler upshift. For a Maxwellian e.d.f. these shifts cause corresponding broadenings.
The spectral power density is given by the Schott-Trubnikov formula [69]

$$\frac{d^2P}{d\omega d\Omega_s} = \frac{e^2\omega^2}{8\pi^2\varepsilon_0 c}\sum_{\ell=1}^{\infty}\left[\left(\frac{\cos\theta-\beta_\parallel}{\sin\theta}\right)^2 J_\ell^2(\xi)+\beta_\perp^2 {J'_\ell}^2(\xi)\right]\frac{\delta\left(\left[1-\beta_\parallel\cos\theta\right]\omega-m\omega_{ce}\right)}{1-\beta_\parallel\cos\theta} \tag{1.58}$$

with

$$\xi := \frac{\omega}{\omega_{ce}}\beta_\perp\sin\theta, \tag{1.59}$$

that yields the following emissivity $j(\omega,\theta)$ in for a given e.d.f. f [69]:

$$j(\omega,\theta) = c^3\int\frac{d^2P}{d\omega d\Omega_s}\left(1-\beta_\parallel\cos\theta\right)f\left(\beta_\parallel,\beta_\perp\right)2\pi\beta_\perp d\beta_\parallel d\beta_\perp \tag{1.60}$$

In a thermal tokamak plasma (the magnetic field decreases radially strictly monotonically and the plasma size is limited such that the resonance ω occurs at only one position r and harmonic) the observed intensity for an optically thick harmonic (e.g. X2) relates directly to the T_e profile [69]

$$I(\omega) = \frac{\omega^2 T_e(r)}{8\pi^3c^2}. \tag{1.61}$$

This principle is regularly used in a configuration with perpendicular observation (minimal Doppler broadening) from the LFS as a T_e diagnostic with excellent spatial and good temporal resolution [69]. Despite the optimization for T_e measurement, it can be significantly disturbed by deviations from a Maxwellian. This unwanted disturbance can hardly yield information on the suprathermal electrons since it is a complicated integral of the e.d.f., ω_{ce} and θ.
In contrast to that, there are several electron cyclotron emission (ECE) diagnostic configurations that are optimized to extract more detailed information on the suprathermal part of the e.d.f.. These are explained in the following.

Vertical ECE

By observing the plasma in the vertical direction the energy (relativistic downshift) can be determined directly from the observed frequency since the magnetic field is practically constant along the view line and the Doppler shift is not present ($\theta = \pi/2$).
A drawback of this approach is that the measurement is line integrated since the emitting suprathermals are tenuous and therefore generally constitute an optically thin population. This also leads to the necessity of a beam dump on the other side of the plasma, in order to avoid signal from reflections disturbing the measurement. [68]

HFS ECE

Viewing from the HFS, still perpendicular to the magnetic field, one obtains measurements with the frequency proportional to B/γ, thus depending on the product

γR. This complicates the interpretation of the data that is integrated over about one optical depth in radial direction from electrons of correspondingly varying energy. [68]

Oblique LFS ECE

While the Doppler upshift is unwanted and avoided by perpendicular viewing direction in the ECE diagnostic arrangements discussed up to now, it is the main point of interest in the oblique LFS configuration.
The measurement is usually tangential in order to limit the observation to a well-defined minimal radius. Since a maximal radius can be chosen by ω and $k_\parallel$, spatially and energetically localized measurements are possible. [68, 70]

1.7.2 Hard X-ray bremsstrahlung emission

During Coulomb collisions (mainly with plasma ions, but also electrons and the first wall), electrons emit continuum bremsstrahlung emission. The energy of the emitted radiation depends on the impact parameters and ranges up to the electron's initial energy. For suprathermal electrons in tokamak plasmas it lies typically in the HXR range (5-500 keV). See appendix B for more details.
Due to relativistic effects the emission is enhanced in the forward direction of the incident electron, even if its energy is only slightly relativistic ($\gtrsim 20$ keV). The emission anisotropy then increases rapidly for electrons towards and beyond relativistic energies ($\gtrsim 511$ keV) [71, 72, 73]. Therefore, an anisotropic suprathermal part of the e.d.f. results, in general, in anisotropic HXR emission.

Most HXR diagnostics consist of cameras with detectors behind thick tungsten or lead collimators. Each detector (or pixel) of the camera then observes the integrated emission along its line of sight (LoS). The simplest systems are single detectors behind pinholes [74, 75]. Multi-detector cameras can be arranged with one-dimensional (1D) detector arrays in the poloidal plane as a single camera or tomographic system [76], as one- or two-dimensional cameras with a tangential view [72, 77] or combined tomographic and tangential systems [1].

The originally employed scintillation detectors are still in use [74]. New systems, however, usually implement more compact high-Z semiconductor detectors such as cadmium-telluride ($CdTe$), that were first adopted in Tore Supra [76] and subsequently on other tokamaks including TCV [1]. On the low energy side (2-20 keV), silicon drift detectors (SDDs) are also used [78, 75].
The photon statistics in the HXR-range are usually quite low in today's tokamaks. To increase the time resolution, the diagnostic can be operated in current mode, integrating over the whole incident photon energy range [77]. However, the more common operation mode is as a spectrometer. Here, the individual incident photons appear as pulses in the signal. These are detected and analyzed using analogue [76] or digital [1, 2] pulse processing, in order to obtain time resolved spectra. The statistics, and thereby the resolution, can be increased by techniques such as coherent and conditional averaging [62, 79].

Direct data analysis is quite limited but still possible. In the poloidal plane, the HXR emission is still nearly isotropic, since the e.d.f. anisotropy is mainly parallel to **B**. Therefore, using standard tools [80], tomographic inversion allows one to retrieve 1D radial or two-dimensional (2D) poloidal HXR emission profiles [76, 62]. Subsequently, the emission can be fit to a sum of two Maxwellians (Bi-Maxwellian) in order to obtain suprathermal electron and density profiles [62]. Multi-Maxwellian fitting of the e.d.f. with 4 parameters (including anisotropy) has been demonstrated in the PLT tokamak for LHCD, but without any spatial resolution [81], which is required for highly localized heating schemes such as ECRH. A general inversion from HXR measurements to three-dimensional (3D) e.d.f.s is impossible, since the problem is highly under-determined and badly conditioned for realistic experimental data (limited number and position of detectors). One relies therefore, as in the case of ECE, strongly on modeling of the e.d.f. in conjunction with synthetic diagnostics, described in the following section.

1.8 Electron distribution function modeling

The e.d.f. f (Sec. 1.6) is the solution of the Boltzmann equation

$$\frac{\partial f}{\partial t} + \mathbf{v}\cdot\nabla_{\mathbf{r}} f + q_e \left[\mathbf{E}(\mathbf{r},t) + \mathbf{v}\times\mathbf{B}(\mathbf{r},t)\right]\cdot\nabla_{\mathbf{p}} f = \left.\frac{\partial f}{\partial t}\right|_C \tag{1.62}$$

in 3D space, 3D momentum space and time. A general analytic solution of the equation is not available and it becomes clear quite easily, that numerical simulations in seven dimensions (7D) are not feasible. However, an inspection of the time scales and spatial symmetries involved establishes that this is not necessary, since the model can be reduced by several dimensions without losing significant information. The timescales order as

$$\frac{1}{\omega_{ce}} \ll \tau_{\mathrm{t}} \leq \tau_{\mathrm{b}} \ll \tau_{\mathrm{dt}} < \tau_{\mathrm{c}}, \tag{1.63}$$

with the gyro-motion being the fastest, followed by the transit time (τ_{t}) of passing particles, bounce time (τ_{b}) of trapped particles, the collisional detrapping time (τ_{dt}) for trapped particles and the collision time (τ_{c}) for passing particles due to Coulomb collisions. At a comparably slow timescale, but depending on the electric field and assumed diffusion coefficients, lie the electric field acceleration time (τ_{e}) and quasilinear diffusion time (τ_{ql}), respectively.
We are only interested in modeling at the timescales τ_{dt}, τ_{c}, τ_{e} and τ_{ql}, so the fast gyro-motion can be averaged out easily, yielding the electron drift kinetic equation

$$\frac{\partial f}{\partial t} + \mathbf{v}_{gc}\cdot\nabla_{\mathbf{r}} f = \mathscr{C}\left(f\right) + \mathscr{Q}^{\mathrm{RF}}\left(f\right) + \mathscr{E}\left(f\right) + \mathscr{H}\left(f\right) + \mathscr{T}\left(f\right) + \mathscr{S} \tag{1.64}$$

with the collision ($\mathscr{C}$), quasilinear RF diffusion ($\mathscr{Q}^{\mathrm{RF}}$), electric field ($\mathscr{E}$), synchrotron radiation ($\mathscr{H}$) and transport operators ($\mathscr{T}$) and optional source or sink terms ($\mathscr{S}$) on the r.h.s.. The quasilinear RF diffusion operator is usually provided by a ray-tracing code (LHCD, ECRH/CD), while NBH systems enter in the source term. The collision, electric field and radiation operators are well known from theory, whereas the transport term's diffusion coefficients have to be set by the

experienced user in comparison to the experimental observations in order to obtain reasonable results.
Spatially, there is obviously the toroidal symmetry of the tokamak configuration that can be used. If there is a significant magnetic field ripple it can be mimicked by an additional loss term. In the poloidal plane, the situation is a bit more complicated and requires a treatment in conjunction with the circular and bounce motion on the τ_t and τ_b timescales. Consequently, for the usual case of a single magnetic field minimum on the LFS, the e.d.f. can be bounce-averaged (over the circular and bounce motion), including a flux surface averaging of all plasma parameters in play. The e.d.f. is then defined on the flux surfaces. Strictly speaking, its numerical representation at each radial point is at the point of minimum magnetic field, where all trapped and passing electrons are present. The local distribution at an arbitrary point in the poloidal plane is obtained by mapping of the velocity space along increasing magnetic field. [82, 83]
These approximations result ultimately in the drift kinetic / Fokker-Planck equation for the e.d.f. in 3D. It comprises the radial spatial dimension and two dimensions in velocity space (parallel and perpendicular to $\mathbf{B}$). One can solve the equation for a stationary or time-dependent solution.

1.8.1 Synthetic diagnostics

Comparison of theory, numerical simulations and experimental measurements are important in physics in general, but crucial in the field of suprathermal electron dynamics. On the one hand, the theoretical model and numerical simulations are well-founded and robust, but a few aspects, such as suprathermal electron transport, require an empirical model with free parameters. On the other hand, the highly convoluted dependencies of experimental measurements (ECE, HXR) prohibit a direct inversion for the e.d.f.. This dilemma can be faced by employing synthetic diagnostics, that are available for both ECE and HXR.

Synthetic ECE diagnostic

For a synthetic ECE diagnostic, several effects need to be taken into account making the efficient implementation of such a module a challenging task. First, EC radiation is emitted at each position in the plasma, according to (1.60). This can be computed quite easily. But then, the wave does not propagate straight to the diagnostic, its path has to be computed by ray-tracing. Furthermore, it can be attenuated by absorption elsewhere in the plasma. Moreover, an additional complication arises, at least in some configurations, from reflections at the first wall.

Synthetic HXR diagnostic

A synthetic HXR diagnostic is, in comparison to ECE, easier to implement since the LoS (chords) are straight and re-absorption and reflection are negligible. In principle, it is sufficient to compute the emission in the detector direction along the detector's chords and integrate it. However, the HXR emission can also be computed in the whole poloidal plane, which provides additional information.

This is then followed by a line integration along the individual chords, yielding the same result as the first method at increased computational effort.

1.9 Outline

The introduction (Ch. 1) is followed by the description of the tools used in the course of the thesis (Ch. 2). Subsequently, the most important tools, the hard X-ray tomographic spectrometer (HXRS) diagnostic and the Fokker-Planck codes CQL3D and LUKE are introduced in Ch. 3 and Ch. 4, respectively.
The toroidal and poloidal HXR emission asymmetries are presented in Ch. 5, before the ECRH/CD suprathermal electron dynamics including transport and quasi-linear (QL) effects are addressed in Ch. 6.
Furthermore, the interaction of suprathermal electrons with internal MHD events like sawtooth crashes and further MHD instabilities is examined in Ch. 7, followed by the electron fishbone study in Ch. 8.
Finally, the conclusions are drawn (Ch. 9).

Chapter 2

Experimental and numerical tools

An overview of the experimental and numerical tools applied to suprathermal electron studies in tokamak plasmas is presented in this chapter. The main experimental tool is TCV, including its control, ECRH/CD and diagnostic systems (Sec. 2.1–2.4). The thesis work included calibration and installation of the HXRS diagnostic, improvements in the TXDA (remote control from Vsystem via PLC), reactivation of the PHAV and XTePro and the database integration of and responsibility for all these diagnostics. The elementary and high level data analysis tools (Sec. 2.5–2.6) are original contributions; equally the TCV data interfaces to the Fokker-Planck codes CQL3D (CQL3Dpy) and LUKE (Sec. 2.7) together with post-processing tools including FPCDF (Ch. 4).

2.1 TCV

The main experiments for this thesis were performed at the Tokamak à Configuration Variable (TCV) (Fig. 2.1, Tabs. 2.1–2.2) [85] at the École Polytechnique Fédérale de Lausanne (EPFL), Centre de Recherches en Physique des Plasmas (CRPP) in Lausanne. This conventional aspect ratio tokamak (major radius (R) 0.88 m, minor radius (a) 0.25 m) is a major European fusion facility [86, 87], inte-

Vacuum vessel	
material	stainless steel (DIN 1.4429 /AISI 316LN)
R	0.88 m
height (poloidal cross section)	1.54 m
width (poloidal cross section)	0.56 m
thickness	10 mm
internal surface	23 m^2
First wall	
material	polycrystalline graphite (R6650MX2)
number of graphite tiles	1692
coverage	> 90 %

Table 2.1: Main TCV parameters [84]

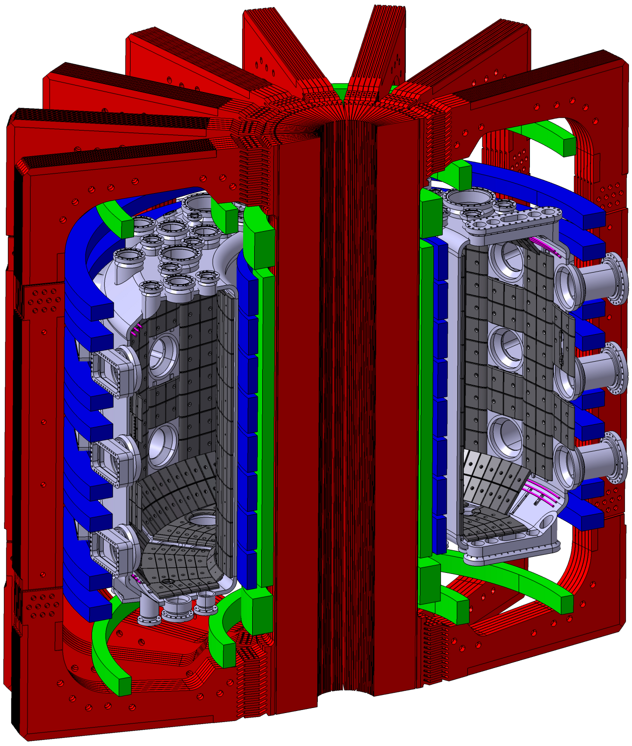

Figure 2.1: TCV half cut with TF coils (red), PF shaping coils (blue), CS and stray-field compensation coils (green), fast vertical control feedback coils (purple), vacuum vessel with ports (light gray) and graphite tiles (dark gray).

Coil system	coils	power supplies	B_{max}	I_{max}
TF	16	1	1.54 T (on axis)	
CS	7	2		27 kA
PF	16	16		7 kA
In-vessel feedback & PF	2	1		2 kA

Table 2.2: TCV magnetic field, coil and power supply parameters [84]

TCV plasma parameter	value
R	0.88 m
a	0.25 m
ϵ	3.5
κ	$[0.9, 2.8]$
δ	$[-0.8, 0.9]$
I_p	$\leq 1.2\,\mathrm{MA}$
duration	$\approx 2\,\mathrm{s}$
Core n_e	$\left[5\cdot 10^{18}, 2\cdot 10^{20}\right]\mathrm{m}^{-3}$
Core T_e (ohmic)	$\leq 1\,\mathrm{keV}$
Core T_e (ECRH/ECCD)	$\leq 15\,\mathrm{keV}$
Core ion temperature (T_i)	$\leq 1\,\mathrm{keV}$

Table 2.3: TCV plasma parameters [84]

grated in the medium-size tokamak (MST) program. Besides supporting ITER by carrying out studies relevant for this next step fusion experiment, its mission is also to explore alternative paths to a fusion reactor [86].
The elongated rectangular shape of the vacuum vessel and first wall cross section and the 16 individually controllable shaping (PF) coils give TCV unique variable shaping capabilities that are also reflected in its name. In general, the range of plasma parameters that can be obtained in TCV is large (Tab. 2.3). It is only the combination of this flexibility with a fast real-time control system [88], integrated with an extremely high power density ECRH and ECCD system and state of the art diagnostic systems, that allows the experiment to explore the frontiers of MCF plasmas in several fields.
A salient example of a configuration recently created and studied for the first time at TCV is the novel "snowflake" divertor configuration, with a second-order null point and four divertor legs instead of two, which indicates a possible path towards reducing the divertor heat loads in future reactors [89]. Important results have been obtained by applying ECRH and ECCD (system details in Sec. 2.3): the creation of ITBs [90, 91], fully non-inductive current drive [12, 13, 14] and control of the sawtooth and ELM cycles [15, 16, 92, 93, 94] are just a few examples.

2.1.1 TCV coordinate and sign conventions

TCV is subdivided into 16 sectors that are numbered in the trigonometric positive direction (counter-clockwise) seen from the top. The coordinate conventions for the cylindrical (R, ϕ, z), toroidal (r, θ, ϕ) and Cartesian (x, y, z) coordinate systems in TCV are listed in Sec. C.2.1.

2.2 TCV control systems

TCV features a hybrid (analogue-digital) control system [95] that has recently been upgraded to a distributed control system, the système de contrôle distribué

(SCD) [88]. Some of the control system's capabilities, such as the real-time equilibrium reconstruction and shape control [96], were not strictly required for the studies in this thesis. Besides the control capabilities related to the auxiliary heating system, which are discussed in the next section, one important feature was the newly implemented real-time non-linear digital density controller [97]. The density is now well-controlled in the flat-top phase, even during ECRH power changes.

Operationally, the main plasma parameters are defined at specified times using the MGAMS interface [98] and then interpolated to, typically, a 1 ms timescale. Many parameters can be scanned during a shot: possible examples are a scan of δ from 0.4 to -0.4, a κ scan from 1.5 to 1.1, I_p ramps by more than $+100\,\%/-50\,\%$ or a scan of the radial ECRH deposition location via a B_ϕ ramp throughout a discharge of ≈ 2 s duration. Often, it is useful to apply such scans in steps with rapid changes ($\approx$ 10–100 ms) such that (conditional) averaging is possible within the intermittent constant phases (several 100 ms). In general, the unique capabilities of the TCV control system were well exploited but were not a limiting factor for the dedicated experiments in the frame of this thesis.

2.2.1 Scenarios

A scenario is an umbrella term for or a category of certain (tokamak) plasma discharges. It can be a quite broad concept (for example (e.g.) ohmic or fully non-inductive scenario) but also refer to a very specific type of discharges defining many plasma parameters, including their time evolution. Here, the term alone will be used in its broader sense. However, more specific, named scenarios will be defined by their main plasma parameters, such as shape, B_ϕ, I_p and n_e or also auxiliary heating.

The scenarios T, P and D, for instance, that were mainly designed to study toroidal HXR emission asymmetry, poloidal asymmetry and suprathermal electron diffusion, respectively, are also analyzed in other context and therefore a consistent naming is important.

2.3 TCV auxiliary heating systems

2.3.1 ECRH/ECCD

The TCV ECRH system (Fig. 2.2) disposes extremely high power, especially relative to the plasma size, and includes ECCD capabilities. At its maximum, it comprised nine gyrotrons, each generating a power of 500 kW.

2nd harmonic

The 2nd harmonic gyrotrons (originally six) emit at the second harmonic (of ω_{ce}) at 82.7 GHz in linear polarization. The matching optics units (MOUs) at the gyrotron RF windows condition the wave for good coupling into the transmission lines and the plasma. They have integrated grating polarizers to convert the polarization to elliptical in order to set the X-mode and complementary O-mode

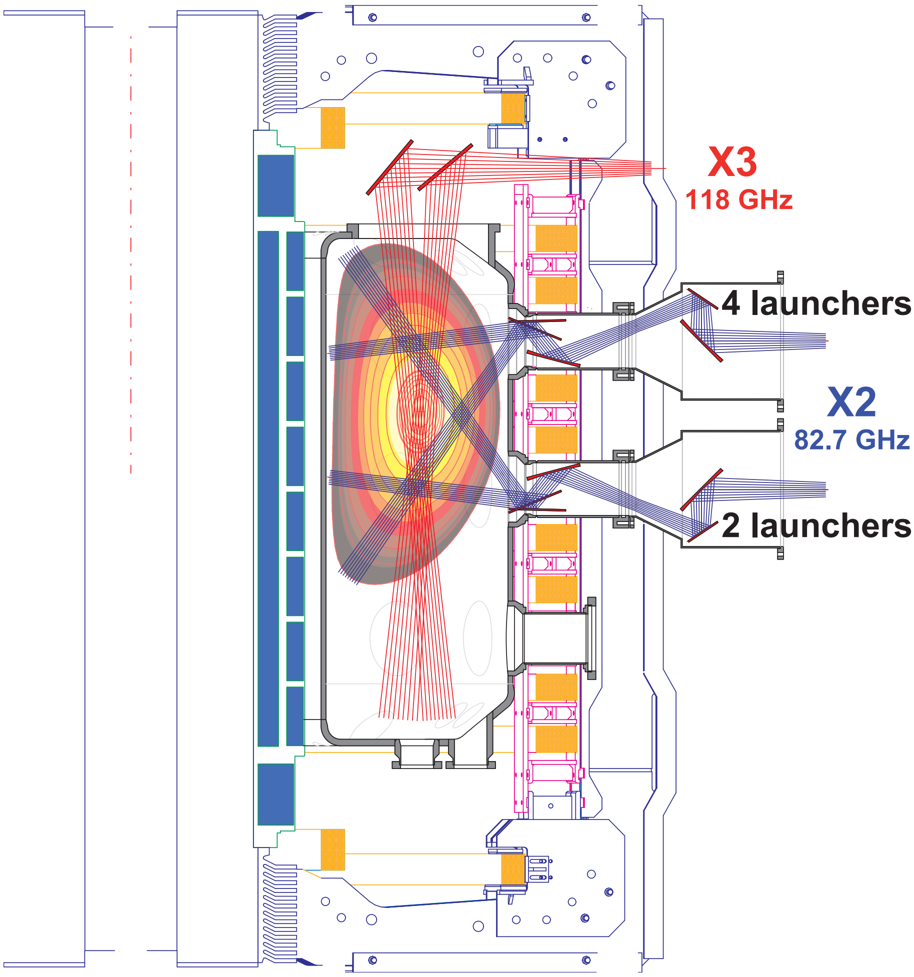

Figure 2.2: TCV auxiliary heating system as of 2013: 6 X2 launchers from the LFS and the mirror for the 3 X3 gyrotrons on the top of the 4.5 MW ECRH/ECCD system. [84]

fraction, that can be modified between plasma discharges for each gyrotron individually. Usually the X-mode is used for heating and CD and therefore the system is known as X2. A non-zero O2 fraction is only programmed for specific experiments. From the MOUs to the tokamak, the waves are transported in waveguides where they propagate in vacuum as narrow beams. Each of these six transmission lines is connected to an individual launcher mirror, located laterally on the LFS of the plasma, two at $z = 0$ and four at $z = 46\,\text{cm}$.

3rd harmonic

The other three gyrotrons emit at the third harmonic (of ω_{ce}) at 118 GHz. The waves are polarized in X-mode, transported by individual waveguides and then launched from a common mirror at the top of the plasma. This insures a long path for the X3 wave along the vertical resonance layer inside the plasma, which is necessary due to the lower lineic absorption as compared to X2.

Operational flexibility and control

For each discharge, the gyrotrons to be used are selected and the polarization is set. Also, the toroidal angle of the six lateral launchers, that is the rotation around the port axis, cannot be changed during a discharge. However, the poloidal angle of all seven launchers (axis perpendicular to the radial direction) can be changed individually during a discharge on the ms timescale. The power of the selected gyrotrons can be modulated during a discharge in groups, the so-called clusters A and B of three X2 gyrotrons each and the three X3 gyrotrons. For the X2 gyrotrons the power can be set to 0 or a value in the interval $[200, 500]\,\text{kW}$ arbitrarily on a 1 ms time grid. Faster modulation is possible via manual settings, but then restricted to simple waveforms. The normal settings allow one to pre-program the poloidal launcher angles and the gyrotron cluster power time traces or to control them in real-time using the SCD [88]. In any case, the pulse length of each cluster is limited to 2 s. [22, 99, 84]

2.3.2 Neutral beams and Upgrades

The heating power of active diagnostics in TCV is negligible, except for the diagnostic neutral beam injector (DNBI) where it is nevertheless small compared to ohmic and EC heating (50 keV at equivalent 1.6 A: $P_{\text{inj,DNBI}} \leq 80\,\text{kW}$) [100].
Currently, the TCV heating system is being upgraded with a 1 MW neutral beam injector (NBI). Further upgrades of the ECRH/CD system with additional gyrotrons are also foreseen [101, 102].
Other heating systems such as LHCD or ICRH are not well suited for TCV since they require antennas that are well aligned to the plasma shape.

2.4 TCV diagnostics

TCV has a large set of diagnostics covering a wide range of plasma parameters at high resolution. In this section the important characteristics of the diagnostics used in this thesis are presented. For further details beyond the scope of this work the author refers to the given references and references therein.

2.4.1 Magnetic diagnostics

Several magnetic diagnostics are installed in TCV. The most important ones, measuring poloidal magnetic field changes, the plasma current (I_p), the loop voltage (V_{loop}) and the toroidal flux, are described in the following.

Magnetic probes / Mirnov coils

The magnetic probes, also called $\dot{B}$ probes or Mirnov coils, measure the change of the B_θ component tangential to the vacuum vessel. The probes are implemented as flat rectangular pick-up coils located behind the first wall graphite tiles just inside the vacuum vessel. Therefore, they are not limited by the finite magnetic diffusion time of the conducting vacuum vessel, allowing a higher time resolution than external magnetic diagnostics.
In sectors 3, 7, 11 and 15 (angular distance $\pi/2$), poloidal arrays of 38 probes each are installed. At $z = -35$ cm, $z = 0$ and 35 cm, toroidal arrays of 8 equally spaced probes on the HFS and 16 equally spaced probes on the LFS, supplemented by a 17$^{\text{th}}$ probe between sector 16 and 1, are installed. The signal of the poloidal arrays in the opposite sectors 3 and 11 are always acquired and used for plasma position and shape control as well as for equilibrium reconstruction. One of the toroidal arrays can be selected to be acquired too. Usually the toroidal array closest to the planned position of the plasma magnetic axis is selected and can then be used in MHD mode analysis for toroidal mode numbers up to $n = 16$. [103, 84]

Plasma current estimator The dense poloidal Mirnov coil array of TCV can be seen as a discrete approximation of a Rogowski coil and therefore provides I_p via the plasma current estimator [84].

Flux loops

38 flux loops are wound outside the TCV vacuum vessel close to the position of the Mirnov coils of the poloidal arrays inside the vessel. Additionally, the current in all poloidal field coils (transformer and shaping) except central solenoid is measured by a dc transducer. The voltage in the flux loops is measured, giving direct information on the poloidal flux derivative and the loop voltage in the plasma. The integrated signal is used to obtain the poloidal flux. [103, 84]

2.4.2 Far infrared interferometer (FIR)

The far infrared interferometer (FIR) is an active diagnostic for line-integrated n_e measurements at high time resolution.
Its main component is a 14-channel Mach-Zehnder interferometer that measures the line-integrated electron density along parallel chords in the vertical direction (Fig. 2.3). A continuous wave (CW) at 184.3 μm is emitted by a laser and split into a reference beam and the 14 probe beams crossing the plasma [104, 84].

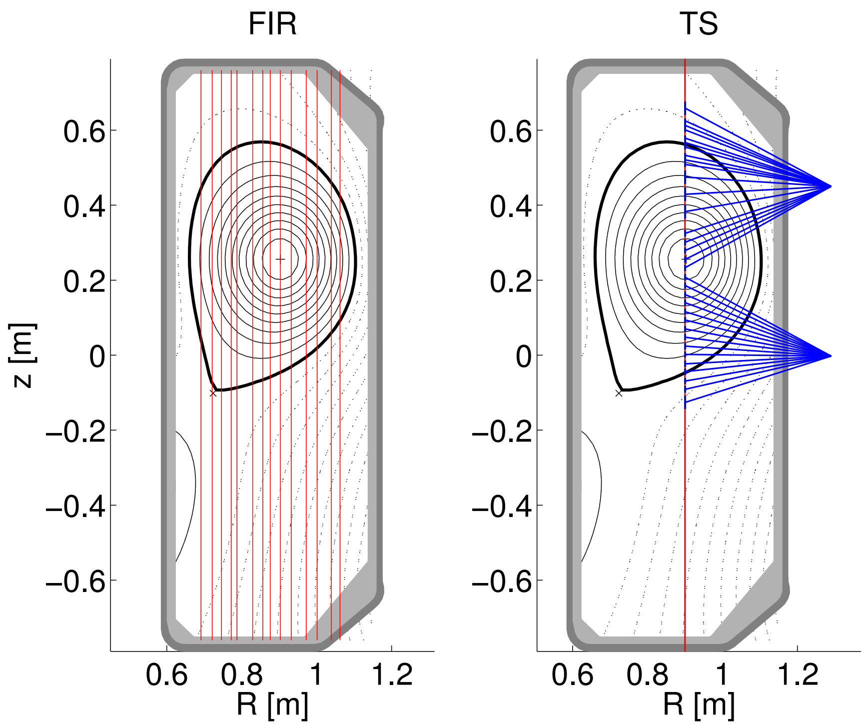

Figure 2.3: Chords of the FIR diagnostic and laser path (red), scattering volumes and central observation lines (blue) of the TS diagnostic at TCV (shot 49640).

The phase shift with respect to the reference is proportional to the line-integrated n_e along the beam path. The density corresponding to a shift of 2π is defined as a fringe. Fluctuations and noise can cause a so-called "fringe jump", whereby the fringe counter artificially adds or subtracts a whole fringe.
In post-shot analysis, this can be detected fairly easily and data corruption can be prevented. However, since one of the central chords is used as the n_e observer for the density control, a fringe jump on this channel can modify the plasma scenario significantly, effectively invalidating the shot and even potentially leading to disruption.
Owing to the vertical beam propagation, all TCV plasma shapes are covered. A radial density profile can be obtained by generalized Abel inversion (tomography) using the GTI code (Sec. 2.6, [105]). The beat-frequency of the interferometer (100 kHz) limits the diagnostic's time resolution [106]. The acquisition frequency is typically set to 20 kHz.

2.4.3 Thomson Scattering (TS)

The TCV Thomson scattering (TS) system is an important active diagnostic providing local n_e and T_e measurements.
Three identical Nd:YAG lasers emit laser pulses at a wavelength of 1.06 μm that are injected in the TCV tokamak along a vertical line at $R = 0.9$ m. 35 filter polychromators, each with 3 or 4 spectral channels, measure the spectrum of the Thomson scattered light from the volume defined by the intersection of laser and

observation LoS (Fig. 2.3). The electron density is proportional to the intensity of the scattered light while the electron temperature can be deduced from the spectral shape. Periodically, the system is absolutely calibrated using Raman scattering from N_2; on a shot-to-shot basis, the FIR line integrated measurements are used to obtain reliable n_e profiles. The T_e measurement only requires a relative calibration of the spectral channels.
The repetition rate of the lasers is 20 Hz. In sufficiently high density plasmas (typically $n_e\left(\rho=0\right)\gtrsim 2\cdot 10^{19}\,\mathrm{m}^{-3}$) the lasers are fired individually with a preselected time spacing of typically 16.7 ms. For lower density the three lasers are fired simultaneously (every 50 ms) to obtain a sufficiently high signal-to-noise (S/N) ratio.
The observation volume size and therefore the space resolution depends on the integration length of the channels that is 12 – 36 mm, varying for different vertical positions. This corresponds to a radial resolution of about 6 %, depending on the plasma elongation (κ). The filter polychromator set (3 or 4) is usually chosen according to the location in the plasma (center or edge) and cover the T_e range 50 eV–20 keV. [107, 84]
The error in the T_e measurement caused by suprathermal electrons (as compared to a strict Maxwellian) is, in the measurement geometry and parameters of TCV, negligible [108, 109].

2.4.4 Soft X-ray (SXR) diagnostics

The plasma in tokamaks usually radiates significant power in the soft X-ray (SXR) range (1–10 keV), with the main contribution from continuum radiation, namely bremsstrahlung (free-free) and recombination (free-bound) radiation. Line radiation may play an important role in the edge of the plasma or if high-Z impurities are present. The continuum radiation from electron-ion collisions is given by [110, 69]

$$\begin{aligned} j\left(\omega\right) =& n_e n_i Z^2\left(\frac{e^2}{4\pi\varepsilon_0}\right)^3\frac{4}{3\sqrt{3}m_e^2c^3}\left(\frac{2m_e}{\pi T_e}\right)^{1/2}\exp\left(-\frac{\hbar\omega}{T_e}\right)\\ &\times\left[\bar{g}_{ff}+G_n\frac{\xi}{n^3}\frac{\chi_i}{T_e}\exp\left(\frac{\chi_i}{T_e}\right)+\sum_{\nu=n+1}^{\infty}G_\nu\frac{Z^2R_y}{\nu^2T_e}\frac{2}{\nu}\exp\left(\frac{Z^2R_y}{\nu^2T_e}\right)\right], \end{aligned}\tag{2.1}$$

with the free-free Gaunt factor ($\bar{g}_{ff}$) and the Gaunt factors ($\bar{g}_n$,$\bar{g}_\nu$) for the lowest unfilled shell (first ionization potential (χ_i), ξ holes available) and all other shells, respectively.
In the case of multiple ion species the individual contributions from (2.1) have to be added. For negligible recombination radiation and equal $\bar{g}_{ff}$ the total emission can be written as [111]

$$I\left(\omega\right)=1.5\cdot 10^{-38}n_e^2Z_{eff}\frac{1}{\sqrt{T_e}}\exp\left(\frac{-\hbar\omega}{T_e}\right)\frac{\mathrm{W}}{\mathrm{m^3eV}}\tag{2.2}$$

with the effective ion charge (Z_{eff}) defined as

$$Z_{eff}=\frac{\sum_i n_iZ_i^2}{\sum_i n_iZ_i}.\tag{2.3}$$

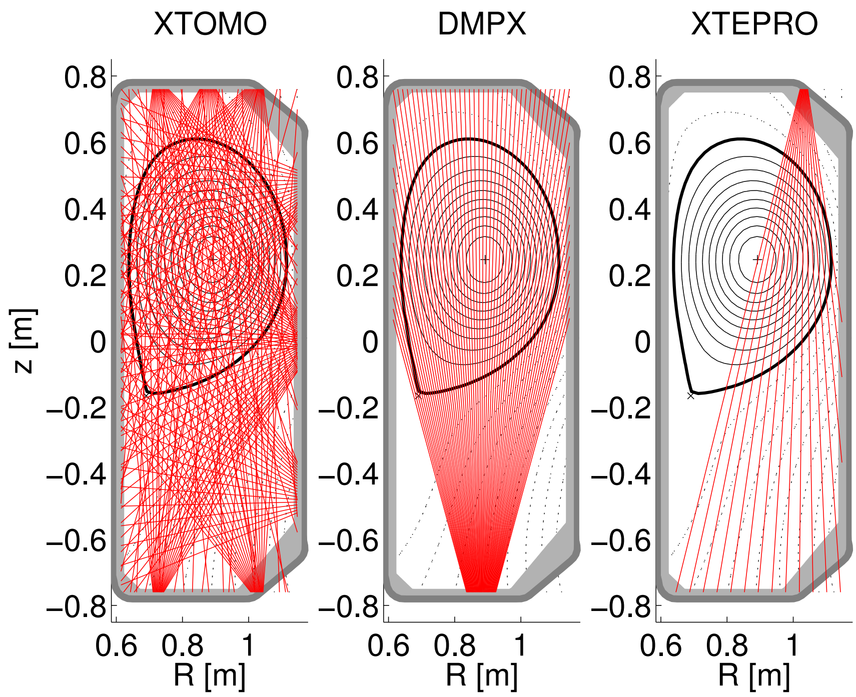

Figure 2.4: Lines of sight of the most important SXR diagnostics at TCV: XTOMO cameras 1–8 and 10 (clockwise numbering), DMPX top camera and XTePro in shot 49640.

The SXR emission intensity is therefore proportional to the square of n_e and to Z_{eff}, and depends strongly on T_e. Hence, SXR measurements do not directly provide an individual plasma parameter. Also, the measurements are typically line-integrated along LoS, as in the case of HXR, and require therefore further assumptions or tomographic systems. Nonetheless, since the emission increases both with n_e and T_e and the high emission allows high time resolution, SXR diagnostics are well placed to observe MHD instabilities such as sawteeth and NTMs. Furthermore, since the T_e-dependence is, together with the ω-dependence, exponential, a few measurement points or windows in the exponential slope allow one to determine T_e.

Soft X-ray tomography (XTOMO)

The TCV soft X-ray tomography (XTOMO) system consists of 10 pinhole cameras with 20 channels each. The LoS lie in the poloidal plane of sector 11 and cover the whole poloidal cross section of the vacuum vessel (Fig. 2.4). The detectors, CENTRONIC LD20-5T photodiodes, lie behind a toroidal collimator front plate, a 47 μm thick beryllium (Be) vacuum window acting as a low energy filter and a tungsten (W) pinhole for poloidal collimation. The detection efficiency is shown in Fig. 2.5 and covers the range 1–20 keV [112]. The time resolution is 100 kHz [84]. The spatial resolution in the poloidal plane depends on the tomographic inversion of the line integrated data and is in the order of 2 cm [80, 105].

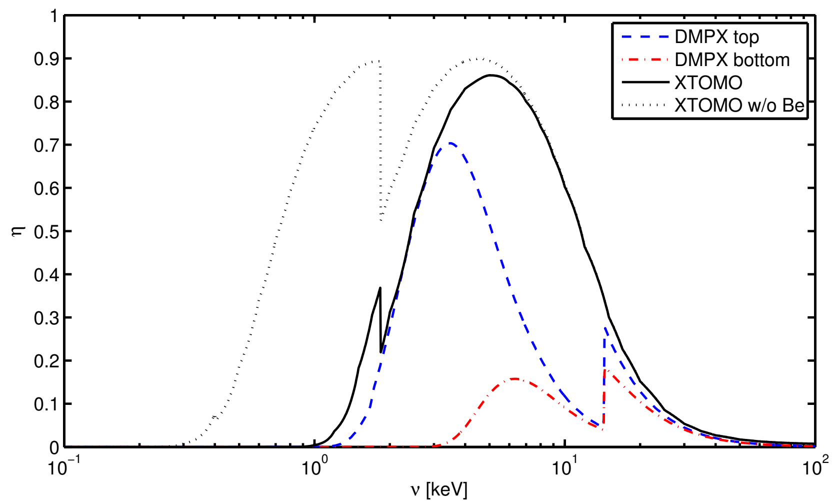

Figure 2.5: Detection efficiency of the DMPX top and bottom camera (shot 49640, typical setting) and the XTOMO detectors with and without the Be filter (data from [112, 113, 114, 115]).

DMPX

The duplex multiwire proportional X-ray counter (DMPX) is a high spatial and temporal resolution X-ray diagnostic in the range 2–30 keV. It is installed on the central bottom port in sector 9 of TCV. It consists of two planar multiwire proportional X-ray counter (MPX) chambers behind a Be vacuum window, a slot-hole and a helium-filled duct. The chambers are usually filled with a mixture of 90 % krypton (Kr) (detection gas) and 10 % methane (CH_4) at atmospheric pressure, with the option to replace Kr by xenon (Xe) or argon (Ar). The radiation from the plasma sees first the top chamber with 64 channels and then the 32-channel bottom camera. Their high voltage (HV) can be set independently (typically 1800 V) according to the expected SXR flux. Interchangeable filters can be placed in front of both chambers to adjust the low energy cut-off. The detection efficiency in the typical configuration is shown in Fig. 2.5.
The 64 and 32 chords view at the plasma from below with a mean spatial resolution (spacing) of 7.9 mm and 16.3 mm, respectively, at the midplane of the TCV vacuum vessel (Fig. 2.4). The time resolution is limited by the amplifier signal bandwidth of 50 kHz. The signal is typically acquired at 250 kHz. [116]
The line-integrated measurement already allows one to observe sawteeth and NTMs and more details can be extracted using the Abel-type inversion in the GTI code (Sec. 2.6, [105]), optionally including independent LFS and HFS profiles for poloidal emission asymmetry analysis. Furthermore, T_e profiles can then be computed from the two radial emission profiles (obtained from the top and bottom camera).

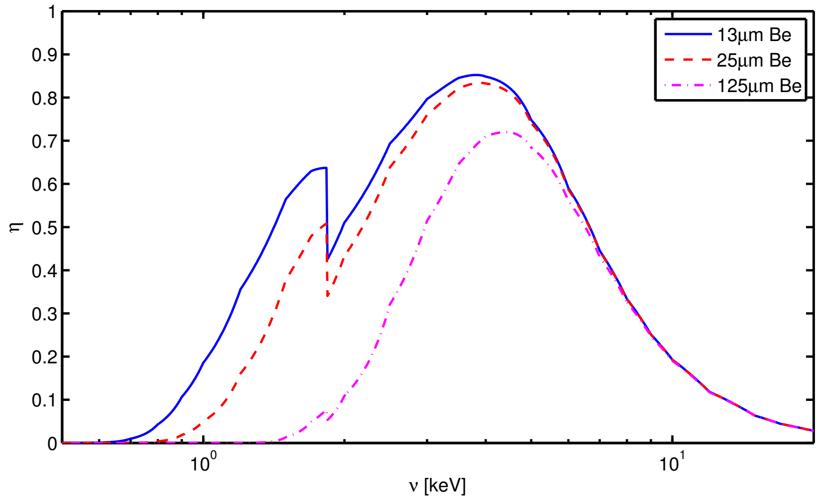

Figure 2.6: Detection efficiency of the XTePro detector sets for each of the 3 Be filters (estimation based on data from [117, 113, 114]).

XTe

The soft X-ray electron temperature (XTe) diagnostic consists of four equivalent silicon (Si) diodes, each behind a different filter, observing the plasma along a vertical LoS at $R = 0.9\,\mathrm{m}$ from the top. Due to the different spectral detection efficiencies defined by the filters, the signal ratios yield an indicative weighted LoS temperature; in particular, making the assumption of an adjusted parabolic T_e profile

$$T_e(\rho_\psi) = T_{e,0}\left(1-\rho_\psi^2\right)^{\alpha_{T_e}}, \qquad \alpha_{T_e} = 1.5, \tag{2.4}$$

one can then estimate the central electron temperature ($T_{e,0}$). The advantage of this technique is the much better time resolution compared to Thomson Scattering.

XTePro

The XTe profiles (XTePro) diagnostic is based on the same concept as the XTe, but with additional spatial resolution. Therefore it has 16 chords viewing the plasma from the top in sector 15, covering the whole LFS part of the poloidal plasma cross section (Fig. 2.4). The system consists of 3 AXUV-16EL0 diode arrays behind Be filters of 13, 25 and 125 μm, each of them having essentially the same 16 LoS. The low energy cut-off ($\eta = 20\,\%$) lies at about 1.0, 1.3 and 2.3 keV, respectively, while the high energy cut-off lies, due to the thin detectors, at about 10 keV (Fig. 2.6).
In the data analysis process, first the the measurements are mapped to emission profiles for each of the 3 arrays independently using the general tomographic inversion (GTI) code (Sec. 2.6, [105]). Subsequently, the local emission ratios allow the computation of radial T_e profiles.

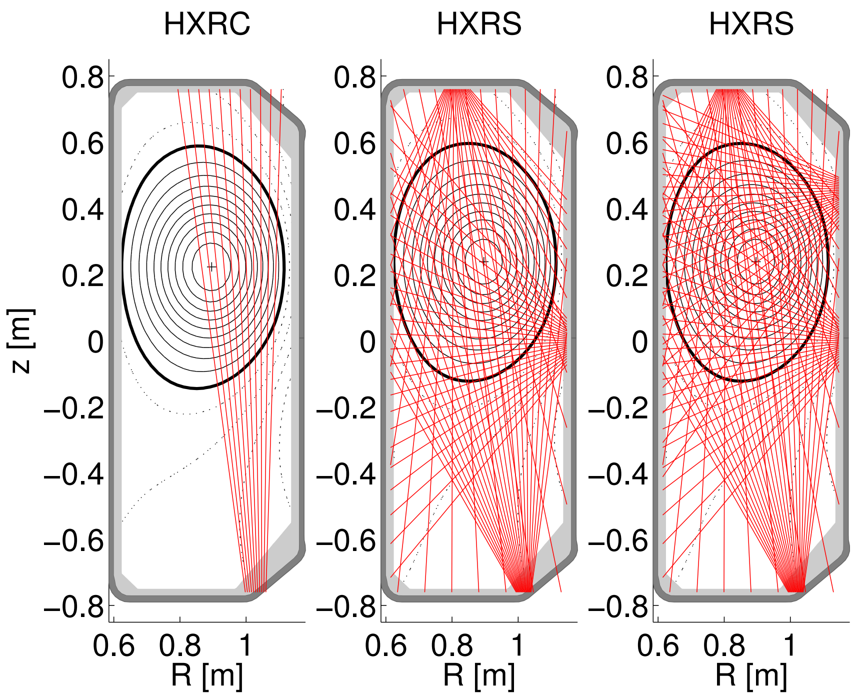

Figure 2.7: Lines of sight of the HXRC (left), the HXRS in the current stage with 3 cameras (middle) and in the final stage with 4 cameras (right).

2.4.5 ECE diagnostics

ECE radiometers observe the plasma from the high-field-side (HFS, bandwidth 78 – 114 GHz) [118], the low field side (LFS, 65 – 100 GHz) [119, 120] and the top (vertical ECE).

2.4.6 HXRS

The HXRS is the main HXR diagnostic at TCV, and also the key instrument for experiments carried out in the course of this thesis, in which the first 3 (LFS midplane, top, bottom) cameras were successively procured, calibrated and installed on TCV. In the final design this tomographic system will consist of 4 cameras (the 4$^{\text{th}}$ in a LFS upper port) with 24 LoS each covering the whole poloidal cross section, resulting in a space resolution of a few cm (Fig. 2.7). The two LFS cameras can be rotated by 90 deg providing toroidal coverage in the co- and counter-I_p directions. [1]
The detectors are $CdTe$ diodes with an energy resolution of 7 keV and cover a primary range from 13 to 300 keV. The full-pulse digital data acquisition operates at 12 Msamples/s and is followed by digital post-processing, which provides the time and energy of every single measured photon, and consequently allows for data analysis based on arbitrarily chosen energy bins and time resolution. The latter depends on the photon statistics, with the detection system capable of handling up to 500 000 counts per second (cps). [2]

Figure 2.8: The TXDA diagnostic with its graphite cap (left) and in-vessel view of the diagnostic in its final position (right). [84]

A more detailed description follows in Ch. 3; further reading: [1, 121].

2.4.7 HXRC

The hard X-ray camera (HXRC) was the predecessor and the basis for development of the HXRS on TCV. One of the two cameras of the HXR tomography of Tore Supra [76] was on loan and installed in a bottom port of sector 4 during several thousand plasma discharges. The 14 vertically viewing chords covered the LFS of the poloidal plasma cross section (Fig. 2.7) [122]. The detectors are also 2 mm thick $CdTe$ diodes, but with a square surface of $5 \times 5\,\mathrm{mm}^2$ as compared to the $2 \times 2\,\mathrm{mm}^2$ of the HXRS. The most relevant difference, however, is the analogue pulse processing providing only count numbers above 8 energy thresholds (changeable from shot to shot) and typically 10 ms time intervals. The collimator is designed as a pinhole with lower effective thickness (stainless steel and lead of 3 cm in total instead of the HXRS 2.9 mm tungsten) and no specific surrounding shielding in addition to the structure material.
Several important results have been obtained using this diagnostic on TCV [123], including suprathermal electron transport [3], ECCD [124] and X2-X3 synergy studies [125, 126]. Some of these scenarios are revisited in this thesis using the improved capabilities of the HXRS system.

2.4.8 TXDA

The tangential X-Ray detector array (TXDA) comprises 6 $CdTe$ detectors (plus a shielded one for background measurements). The lines of sight are parallel, defined by two perpendicular sets of W Soller collimator plates and passing through a Be vacuum window. The collimator and detector housing is very compact, is located close to the plasma and can be turned allowing extreme tangential observation of the plasma at different positions (Fig. 2.8). Besides structural shielding, it is also shielded against the heat flux of the plasma by a graphite cap. The TXDA measures the photon flux (from 10^5 to 10^9 photons/cm²s) without energy resolution (sensitive to 2–200 keV) at a high digitization rate of typically 250 kHz (100 kHz amplifier bandwidth).

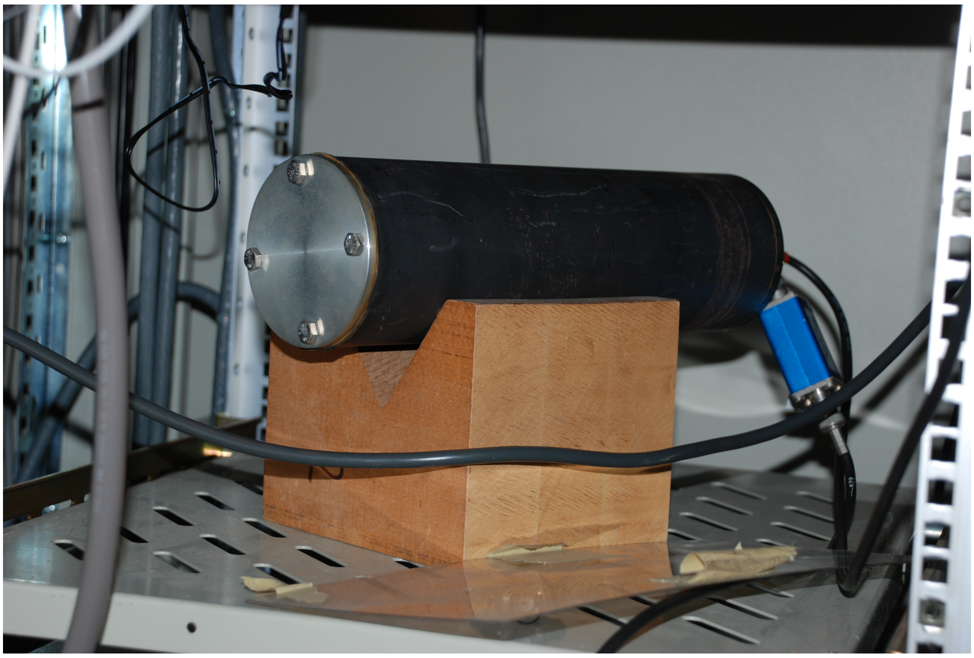

Figure 2.9: The PMTX diagnostic in ilôt SE. [84]

2.4.9 PMTX

The photomultiplier tube for hard-X rays (PMTX) is installed in ilôt SE a few meters outside the TCV tokamak (Fig. 2.9). It observes bursts of radiation in the MeV range that are produced by highly relativistic electrons (typically in the runaway regime) colliding with the first wall at a time resolution of 250 kHz.

2.4.10 PHAV

The vertical pulse height analyser (PHAV) consists of a SDD with a vertical LoS connected to amplifiers and a multichannel analyzer (FAST ComTec MCA-3 installed in `crpppc271`). It measures the X-ray spectra in the range of 1 to 20 keV within intervals of typically 50 ms, resulting in a time resolution of 20 spectra/s.
Similar to the HXRS, the diagnostic features two filter wheels. Behind them, there is the Be window in the zirconium (Zr) collimator and finally the detector (Fig. 2.10). The first wheel is usually set to the position where no filter is in place. At another position, there is an iron-55 (^{55}Fe) source that is moved in front of the detector for calibration. The second wheel contains a variable slit. A feedback system changes the size of this slit according to the measured X-ray flux. This solution prevents the system from saturation and ensures operation in an optimal range.
During this thesis work the diagnostic was re-installed at TCV, commissioned and calibrated. Furthermore, the acquisition cycle and connection to the MDS+ database was fully automated.

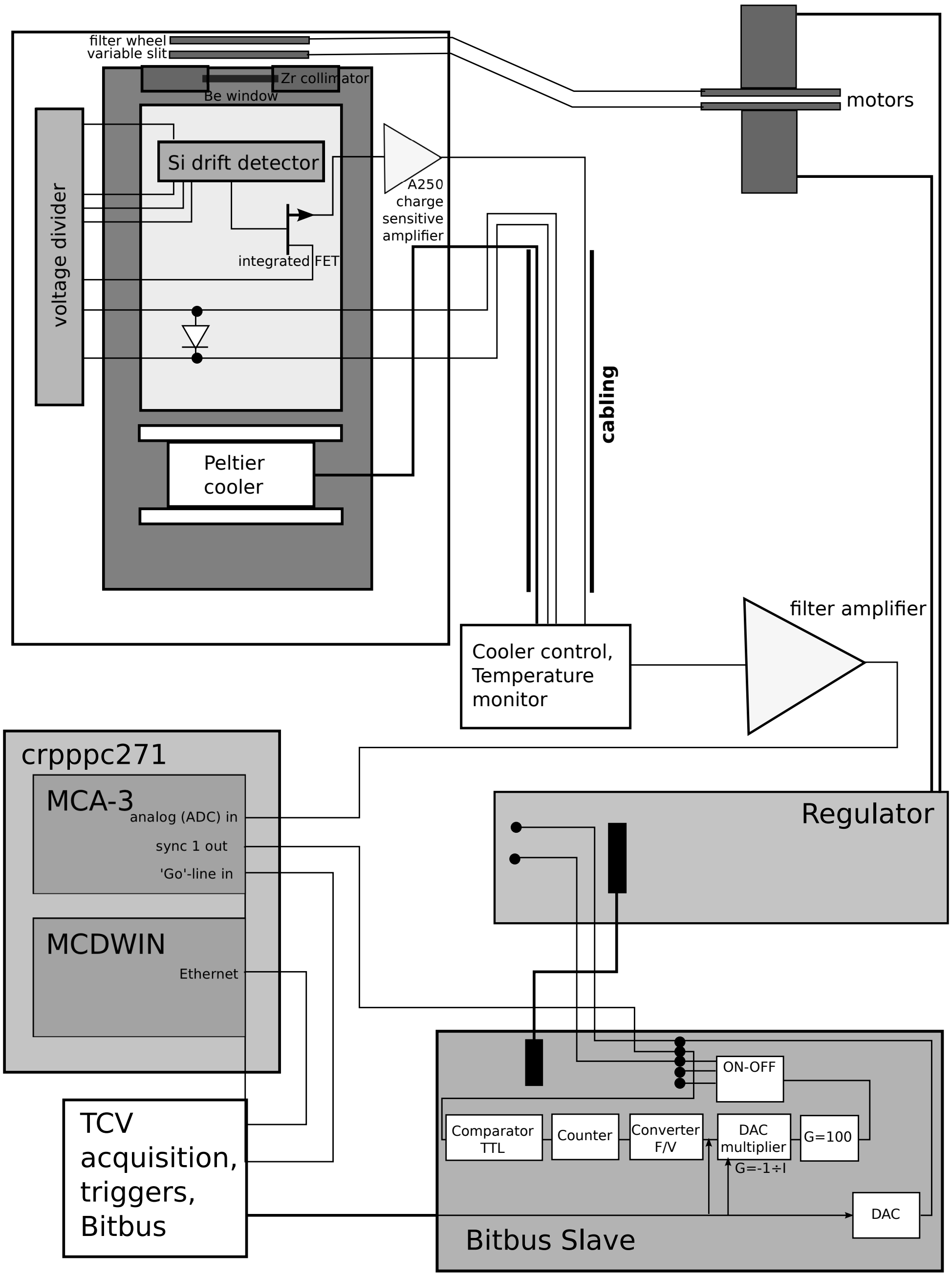

Figure 2.10: Schematic drawing of the PHAV diagnostic.

2.5 Elementary data analysis tools

Several standard elementary data analysis and processing tools were used in this thesis. The most important ones are listed and specified in the following.

2.5.1 Coherent and conditional averaging

Conditional averaging is a technique in statistics to extract coherent information on repeated spatio-temporal structures from experimental and/or simulated data. The technique increases the statistics and suppresses incoherent features like noise. It is often applied in plasma physics, for instance in turbulence [127, 128, 129].
Since the terms coherent and conditional averaging are not always defined in the same way in literature they are specified here for clarification: coherent averaging means to average several periodically repeated time samples of a signal that are usually associated to a stimulus that is applied to the system at the same period. An example used in the following is the application of periodic ECRH pulses to investigate the response of the plasma. Conditional averaging, by contrast, averages repeated time samples with respect to a trigger event, that is, in general, nonperiodic. The trigger event timing is usually not controlled by the experimentalist but occurs at random times. The length of time between the trigger events usually follows a certain probability distribution. An example are sawtooth crashes as trigger events and the coherent information on the plasma evolution prior and subsequent to these MHD events.

2.5.2 Filtering

If not stated otherwise low-, high- and band-pass filters are realized by a 2$^{\text{nd}}$ order Butterworth filter.

2.5.3 Singular value decomposition (SVD)

The singular value decomposition (SVD) allows one to extract dominant structures from a 2D data matrix. Its mathematical definition and main properties are stated in the following theorem [130]:

Theorem 1. *1. For $A \in \mathbb{K}^{m\times n}$ ($\mathbb{K} = \mathbb{R}$ or $\mathbb{K} = \mathbb{C}$) $\exists$ unitary matrices $U \in \mathbb{K}^{m\times m}$, $V \in \mathbb{K}^{n\times n}$ and a rectangular diagonal matrix $\Sigma \in \mathbb{R}^{m\times n}$ (i.e. $\Sigma_{jk} = \sigma_j \delta_{jk}$) with $A = U\Sigma V^H$ and $\sigma_1 \geq \sigma_2 \geq \ldots \geq \sigma_{\min\{m,n\}} \geq 0$. This factorization is called singular value decomposition of A and σ_j are the singular values (of A).*

2. $\Sigma \in \mathbb{R}^{m\times n}$ is uniquely determined, σ_j^2 is eigenvalue of $A^H A$.

3. $\sigma_{\mathrm{rank}(A)} > 0 = \sigma_{\mathrm{rank}(A)+1}$.

4. $\|A\|_2 = \sigma_1$

Figure 2.11: An example of simple image compression by SVD: original picture on the left (full rank 639 × 875 8 bit integer matrix A, 560 KB) and $\sum_{j=1}^{20} \sigma_j u_j v_j^H$ rounded to 8 bit integers (30 KB for storage of σ_j, u_j and v_j for $j = 1,\ldots,20$) on the right. Picture of HXRS camera 5 cassette taken from [121].

5. *With $u_j \in \mathbb{K}^m$ and $v_j \in \mathbb{K}^n$ being the j^{th} columns of U and vV, respectively, it holds that*

$$A = \sum_{j=1}^{\mathrm{rank}(A)} \sigma_j u_j v_j^H. \tag{2.5}$$

The last point states that it is sufficient to take only the rank(A) first singular values (σ_j) and orthogonal columns into account in order to reconstruct the full matrix A exactly. Taking only the first few dominant σ_j and u_j, v_j still recovers the main features, but with a loss of information, represented by the omitted terms of (2.5). This can be used in image compression as shown in Fig. 2.11.
Theorem 1, 2., only states that Σ is uniquely determined. It turns out that for non-degenerate σ_j the corresponding vectors u_j and v_j are also uniquely determined up to a phase factor (± 1 for real numbers), which is the same for u_j and v_j. This is usually the case for experimental and simulated data matrices. If the matrix A contains spatio-temporal data with the first dimension of A corresponding to space and the second one corresponding to time, the SVD reveals the dominant spatial structures in u_j (topos) and the corresponding time evolution in v_j (chronos) with the importance given by σ_j. Rotating spatial structures are resolved by two sets of σ_j, topos and chronos; the σ_j are nearly equal and a phase shift of 90 deg is present in both the topos and chronos.
This SVD analysis turns out to be extremely useful for mode analysis of tokamak plasmas, where the spatial structure (mode numbers) and the temporal evolution (mode frequency) can be easily separated. For modes at constant frequencies the results are in agreement with other methods like band-pass filtering. An advantage is that the SVD can resolve arbitrary time evolution, including simple jumps or ramps and, more interestingly, sawteeth and frequency-changing modes, without any prior assumptions or model development.

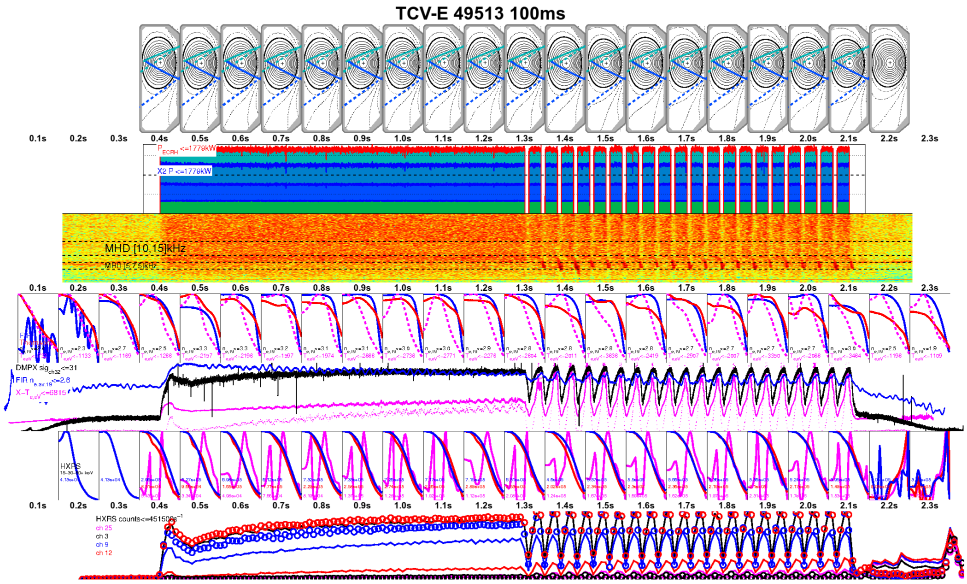

Figure 2.12: An example of a snapshot showing the equilibrium and ECRH launcher angles, ECRH injected power profiles, magnetic probe spectrogram, n_e, T_e (and SXR) radial profiles and time traces from TS, FIR, XTe and DMPX and finally HXRS radial profiles and time traces.

Least-squares fitted topos

Often, spatio-temporal data of different sources are closely related, for instance the signals of the LFS and the HFS toroidal magnetic probe arrays. In such a case, one can perform the SVD for all signals together, or for both systems individually. In the first case, the influence of each source depends on its relative normalization. In the second case, the chronos differ in general; an example are rotating structures, represented in a superposition of 2 topos-chronos pairs: within a system phase shifts introduced in the chronos are canceled by corresponding phase shift in the topos, but the phase shifts of the two systems differ in general. In both cases it is problematic if one of the data sources has a much worse S/N ratio, since the noise enters in and perturbs the SVD.

If so, an alternative and especially useful solution is the method of least (mean) squares (LS)-fitted topos: the secondary (noisy) signal topos are not computed by the SVD, but LS-fitted to the chronos of the SVD of the primary data source. The LS-fitted topos are therefore the best approximation to the spatial structure corresponding to the common chronos, but not topos as defined above. As for any fit, the difference from the original signal needs to be well monitored to ensure that it is reasonable.

2.5.4 Snapshots framework

A new data analysis tool, the "snapshots", was developed and implemented in the course of this thesis. This framework allows one to create figures and time traces of TCV diagnostics data and puts these automatically together into a portable

network graphics (PNG) file in full high definition (Full-HD) resolution. Therefore small individual PNGs are created for each diagnostic or analysis result and then put together according to an extensible markup language (XML) parameter file by a Python script. The storage requirements of the resulting PNGs are low and due to their immediate availability they are well suited to get a fast overview of the data. The data can be easily accessed through a web browser or an image viewer without time-consuming MDS+ connections. Snapshots are regularly used to display information on the previous discharge in the TCV control room and integrated in the CRPP-wiki for fast preliminary post-shot analysis.
An example is the TCV-E snapshot, showing ECRH/CD, MHD, n_e, T_e, SXR and HXR data (Fig. 2.12).

2.6 General tomographic inversion (GTI)

2.6.1 Motivation and implementation

At TCV, many diagnostics provide line integrated measurements of local quantities along multiple LoS. Tomography is a way to extract local information from these measurements; i.e. to solve the problem of inverting the operator that maps profiles in the plasma (1D, 2D or higher) to the measured data via line integration. This inverse problem is, especially in a tokamak, usually undetermined due to the low number of chords (often limited by space constraints or cost) and in general badly conditioned, such that additional assumptions are required in order to obtain realistic reconstructions of the profiles. Additionally, the problem can be simplified by assuming toroidal or poloidal symmetry. The former is not necessary if all measurements are taken in the same poloidal plane. The latter is usually required for systems with only one camera (Abel-type inversion).
Among the set of tomographic inversion methods the most common ones were compared at TCV for XTOMO [80]. The minimum Fisher information (MFI) shows the best results, as compared to linear regularization (actually a special case of MFI) and maximum entropy methods. The underlying software implementation was, however, not very flexible. For other line-integrating multi-chord diagnostics (FIR, DMPX and HXRC and) there were also only individual and quite limited tomographic inversion solutions available. This complicated any data comparison or integration. Furthermore, any extension and the maintenance of the software requires more work and users need to be familiar with different interfaces. Facing this situation, it was not very tempting to implement another different solution for the HXRS diagnostic.
Therefore, the GTI code was written in order to provide a unique, powerful and flexible solution for a whole set of diagnostics. Prior to implementation, a list of design goals was specified ([105], where more technical details can be found too). The main specification is that a framework with well defined and stable interfaces enables the integration of multiple diagnostics, several inversion algorithms and different space, time and other (e.g. energy) discretization. This provides, together with optional pre- and post-processing features, high flexibility and good extensibility. Additionally, the numerical effort was reduced by far (parts by several orders of magnitude) as compared to previous implementations. This allows

a session leader at TCV to use tomographic information from a plasma shot already to plan the following one.

2.6.2 Capabilities

Diagnostics

The GTI code supports the multiple camera diagnostics XTOMO, HXRS, absolute extreme ultraviolet bolometer cameras (AXUV) and foil bolometers (BOLO), the (essentially) single camera diagnostics DMPX, FIR, HXRC and XTePro and the tangentially viewing fast visible camera (FastCam).

Discretization

Square pixels as in [80], more specifically finite differences on a rectangular domain in the poloidal plane that is divided into squares, are available as one of the possible discretizations (base functions of the computed solutions) and called "SquarePixels" in the GTI code. The more general "RectangularPixels" discretization is not restricted to squares, also rectangles can be used, which, in addition, also cover the toroidal direction, using the resulting body of rotation, a ring with rectangular cross section. Similarly, there are finite element method (FEM) grids available, either based on rectangular pixels that are split in two triangles each in order to obtain a triangulation or by using arbitrary triangulations (e.g. Delauney from a set of points).
In addition to these 2D grids that are independent of prior information, two grids that are based on the flux surfaces from the LIUQE equilibrium reconstruction are also supported. The first one is a finite difference grid ("Flux2D") with a certain number of sectors in radial (ρ_{pol}) and angular (poloidal angle (θ)) direction. Using only two angular sectors one can investigate poloidal asymmetries using one-camera diagnostics (HFS-LFS or up-down, depending on the camera position). The second one ("Flux2DFEM") is a FEM discretization based on a triangulation with the number of triangles on a flux surface increasing from the magnetic axis to the LCFS in order to keep the element size as constant as possible. The "Flux2DFEM" discretization does not use any preferred direction inside the LCFS while the "Flux2D" finite difference operator aims at lower variations in the angular as compared to the radial direction.
For an Abel-type inversion the "Flux1D" discretization can be used, a 1D finite difference grid on ρ_{pol}. For density-related inversions, e.g. FIR, also a small set of base functions from radial n_e Thomson scattering profiles can be used ("SVDThomson1D"), that are, themselves, defined on the "Flux1D" grid.

T-matrix

The T-matrix is the linear map from the base function coefficients on the discretization to the measurement in the diagnostic's channels. It includes all calibration factors and the étendue (G). The key part, however, is the computation of the line integration. For this, the thin chord approximation is used, i.e. the integration along the diagnostic LoS is approximated by the integration along an ideal line in the center of the chord. Original algorithms were developed in order to minimize the numerical effort of the T-matrix computation. Only the initial T-matrix algorithm for "SquarePixels" was based on Xiaolin Wu's line drawing algorithm [131] but outperformed and consequently replaced by the more general algorithm used for "RectangularPixels".

Inversion methods

The quite basic zero, first and second order regularization methods are special cases of the MFI regularization that is used in the following if not stated otherwise. The algorithm was more efficiently, but also more simply and flexibly implemented using object oriented programming (OOP). The "LeastSquares", a simple LS solver for the linear system, is applied for the "SVDThomson1D" discretization and only useful in such over-determined and well-conditioned cases.

Pre- and post-processing

The measured signal can be pre-processed using coherent and conditional averaging techniques. Also, the time resolution can be changed via automatic interpolation / smoothing. Low-, high- and band-pass filters can be applied both in pre- and post-processing, i.e. before the inversion on the individual channels and after the inversion on the solution. Also, a Fourier transform can be used in order to perform the inversion in the frequency domain, but this is hardly ever used. In contrast to this, the SVD of the solution in order to identify spatial structures with different temporal evolution (such as sawteeth, NTMs) is an important post-processing tool that was extensively used in the course of this thesis.

2.7 Fokker-Planck modeling of the (suprathermal) electron distribution

To model the (suprathermal) e.d.f., Fokker-Planck simulations (Sec. 1.8) were performed using the LUKE [82, 132] and CQL3D [133, 83] codes. In LUKE, the ray-tracing is performed with the integrated C3PO code while CQL3D relies on TORAY, the standard ray-tracing code used at TCV.

Both Fokker-Planck codes also feature a synthetic HXR diagnostic; in LUKE this fast electron bremsstrahlung (FEB) module is called R5-X2. Both use the Coulomb corrected Born approximation, the Bethe-Heitler formula with the Elwert factor (F_E) for electron-nucleus bremsstrahlung (B.8) and the Haug expression for electron-electron bremsstrahlung (B.18).

Synthetic ECE diagnostics could not be used. The one that is coupled to CQL3D, embedded in the GENRAY ray-tracing code, is still in a beta version state and not reliable. For LUKE, the synthetic ECE diagnostic is still in an early development state, and no preliminary version is available.

CQL3D is a well established code used and improved for more than 20 years and benchmarked against other Fokker-Planck codes [134]. It is written in Fortran and requires some standard libraries, including netCDF for data and `pgplot` for graphical output. As an interface to TCV data and the CRPP and EPFL high-performance computing (HPC) capabilities the CQL3Dpy package was implemented in Python in the course of this thesis.

An improved and more flexible TCV database access including temporal evolution and conditional averaging was also implemented for LUKE. This well-documented and supported code was developed later than CQL3D and comes in compact form with a user-friendly graphical user interface (GUI). It is based on a modern MATLAB implementation, featuring many integrated analysis and plotting options, also for shot preparation. In R5-X2, HXRS filter and response are directly taken into account.

More details on the Fokker-Planck codes LUKE and CQL3D can be found in Ch. 4.

Chapter 3

HXRS

3.1 Hardware

3.1.1 Geometry and components

The geometry of the LoS of the diagnostic is shown in Fig. 2.7. During the design up to nine cameras were considered. It was decided to select cameras 2, 4, 5 and 7 of the design phase, whose collective LoS cover the plasmas in TCV best. More cameras would not significantly improve the chosen tomographic system further [1]. In the following, the clockwise numbering (starting at the HFS on the left) of the original design is kept. Therefore, the numbering of the cameras is 2, 4, 5 and 7, although only four cameras are installed on TCV.
The main part of a camera is the cassette (Fig. 3.1), containing all detectors and the pre-amplifier and amplifier electronics inside metallic shielding. On its front, the W collimator is mounted close to the detectors. A surrounding structure holds also the filter wheels in front of the collimator and the additional W shielding. This camera structure is supported off an outer flange which is attached to the port that contains the camera. During operation the camera is in a preliminary rough vacuum to keep the pressure on the Be window well below 1 Atm, for extra safety. A simple glued-in feed-through (SCSI-2 MD68 connector) connects the camera electronics to the BITBUS slave hosting the power supply, the filter wheel controls and the connections to the analog to digital converter (ADC) and acquisition electronics.

3.1.2 Collimator and shielding

The viewing chords are defined by a fan-type Soller collimator made of W. Each detector has its own pinhole channel providing an equal G of $4.4 \cdot 10^{-9}\,\mathrm{m^2 sr}$. While the collimator is 2.9 cm thick, the $CdTe$ detectors are also shielded from the side by stainless steel structural components and at least 2 cm of W. One additional completely shielded detector per camera is used to discriminate against the background noise and uncollimated, highly relativistic photons.

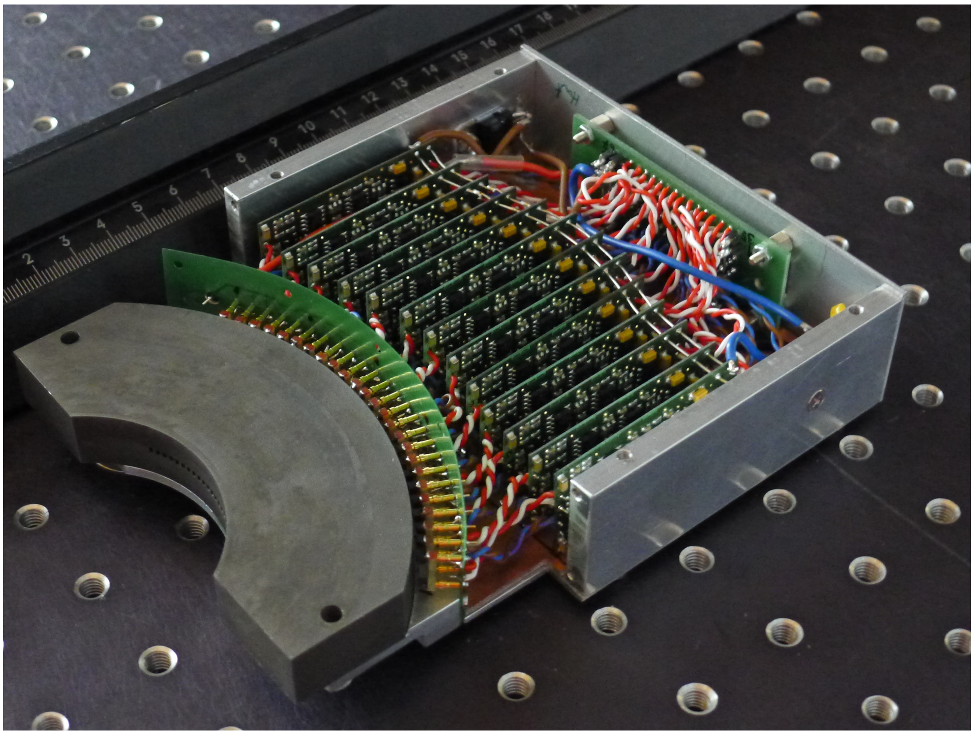

Figure 3.1: Opened cassette of HXRS camera 2 with tungsten collimator in front of the detectors and the amplifier cards.

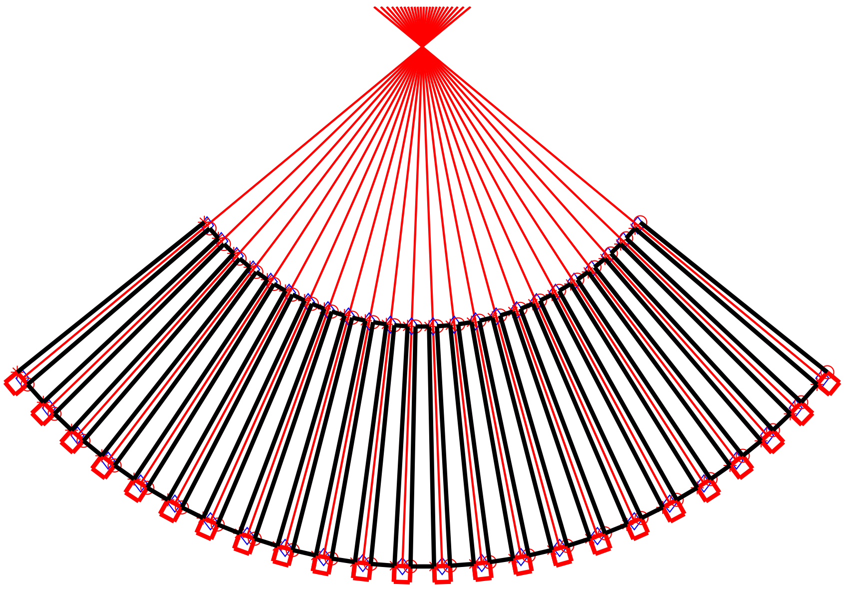

Figure 3.2: HXRS collimator design of camera 5: CdTe detectors (red squares) behind the collimator (black) with lines of sight (red) crossing in one point.

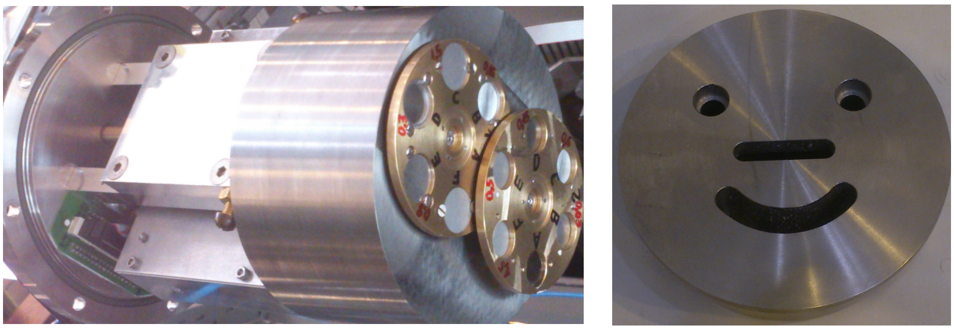

Figure 3.3: HXRS camera 2 with shielding and filter wheels (left); camera 4 front shielding with openings for filter wheel controls, LoS and camera rotation mechanism (right).

Position	prototype	A	B
1	-	-	-
2	0.048 mm *Al*	0.15 mm *Al*	0.03 mm *Al*
3	0.192 mm *Al*	1.5 mm *Al*	0.6 mm *Al*
4	0.95 mm *Al*	0.3 mm *Fe*	0.15 mm *Fe*
5	1.5 mm *Al*	0.8 mm *Fe*	0.5 mm *Fe*
6	2.5 mm *Al*	2.5 mm *Fe*	1.5 mm *Fe*

Table 3.1: Thicknesses of the *Al* and *Fe* filters of the HXRS. The prototype was used in camera 5. A and B compose the final design for the two wheels of each camera, which will also be adopted in camera 5.

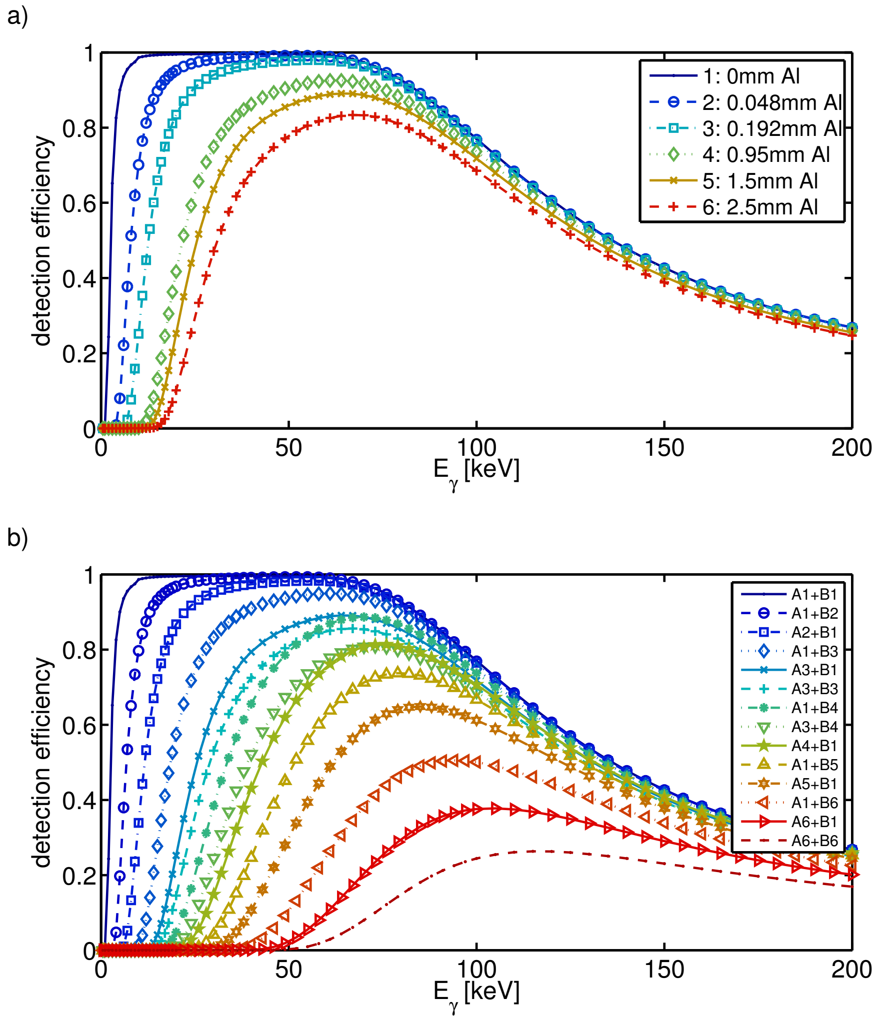

Figure 3.4: HXRS CdTe detector efficiency for a) the prototype filters of camera 5 and b) a subset of the possible combinations of positions in wheels A and B of the final design, as already used in camera 2. The Be window is included.

3.1.3 Filter wheels

Sufficiently good statistics of 100 kcps or more are desirable to obtain a good energy and time resolution. At the same time, the count rate has an upper limit of about 500 kcps due to the finite charge collection and decay time. To stay in this corridor for a wide range of plasma scenarios it is required to adjust the low-energy cut-off accordingly. This is done by putting filters in the LoS in front of the collimator. Two filter wheels with 6 positions each provide 36 absorber combinations (Tab. 3.1, Fig. 3.4). The wheels are turned by a stepping system driven by pressurized air, controlled remotely by the Vsystem via the BITBUS slave.

3.1.4 Detector

Ohmic $CdTe$ detectors manufactured by Eurorad were chosen after a comparison to other options including cadmium zinc telluride (CZT), mercury(II) iodide (HgI_2) and Schottky $CdTe$ detectors. The main advantages of $CdTe$ over the other materials are the high detection efficiency in the desired range of 10 – 300 keV and a fast charge collection enabling high count rates and subsequently providing good statistics. The size of the detector, 2 mm × 2 mm × 2 mm was chosen due to spatial and étendue constraints (area) and a good compromise of detection efficiency at high photon energies and fast charge collection (thickness). The Schottky detector type provides a better energy resolution, but was excluded due to polarization effects that change the detector behavior over time. [121]
By contrast, the long-term stability of the employed Eurorad $CdTe$ detectors was also verified by a calibration check after years of operation during several thousand plasma discharges.

3.1.5 Pre-amplifier and amplifier

The detectors are followed by fast integrators that act as charge collectors, the charge being proportional to the impinging photon energy. The pulses have a characteristic rise time of 400 ns, and the integrators are discharged with a decay time of 4 μs. After this pre-amplifier stage, the collected signal is amplified to the digitizer range of $[-4, 4]$ V.
The integrator and amplifier electronics are on small printed circuit boards (PCBs) close to the detectors in order to minimize the noise that can enter the system in between. Since they heat up significantly, especially in vacuum, they are only switched on and off about half a minute before and after the TCV discharge, respectively. This amply guarantees stability because the system stabilizes within less than 100 ms.

3.1.6 BITBUS slave

There are two BITBUS slaves, each hosting the power supply, triggers and filter wheel control of two HXRS cameras. Furthermore, the 52 (2 × 26) signal wires from the 68 pin connector are unbundled per channel. The pairs (differential output) in individual cables connect with LEMO connectors to the D-tAcq acquisition boards.

3.1.7 Acquisition

The signal is acquired at 12 M$^{samples}/_{s}$ by six D-tAcq ACQ216CPCI 16 channel digitizer cards located in two crates providing the power supply. Each of the crates is connected to two cameras via one of the BITBUS slaves. Integrated filters (5 MHz) prevent aliasing and integrated field programmable gate arrays (FPGAs) enable real-time data processing (not used so far).
Time traces of up to 2.6 s can be stored in the on-board memory (1 GB). After each discharge this data is collected by the acquisition personal computer (PC) `crpppc82` via a 100 Mbit Ethernet connection and stored locally on hard disk drives (HDDs).

3.2 Calibration

The calibration of the HXRS system was performed in three parts: the D-tAcq digitizer cards were calibrated against a sinusoidal signal from a function generator for relative calibration; the detectors were individually calibrated against an americium-241 (^{241}Am) source using a shaping amplifier and a multichannel analyzer (MCA-3); finally, all channels of the assembled cameras were calibrated individually using the MCA-3 setup for relative calibration and one channel per camera additionally against the digital acquisition and pulse processing for absolute calibration.
In the following, the calibration is described more in detail.

3.2.1 ADC and acquisition calibration

The 96 channels of the six 16 channel D-tAcq ACQ216CPCI ADC and acquisition cards are calibrated using a 8 V peak-to-peak sinusoidal signal from a synthesized function generator (WAVETEK model 288). A calibration time trace contains 600 000 samples, acquired at 12 M$^{samples}/_{s}$. The standard calibration signal is a sine wave at 10 kHz, such that 500 periods are acquired. The calibration scaling factor is determined from the root mean square (RMS) of the unbalanced signal (50 Ω, one differential input grounded). The calibration offset is the mean value of the balanced signal (135 Ω).
Furthermore, the signal attenuation vs frequency was measured for sine waves with frequencies from 10 kHz to 20 MHz (unbalanced, 1 MHz balanced) for two channels (one per D-tAcq box) and provided a verification that the anti-aliasing filter works properly (Fig. 3.5).
Finally, the common mode rejection was analyzed by splitting the unbalanced signal into both differential inputs of the D-tAcq channel. From 60 dB at 1 kHz the attenuation decreases slowly monotonically to 50 dB above 1 MHz, followed by a minimum of 40 dB at 5 MHz and an increasingly fast rise to more than 70 dB at 20 MHz.

3.2.2 Detector calibration

The HXRS $CdTe$ detectors were individually calibrated after purchase using an ^{241}Am source. The ^{241}Am source has a main gamma ray (γ) peak at 59.5409 keV

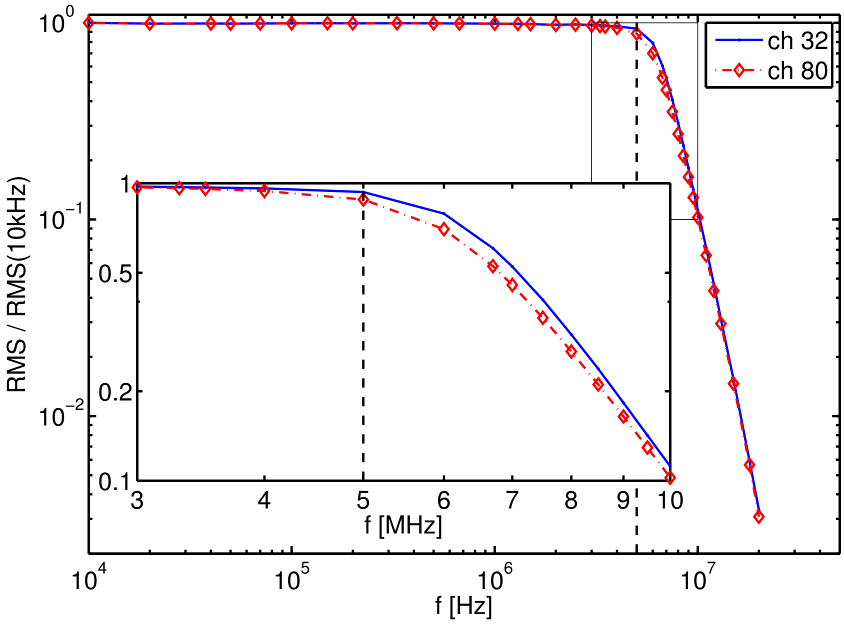

Figure 3.5: HXRS ADC anti-aliasing filter attenuation shown by the normalized RMS value of the sine waves vs frequency of D-tAcq channels 32 and 80. The rectangular area (range [3, 10] MHz) is shown in the zoomed plot in more detail.

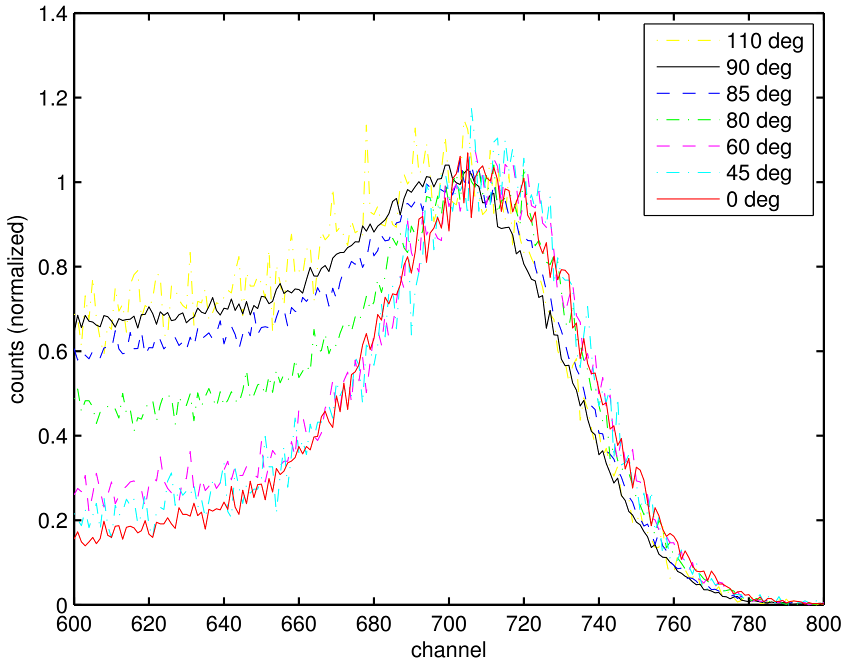

Figure 3.6: Spectra measured with MCA-3 with the HXRS CdTe detector in the prototype amplifier card for different photon incident angles (location of ^{241}Am source; 0 deg in front, 90 deg at the side).

(35.9 % of intensity) that is used for the calibration and two peaks at smaller energy (13.9 keV (37 % and 26.3446 keV (2.27 %)) [135] that are useful to analyze the noise level.
Therefore, the detectors were consecutively set into a reference amplifier card that is connected to an EG&G Ortec 571 shaping amplifier that transforms the pulses into a Gaussian shape. This signal enters a multichannel analyzer (FAST ComTec MCA-3 of the PHAV diagnostic) where the pulse height analysis (PHA) is performed. For the calibration of one detector it takes about 40 min to get sufficient statistics.
The standard deviation (σ) of the main peak (over all detectors) is less then 1.7 %. The mean value (over all detectors) of the full width at half maximum (FWHM) of the main peak is about 10 %. The goal of this test was to check that all detectors work properly. This is only a cross-check and is not used directly in the final camera calibration.
Additionally, the dependence of the spectrum on the incident angle θ of the photons was analyzed by moving the ^{241}Am source to different angular positions with respect to (w.r.t.) the detector. For positions in front of the detector ($\theta \leq 45$ deg) the difference is negligible; it is still small for $\theta = 60$ deg and increasingly significant for $\theta > 70$ deg (Fig. 3.6).

3.2.3 Camera calibration

The detectors are finally calibrated in the assembled camera. The full chain including the amplifier cards, the D-tAcq and the digital pulse processing (absolute calibration) is only performed for one channel per camera. Due to triggering and readout summing up to about 60 s for 1.5 s of data containing about five to ten pulses each, this calibration takes too long to use it for all channels (about two days per channel).
Therefore, the part of the chain up to the amplifier card output (including the detector, integrator and amplifier) is relatively calibrated w.r.t. the absolutely calibrated channel, using the shaping amplifier and the multichannel analyzer as in the individual detector calibration setup, but at higher resolution (≈ 2 h per channel). The remaining part, is also relatively calibrated w.r.t. to the absolutely calibrated channel using the D-tAcq calibration (the digital pulse processing is the same for all channels).
A comparison of the three absolutely calibrated channels (of cameras 2, 5 and 7) shows that the deviation due to the relative calibration is negligible. Therefore there is no significant drawback in the relative calibration.
Due to the fact that for 100 detectors there are only 96 D-tAcq channels, not all channels can be connected at once for the moment. Depending on the plasma scenario and position the connections may be interchanged leaving different channels disconnected. The connections are stored in a lookup table. This table, together with the relative and absolute calibration data is used for the full calibration that is automatically applied in the raw data access functions (available in MATLAB and Python).

3.3 Digital pulse processing

After the data collection the raw time traces are immediately analyzed in `crpppc82` using digital pulse processing. The algorithm is implemented in Python and C and parallelized with mpi4py, resulting in a runtime of less than 70 s for the analysis of all 96 channels. The derived arrival time and energy of each photon are stored locally in MDS+ providing fast data access.
The detection and analysis of the single photons from the acquired time traces is a challenging task at the desired high count rates of several 100 kcps and in view of the significant noise level of a tokamak experiment environment.
To find the best-suited algorithm for the specific HXRS requirements, several standard and advanced pulse processing techniques have been implemented. This was a significant sub-project and an original contribution within this thesis, which explains the considerable length of the present section. The accompanying algorithm benchmarking suite was deliberately designed with broad flexibility, permitting a general study of the pulse detection and analysis problem at high count rates that transcends the specific requirements of the HXRS system. The results of this study are reported in the present section.

Analog versus digital pulse processing

Practically every particle counting spectrometer consists of an analog and a digital part with an ADC in between. In analog pulse processing the digital part only performs a histogram. This was the only solution available till the early 1990s, when digital systems became fast enough to restrict the analog part to the charge collection and preamplification. In the latter scheme, the preamplified signal is directly sampled by a high-resolution ADC that records the time history of each individual pulse, and the pulse processing is performed digitally, either by hardware or by software [136]. In the transitional period, when the performance of digital processors was still relatively low, hybrid systems were also used, in which a digital signal processor (DSP) was triggered by an analog pulse height analyzer (PHA) [137].
The main advantages of analog pulse processing lie in robustness, decades of experience and low cost as compared to digital systems. With some additional effort even the pulse shape can be used to a certain extent to aid the pulse recognition, for instance to discriminate between particle types [138].
Nowadays digital pulse processing is used in commercially available spectrometers [139] as well as in highly specialized applications such as spacecraft [140] and magnetic confinement fusion experiments [1]. The available digital solutions continuously decrease in cost and increase in processing speed and storage, enabling real-time applications as well as storage of the entire time traces acquired. Since the shape of each pulse is known, it can be used to extract more information than just the height of the pulse. Therefore the pulse processing algorithms can be optimized with respect to the pulse characteristics, for instance for neutron - gamma discrimination [141] or to detect the incident position of the particle within a detector [142] and use this information to improve the determination of the particle energy [143].

Furthermore, the time and energy of each detected pulse are available. This allows one to freely choose time and energy bins after the measurement and subsequently to use advanced analysis techniques such as conditional averaging: this is very effective to analyze randomly repeated events such as sawtooth crashes with the HXRS system at a timescale capturing the fast dynamics [62].

Existing techniques

In analog pulse processing the preamplifier signal is shaped by a shaping amplifier. This can be realized either as a single delay line (SDL), a double delay line (DDL) or as a combination of m differentiating capacitor-resistor (CR) and n integrating resistor-capacitor (RC) circuits ($(\mathrm{CR})^m(\mathrm{RC})^n$ filter). In addition, tail (pole-zero) cancellation and baseline restoration are regularly applied to improve the signal properties further. Finally the signal is evaluated using a peak-sensing ADC and the detected pulses are digitally stored in a histogram [144].
In digital pulse processing the same analog techniques can be implemented digitally [145]. However, a large variety of additional methods can also be used, comprising more sophisticated techniques that take the whole time history and pulse shapes into account. Typical such techniques are digital finite impulse response (FIR) and infinite impulse response (IIR) filters [146, 147], cross-correlation (CC) [148, 149] and least (mean) squares (LMS) difference [150] to template pulses, neural network pulse recognition [151], wavelet transform [152, 153] and support vector machine (SVM) pulse sorting [154].

3.3.1 Digital implementation

Although a very wide range of different pulse processing algorithms is compared, a large fraction of these algorithms shares the use of a few fundamental steps in the data analysis. This allows not only the implementation of a general framework for data input/output (I/O), storage and benchmarking, but also a generalization of the algorithm implementation itself. This in turn makes it possible to study more algorithms with little additional effort and facilitates their comparison. The common basic steps are, namely, signal treatment, pulse detection (PD) and PHA. These components are individually presented in the following. Nonetheless, the implementation can be kept flexible enough to treat algorithms that can be only partially or not at all resolved by this sequence of steps or that require additional post-processing.
For all presented algorithms, the signal treatment, PD and PHA methods are listed in Tab. 3.2.

Signal treatment

The signal treatment processes the raw data to provide an input for the pulse detection and analysis. It keeps the signal's original sampling rate and is often realized by the application of filters. Usually the signal treatment is the same for the pulse detection and pulse height analysis, although there are also a few methods where the signal treatment for analysis differs from that for detection. Since most pulse processing algorithms share the same or similar detection and

Algorithm	Detection		Analysis	
Acronym	Signal treatment	PD	Signal treatment	PHA
Trpz2	Trpz2	Dyn. thres.	Trpz2	Level eval.
Trpz1a	Trpz1a: $n_r, n_d = 4$	Dyn. thres.	Trpz1a: $n_r, n_d = 4$	Level eval.
Trpz1as	Trpz1a: $n_r, n_d = 3$	Dyn. thres.	Trpz1a: $n_r, n_d = 3$	Level eval.
Trpz1	Trpz1	Dyn. thres.	Trpz1	Level eval.
Trpz	Trpz	Dyn. thres.	Trpz	Level eval.
CC-LMS	CC	Dyn. thres.	LMS	Level eval.
LMS	LMS	Dyn. thres.	LMS	Level eval.
$(CR)^2(RC)$	$(CR)^2(RC)$	Dyn. thres.	$(CR)^2(RC)$	Level eval.
$(CR)^2(RC)^4$	$(CR)^2(RC)^4$	Dyn. thres.	$(CR)^2(RC)^4$	Level eval.
$(CR)(RC)^4$	$(CR)(RC)^4$	Dyn. thres.	$(CR)(RC)^4$	Level eval.
$(CR)(RC)$	$(CR)(RC)$	Dyn. thres.	$(CR)(RC)$	Level eval.
CIS	Digital band-pass	CIS, rise thres.	Digital band-pass	Rise eval.
PSD	MA filter	Mult. cond.	MA filter	Rise eval.
Canny	Canny	Dyn. thres.	Canny	Level eval.
SDL	SDL	Dyn. thres.	SDL	Level eval.
DDL	DDL	Dyn. thres.	DDL	Level eval.
opt1na	Optimum filter 1	Dyn. thres.	Optimum filter 1	Level eval.
opt2na	Optimum filter 2	Dyn. thres.	Optimum filter 2	Level eval.
opt3na	Optimum filter 3	Dyn. thres.	Optimum filter 3	Level eval.
opt4na	Optimum filter 4	Dyn. thres.	Optimum filter 4	Level eval.
i-500 kcps	Idealized algorithm, detects all pulses spaced by $\geq 2\,\mu$s correctly			
i-1 Mcps	Idealized algorithm, detects all pulses spaced by $\geq 1\,\mu$s correctly			
i-2 Mcps	Idealized algorithm, detects all pulses spaced by $\geq 0.5\,\mu$s correctly			

Table 3.2: List of signal treatment, pulse detection and PHA methods for all presented algorithms.

analysis methods, their main differences lie in the signal treatment. Therefore, the signal treatment parts play the main role in characterizing a pulse processing method.

Pulse detection

In the analysis chain comprising signal treatment and pulse detection, care has to be taken not to introduce a time shift in the particle arrival time. Already in the raw signal, and additionally after filtering using only data points from the past, the peak of a pulse is delayed with respect to the photon arrival time. This is why it can be necessary to apply a time index shift in addition to the basic signal treatment in order to detect the photon at its arrival time instead of the time point at which the corresponding pulse appears in the processed signal after the whole chain from charge collection to basic signal treatment.

Threshold The threshold detection defines the detected pulses as groups of contiguous points exceeding a set threshold value, separated by points below it. The time of each pulse is then defined as the point of maximum value within it. This solution prevents artificial time shifts dependent on the pulse height, such as in the leading edge threshold crossing method, which for this reason is not considered here, in spite of its frequent usage.

Dynamic threshold The dynamic threshold (dyn. thres.) detection algorithm detects local maxima that lie above a set threshold value and identifies them as pulses if they are separated by a minimum, with the maximum to minimum ratio exceeding a set factor. Especially at high count rates this is expected to be advantageous since the signal between two consecutive pulses only has to go down to the specified ratio and not all the way below the threshold value in order to separate these two pulses.

Rise threshold Here, the pulse rise is investigated by selecting monotonically increasing segments of the signal. Since the derivative of the signal is positive in these segments and bounded by sign changes before and after them, this selection is realized by detecting the change-in-sign (CIS). If the signal rise within such a segment exceeds a set threshold value, the start or mean time of this segment is taken as the pulse time.

Multiple conditions Several other detection methods can be grouped under this expression, meaning that they do not look only for maxima but apply additional conditions. For instance the pulse-shape discriminator (PSD) algorithm, operating on a smoothed signal, checks for a signal rise followed by a decrease over three or more consecutive points lying within the integrator decay time [121].

Pulse height analysis

Level evaluation To determine the pulse height the signal is simply evaluated at the points detected by the pulse detection. It should be noted that a statistical average over several points can be achieved by including this averaging in the signal treatment directly.

Rise evaluation The rise of the signal over a certain period, usually defined by the rise threshold detection, is used to determine the pulse height.

3.3.2 Overview of signal treatment algorithms

The methods presented in this section, especially the filters, are all time-invariant. This corresponds to the application where pulse shapes and noise characteristics do not change over time. In time-variant systems, however, the method's parameters should be adjusted accordingly over time. Then the results presented in here can, to a certain extent, be extended to such systems as well.
In Figs. 3.7–3.8 the pulse responses of the most important filter methods presented in the following are compared.

I. IIR filters

Infinite impulse response (IIR) filters are widely used in digital pulse processing, for instance as band-pass filters or to emulate analog filters digitally.

I.a. Digital band-pass filters A tempting approach is the simple use of band-pass filters to remove high frequency noise and low frequency baseline deviation. In the remaining signal only the pre-amplified pulses should appear and be evaluated. However, since the pulses themselves are not sinusoidal but have a wider frequency spectrum, the filter pass band has to be chosen carefully, especially if the pulse and noise spectrum overlap significantly.

CIS method One of the earliest attempts at digital pulse processing for the HXRS diagnostic was based on a digital band-pass filter. The filtered signal, however, cannot be used for (dynamic) threshold detection and level evaluation analysis. In order to yield a working pulse processing method the rise threshold detection and rise evaluation analysis have to be applied on the band-pass filtered signal. Subsequently, the method as a whole is called a change-in-sign (CIS) method [121].

I.b. Analog filters Classic analog pulse shaping amplifiers use a combination of differentiating CR and integrating RC circuits. Their transfer functions are determined by time constants and can be easily implemented digitally, providing a reference for digital pulse processing. The principle can be understood by considering the simplest type $(CR)(RC)$ with one CR and one RC circuit. First, the CR circuit determines the slope of the pulse rise and then its output decays over its time constant. Therefore it acts as a high-pass filter. The RC circuit then integrates the CR output and acts as a low-pass filter. [144]

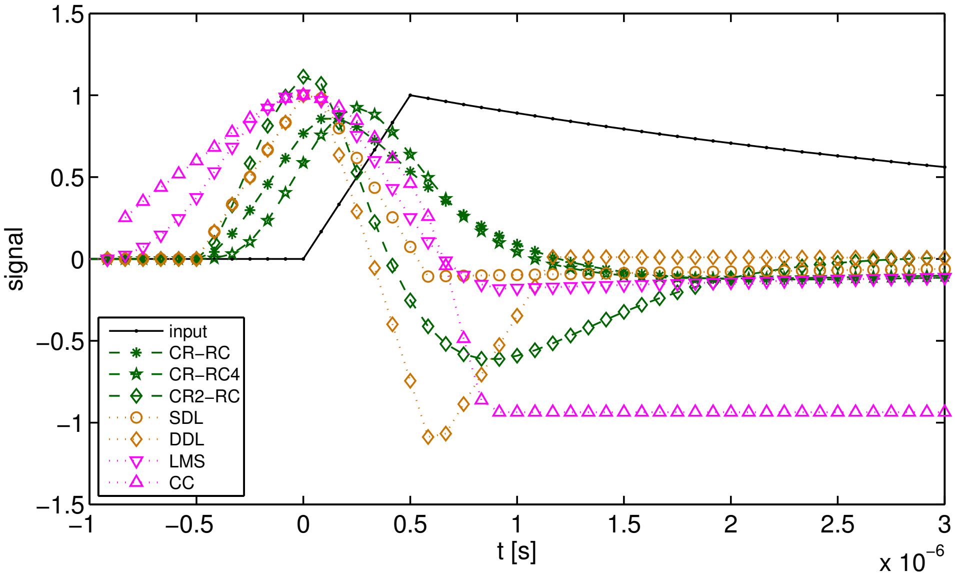

Figure 3.7: Pulse response of the presented IIR, delay line, LMS and cross-correlation filters to a simulated clean input pulse.

$(CR)(RC)^n$ method If the RC integrating step is repeated n times, the noise in the high-frequency range is further reduced and the resulting pulse shape approaches a Gaussian. To keep the peaking time constant, the time constants of the n RC circuits have to be $1/n$ times the time constant of a single RC circuit. This shortening of the time constants shortens the decay after the peak as well. However, adding more circuits increases the complexity of the system and the improvement is only significant for low n. Typically $2-4$ RC circuits are used. [145]

$(CR)^2(RC)^n$ method In the limit of high count rates any pulse detection method is affected by pile-up. To reduce this effect a second differentiating CR circuit is added, which makes the output signal bipolar. This was, for instance, done for the HXRC that was formerly installed on TCV and used $(CR)^2(RC)$ analog pulse processing with a filter time constant of $0.3\,\mu$s [76]. As before, $n > 1$ is expected to yield a slight improvement in performance.

II. FIR filters

Finite impulse response (FIR) filters have, in contrast to IIR filters, an impulse response of finite duration. An analog implementation of these filters is not trivial but can be realized using delay lines or surface acoustic wave (SAW) filters. The digital implementation of discrete-time FIR filters, however, is very simple. The output signal $\mathbf{r}$ is the convolution of the input signal $\mathbf{s}$ and the filter coefficients $\mathbf{c} \in \mathbb{R}^{(N+1)\times 1}$

$$r_i = \sum_{k=0}^{N} c_k s_{m+i-k} \qquad \forall i = 1,\ldots,n, \tag{3.1}$$

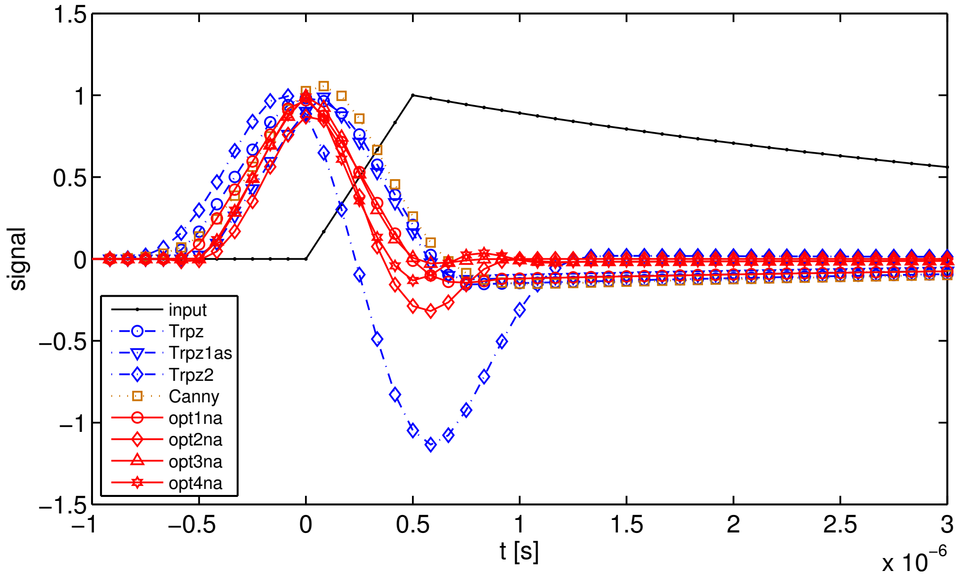

Figure 3.8: Pulse response of the presented FIR filters to a simulated clean input pulse.

where **s** is zero for all indices that are out of range. The common FIR filter definition ($m = 0$) is extended here by a time index shift $m \in \mathbb{Z}$, in order to detect photons at their arrival time, as described in section 3.3.1. The map $f : \mathbf{s} \mapsto \mathbf{r}$ defined by (3.1) is linear $f \in L(\mathbb{R}^{n\times 1})$. Another important property is that the filter coefficients represent the impulse response of a N^{th} order discrete-time FIR filter, which is of length $N+1$ samples.
The impulse responses of the more complicated FIR filters presented in the following, corresponding to their filter coefficients, are compared in Fig. 3.9. Their step responses are shown in Fig. 3.10.

II.a. Delay lines The delay line technique splits the input signal onto several paths of different lengths where each sub-signal is also multiplied by a different weighting factor. The outputs from all the paths are then added to obtain a weighted sum of delayed versions of the raw signal.

SDL method The single delay line (SDL) method uses a single delay line to subtract a delayed and slightly downscaled version of the signal off the signal itself. This leads to a short, nearly trapezoidal pulse with a length of the order of the delay followed by a fast reset to zero. The delay of the line should in no case be smaller than the rise time of the input pulse, otherwise parts of the pulse would already be subtracted while it still rises. To minimize the flat top of the trapezoidal-like pulse the delay should be close to the rise time of the input pulse. This results in a quasi-triangular output pulse without visible flat top, as can be seen in Fig. 3.7. Also, the downscaling factor has to be adjusted according to the pulse decay in order to restore the baseline after the pulse properly.
While noise at the exact delay time frequency is damped, this method includes

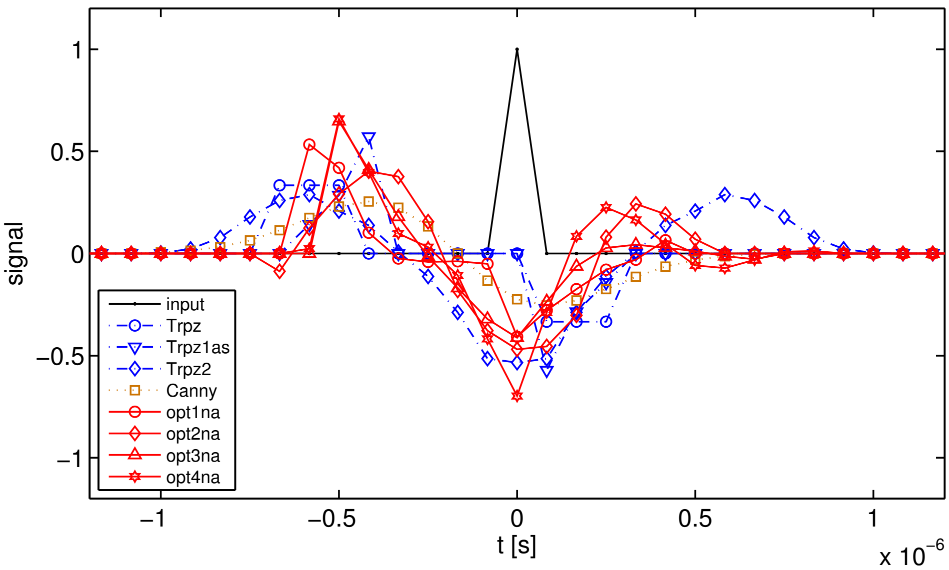

Figure 3.9: Impulse response of the presented FIR filters, being equal to the filter coefficients.

no low-pass filter to get rid of general high-frequency noise.

DDL method The double delay line (DDL) is a series of two SDL circuits to obtain a bipolar pulse instead of a trapezoidal peak. The resulting zero-crossing leads to a better pulse separation whereby even higher count rates can be resolved than with the SDL.

II.b. MA filter A moving average (MA) filter of span S is a FIR filter with S coefficients, all being equal to $1/S$. We restrict S to odd positive integers, meaning that the order of the FIR filter $N = S - 1$ is even ($N \in 2\mathbb{N}$), and we set the time shift to $m = N/2$. Following this definition, the filtered signal at each point in time is the arithmetic mean of the raw signal at that time and the $N/2$ consecutive points before and $N/2$ consecutive points after that point in time.

PSD method The moving average filter is used to smooth the signal for the multiple condition detection in the pulse-shape discriminator (PSD) method.

II.c. Trapezoidal filters Here, the trapezoidal (Trpz) filter family encompasses the basic trapezoidal (Trpz) filter and several FIR filters closely related to it.

Trpz method The step response of the trapezoidal (Trpz) filter is a trapezoidal peak as shown in Fig. 3.10. The filter is specified by the number of samples in the rise (n_r), the flat top (n_f) and the decay (n_d) phases of this peak. It computes the difference between the mean value of n_r samples on the future side of a gap of n_f samples and the mean value of n_d samples on the gap's past side [144]. The response to a ramp from 0 to 1 within a certain rise time is a piece-wise

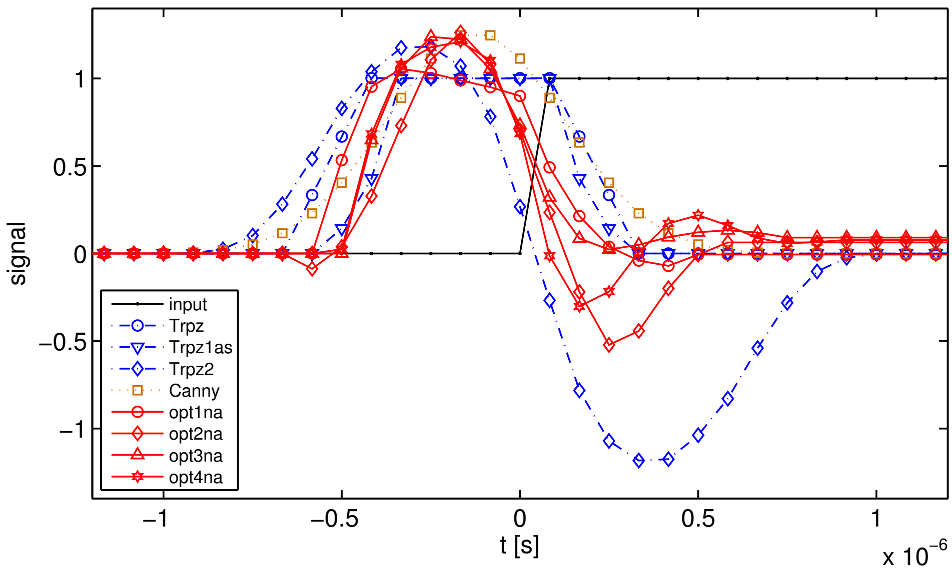

Figure 3.10: Step response of the presented FIR filters.

quadratic function. It is smoothed with respect to the step response and its flat top is shortened by the finite ramp rise time. Without a flat top this response is a quadratic spline approximation to a Gaussian.
In analogy to the SDL, the delay time, corresponding to n_f, should be greater than the rise time of input pulses. The flat top should be as short as possible to obtain Gaussian-like output pulses. However, a short flat top is required in order to account for ballistic deficit [155].
The case $n_r = n_d = 1$ corresponds to a time-discrete SDL method with n_f specifying the delay; for increasing n_r and n_d high-frequency noise is averaged out with increasing effectiveness.

Trpz1/Trpz1a method Starting from the Trpz filter, the Trpz1(a) filter is obtained by computing weighted mean values instead of mean values before and after the gap. If one increases the weights for samples closer to the gap, e.g., this technique can narrow the output pulse. In the Trpz1 method the weights increase linearly towards the gap while an exponential increase is used in the Trpz1a method.

Trpz2/Trpz2a method Applying to the Trpz1(a) method the same step that was taken from the $(CR)(RC)$ to the $(CR)^2(RC)$ and from the SDL to the DDL method to the Trpz1(a) method yields the Trpz2(a) method. This subsequent application of two Trpz1(a) and an integrating window can be represented by a single FIR filter whose coefficients are a convolution of two Trpz1(a) filters and an integrating FIR filter. The latter is similar to a moving average (MA) filter, but uses numerical integration method coefficients (such as $\frac{(7,32,12,32,7)}{90}$ from Boole's rule) instead of the arithmetic mean.
As is the case in going from SDL to DDL, this leads to a bipolar shape and is ex-

pected to increase the throughput at high count rates.

II.d. Canny method The problem of detecting a pulse is similar to edge detection. The Canny edge detector [156], the first derivative of a Gaussian, can therefore be used as a FIR filter.

II.e. Optimum filters The FIR filters presented above represent only a small, very specific set within the space of FIR filters. To overcome the restrictions to filters that follow strict design rules and are determined by only a few parameters, one can look for an optimum FIR filter with respect to well-defined requirements. This can be realized by linear least squares minimization of a functional containing information about the noise and the desired output pulse shape [157, 158].
The basic idea is to optimize the FIR filter coefficients under several constraints in a least squares sense. The two main constraints taken into account are the following: for a given input pulse a desired output should be obtained; and for noise input the output should be zero. Furthermore, specific input frequencies can be suppressed and the pulse response area can be specified. Since all these constraints form an over-determined system of equations there is usually no exact solution. However, a best approximation in a least squares sense, where weighting factors reflect the importance of each constraint, can be found.
The two main constraints, optimum pulse response and noise rejection, can be formulated as follows: the signal $\mathbf{s}$ is written as the sum of a clean pulse signal $\mathbf{s}_\mathrm{c}$ and a noise component $\mathbf{s}_\mathrm{n}$. This results, according to (3.1), in the FIR filter output

$$r_i = \sum_{k=0}^{N} c_k s_{\mathrm{c},m+i-k} + c_k s_{\mathrm{n},m+i-k} \qquad \forall i = 1, \dots, n. \tag{3.2}$$

For noise of mean zero this yields an average output

$$\overline{r}_i = \sum_{k=0}^{N} c_k s_{\mathrm{c},m+i-k} \qquad \forall i = 1, \dots, n \tag{3.3}$$

with variance

$$\sigma_\mathbf{r}^2 = \mathbf{c}^T V \mathbf{c}. \tag{3.4}$$

Here, V is the auto-covariance matrix of the noise $\mathbf{s}_\mathrm{n}$. The variance of the clean signal $\mathbf{s}_\mathrm{c}$ that does not originate from noise, such as pulse shape changes due to different interaction locations in the detector, can be taken into account in the same manner.
The ideal result would be an average output identical to the request, and with zero variance. Generally, this cannot be obtained exactly but a best approximation can be found by minimizing the sum of the weighted difference between the average output $\overline{\mathbf{r}}$ and the desired output $\mathbf{r}_\mathrm{d}$ and the variance $\sigma_\mathbf{r}^2$

$$\sum_i \alpha_{\mathrm{r},i} \|\overline{r}_i - r_{\mathrm{d},i}\|^2 + \alpha_\mathrm{n} \sigma_\mathbf{r}^2 \to \min, \tag{3.5}$$

$\boldsymbol{\alpha}_\mathrm{r}$ being the weighting factors for the request and α_n being the noise weighting factor, all greater or equal zero.

The expression in (3.5) can be written in matrix form. It adopts its minimum at the zero of its gradient, yielding the normal equation

$$\left[\left(\sum_i \alpha_{\mathrm{r},i}\left(\mathbf{s}_\mathrm{c}\mathbf{s}_\mathrm{c}^T\right)_i\right) + \alpha_\mathrm{n} V\right]\mathbf{c} = \sum_i \alpha_{\mathrm{r},i}(\mathbf{s}_\mathrm{c})_i r_{\mathrm{d},i}. \tag{3.6}$$

Its solution is the vector of the $N+1$ optimum FIR filter coefficients $\mathbf{c}$. Additional constraints can be imposed by adding corresponding terms to (3.5) and (3.6) respectively.

The choice of the weighting factors is essential in order to obtain a well-behaved optimum filter. In particular, a low α_n can lead to over-fitting, yielding unacceptably poor performance if the signal $\mathbf{s}$ deviates only slightly from the clean signal $\mathbf{s}_\mathrm{c}$.

III. Least squares and cross-correlation methods

III.a. LMS method The least (mean) squares (LMS) difference from a template pulse can be used to specify a digital filter. The idea is to find the pulse amplitude a such that the template pulse $\mathbf{t}$ of height 1 is optimally scaled to the signal $\mathbf{s}$ (both column vectors of N samples) in a least squares sense.

$$\|\mathbf{t}a - \mathbf{s}\|^2 \to \min \tag{3.7}$$

with $\mathbf{t}, \mathbf{s} \in \mathbb{R}^{N\times 1}$. The obvious choice for the template pulse $\mathbf{t}$ is the clean signal $\mathbf{s}_\mathrm{c}$. To reduce the effect of baseline shifts both the signal and the template are shifted by their mean value before the least squares optimization is effected ($\mathbf{u}$ is a vector with all values equal to 1 and of same size as $\mathbf{s}$ and $\mathbf{t}$).

$$\mathbf{x}_0 = \mathbf{x} - \frac{\mathbf{u}^T\mathbf{x}}{N}\mathbf{u}, \qquad \mathbf{x} = \mathbf{s}, \mathbf{t} \tag{3.8}$$

The linear least squares problem (3.7) is solved by the solution of the normal equation

$$\mathbf{t}_0^T\mathbf{t}_0 a = \mathbf{t}_0^T\left(\mathbf{s} - \frac{\mathbf{u}^T\mathbf{s}}{N}\mathbf{u}\right). \tag{3.9}$$

From the definition of $\mathbf{u}$ it follows that $\mathbf{u}^T\mathbf{u} = N$ and, since

$$\mathbf{u}^T\mathbf{x}_0 = \mathbf{u}^T\mathbf{x} - \frac{\mathbf{u}^T\mathbf{x}}{N}\mathbf{u}^T\mathbf{u}, \tag{3.10}$$

subsequently

$$\mathbf{u}^T\mathbf{x}_0 = 0 \tag{3.11}$$

for vectors $\mathbf{x}_0$ as defined in (3.8). On the other hand, vectors $\mathbf{y}$ with $\mathbf{u}^T\mathbf{y} = 0$ remain unchanged by (3.8): $\mathbf{y}_0 = \mathbf{y}$. Therefore (3.8) and (3.11) are equivalent definitions of a zero mean LMS method template pulse $\mathbf{t}_0$.

Using (3.11) for $\mathbf{x} = \mathbf{t}$ yields directly $\mathbf{t}_0^T\mathbf{u} = 0$, which simplifies (3.9). The pulse amplitude is then given by

$$a = \frac{\mathbf{t}_0^T}{\|\mathbf{t}_0\|^2}\mathbf{s}. \tag{3.12}$$

Comparison to (3.1) reveals that (3.12) defines the coefficients of a FIR filter of order $N-1$:

$$\mathbf{c} := \frac{\mathbf{t}_0}{\|\mathbf{t}_0\|^2}. \tag{3.13}$$

Conversely, FIR filters with coefficient sum zero ($\mathbf{u}^T\mathbf{c} = 0$) can be represented by the LMS method, since the template pulse defined by

$$\mathbf{t}_0 := \frac{\mathbf{c}}{\|\mathbf{c}\|^2} \tag{3.14}$$

fulfills (3.11).

III.b. Cross-correlation detection Using the notation of section 3.3.2 the normalized cross-correlation (CC) of a signal and a template pulse can be written as

$$c = \frac{\mathbf{t}_0^T\mathbf{s}_0}{\|\mathbf{t}_0\|\,\|\mathbf{s}_0\|} \in [-1,1]\,. \tag{3.15}$$

This can be directly used as a non-linear filter for pulse detection [149]. A clear advantage of this filter is that it ideally responds equally to the pulse shape, no matter what its amplitude is. However, since it does not respond to the amplitude of the pulse, a different method has to be used for the pulse height analysis. This could be any of the PHA methods discussed earlier; however, the formal similarity between the cross-correlation detection and the LMS method suggests to combine these two for an optimal result.

IV. Wavelet transform

A discrete wavelet transform is used to detect patterns in signals that may occur on different timescales. This is for instance successfully applied in sawtooth detection using the Canny edge detector as wavelet [152] to detect sawtooth crashes whose length may vary.
In the present pulse processing application, however, the rise and decay times of the pulses to be detected are practically constant and usually well known. Therefore, pulse detection algorithms can be well-tuned to the pulse characteristics. It is not necessary to scan different timescales using a wavelet transform since the timescale over which the pulses occur is already known. Hence, it is not expected that the use of the wavelet transform would improve well-tuned pulse detection algorithms. However, if the pulse rise and decay times are not known, this method may be advantageous [153].

3.3.3 Benchmarking methods

A detailed comparison and benchmarking of the presented algorithms is carried out using experimentally measured as well as simulated signals. The analysis concentrates on simulated signals where the particle arrival time and energy are exactly known and arbitrary count rates and noise can be investigated. Nonetheless the use of experimentally measured noise in the simulation as well as the analysis of full experimental signals are necessary to ensure the validity of the signal simulation models.

Signal simulation model

The signal simulation model comprises the steps from the particles arriving at the detector via the charge collection in the pre-amplifier and the amplification up to the digitization of the signal.

Particles The particle arrival times are modeled using a Poisson distribution whose free parameter is determined by the desired average count rate. The particle energy can be modeled using different spectra, e.g. monochromatic or polychromatic, exponentially distributed or uniformly distributed. The vectors of particle arrival times and energies are fed into the pre-amplifier model and kept as reference for the benchmark evaluation.

Detector Since we are interested in the performance of the pulse detection algorithms, the detector model assumes simply that all modeled particles are detected at their exact incident energy. In a real system this energy may be smaller than the total energy of the particle, e.g. in the case of Compton scattering of photons. However, we do not concern ourselves here with the analysis complications arising from such events.

Pre-amplifier The pre-amplifier model accepts arbitrary particle arrival time and energy vectors. It is the first step in which the full time trace is modeled: the output pulses are defined by the charge collection time and the integrator decay time.

Amplifier The amplifier's purpose is to amplify the pre-amplifier output to the digitizer input range without disturbing the pulse shape significantly. Since these requirements are met quite easily in practice, this stage can almost be neglected in the signal simulation model.

Noise The noise sensitivity is important in the benchmarking; therefore, different forms of noise (white Gaussian, $1/f$ and experimentally measured) can be used and entered at the pre-amplifier as well as after the amplifier stage [159]. In the following analysis the experimentally measured noise is taken from HXRS data on the TCV tokamak discharge 46061, partially shown in Fig. 3.11.

Benchmarking figures of merit

Main figures of merit

Detection efficiency The parameters reflecting the detection performance are the true positive, false negative and false positive detection rates. Here, positive / negative stands for the detection result of the algorithm and true / false if this agrees with the simulation, in each case normalized to the number of simulated particles. The true positive rate (a simulated particle is detected) should obviously be as close to unity as possible, while the false negative (a simulated

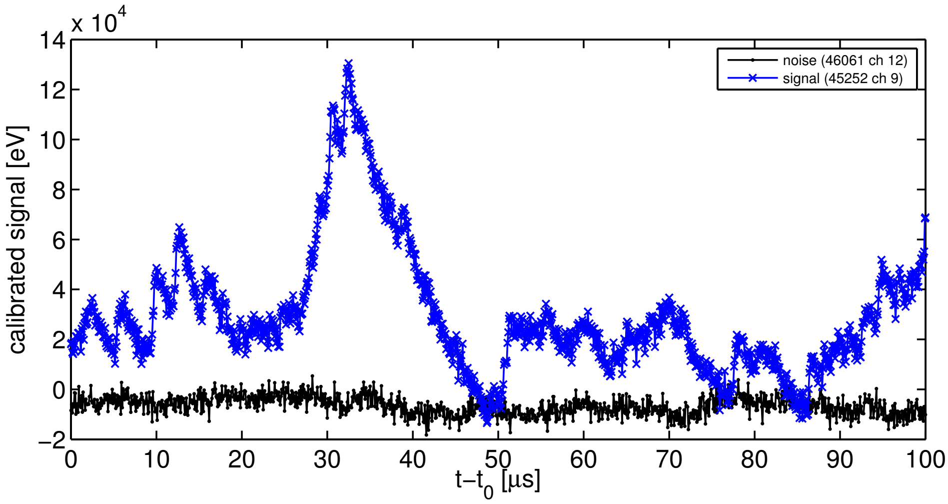

Figure 3.11: Experimentally measured time traces for noise only (TCV discharge 46061, HXRS chord 12, $t_0 = 0.8\,\mathrm{s}$) and signal with photons arriving at the detector (TCV discharge 45252, HXRS chord 9, $t_0 = 0.8\,\mathrm{s}$).

particle is not detected) and false positive (a particle that was not simulated is detected) rates should be as small as possible.

Energy accuracy To obtain high energy resolution the energy deviation has to be minimal. At high count rates where significant pile-up occurs the energy deviation is expected to increase accordingly. Note that the energy under discussion here is the energy transferred by the incident particle to the detector, which is assumed to be the total particle energy, as stated already in section 3.3.3.

Additional figures of merit

Time resolution The time resolution of the detection is not analyzed in detail since the deviation in the particle arrival time is, for all investigated algorithms, in the order of the sampling interval. In specialized applications, such as positron emission tomography (PET) using time of flight measurements, the time resolution plays a major role and can be enhanced by increasing the sampling rate or applying interpolation around the detection time. This works in a straightforward manner for all methods presented here.
The standard application, however, is to build spectrograms or time traces in spectral channels. Hence, the single pulses are grouped in energy and time intervals. The length of the latter can be effectively shortened by several orders of magnitude using techniques such as conditional averaging, which improve statistics by adding over different realizations of statistically similar events (e.g., periodic phenomena). Still, to get useful statistics, the time grouping interval needs to be much longer than the sampling interval length and is therefore much longer than the detection time error.
As an example, asking only for quite poor statistics (1000 pulses) from a system

detecting a pulse in average every 10 samples requires more than 10^4 conditional averaging events in order to get a time resolution (grouping interval length) close to the sampling rate.

Computational performance and complexity Since digital pulse processing inherently involves high sampling rates (typically in the M$^{samples}/_{s}$ to G$^{samples}/_{s}$ range), the computational performance plays an important role. Execution time and storage requirements are the main issues. Parallelization and its scaling may also play a role in certain applications but can be neglected for the HXRS system in which the number of detectors exceeds the number of available processor cores.

Real-time applicability Directly related to the computational performance is the question whether or not the algorithms can be implemented in real-time, for instance directly in FPGAs. This is essential if the measurement is used in a control cycle, for systems with low storage capacities relative to input channels and acquisition rate and for continuously operating systems.

3.3.4 Results: algorithm benchmarks

The benchmark analysis is presented in this section.

Analyzed algorithms

All algorithms analyzed and presented in this study are listed in Tab. 3.2. Therein, for each algorithm abbreviation, the corresponding signal treatment algorithm for detection (as presented in section 3.3.2), the detection method (section 3.3.1), the signal treatment for analysis (section 3.3.2) and the PHA (section 3.3.1) applied are specified. All algorithms using dynamic threshold detection can also be used with ordinary threshold detection, yielding a slightly degraded performance at reduced computational effort.

Optimum filter parameters In the benchmarking analysis four optimum FIR filters are investigated. They are all optimized with respect to the noise present in the HXRS system but the requested output differs.
The outputs requested for filters 1 and 2 are based on the clean signal responses of the Trpz1as and $(CR)^2(RC)^4$ method respectively. For the filters 3 and 4 cusp responses are requested. In the case of number 3 the cusp rises within 6 points, defined by

$$r_{\mathrm{d},i} = \frac{1}{2}\left[\frac{i}{6} + \left(\frac{i}{6}\right)^3\right],\ i = 1,\ldots,6 \tag{3.16}$$

and the cusp decay is symmetric, followed by 23 zeros. For number 4 the rise is requested to take place within only 4 points and the linear contribution is replaced by a quadratic one, both in order to optimize for a very fast response. After the cusp rise defined by

$$r_{\mathrm{d},i} = \frac{i^2 + i^3}{80},\ i = 1,\ldots,4 \tag{3.17}$$

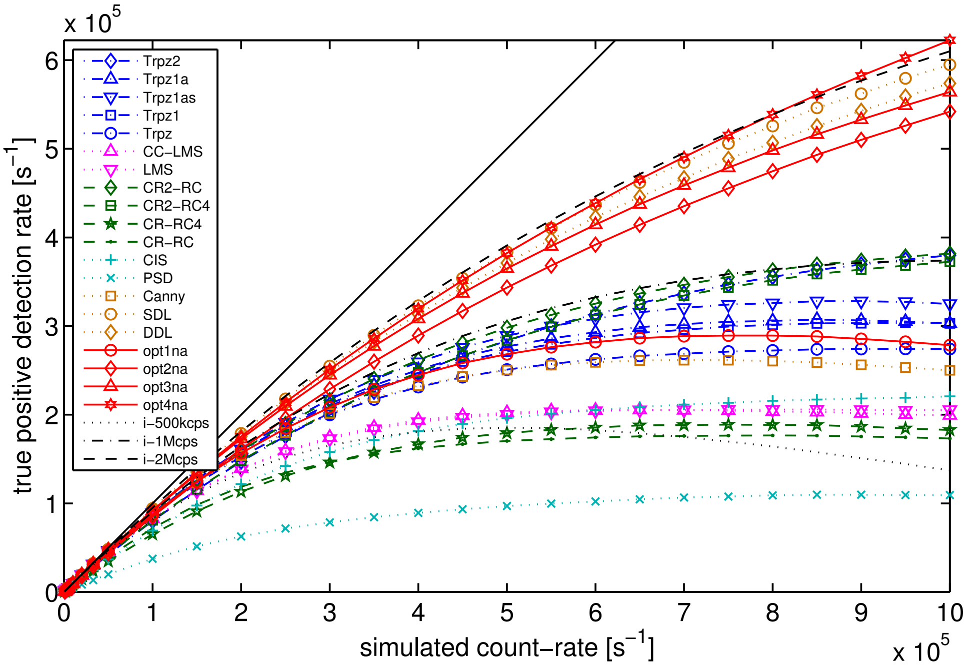

Figure 3.12: True positive detection vs simulated count rates for all analyzed algorithms including three idealized reference ones: 20 keV photons with experimental and Gaussian ($\sigma = 1$ keV) noise.

and the symmetric cusp decay, the subsequent zero is followed by a small negative dip ($r_{\mathrm{d},9} = -1/40$) before the final zeros. It turns out that in the case number 4 the request can never be met since it is on a smaller time scale than the pulse. However, the response is optimized to be as fast as possible in order to get good pulse separation at high count rates.

Idealized algorithms To provide an absolute comparison of the detection efficiency, idealized algorithms are used. These are not real algorithms; rather, they use the particle simulation without processing. They are characterized by a specific detection frequency and detect all pulses that are at least separated by the timescale corresponding to this frequency. Here, the idealized algorithms i-500 kcps, i-1 Mcps and i-2 Mcps are used for the performance comparison.

Detection efficiency

Count rates All presented algorithms are directly compared to each other and to the idealized cases in Fig. 3.12 with respect to their true positive detection rate. The photon energy of 20 keV and signal noise correspond to the typical HXRS operational point while the count rate range is extended well beyond the HXRS limits (operational point: 100–400 kcps), especially toward higher frequencies, to better visualize the performance limitations of the detection algorithms. In addition to the experimentally measured noise, a white Gaussian noise component of $\sigma = 1$ keV is added in the pre-amplifier stage.

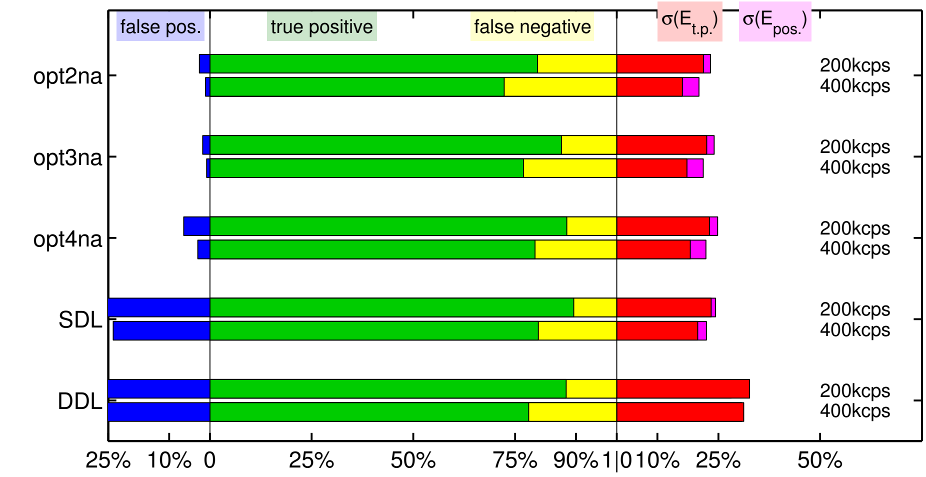

Figure 3.13: Comparison of figures of merit for the 5 algorithms achieving the best count rate performance for 20 keV photons at 200 and 400 kcps with experimental and Gaussian ($\sigma = 1$ keV) noise. From left to right the 5 figures of merit are the false positive detection rate, the true positive detection rate, the false negative detection rate, the energy standard deviation derived from true positive detection and the energy standard deviation including all (true and false) positive detection. The true positive and false negative detection rate bars are stacked since they add up to one. In contrast, the two energy deviation bars are not stacked but overlaid, starting from the same origin, labeled at the horizontal axis.

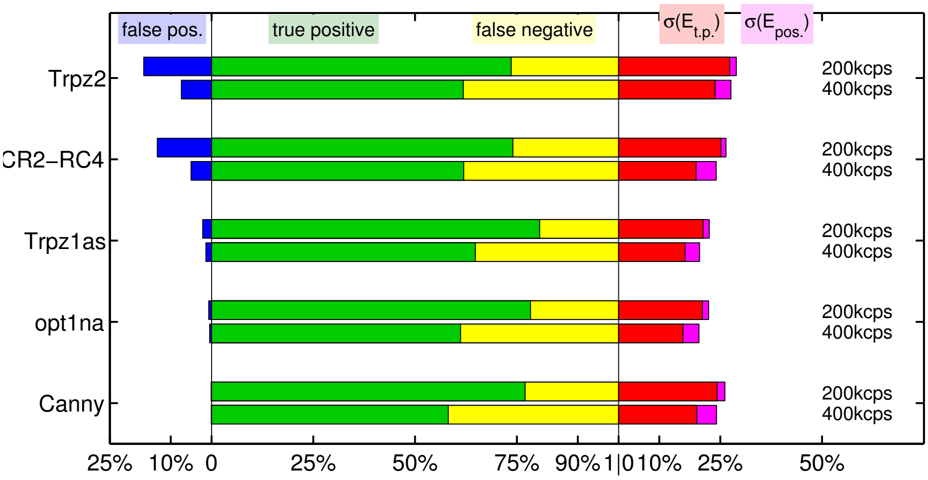

Figure 3.14: Comparison of figures of merit as in Fig. 3.13 for 5 algorithms with intermediate count rate performance for the same modeled signal as in Fig. 3.13.

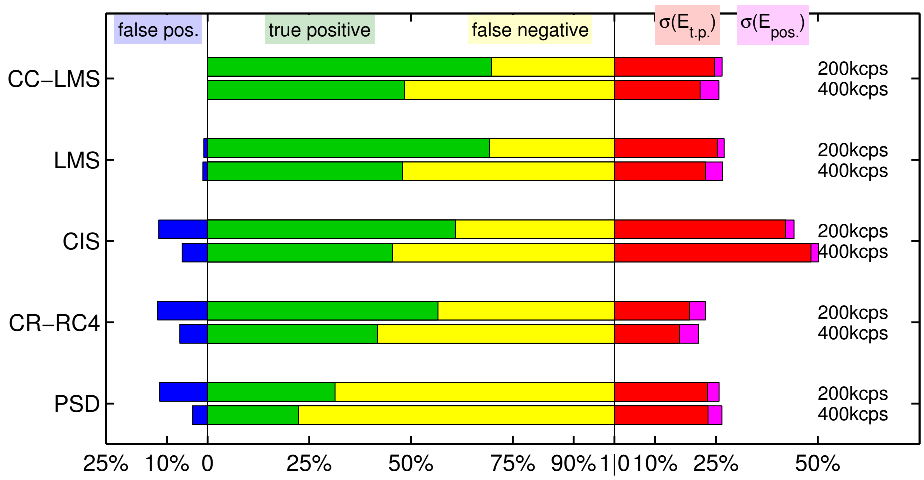

Figure 3.15: Comparison of figures of merit as in Fig. 3.13 for 5 algorithms with relatively poor count rate performance for the same modeled signal as in Fig. 3.13.

Very restrictive algorithms aiming to recognize the whole pulse shape, represented here by the PSD, are very limited in the count rate and stay far below the ideal 500 kcps limit. The other investigated algorithms can be classified into three distinct groups; within each group a change of simulation parameters may still yield a reordering.
In the lowest group we find the simple CIS algorithm and the analog methods using only one differentiator. The LMS and CC-LMS show similar performance and are therefore assigned to this group as well, although they approach the second group for lower count rates.
The main, middle group contains mainly FIR filters including the trapezoidal and the Canny algorithms as well as the optimum filter 1 (opt1na). The best performance in this group is achieved by double differentiation IIR and FIR filters coming close to the idealized 1 Mcps case.
The top performance with respect to true positive detection rate is obtained with the other optimum filters 2, 3 and 4, and by delay line algorithms. All of these approach the performance of the idealized 2 Mcps detection.

False detection Although the true positive detection or throughput at high count rates is an important parameter, the classification made in the previous section is certainly not a general one. One parameter demonstrating this is the percentage of false positive detection, plotted in Figs. 3.13–3.15.
In the top group (Fig. 3.13) it can be clearly seen that the delay line algorithms, especially the double one, are unusable in the present parameter range since the noise leads to an unacceptable fraction of false positive detection.
Within a selection of the middle group with good throughput (Fig. 3.14), the FIR filter algorithms based on one differentiation suffer from practically no false positive detection while those using a second differentiator (Trpz2 and $(CR)^2(RC)^4$) do have a finite false positive fraction, albeit still arguably fairly low.

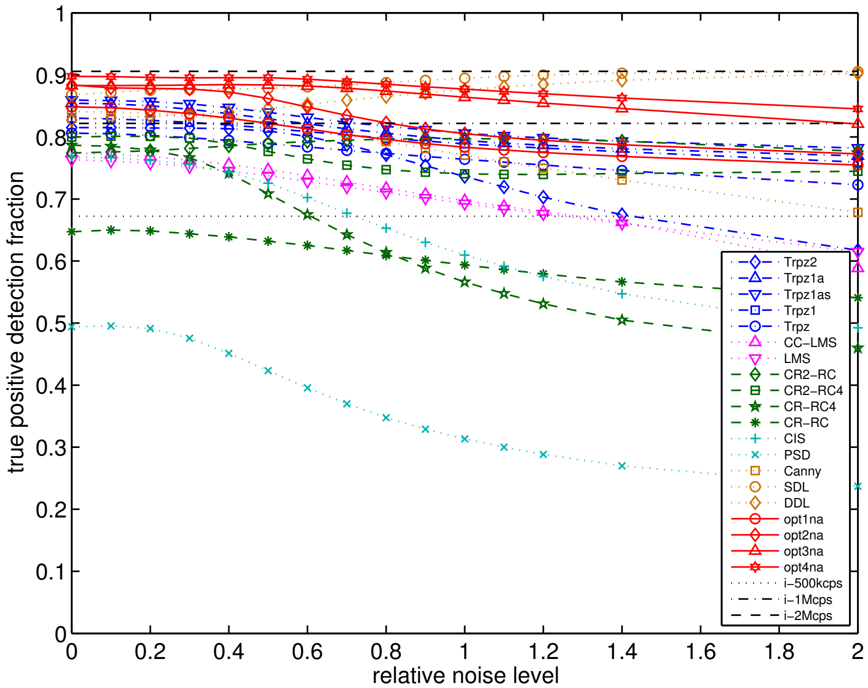

Figure 3.16: True positive detection vs relative noise level (w.r.t. the noise used in Fig. 3.12) for all analyzed algorithms incl. 3 idealized reference ones for 20 keV photons.

For the algorithms in the bottom throughput rung (Fig. 3.15), there is a very similar subdivision. Here, the CC-LMS and LMS algorithms select the pulses quite restrictively and are therefore very resistant to false positive detection. In the case of the CIS and PSD algorithms, a significant false detection level is observed, attributable to the limited noise filtering.

Noise sensitivity The comparisons of the algorithms in the count rate scan, especially the false detection analysis, lead one to expect significant differences in the algorithms' noise sensitivity. This is now studied, again around the HXRS operational point defined in section 3.3.4, by varying the noise level from 0 to 200 % at a fixed simulated count rate of 200 kcps. This noise level scan is equivalent to a photon energy scan since both result in scans of the signal-to-noise ratio.

True positive detection The resulting true positive detection fraction is shown in Fig. 3.16. Substituting the experimentally measured noise by white Gaussian noise with $\sigma = 5\,\mathrm{keV}$ yields essentially the same result, shown in Fig. 3.17.
One of the main observations is that at a low noise level the classification into 3 groups breaks down. All investigated algorithms except $(CR)(RC)$ and PSD detect about $75 - 90\,\%$ of the simulated pulses if the noise stays below $40\,\%$ of the reference level. However, as the noise rises above $50\,\%$ of the reference level, the optimum and single Trpz FIR filters, as well as the $(CR)^2(RC)^n$ analog methods are hardly affected while the other methods are quite significantly degraded, es-

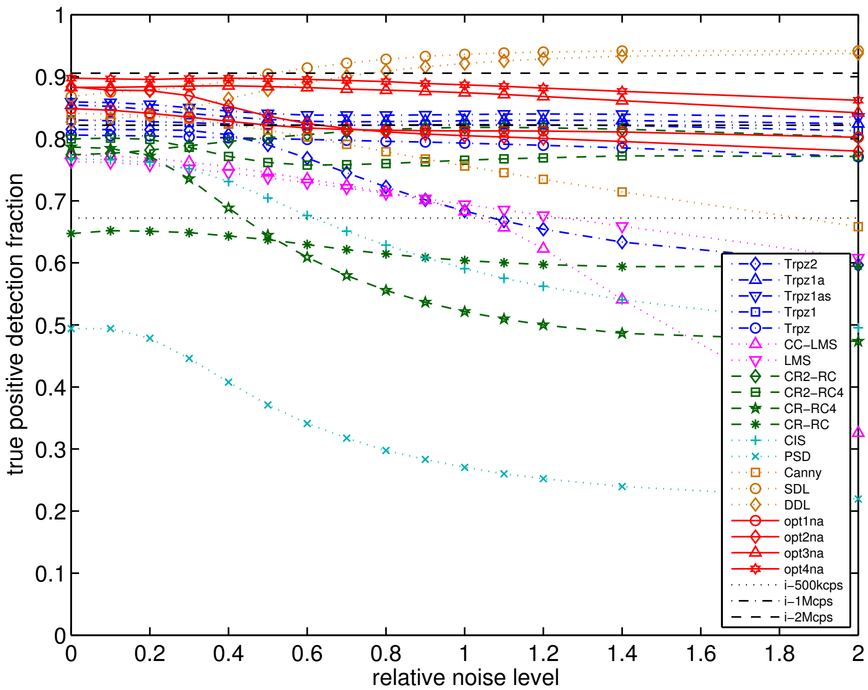

Figure 3.17: True positive detection vs relative noise level (w.r.t. pure white Gaussian noise; $\sigma = 1\,\mathrm{keV}$ at the pre-amplifier stage and 5 keV after the amplifier stage) for all analyzed algorithms incl. 3 idealized reference ones for 20 keV photons.

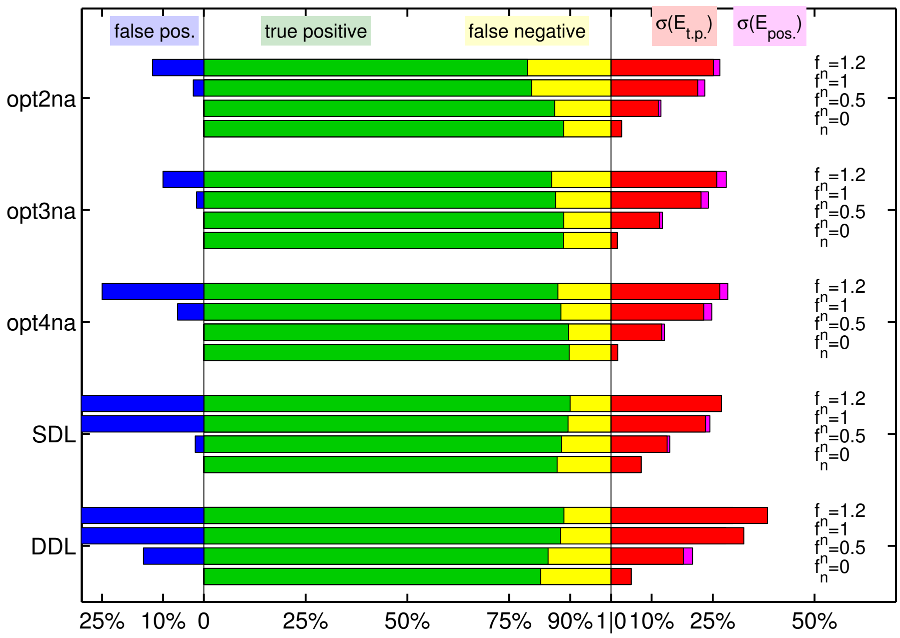

Figure 3.18: Comparison of figures of merit as in Fig. 3.13 for the 5 algorithms achieving the best count rate performance for 20 keV photons at 200 kcps for several relative noise levels $f_{\mathrm{n}} \in \{0, 0.5, 1, 1.2\}$ (selected from Fig. 3.16).

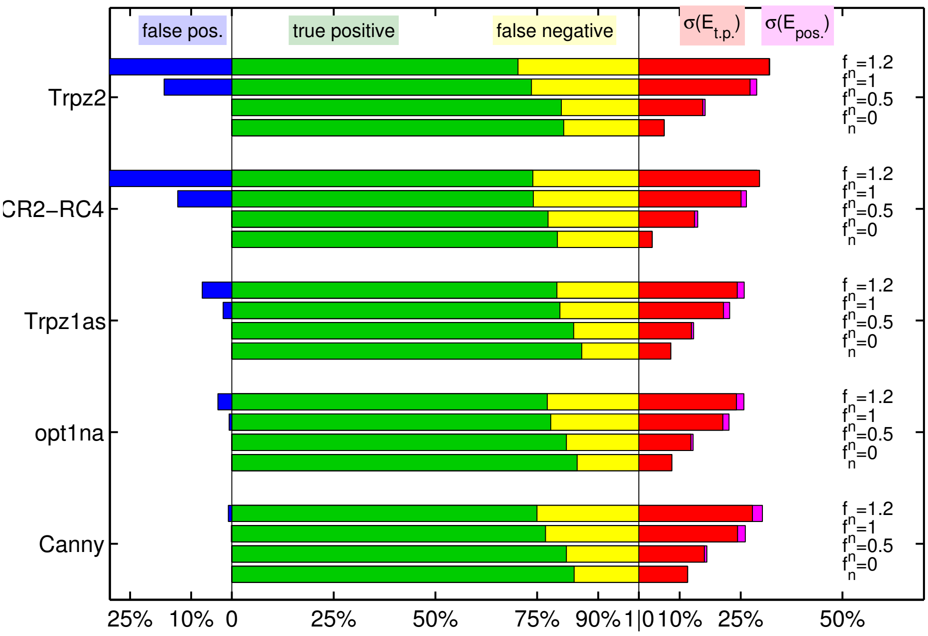

Figure 3.19: Comparison of figures of merit as in Fig. 3.18 for 5 algorithms with intermediate count rate performance for the same modeled signal as in Fig. 3.18.

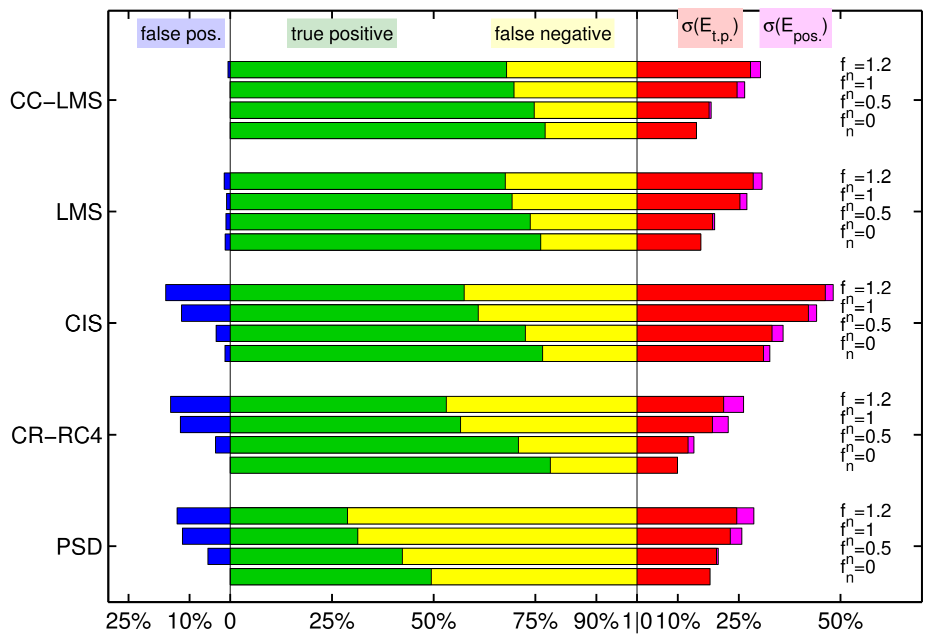

Figure 3.20: Comparison of figures of merit as in Fig. 3.18 for 5 algorithms with relatively poor count rate performance for the same modeled signal as in Fig. 3.18.

pecially the $(CR)(RC)^4$ and CIS methods. The delay-line algorithms represent a special case: their performance appears, paradoxically, to increase with noise, but this is an artifact as discussed in the following.

False positive detection The increase in the true positive detection performance of the delay line algorithms with increasing noise can be understood by looking at the false detection rate, shown among the other figures of merit in Fig. 3.18. It is evident that the very limited noise rejection of the delay line algorithms leads to an extremely high false positive detection rate at a significant noise level, reaching in fact over 300 % for the DDL (well beyond the range accommodated by Fig. 3.18). This results in spurious false positive detections that coincide but are uncorrelated with real pulses, leading them to be wrongly classified as true positive. As a consequence, the use of delay lines should be avoided if there is significant noise in the signal.
Again, the main algorithms of each group are shown in figures 3.18–3.20, for four different relative noise levels. The algorithms with strongly noise-degraded true positive detection rate (PSD, $(CR)^m(RC)^4$, CIS, Trpz2) also show the highest noise sensitivity regarding false positive detection. Hence, their usage should be limited to low noise applications too. In contrast to that, the false positive detection rate of the optimum and single Trpz FIR filters is also barely affected by the increasing noise level. Only the opt4na filter, which is most optimized for fast response, should be used with some caution at significantly higher noise levels.

Energy accuracy

Regarding the energy accuracy the most salient observation is that all algorithms exhibit a significant energy deviation of at least 15 % at the HXRS operational point. This is, however, reasonable under the demanding conditions of high count rates and pulse heights in the range of the noise level. Figures 3.13–3.15 indicate that most algorithms lie near the high energy accuracy limit achieved by several FIR and the $(CR)(RC)^4$ IIR filters. Only the CIS and the DDL algorithms are highly disturbed due to their poor noise filtering.
As for the previously discussed figures of merit, the energy accuracy is also affected by a changing signal-to-noise ratio. As can be seen in figures 3.18–3.20, the energy deviation, as expected, increases with the noise level. Interestingly, however, several algorithms exhibit a significant energy deviation even when the noise level is equal to zero. This effect is generally stronger for algorithms with low count rate performance. Those suffer mainly from poor pulse separation which causes consecutive pulses to influence both the pulse detection and the pulse height analysis of each other.

Experimental validation

The simulation-based benchmarking was validated using an experimentally measured signal from the HXRS diagnostic (TCV discharge 45252, time trace part shown in Fig. 3.11). Around the HXRS operational point (100 – 400 kcps) the positive detection rate was compared to a reference method ('opt4na'). As can be

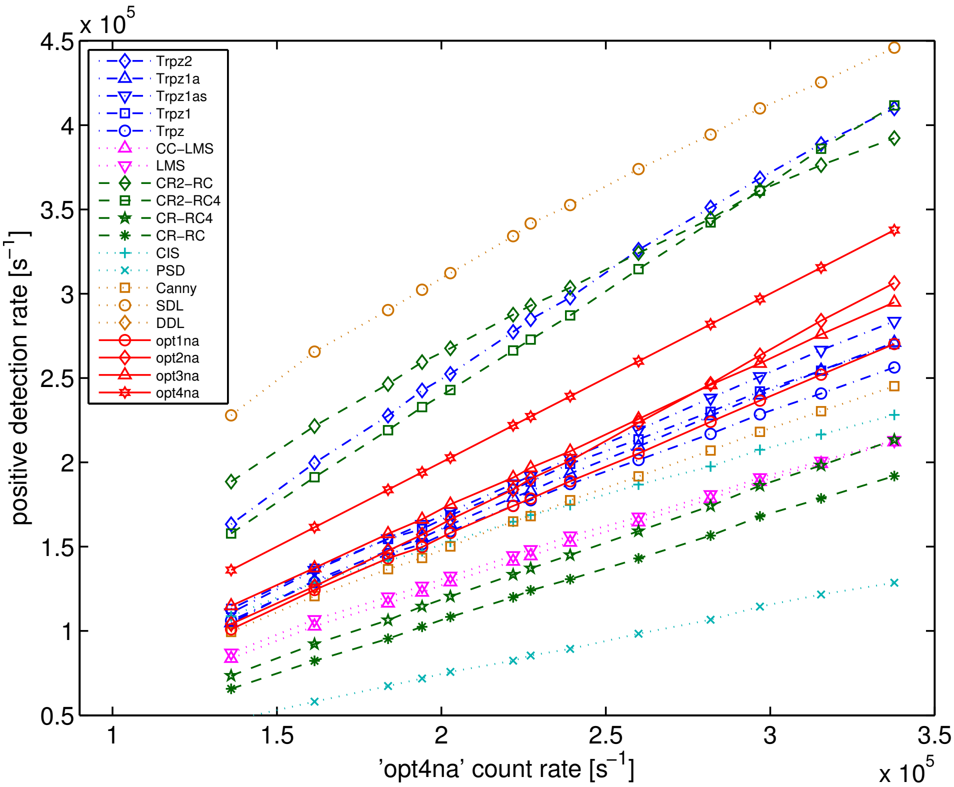

Figure 3.21: Experimental positive detection vs the 'opt4na' count rate for all analyzed algorithms and a threshold of 13 keV for the signal of HXRS chord 9, TCV discharge 45252, $t = [0.4, 1.7]$ s, 13 time bins of 100 ms each. Except for CIS and PSD, dynamic threshold detection was used. The DDL trace lies outside the range of the plot due to very high false positive detection.

seen in Fig. 3.21, the result of the simulation is essentially reproduced. Only the double differentiating methods (Trpz2, $(CR)^2(RC)^n$) and the delay line methods report a significantly higher count rate. This is mainly due to an increased false positive detection.

Computation / Real-time applicability

The computational effort required by most of the algorithms discussed here is quite limited. To give a quantitative measure we list the central processing unit (CPU) time required by our implementation on a single core of a present x86-64 CPU (Intel Core i7-2760QM) for 2 s acquired or simulated signal at 12 M$^{samples}/_{s}$: the signal treatment using digital FIR or digitally emulated analog filters takes about 1 s, only the cross-correlation and digital band-pass filters require significantly higher computational effort (about one order of magnitude). The threshold or rise threshold detection takes about 1.5 s while the use of a dynamic threshold or multiple condition detection increases the computational time as well. The level or rise evaluation analysis is negligible (about 10 ms). Algorithms with significantly increased computational effort (about one order of magnitude) are therefore the CC-LMS, CIS and PSD algorithm. The post-processing to obtain a histogram in time and energy bins takes about 2 s at high count rates and is significantly lower at low count rates. The real-time applicability is already proven for digitally implemented $(CR)^m(RC)^n$ filters in [145] and digital FIR filters in [146], at sampling rates well beyond that of the HXRS. It is planned to implement real-time pulse processing for the HXRS system too, using the FPGAs on the digitizer cards (D-tAcq ACQ216CPCI).

3.3.5 Conclusions

A complete set of digital pulse processing methods was individually described, jointly implemented and compared within a general benchmarking framework. This ensures the general applicability of the presented results for any kind of digital pulse processing application, far beyond the scope of the specific measuring apparatus to which these results were first applied [62]. Although the focus was initially placed on high count rates and significant noise levels, the extension of the analysis to both low count rates and noise levels was straightforward and seamlessly integrated.

The main message is that the implementational and computational effort of essentially all the methods presented is comparable while the results differ significantly. Therefore the importance of making the right choice of pulse processing method should not be underestimated.

The best overall performance was obtained by optimum FIR filters that were also superior on each of the individual benchmarking figures of merit. Therefore these filters are clearly the top choice. FIR filters constructed on the basis of trapezoidal filters, along with the analog $(CR)^2(RC)^n$ method, lie only slightly behind. Since the filters of the Trpz family are among the easiest to implement, they can also be a reasonable solution if one wants to avoid the optimization process. The $(CR)^2(RC)^n$ is consequently the best-performing method that can be easily implemented as an analog system [76].

The use of delay lines should only be considered for virtually noiseless systems. Other algorithms studied, such as the $(CR)(RC)^n$, CC-LMS, LMS, PSD and CIS methods, are not recommended, especially not in high count rate applications.
Consequently, the opt4na method with dynamic threshold detection (opt4naS) is used as the standard pulse processing method of the HXRS diagnostic for all experimental data analysis in this thesis.

Chapter 4

Fokker-Planck modeling

A concise overview of Fokker-Planck modeling using LUKE and CQL3D is presented. It focuses on specific capabilities required for the studies in this thesis and original contributions to the two codes, rather then reproducing all the information that can be found in the user manuals [82, 83].

4.1 CQL3D

4.1.1 Implemented models

Collisions

CQL3D features four supported collision models: 0: fully non-linear coefficients from background Maxwellian and suprathermal e.d.f.; 1: only background; 2: only suprathermal, background ignored; 3: only background to 0th order and fully both contributions to higher order of polynomial Legendre expansion.
The last, “partially-nonlinear” model [160] is the common setting since it avoids thermal runaway but still conserves momentum in electron-electron collisions [83]. It was used for all simulations in the course of this thesis.
In addition to the selection of the collision model, further parameters allow the user to modify individual contributions to the collision operator. This is mainly to analyze how strongly they affect the results; in normal operation the default, physical values are used. One can include/exclude each of the particle species, modify the Coulomb logarithm, impose quasi-neutrality, reduce the magnetic well (trapped-passing boundary) and set the importance of pitch angle scattering (`scatfrac`).

Transport

A radial diffusion and pinch operator simulates energy and particle transport. Radial profiles of the suprathermal electron diffusion coefficient can be specified and are scaled with a global parameter (`difusr`). Further coefficients define the velocity dependence. Several options of pinch velocity can be used to maintain the density profile.

4.1.2 CQL3Dpy interface

To use CQL3D efficiently, the CQL3Dpy Python interface was implemented in the course of the thesis and all simulations were performed using this interface (except for initial tests verifying consistency with previously run simulations). It requires only an XML parameter file as input. From that information it creates the directory and file structure, where it writes derived parameters and the data collected directly from MDS+. The equilibrium and ray tracing are obtained from TORAY, which is executed automatically with the specified settings. Eventually, CQL3D is launched when all input data has been prepared.
The default settings are specified in a default parameter file. To perform parameter scans, "runs" are specified by partial parameter files, where only a few parameters (overriding the default values) are set, e.g. increased transport or reversed B_ϕ. As compared to the standard CQL3D parameter file, which is actually created as input for CQL3D, the new XML parameter files feature links and external parameters. Links are useful if parameters depend on each other, e.g. the time index for which the results are plotted should usually be equal to the number of time steps. External parameters have multiple purposes: they specify parameters for TORAY, the synthetic HXR diagnostic chords, radial transport profiles and many more options. This includes another feature: all profiles and other experimental data (n_e, T_e, χ_e, Z_{eff}, E_ϕ) are filled with values from MDS+.
When calling CQL3Dpy from the command line (`cql3dpy.py`) one has to specify the shot number, time and run. Additionally one can run the simulation not only on the same machine (default option), but the calculation can be transferred to another machine, such as one of the available HPC clusters. Furthermore, there is an additional script (`run_cql3dpy.py`) that allows one to start simulations for a set of discharges, points in time and parameter sets (runs) with a single command. This also includes a simple scheduler adjusting the number of parallel simulations to the available resources. The results are then easily retrieved using supplied shell scripts.

4.2 LUKE

4.2.1 Implemented models

Collisions

LUKE implements the Belaiev-Budker relativistic collision model [161].

Transport

Radial diffusion is also implemented in LUKE. One can choose the standard transport model, where the diffusion coefficient is zero below and constant above a threshold momentum, usually three times the reference velocity (v_{ref}). Additionally, a magnetic turbulence model is available, where the diffusion coefficient depends upon parallel velocity (zero up to a threshold velocity, then increasing linearly with the difference to the threshold velocity in parallel direction). In both cases the goal is mainly to prevent loss of the thermal bulk.

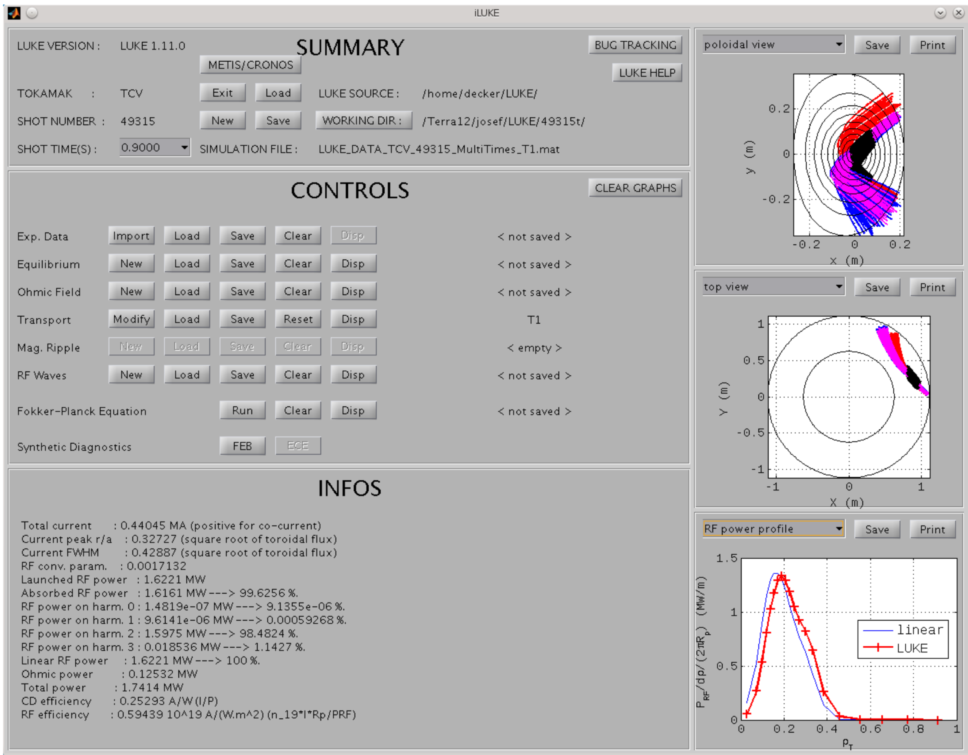

Figure 4.1: The GUI of LUKE, iluke, with the controls on the top left main part, the information and computation launch area on the bottom left and the plotting column on the right. In this screenshot the results of C3PO ray tracing and the comparison of linear and non-linear RF absorption are shown, and information on the LUKE results are displayed.

The radial dependence of the diffusion and pinch operators can be set by two coefficients that define a parabola.

4.2.2 User interfaces

CLI `irunluke`

The traditional command-line interface (CLI) of LUKE, `irunluke`, consists of a data overview and main menu as a starting point to several sub menus or dialogues. From the main menu simulation data can be loaded and saved, and the calculations can be launched locally or sent to remote clusters. In the sub menus and dialogues experimental and external data can be loaded and parameters can be modified. It allows the user to access all main features of LUKE and also offers the possibility to produce high quality result plots.

GUI `iluke`

The GUI `iluke` was recently developed and inherits already practically all features from `irunluke` while it also provides additional capabilities. The interface

to the TCV MDS+ database was greatly improved with the new "MultiTimes" option that allows one to load and simulate several time points of a discharge in parallel. This is currently extended to provide the capability to simulate the e.d.f. time evolution.
The integrated "matRemote" package provides a smooth interface to remote machines like HPC resources, facilitating the handling of large simulations.

4.3 FPCDF

The FPCDF is a set of Python objects and functions to represent, analyze and compare results from the Fokker-Planck codes. It was implemented in the course of this thesis to enable a reasonable comparison of LUKE and CQL3D, whose output formats are completely different and can therefore not be compared directly.
The core of the package is the set of 3D, 2D and 1D function objects whose subtypes are `Edf3D`, `Edf2D` and `Edf1D` representing the e.d.f., and `Rrf3D`, `Rrf2D` and `Rrf1D` representing the RF QL operator. A 3D object can be constructed from either a LUKE or CQL3D output file. Additionally, a numerical representation of a Maxwell-Jüttner distribution can be constructed from given n_e and T_e profiles. From the 3D object, a 2D object in momentum space at a given poloidal position $\left(r,\theta_{\mathrm{pol}}\right)$ can be extracted. Subsequently, the 1D object results from a cut at a given pitch angle (θ).
Each object comes with useful functions. Most importantly, plotting functions create a visual representation and overlaying allows a comparison of different e.d.f.s. The `Edf2D` object also integrates a synthetic HXR diagnostic, computing the emission from its poloidal location in arbitrary directions. Furthermore, rather simple functions, such as the calculation of the density or n_e profile by phase space integration, are provided too.
In addition to the objects there are Python scripts and functions that make use of the objects to create more complicated plots or perform sophisticated data analysis by putting the capabilities of the objects together.

4.3.1 Poloidal angle dependence of e.d.f. and pitch angle

By defining the relative magnetic field (Ψ) as the ratio of the local magnetic field (B) to the minimum magnetic field (B_0) on a flux surface

$$\Psi\left(r,\theta_{\mathrm{pol}}\right)=\frac{B\left(r,\theta_{\mathrm{pol}}\right)}{B_0\left(r\right)}, \tag{4.1}$$

a relation between the local pitch angle (θ) and the pitch angle at minimum magnetic field (θ_0) follows from conservation of energy and magnetic moment:

$$\sin^2\theta=\Psi\sin^2\theta_0. \tag{4.2}$$

Therefore, θ can be expressed by Ψ and θ_0, and vice versa

$$\theta\left(r,\theta_{\mathrm{pol}},\theta_0\right)=\arcsin\sqrt{\Psi\left(r,\theta_{\mathrm{pol}}\right)\sin^2\theta_0}, \tag{4.3}$$

$$\theta_0\left(r,\theta_{\mathrm{pol}},\theta\right)=\arcsin\sqrt{\frac{\sin^2\theta}{\Psi\left(r,\theta_{\mathrm{pol}}\right)}}. \tag{4.4}$$

This yields, according to the approximations in LUKE and CQL3D [82, 83], the local e.d.f. as a function of the e.d.f. at B_0

$$f\left(r,\theta_{\text{pol}},p,\theta\right)=f_0\left(r,p,\theta_0\left(r,\theta_{\text{pol}},\theta\right)\right) \tag{4.5}$$

These expressions are also used in FPCDF to compute the local e.d.f. from the `Edf3D` object, including the local trapped-passing boundary (θ_{tp}).

4.3.2 Additional data analysis functions

Complementary to FPCDF, a set of data analysis and plotting functions was implemented in MATLAB, especially for comparison with experimental data. These functions can easily access the extensive toolbox of MATLAB functions for data analysis that had already been implemented previously.

4.4 Benchmarking

This thesis represents the first extensive benchmarking of the codes CQL3D and LUKE to each other; the experimental results obtained in the following were analyzed in conjunction with both codes, and the individual strengths and deficits of the codes are discussed there.

One of the main observations is that both codes tend to underestimate the photon flux and temperature for TCV discharges that are close to the runaway limit. In such cases, LUKE is usually a bit closer to the experiment than CQL3D.

The CPU time of a standard run is comparable for both codes and is about 1 h on a single node (Intel Xeon 5500/Core i7, 18 GB random-access memory (RAM), fedora 19 64 bit operating system (OS)). While LUKE uses multithreading capabilities of MATLAB and MUMPS, the current CQL3D version is restricted to a single thread. Nevertheless, parallel computation on many nodes or clusters is available for modeling on independent points in time and parameter scans; via the `matRemote` interface of LUKE and the CQL3Dpy interface for CQL3D.

In comparison, CQL3D is slightly more memory-efficient, but for both codes a standard run requires less than 16 GB of RAM (available on all used compute nodes), which may be exceeded by high-resolution computations. Such computations were performed to check if the default resolution is sufficient and did indeed not show any significant deviations. Due to the often narrow spatial deposition profiles and resonance curves in phase space of ECRH/CD, such a verification is very important. In this regard, LUKE features an adaptive radial grid whose resolution is refined at the deposition location calculated by C3PO and kept more coarse where no auxiliary heating is applied. This reduces the computational effort as compared to an equidistant grid with the same accuracy.

The GUI of LUKE provides a very intuitive interaction with the data and parameters and the interactive plots ensure that the user keeps track of their plausibility. The integrated ray-tracing optimizer is very useful for experiment preparation. Additional integrated tools provide many features for shot analysis beyond the scope of the Fokker-Planck (F-P) modeling itself.

In contrast to that, CQL3D is more old-fashioned and does not come with such a nice interface or additional features. However, the newly implemented CQL3Dpy interface enables efficient usage since it only requires small parameter files and the launch command. This “fire-and-forget” therefore facilitates large parameter scans that are lengthy to do with a GUI that requires recurring user interaction for guidance.

Chapter 5

HXR emission asymmetries

5.1 Theoretical background

The angular distribution of the HXR emission from a certain point in the plasma depends only on the e.d.f. in that point, as already mentioned in the introduction (Sec. 1.7.2). The difference introduced by the ion distribution function (i.d.f.) (w.r.t. $T_i = 0$ and neutrality) is usually neglected and Z_{eff} enters only as a scaling factor. Therefore, an anisotropic e.d.f. emits, in general, anisotropic bremsstrahlung, in contrast to a Maxwellian, emitting bremsstrahlung isotropically.
Furthermore, the e.d.f. is not constant on a flux surface: θ (and θ_{tp}) changes due to varying **B**, some electrons are trapped and cannot reach parts of the flux surface on the HFS. For different anisotropic e.d.f.s this effect is also different in general.
These effects lead to asymmetric observations by the HXRS in the toroidal direction (when in horizontal position) and in the poloidal plane. From these asymmetry measurements details on the underlying e.d.f. anisotropy can be inferred in conjunction with theory and simulations.

5.1.1 Relativistic effects

The bremsstrahlung emission of a slow (non-relativistic) electron is close to isotropic; the relative difference between forward and backward emitted energy at 1 keV incident energy is less than 25 % and proportional to the incident momentum in the non-relativistic limit. These values are reduced by far for an e.d.f., except if it is highly anisotropic. Relativity leads to a much more enhanced emission in the forward direction, but this effect is also still quite small for thermal electrons in TCV ($T_e \approx 1$ keV) that emit in the SXR range, where emission anisotropy can be therefore neglected.
For suprathermal electrons the situation is different. Already for incident electron kinetic energies of 12 keV the forward emission is doubled w.r.t. the backward emission over the whole photon energy range (Fig. 5.1). At energies of 100 keV to 1 MeV first the backward and then also the perpendicular emission becomes insignificant as compared to the forward emission (Fig. 5.2). Interestingly, in the case of high energy loss ($p \approx k$) the maximum emission does not lie in the straight forward direction but slightly off it.

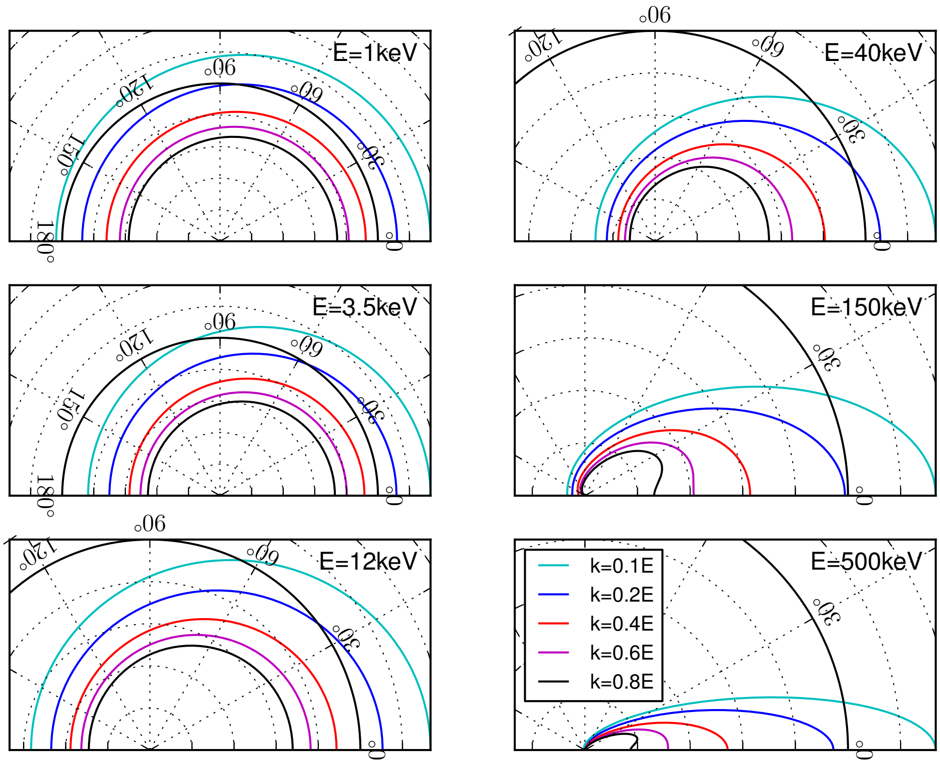

Figure 5.1: Angular dependence of bremsstrahlung emission for electron-nucleus collision given by (B.10). The incident electron kinetic energy (E) varies from 1 to 500 keV from the first to the last plot. Each plot shows the bremsstrahlung energy emitted at fractions of E (0.1, 0.2, 0.4, 0.6, 0.8) for angles θ from 0 to 180 deg. The emitted energy is symmetric w.r.t the axis of electron incidence ($\theta = 0$). Each plot is scaled to the maximum forward emission at 10 % of E (given in Fig. 5.2).

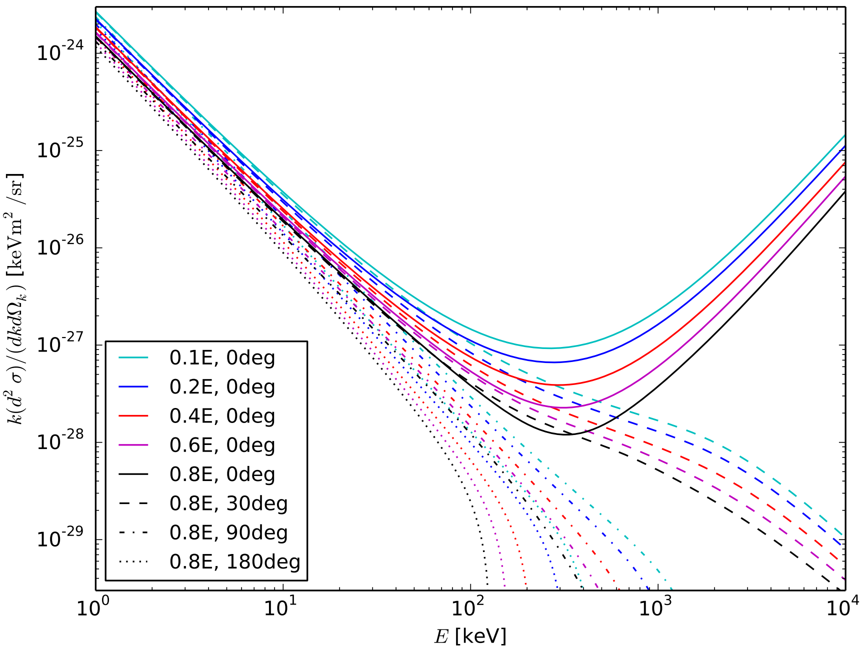

Figure 5.2: Bremsstrahlung emission for electron-nucleus collision given by (B.10) vs incident electron kinetic energy (E). The bremsstrahlung energy emitted at fractions of E (0.1, 0.2, 0.4, 0.6 and 0.8, different colors) in forward, forward cone, perpendicular and backwards direction (0, 30, 90 and 180 deg, different line style).

Generally, the higher the electron energy, the more the bremsstrahlung emission is focused in the forward direction. Therefore, the phase space anisotropy of the highest energy electrons contributes most to the bremsstrahlung emission anisotropy. Hence, asymmetry measurements are most efficient to study the suprathermal (and runaway) tail of the e.d.f..

5.1.2 Trapped and passing electrons

While passing electrons can collide at any position on the field line (flux surface) and therefore emit bremsstrahlung from everywhere, trapped electrons move only in a LFS section of the field line (flux surface) and can only radiate bremsstrahlung from there. Also, $v_\parallel$ of barely trapped and barely passing electrons is much lower on the HFS than on the LFS. This increases the probability of collisions on the HFS as compared to the LFS, due to the longer time these electrons spend on the HFS.

Hence, anisotropies in the e.d.f., especially in the region of trapped and barely passing electrons, also have an effect on the localization of the bremsstrahlung sources, that is (i.e.) the emission patterns depend on the location on the flux surface (along the field line).

The measurement of such asymmetries therefore provides information on the e.d.f. especially in the trapped region and around the trapped-passing boundary.

5.2 Toroidal emission asymmetry

For HXR emission in the forward and backward toroidal direction the relativistic effects play the main role, whereas the asymmetry of emission from suprathermal electrons in the trapped region can be neglected. For plasmas with ECRH only ($n_\parallel = 0$) the anisotropy in the e.d.f. is only created by the inductive field and expected to be small. With increasing $n_\parallel$, driving current in the I_p direction (co-ECCD), the number and energy of suprathermal electrons in the CD direction increase, and therefore also the HXR emission and photon temperature (T_γ) in the forward cone. In the case of counter-current ECCD (cnt-ECCD), the interplay of toroidal electric field (E_ϕ) and EC-driven acceleration becomes important; depending on the specific parameters one can expect either higher emission in the forward or backward direction.

5.2.1 Experimental setup

The HXR emission measurement along LoS in both toroidal directions, grazing flux surfaces at different radial locations (Fig. 5.3) is especially sensitive to the forward-backward asymmetry of the e.d.f. in the phase space $v_\parallel$ direction. These outer 5 chords each in the co- and counter-I_p directions provide also some space resolution. The inner 14 chords, whose view is limited by the inner wall, are already more sensitive to asymmetries in the regions with significant $v_\perp$.

Two main sets of experiments were carried out with this measurement setup. In the first set, ECCD at the maximal available X2 power was deposited with a broad deposition profile in the plasma center to achieve high phase space asymmetry

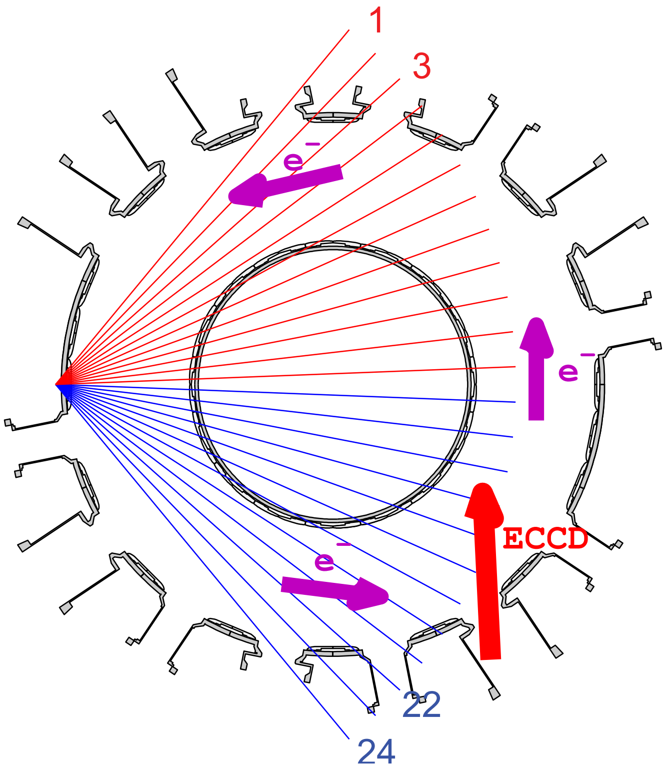

Figure 5.3: Toroidal HXR emission asymmetry measurement scheme: top view of TCV with the chords of HXRS camera 5 in horizontal position.

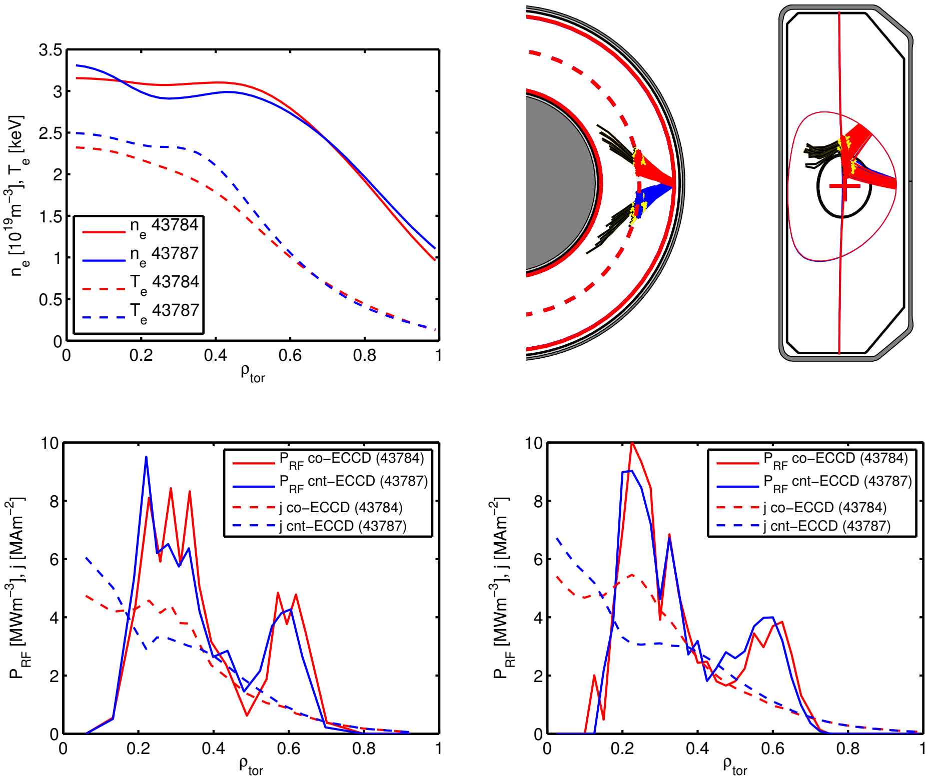

Figure 5.4: X2 power deposition in TCV discharges 43784 (co-ECCD, red) and 43787 (cnt-ECCD, blue). Top left: radial plasma profiles; top right: ray tracing: top view and poloidal cross section, the absorption location is indicated in yellow; bottom: radial ECRH power deposition and current profiles from LUKE (left) and CQL3D (right) based on the measured E_{ϕ}.

with little spatial dependence. This was performed both with co- and cnt-ECCD at the same I_p value in separate discharges. Secondly, a scan of $n_{\|}$ was realized by sweeping the ECCD toroidal injection angle (of a single equatorial launcher) within a discharge.

5.2.2 Co- and cnt-ECCD comparison

This set of experiments has the same main plasma parameters (shape, B_{ϕ}, I_p, n_e) which will be referred to as scenario T in the following. The radial profiles of the two discharges for co- and cnt-ECCD are also well matched (Fig. 5.4). The RF deposition profile is essentially the same, except for inverted toroidal injection angle (and consequently $n_{\|}$) resulting in a correspondingly different current profile. These latter profiles are computed by LUKE and CQL3D, whose results correspond well to each other. V_{loop} is controlled such that I_p is the same in both discharges.

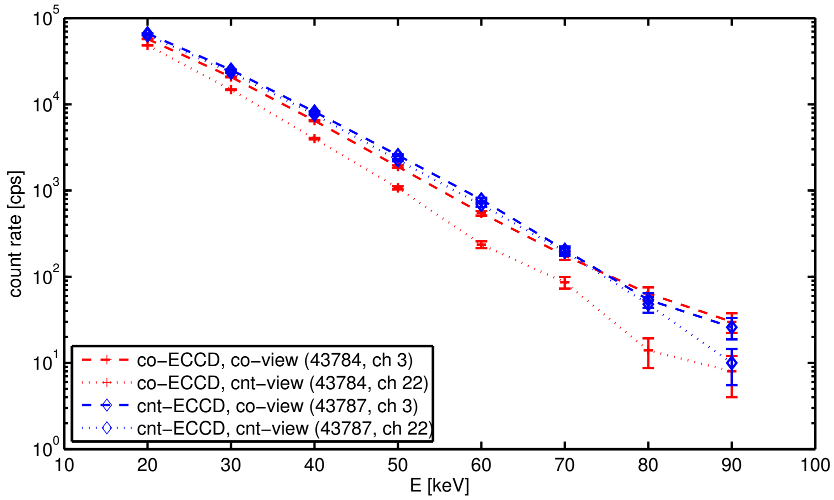

Figure 5.5: Experimental measurement of the co- and cnt-ECCD HXR emission asymmetry in TCV: comparison of the symmetrically viewing HXRS chords 3 (co-I_p, dashed) and 22 (cnt-I_p, dotted) in TCV discharges 43784 (co-current ECCD, red +) and 43787 (counter-current ECCD, blue $\diamond$).

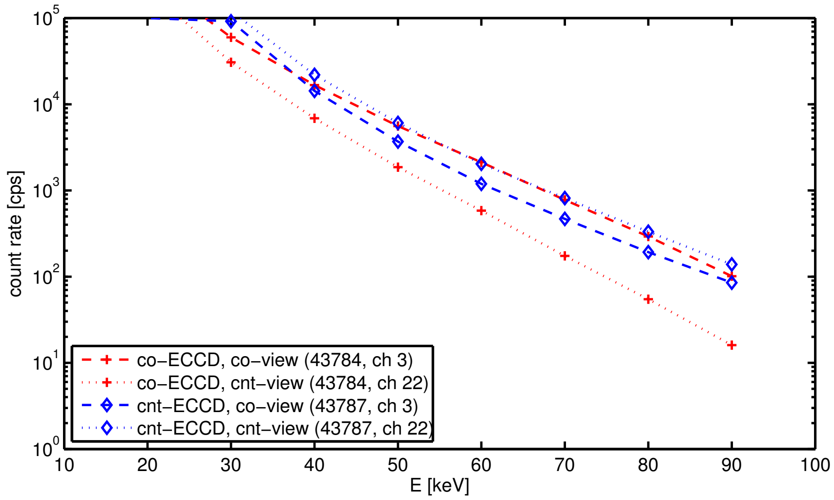

Figure 5.6: LUKE R5X2 simulation of the co- and cnt-ECCD HXR emission asymmetry in TCV: comparison of the symmetrically viewing HXRS chords 3 (co-I_p, dashed) and 22 (cnt-I_p, dotted) in TCV discharges 43784 (co-current ECCD, red +) and 43787 (counter-current ECCD, blue $\diamond$). In 43784, E_ϕ is lowered to 50% to account for anomalous effects.

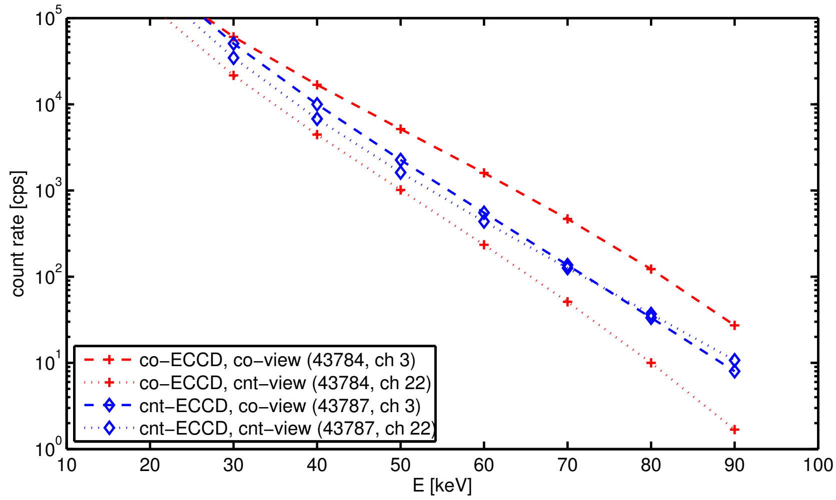

Figure 5.7: CQL3D simulation of the co- and cnt-ECCD HXR emission asymmetry in TCV: comparison of the symmetrically viewing HXRS chords 3 (co-I_p, dashed) and 22 (cnt-I_p, dotted) in TCV discharges 43784 (co-current ECCD, red +) and 43787 (counter-current ECCD, blue $\Diamond$). In 43787, E_ϕ is increased to 220% to account for anomalous effects.

Experimental result

The experimental result in the co-current ECCD (co-ECCD) case is, as expected, a clearly visible asymmetry, most obviously discerned as a difference between the co-viewing chord 3 and cnt-viewing chord 22 (Fig. 5.5). By contrast, no such toroidal HXR emission asymmetry is observed in the cnt-ECCD case (same figure). The latter result was wholly unexpected. As discussed below, however, modeling offered a clear explanation for this effect. Indeed, it depends on the interplay between the electron acceleration by the RF wave, which enhances the suprathermal tail in the co-current direction, and E_ϕ, which pushes the whole electron distribution function, and especially the faster electrons with lower electron collision frequency (ν_e), in the counter current direction (by virtue of their negative charge). Consequently, wither a reduced or an inverted toroidal asymmetry is in principle possible in the cnt-ECCD case, and it is very likely that the cancellation of the two effects is due to the specific plasma parameters but cannot be expected in general.

Comparison to modeling

Since theory can only give a qualitative estimation of the HXR emission asymmetry, modeling is required for quantitative comparison of the experiment to theoretical predictions. The LUKE and CQL3D codes were both run for the plasma parameters in the flat-top of the experimental discharges. While the computed RF absorption and CD profiles are essentially equal, there are some differences in the e.d.f. that result in somewhat different HXR emission predictions.

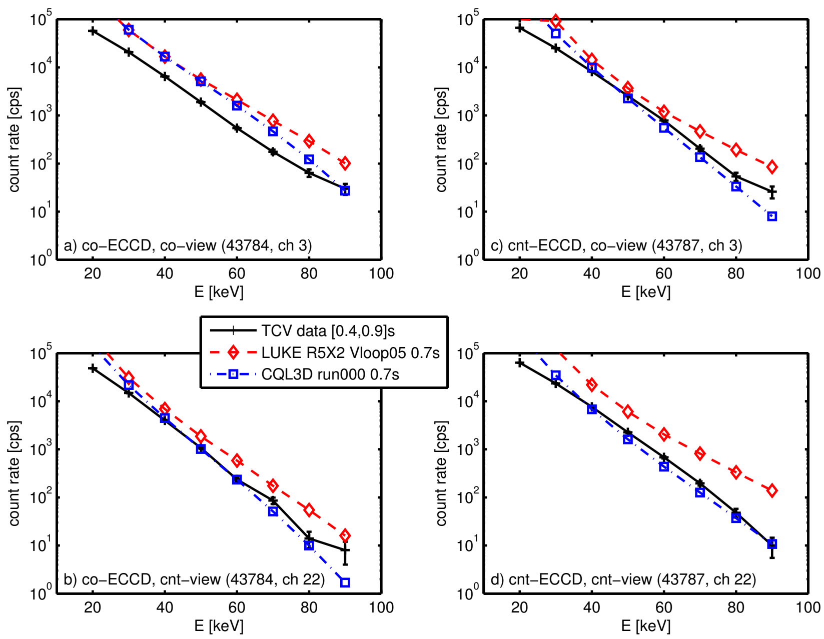

Figure 5.8: Comparison of the co- and cnt-ECCD HXR emission asymmetry results (Figs. 5.5–5.7) from experimental measurements in TCV (black line, +) to simulations using LUKE R5X2 (red dashed, ◊) and CQL3D (blue dashed-dotted, □): a) 43784 chord 3 (co-ECCD, co-I_p-view), b) 43784 chord 22 (co-ECCD, cnt-I_p-view), c) 43787 chord 3 (cnt-ECCD, co-I_p-view), d) 43787 chord 22 (cnt-ECCD, cnt-I_p-view). E_ϕ adjustments as in Figs. 5.6–5.7.

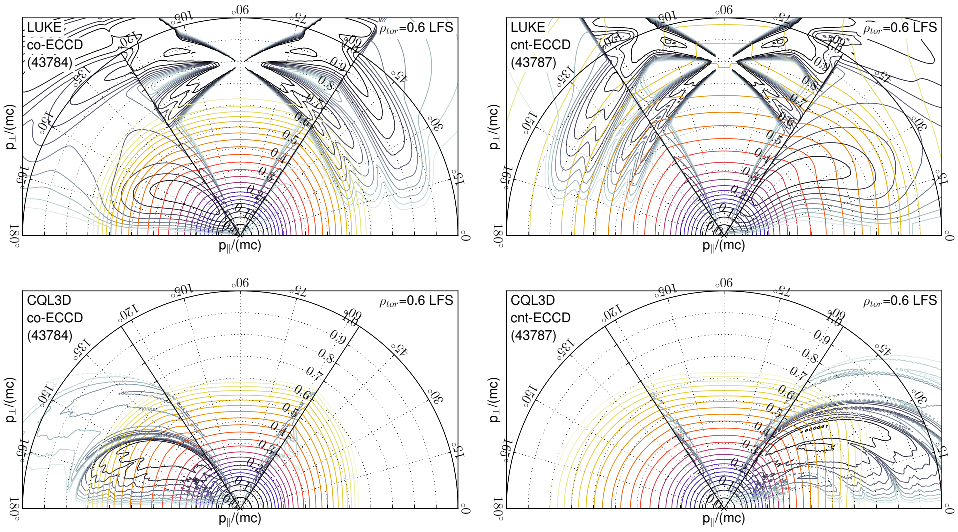

Figure 5.9: Modeled e.d.f. (color) and RF resonance (gray) in phase space at outer absorption peak ($\rho_{\text{tor}} = 0.6$) for TCV discharges 43784 (co-ECCD, left) and 43787 (cnt-ECCD, right) from LUKE (top) and CQL3D (bottom). E_ϕ adjustments as in Figs. 5.6–5.7.

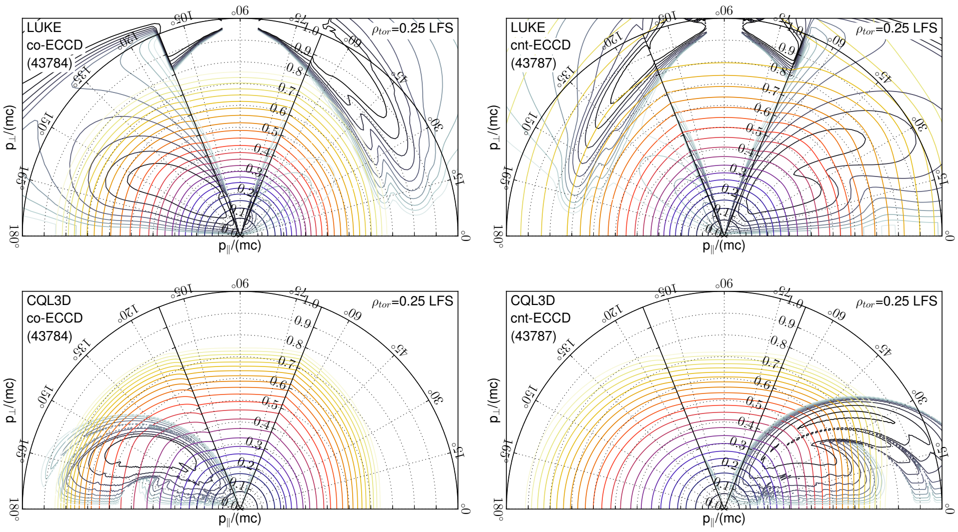

Figure 5.10: Modeled e.d.f. (color) and RF resonance (gray) in phase space at core absorption peak ($\rho_{\text{tor}} = 0.25$) for TCV discharges 43784 (co-ECCD, left) and 43787 (cnt-ECCD, right) from LUKE (top) and CQL3D (bottom). E_ϕ adjustments as in Figs. 5.6–5.7.

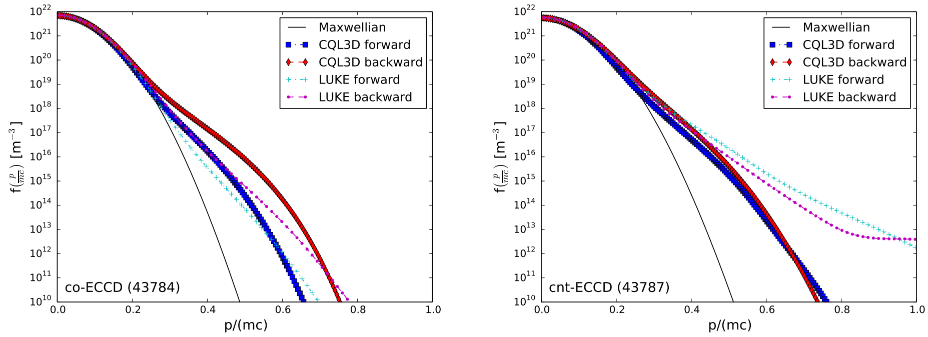

Figure 5.11: LUKE and CQL3D e.d.f.s at core absorption peak ($\rho_{\rm tor}$ = 0.25) in the forward and backward (w.r.t. I_p) direction for TCV discharges 43784 (co-ECCD, left) and 43787 (cnt-ECCD, right). E_ϕ adjustments as in Figs. 5.6–5.7.

LUKE LUKE predicts generally a slightly overly energetic suprathermal tail, resulting in a reduced slope of the spectrum for high photon energies, i.e. increased photon temperature (Fig. 5.6). In the co-ECCD discharge the electron acceleration is significantly overestimated. It turns out that a reduction of $V_{\rm loop}$ to 50 % of the experimentally measured value lowers the contribution of E_ϕ, such that LUKE recovers the experimental HXR measurements (Fig. 5.8a+b). The modification of the electric field acceleration accounts for uncertainties of parameters determining E_D, including unmeasured local dependencies and abnormalities.
In the cnt-ECCD case, LUKE does not require such adjustments of E_ϕ, the simulation with a standard $\chi_{se} = 0.2\,{\rm m}^2{\rm s}^{-1}$ reproduces the experiment reasonably well (Fig. 5.8c+d).

CQL3D The CQL3D code estimates the photon temperature better, but here too a high sensitivity on E_ϕ is observed. While, in contrast to LUKE, the co-ECCD case is well matched quantitatively, the cnt-ECCD case shows inverted HXR asymmetry, i.e. only a negligible contribution of the induction on the suprathermal population. To recover the experimental observation of cancellation (Figs. 5.7, 5.8c+d), the experimental value of $V_{\rm loop}$ has to be multiplied by a factor of 2.2, as discussed more in detail in the next section.

Modeled e.d.f.s The e.d.f.s at the secondary and central RF absorption peaks are shown in Figs. 5.9 and 5.10, respectively. The resonance curves are in general the same, except for the X3 included by LUKE that is not significantly absorbed. However, some differences can still be perceived, such as the fact, that the resonance is narrower for CQL3D.
To investigate the smaller differences in the modeled e.d.f.s quantitatively, the forward and backward cut are displayed in Fig. 5.11. For the co-ECCD case, where CQL3D reproduces the experiment well, the forward-backward asymmetry gets significant at $p/mc \gtrsim 0.3$. In LUKE, the e.d.f. follows essentially a straight line from there towards higher momentum. With unmodified E_ϕ the opening angle (between forward and backward cut) is comparable to that in CQL3D, resulting in

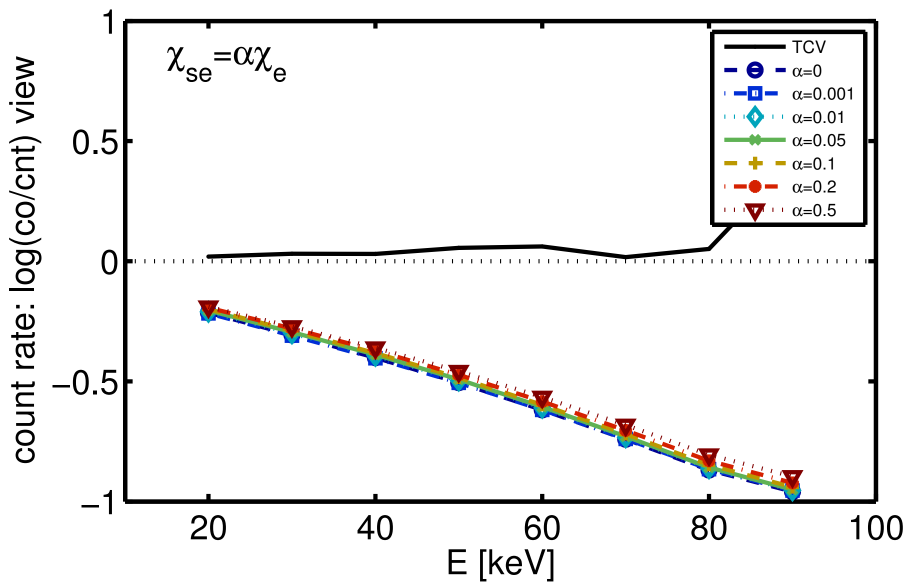

Figure 5.12: Difference in the logarithmic HXR emission spectra along co- and cnt-view chords in 43787 (cnt-ECCD) for various values of χ_{se} in colors compared to the experimental measurement in black.

a high number of relativistic electrons, that are not observed in the experiment. While the modification of E_ϕ accounts for that correctly in the relativistic region, it influences, of course, the whole e.d.f., resulting inter alia in an underestimated ohmic current.

In the cnt-ECCD case, where LUKE reproduces the experiment without adjustments, the e.d.f. is essentially symmetric in the $v_\parallel$ direction. In CQL3D, the E_ϕ modification again reproduces the correct behavior in the high energy range, where the ratio to E_D is important. In the low energy range, however, the E_ϕ change yields unwanted perturbations too, such as a significantly overestimated I_p.

5.2.3 Suprathermal electron transport and electric field

One of the main results of the comparison of toroidal HXR emission to modeling (Sec. 5.2.2) is its dependence on suprathermal electron transport and electric field, to be discussed more in detail here.

Suprathermal electron diffusion

Since anomalous suprathermal electron transport is regularly observed in TCV ([3], Sec. 6.1), the first attempt to reproduce the experimental observations was a scan of χ_{se}. Unexpectedly, however, a variation of χ_{se} does not affect at all the difference in HXR emission spectrum between co- and counter-current views (Fig. 5.12). An increased diffusion coefficient only scales the modeled HXR spectra down, while their slope remains constant. The explanation for this insensitiv-

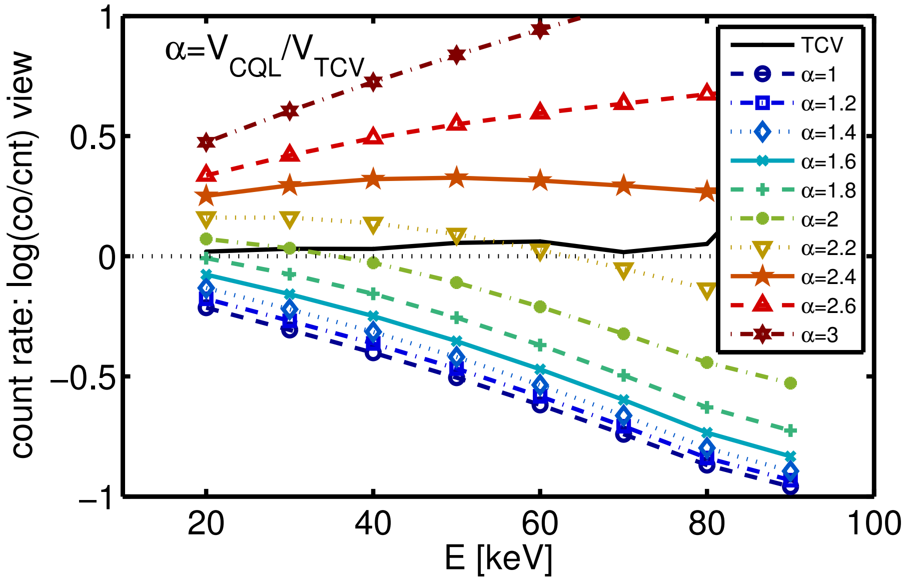

Figure 5.13: Difference in the logarithmic HXR emission spectra along co- and cnt-view chords in 43787 (cnt-ECCD) for various values of V_{loop} in colors compared to the experimental measurement in black.

ity is apparently that the diffusion reduces the concurrent effects of ECCD and acceleration in the static electric field by the same amount.

Electric field

As already discussed above, the experimental observations can be recovered, at least in the suprathermal / HXR range, by changing the electric field while leaving the transport coefficients constant. By performing a scan of V_{loop} ($\propto E_\phi$), CQL3D is able to produce all cases of asymmetry in the cnt-ECCD case. For low V_{loop}, the fast electrons move mainly in the direction dictated by ECCD, resulting in higher cnt-view HXR emission, which decreases with increasing V_{loop}, being equal to the co-view emission at around $V_{\text{loop,CQL3D}} = 2.2\,V_{\text{loop,TCV}}$, before the latter dominates (Fig. 5.13). At sufficiently high E_ϕ a significant fraction of the fast electrons are accelerated to runaway energies.

5.2.4 Scan of $n_\parallel$

To investigate the influence of $n_\parallel$ on the e.d.f., the toroidal injection angle (ψ) was varied in a set of TCV discharges. The equatorial launchers in horizontal position can perform such a scan within a single discharge, where the lower limit is defined by the launcher design (8 deg) and the upper limit is approached due to greatly reduced absorption at $\gtrsim 30$ deg when the resonance in the plasma is no longer reached. For window protection reasons, one launcher was used for co-ECCD and the other one for cnt-ECCD.

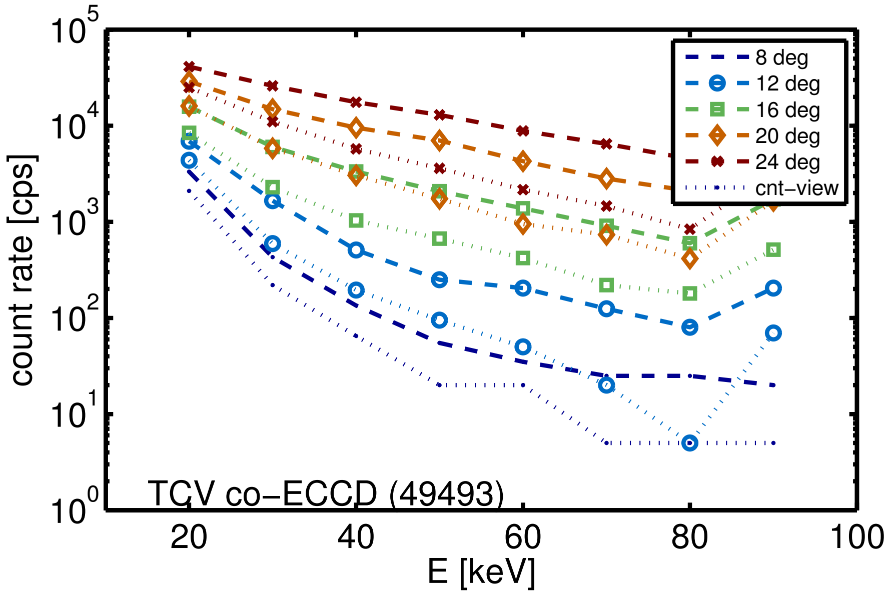

Figure 5.14: Experimental measurement of the HXR emission asymmetry in TCV for varying co-ECCD injection angle ($n_\parallel$): comparison of the symmetrically viewing HXRS chords 3 (co-I_p, dashed) and 22 (cnt-I_p, dotted) in TCV discharge 49493.

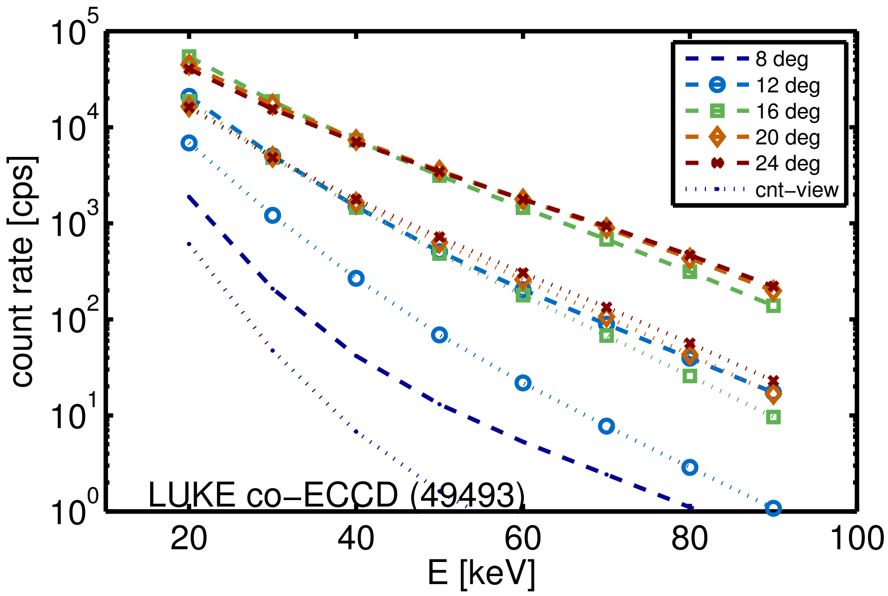

Figure 5.15: LUKE R5X2 simulation of the HXR emission asymmetry in TCV for varying co-ECCD injection angle ($n_\parallel$): comparison of the symmetrically viewing HXRS chords 3 (co-I_p, dashed) and 22 (cnt-I_p, dotted) in TCV discharge 49493.

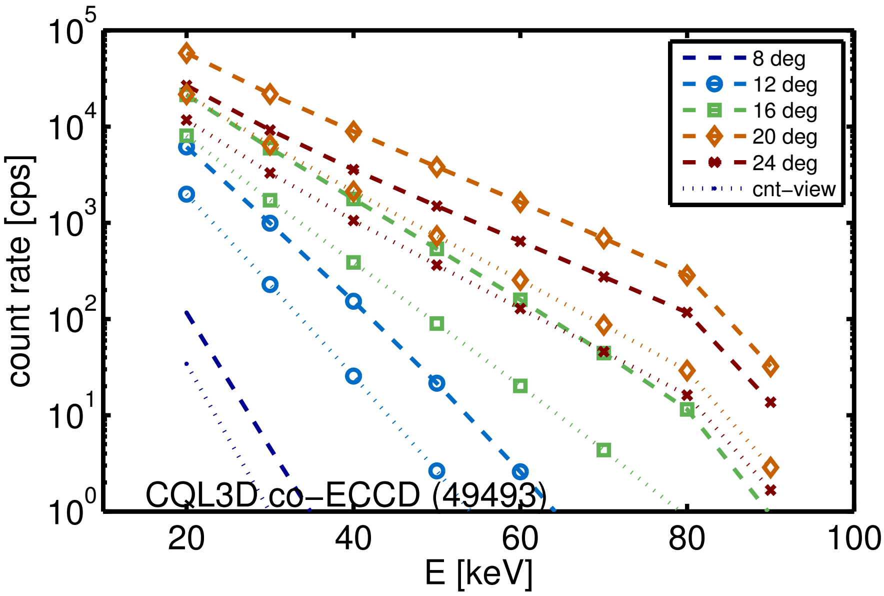

Figure 5.16: CQL3D simulation of the HXR emission asymmetry in TCV for varying co-ECCD injection angle ($n_\parallel$): comparison of the symmetrically viewing HXRS chords 3 (co-I_p, dashed) and 22 (cnt-I_p, dotted) in TCV discharge 49493.

Co-ECCD injection angle steps

In the elliptic TCV plasma 49493 (scenario P), the angle was kept constant for 0.2 s at each of 5 different values (in the co-ECCD direction) and moved from one position to the next in about 0.15 s. Throughout the scan of $\psi \in \{8, 12, 16, 20, 24\}$ deg, the HXR emission increases, and it increases more rapidly at higher energies and in the co-view channel of the HXRS (Fig. 5.14), in agreement with qualitative theoretical predictions.

The simulations with LUKE (Fig. 5.15) and CQL3D (Fig. 5.16) reproduce the experiment also quantitatively quite well. One apparent difference is that the simulated forward and backward emission both seem to saturate in the range 16 – 24 deg, where the emission continues to increase with angle in the experiment. More precisely, the emission is essentially constant with a slightly flattening slope for LUKE. For CQL3D it still increases from 16 to 20 deg, before it actually decreases at 24 deg.

To investigate this discrepancy, we concentrate on the CQL3D simulation for $\psi =$ 20 deg where the experimental result is better matched than with LUKE. There are no significant differences in the input parameters from one code to the other. However, the radial profiles, especially of T_e, are flattened in the center and increase outside the inversion radius because the TS measurement happens to coincide with the end of a sawtooth crash. This hints that the difference originates either from the sawtooth dynamics that are examined later in Sec. 7.1 or generally from uncertainties in the underlying profiles.

Here, a detailed look at the modeled e.d.f.s at the RF absorption maximum for each $n_\parallel$ step (Fig. 5.17) can already improve our understanding. First, there is

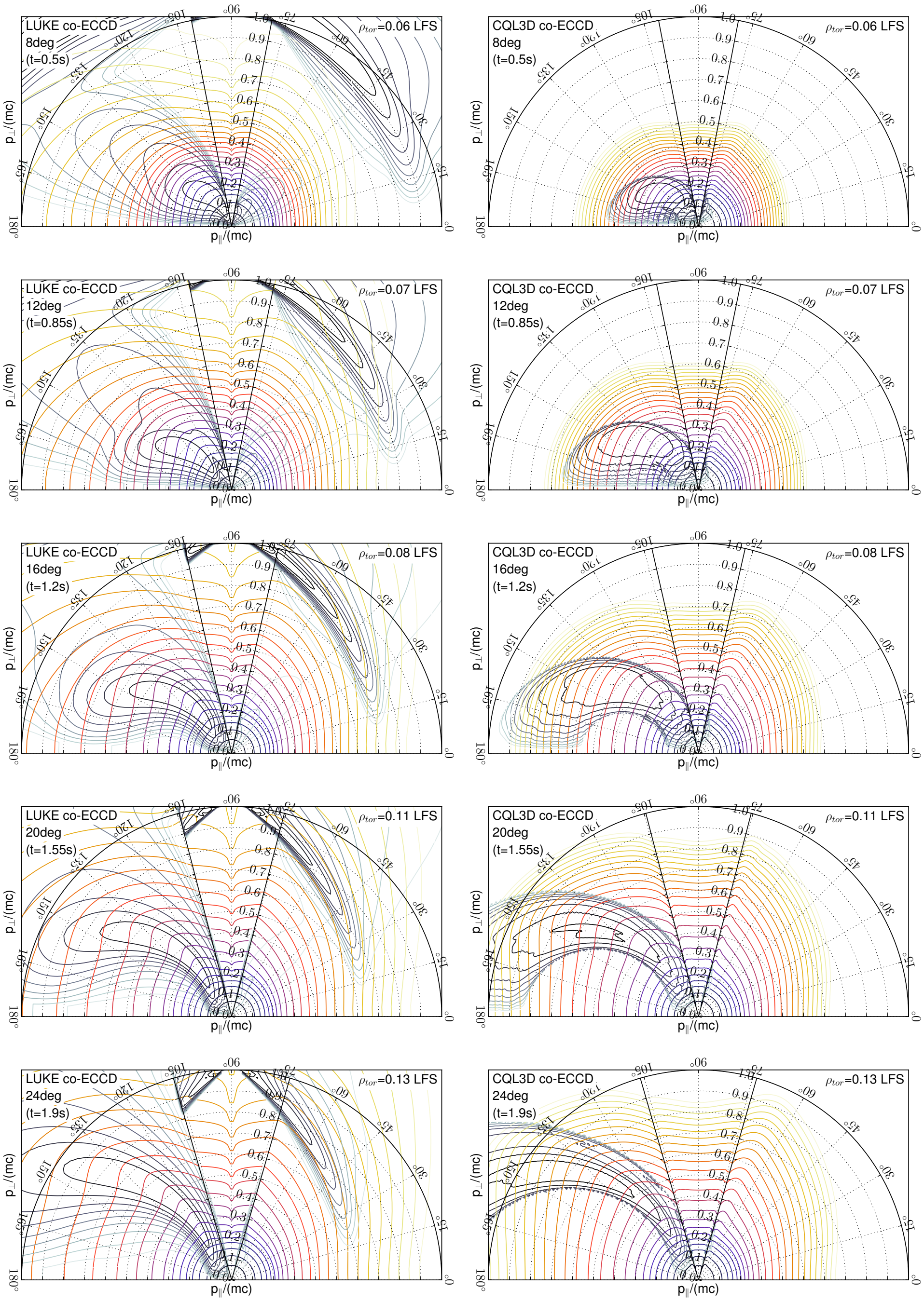

Figure 5.17: Modeled e.d.f. (color) and RF resonance (gray) in phase space at the RF absorption peak for varying co-ECCD injection angle ($n_\parallel$, increasing from top to bottom) in TCV discharge 49493 from LUKE (left) and CQL3D (right).

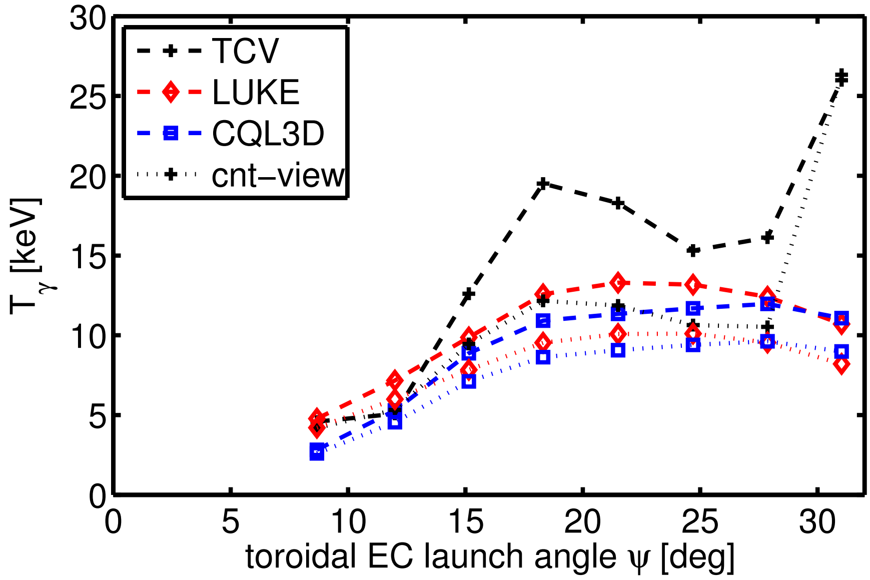

Figure 5.18: Measured and modeled photon temperature (T_γ) for varying toroidal EC injection angle ψ in TCV discharge 43205 ($\psi > 0$ means co-ECCD). The experimental measurements in TCV (black +) are compared to LUKE (red ◊) and CQL3D (blue □) for co-view (dashed) and cnt-view (dotted).

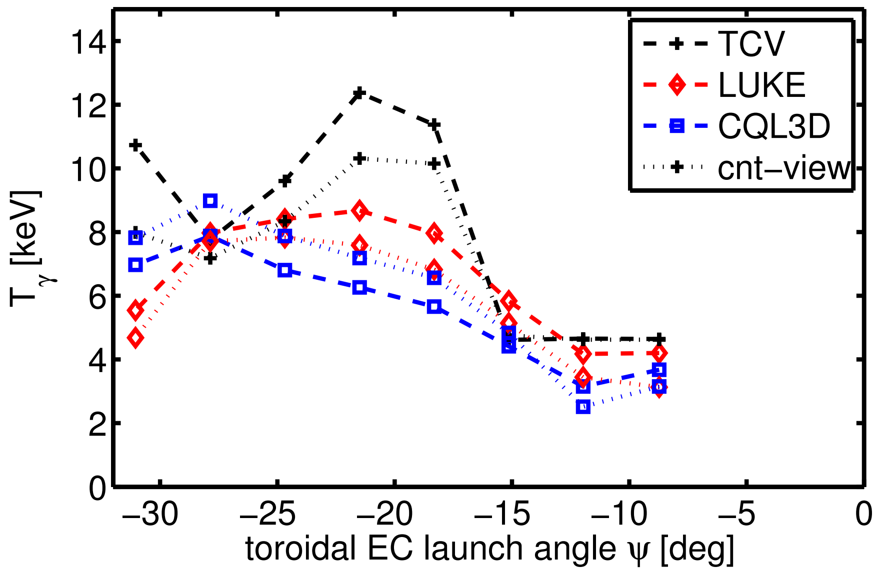

Figure 5.19: Measured and modeled photon temperature (T_γ) for varying toroidal EC injection angle ψ in TCV discharge 43206 ($\psi < 0$ means cnt-ECCD). The experimental measurements in TCV (black +) are compared to LUKE (red ◊) and CQL3D (blue □) for co-view (dashed) and cnt-view (dotted).

a good agreement between the two codes in the general picture, e.g. that the suprathermal electron population increases with $n_\parallel$. Furthermore, the resonance arch becomes narrower and approaches the trapped-passing boundary, resulting in an increased $v_\perp$ component of the maximal suprathermal tail whereas the tail in the parallel direction increases less, especially for high $n_\parallel$. Transport and magnetic reconnection events during sawtooth crashes may, in principle, redistribute and accelerate these fast electrons and therefore increase the suprathermal tail (and HXR emission) in the parallel direction.
As we will see later (Sec. 7.1), the transport due to sawtooth crashes can explain only a minor part of the observed discrepancy; T_γ does not change that significantly during a sawtooth period. The discrepancy seems to originate mainly from an anomalous effect (equivalent to a modification of E_ϕ), in conjunction with measurement errors on n_e, T_e and Z_{eff} that determine E_D.

Co- and cnt-ECCD injection angle scans

In the discharges 43205 and 43206, co- and cnt-ECCD were realized in scenario T ($\delta = 0.3$, initially higher central electron density ($n_{e,0}$) than scenario P) with a continuous sweep of the toroidal EC injection angle (ψ) from ± 8 deg to ± 35 deg. For the co-ECCD case the results are essentially the same as for the previously discussed scenario P. Summarized, we see an increase of the forward HXR emission T_γ with $n_\parallel$ that is again limited in the simulations, whereas the increase appears stronger in the experiment (Fig 5.18). This can be explained by changing MHD/sawtooth dynamics that lead to a density drop (to values comparable to discharge 49493 presented above), increasing the effect of E_ϕ that is underestimated when the field is close to E_D. Later, around $\psi = 25$ deg, there is an experimental emission drop when the MHD/sawtooth dynamics change again and n_e recovers. At angles above $\psi = 30$ deg, the codes predict a significant absorption drop eventually reaching 0 while reflections and scattering still yield a finite absorption in the experiment.
With the knowledge gained so far, the result for the cnt-ECCD $n_\parallel$ scan is not surprising: the HXR emission and T_γ increase with the absolute value of $n_\parallel$ (Fig. 5.19). As in Sec. 5.2.2, LUKE reproduces the difference of co- and cnt-I_p emission correctly whereas CQL3D predicts a comparatively too high emission and T_γ in the counter-current view direction, if the influence of E_ϕ is not adjusted. The sawtooth crash dynamics and their influence on n_e play, as in the co-ECCD case, a major role in the region around $|\psi| = 20$ deg, but here they increase T_γ in both the co- and cnt-I_p directions. The observations at the $n_\parallel$ limit are also analogous to the co-ECCD case.

5.3 Poloidal emission asymmetry

5.3.1 Magnetic field line helicity

To unambiguously separate the effect of magnetic field line helicity from phase space-effects, which also influence the poloidal HXR emission asymmetry, one has to reverse the toroidal magnetic field (B_ϕ). A change of the plasma current

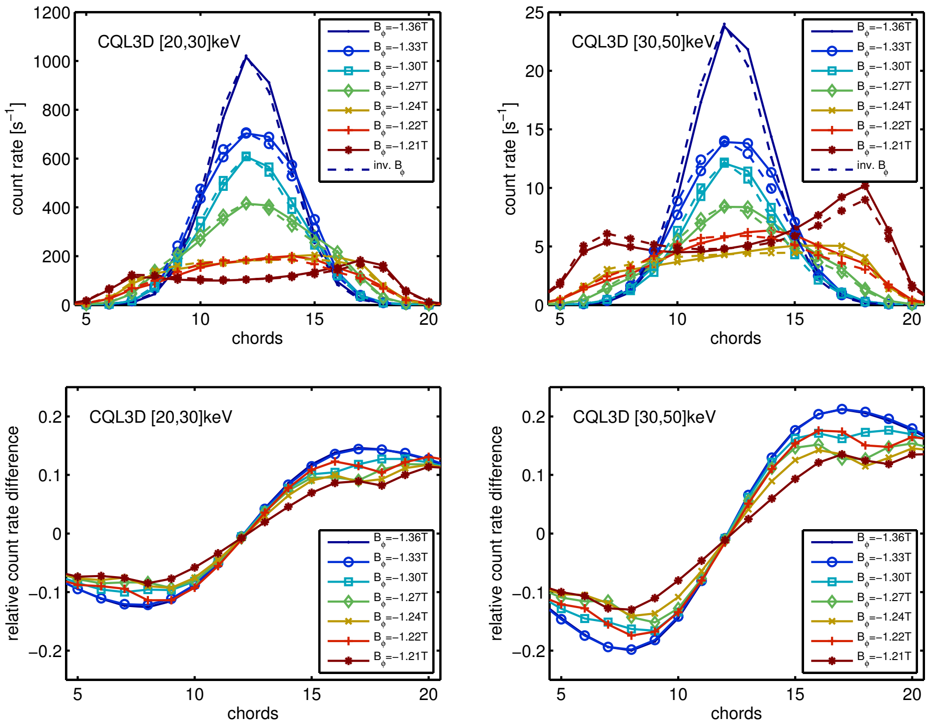

Figure 5.20: Modeling of the magnetic field line helicity effect on poloidal asymmetry observed by HXRS camera 2 in discharge 49118. For different B_ϕ (ECRH absorption location) the actual and inverted B_ϕ cases are compared at low (left) and higher (right) HXR energy, by plots of simulated count rate from CQL3D (top) and its relative difference between the actual and inverted B_ϕ case (bottom).

(I_p) direction has no effect since it reverses both the helicity and the forward direction of the e.d.f.. Of course, EC launcher angles and MOUs have to be adjusted according to changes in B_ϕ and I_p, otherwise much more would change.
Since the magnetic field line inclination w.r.t. the toroidal direction changes with the poloidal radius and according to the q-profile, the effect of helicity should be less prominent very close to the axis as compared to off-axis locations.

Magnetic field sign and radial absorption location

The effect of magnetic field line helicity on the poloidal HXR emission asymmetry measurement at different radial locations is investigated in discharge 49118 (scenario P). There, B_ϕ is scanned from $-1.43\,\mathrm{T}$ to $-1.18\,\mathrm{T}$ while $1.75\,\mathrm{MW}$ of pure ECRH is constantly injected. This changes the location of the ECRH resonance layer and shifts the ECRH absorption from mid-radius to far HFS.
Since the experiment was not repeated at reversed field because of limited experimental time, we rely on modeling. Using CQL3D with a usual suprathermal electron transport of $\chi_{se} = 0.5\,\mathrm{m}^2\mathrm{s}^{-1}$ one observes a significant change of poloidal asymmetry in HXRS camera 2 due to B_ϕ reversal for all heating locations (Fig. 5.20). As expected, the modification is larger at higher HXR energies. That the

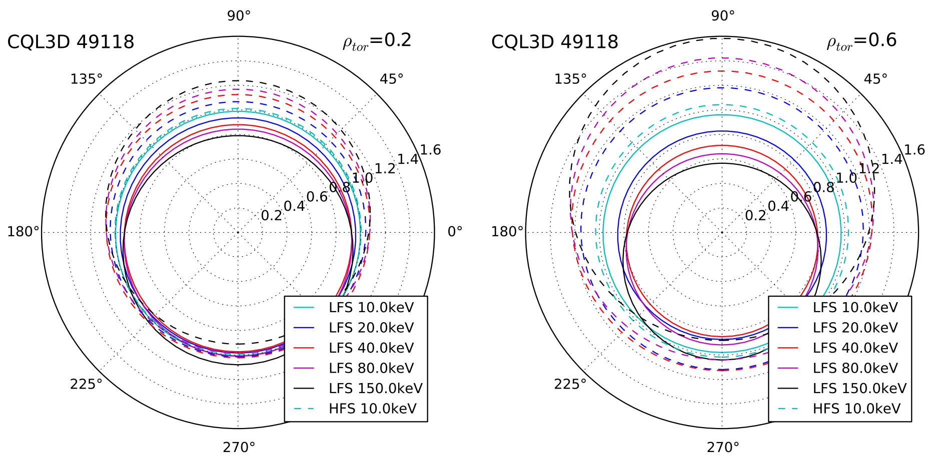

Figure 5.21: Modeling of the magnetic field line helicity effect on local HXR emission in discharge 49118 at $t = 1.3\,\mathrm{s}$ ($B_\phi = 1.22\,\mathrm{T}$). For the indicated radial position ($\rho_{\mathrm{tor}} = 0.2$ left, $\rho_{\mathrm{tor}} = 0.6$ right) the HXR emission from the point on the LFS (continuous line) is compared to the emission from the point on the HFS (dashed line) at the same flux surface. The angular coordinate is the emission direction (0 deg towards LFS, 90 deg upwards, 180 deg towards HFS, 270 deg downwards). The radial coordinate represents the emitted power at a given HXR energy, normalized over the averaged power at this energy. The power is averaged over all directions and emission locations (HFS, LFS). Colors indicate the photon energy.

asymmetry increases with field line inclination and photon energy can also be seen from the local HXR emission on the LFS and HFS (Fig. 5.21).
Looking at the relative change in the channels (Fig. 5.20) the theoretically predicted dependence on the radially varying field line inclination is essentially the same, no matter where the heating is applied. For experimental verification, however, off-axis ECRH is crucial. First, to have higher count rates and therefore better statistics and smaller error bars in the channels integrating along the largest inclination. Secondly, the gradient also plays a significant role. It is very steep for central heating and therefore a small radial shift of the plasma has a larger impact than the helicity. For off-axis heating, however, the profile is essentially flat, limiting the influence of the radial position, which can be difficult to control, especially between a pair of discharges with opposite toroidal magnetic field.

Magnetic field reversal experiments

Since the HXRS was installed on TCV, B_ϕ was only inverted for about one week, resulting in a very limited number of field reversal experiments and no dedicated shots were attributed to this study. Nevertheless, one pair of shots, scenario B, emitted significant HXR bremsstrahlung such that the parasitic HXRS measurement provides good statistics. Discharge 48836, with $B_\phi = -1.45\,\mathrm{T}$, was repeated as 49673, with $B_\phi = +1.45\,\mathrm{T}$. The main plasma parameters such as electron density and shape were well matched; the plasma current ($|I_p| = 120\,\mathrm{kA}$) and

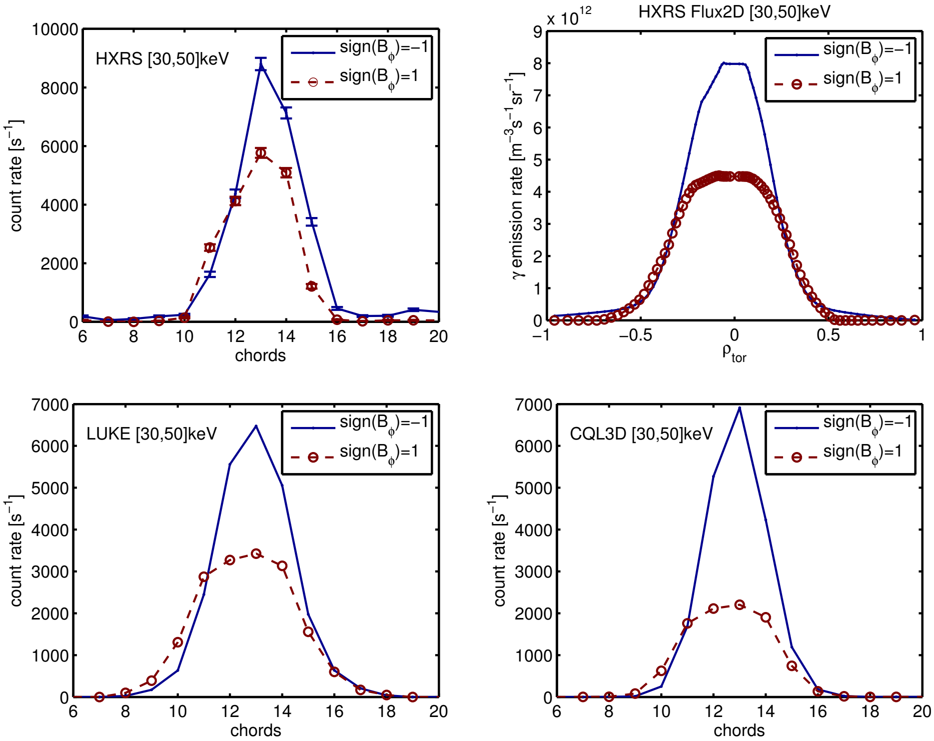

Figure 5.22: Measurement and modeling of poloidal asymmetry observed by HXRS camera 2 for sign$\left(B_{\phi}\right) = \pm 1$. From the measurement (top left), the emission is reconstructed by GTI (top right) separately on the HFS (indicated by negative ρ) and on the LFS (positive ρ). The synthetic diagnostics are shown at the bottom (LUKE left, CQL3D right).

X2 launcher angles were inverted too.
Only the vertical position was off by 2 cm, shifting the central RF deposition somewhat off-axis ($\Delta\rho_{\mathrm{tor}} = 0.07$). This results in a broader emission profile (Fig. 5.22). Also, a smaller horizontal shift is clearly visible in the HXRS signals and one cannot tell from the raw data if the poloidal asymmetry changes. However, independent tomographic inversion on the HFS and LFS using GTI enables a comparison and shows that there is no significant change in asymmetry (Fig. 5.22). The modeling results (same Fig.) reproduce the measurement.
Comparison to field-reversed simulations as done for scenario P before show that the expected effect on poloidal asymmetry is small in the case of central RF deposition. For central channels the change is less than 3 % and for outer channels with low statistics it is up to 5 %, so less than the error bars of the measurement. This is in agreement with the measurement, which indeed cannot resolve any field reversal effect on asymmetry for scenario B.

5.3.2 Phase space effects

The magnetic field line helicity effect can be separated quite easily in principle as has just been demonstrated. The main phase space effect is the change of θ_{tp} with θ_{pol} (4.2) and the subsequent modification of the e.d.f. (4.5). That is, if the suprathermal tail is larger in the trapped region, the HXR emission is larger on the LFS, because the trapped particles don't reach the HFS. In the more common case where mainly passing electrons are heated, the emission on the HFS is enhanced since there their $v_\perp$ component is relatively increased and, mainly, because the less energetic electrons don't contribute to the density on the HFS.
The details of the distribution function in phase space, especially around the trapped-passing boundary, are, however, quite difficult to track and require well-thought-out experiments. In the course of this thesis, the scenario P was developed for this purpose. The shape of the HFS wall limited plasma is elliptic to facilitate tomographic inversion, with an elongation of $\kappa = 1.5$; the density is set to 1.15 fringes ($n_{e,0} \approx 2.3 \cdot 10^{19}\,\mathrm{m}^{-3}$) and the current is kept at $I_p = 300\,\mathrm{kA}$. A first series of discharges (scenario P1) were carried out at $z = 23\,\mathrm{cm}$ to increase the radial resolution of HXRS camera 2. In this series, the toroidal injection angle was $\psi = 10\,\mathrm{deg}$ co-ECCD. After the installation of camera 7, another series of discharges (scenario P2), with more central deposition and $\psi \approx 20\,\mathrm{deg}$ co-ECCD were performed at $z = 0$.
Starting from these values, a few of the parameters were scanned to investigate their influence on the anisotropy of the e.d.f. by means of HXRS poloidal asymmetry measurements in comparison to modeling. It should be noted that the maximal asymmetry changes due to magnetic field line inclination are about 10 times smaller in relative terms than the change in B_ϕ (or I_p) as demonstrated above and verified for all analyzed discharges, with $\lesssim 20\,\%$ asymmetry change for a B_ϕ flip (200 % change).

5.3.3 Poloidal angle scan

The first and most interesting scan is the variation of the poloidal angle (θ) of the RF absorption location while keeping its radial position (ρ_{tor}) constant. A

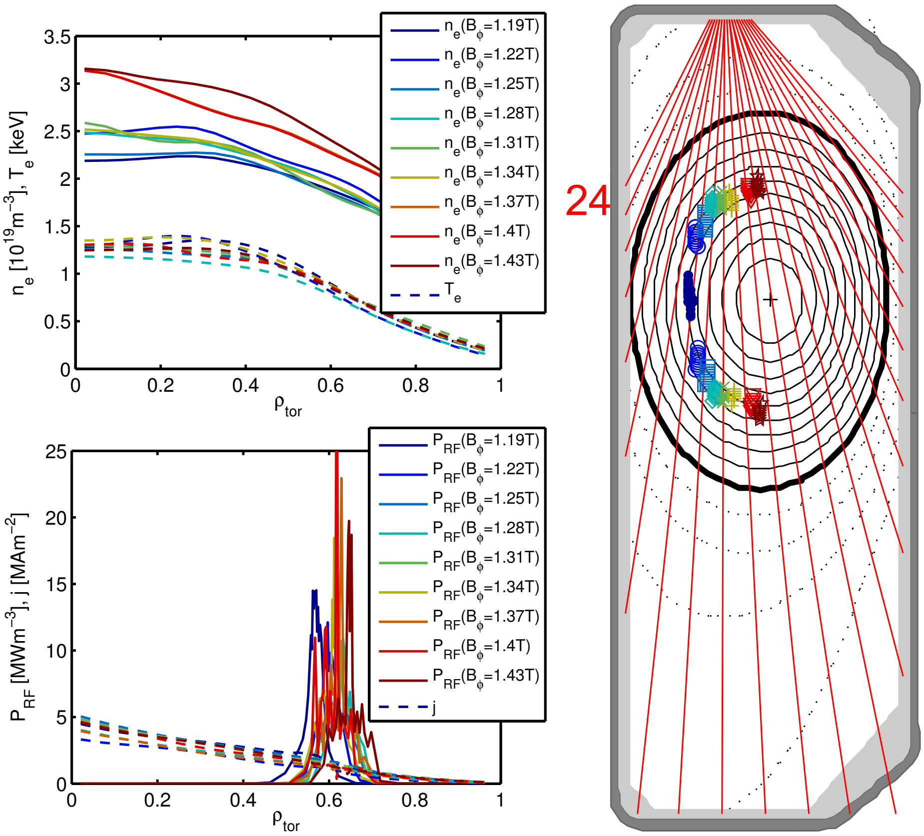

Figure 5.23: Radial plasma profiles (top left) and radial RF power deposition and current profiles from LUKE (bottom left, $\chi_{se} = 2\,\mathrm{m}^2\mathrm{s}^{-1}$) in the poloidal asymmetry poloidal angle scan, where the poloidal angle of the RF absorption location was varied from 180 to 90 and 270 deg (B_ϕ = 1.19 T – B_ϕ = 1.43 T, right). The LoS of camera 2 are numbered 1 through 24.

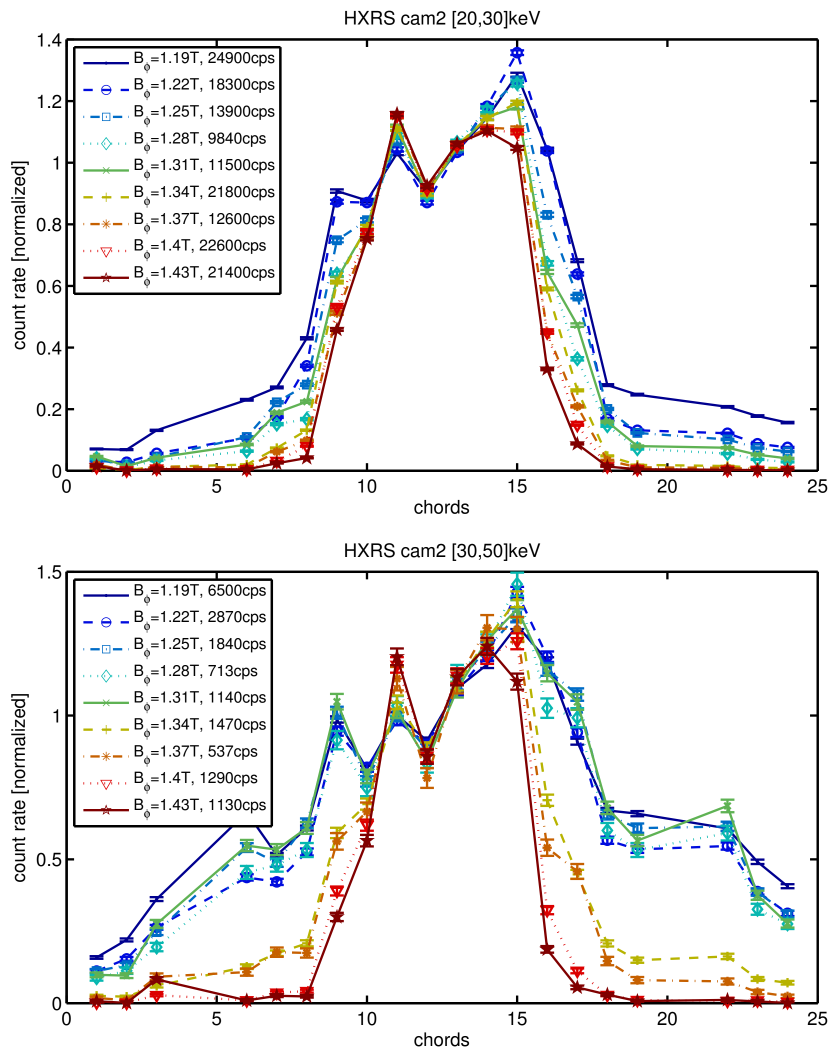

Figure 5.24: Normalized HXRS measurement of the poloidal asymmetry in the poloidal angle scan for $E_\gamma \in [20,30]$ keV (top) and $E_\gamma \in [30,50]$ keV (bottom). The normalization factor in cps is indicated in the legend.

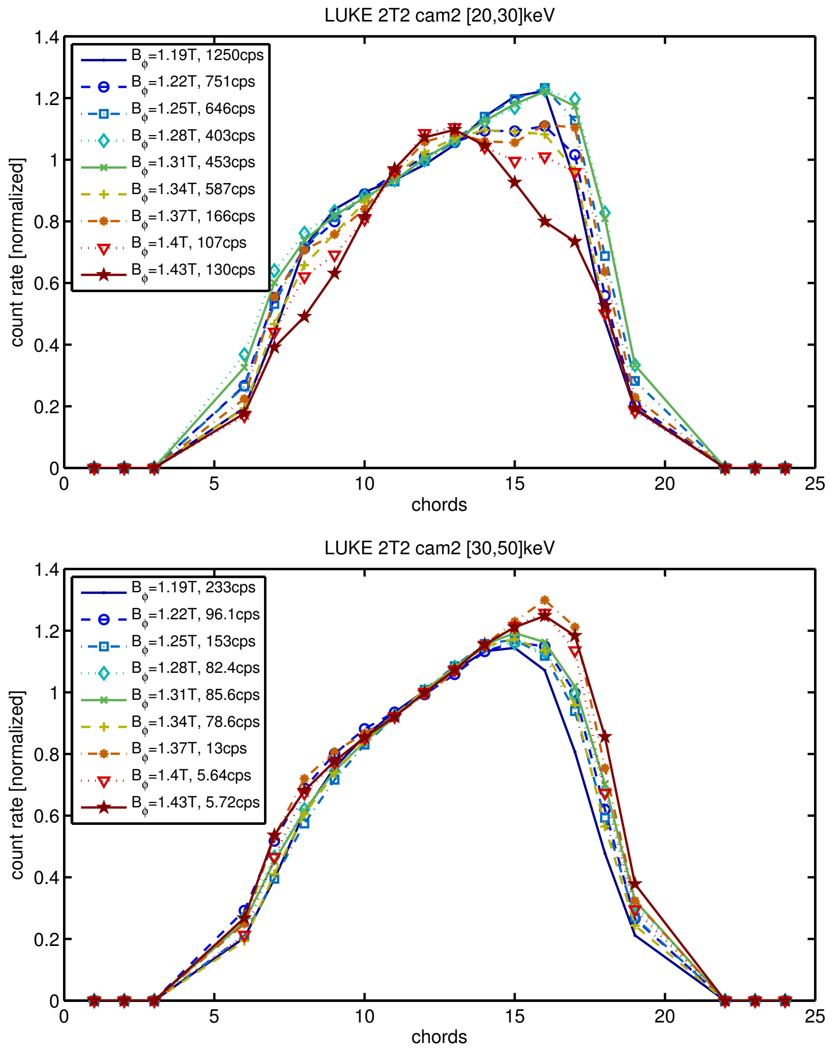

Figure 5.25: Normalized HXR emission from LUKE modeling of the poloidal asymmetry in the poloidal angle scan for $E_\gamma \in [20,30]$ keV (top) and $E_\gamma \in [30,50]$ keV (bottom) with suprathermal electron transport of $\chi_{se} = 2\,\mathrm{m}^2\mathrm{s}^{-1}$. The normalization factor in cps is indicated in the legend.

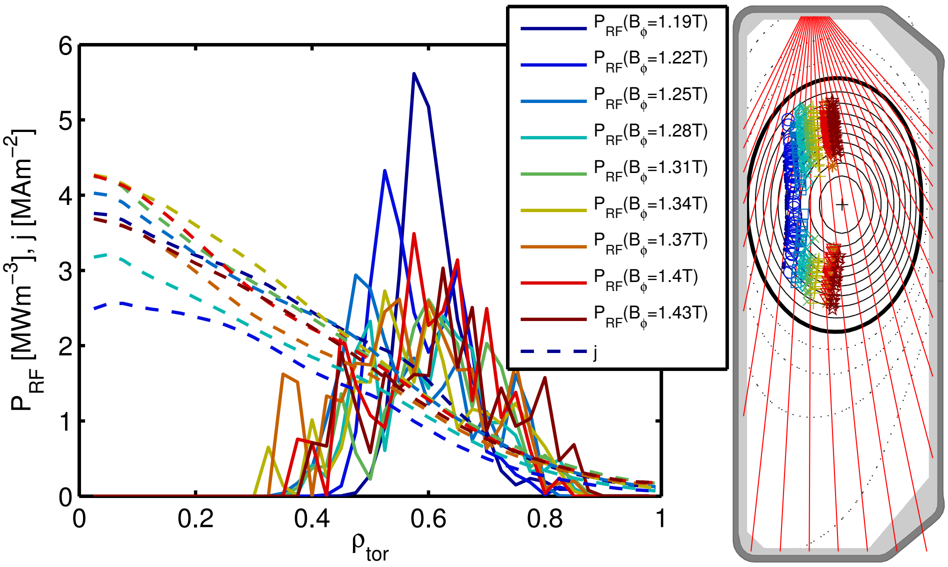

Figure 5.26: Emulated scattering in CQL3D broadens the deposition profile (left vs ρ_{tor}, right in the poloidal plane); compare with Fig. 5.23.

series of 9 discharges were carried out. B_ϕ was changed in steps of 0.03 T from 1.19 T (base discharge of scenario P1) to 1.43 T, moving the resonance layer from the HFS at $\rho_{\mathrm{tor}} = 0.6$ to the R position of the magnetic axis. By changing the X2 launcher angles according to ray-tracing on the prototype discharge, the absorption location is kept at $\rho_{\mathrm{tor}} = 0.6$ and the toroidal injection angle (ψ) at 10 deg co-ECCD. The obtained absorption locations (Fig. 5.23) correspond to the plan and the difficult requirement of keeping the other plasma parameters constant as well throughout the shot series was met in a very satisfactory way (same Fig. 5.23).

Experiment

Although there is a slight variation in the count rates, mainly due to small n_e deviations, a clear and monotonic trend is obvious from the normalized HXRS measurement (Fig. 5.24). The poloidal HXR emission asymmetry decreases when moving the RF absorption from the HFS to a position above / below the magnetic axis. The photon temperature on the chords decreases from $T_\gamma \approx 20$ keV to $T_\gamma \approx 5$ keV and is poloidally symmetric for all discharges.
This is in agreement with the theoretical prediction: on the HFS only passing electrons are heated directly by the wave and the only collisionally heated trapped electrons on the LFS emit less HXRs; whereas heating at full field also heats the trapped electrons that don't reach the HFS and emit on the LFS while the passing electrons receive a lower fraction of the total RF power in that case.
To validate if the trapped/passing difference also quantitatively accounts for the observation or is small as compared to other effects, modeling is required.

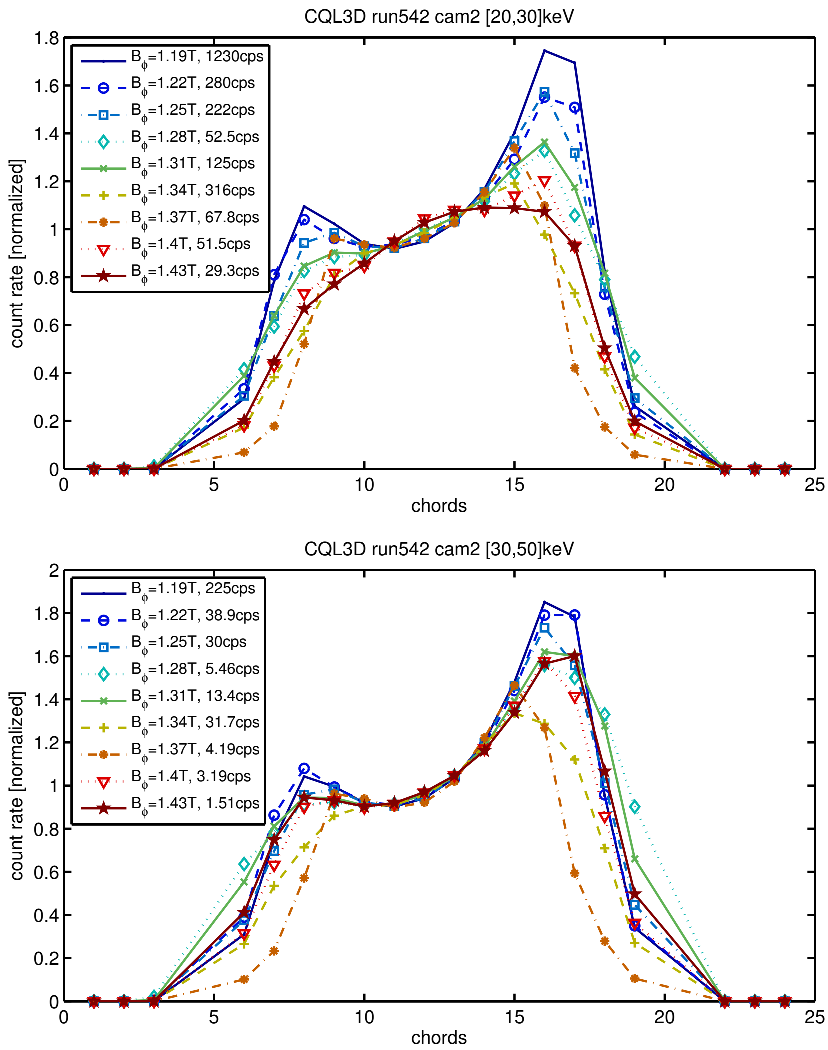

Figure 5.27: Normalized HXRS emission from CQL3D of the poloidal asymmetry in the poloidal angle scan for $E_\gamma \in [20,30]$ keV (top) and $E_\gamma \in [30,50]$ keV (bottom) with RF scattering emulated by random launch perturbations of ± 4 cm and ± 8 deg and suprathermal electron transport of $\chi_{se} = 0.5\,\mathrm{m}^2\mathrm{s}^{-1}$. The normalization factor in cps is indicated in the legend.

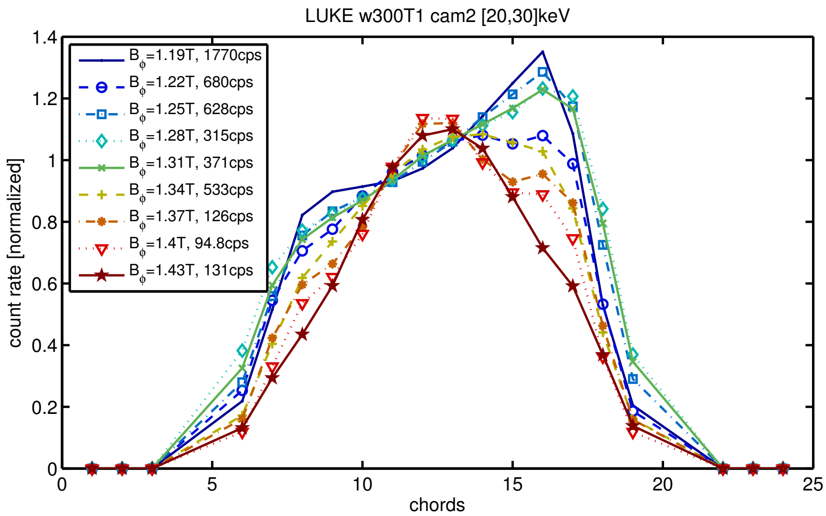

Figure 5.28: Normalized HXRS emission from LUKE of the poloidal asymmetry in the poloidal angle scan for $E_\gamma \in [20,30]$ keV with RF scattering emulated by RF beam broadening to 300 % and suprathermal electron transport of $\chi_{se} = 1\,\mathrm{m}^2\mathrm{s}^{-1}$. The normalization factor in cps is indicated in the legend.

Modeling

While modeling of the θ scan seems to be, at first glance, easier than producing such a clean series of experiments, it turns out to be extremely difficult to model discharges with such far off-axis heating ($\rho_{\mathrm{tor}} \gtrsim 0.6$) correctly. The main issue is that both codes (TORAY/CQL3D and C3PO/LUKE) predict invariably a broader emission profile (from chords 7, 8 to 17, 18; Fig. 5.25) than measured by the HXRS (chords 9 to 16; Fig. 5.24). This discrepancy is larger for the discharges with high B_ϕ, while those with HFS RF deposition show better agreement in this respect.
To reproduce the poloidal asymmetry change observed in the experiment, the radial transport in LUKE needs to be increased to $\chi_{se} = 2\,\mathrm{m}^2\mathrm{s}^{-1}$. With this large transport the normalized emission profiles for $E_\gamma \in [20,30]$ keV are well reproduced. At higher energies, e.g. $E_\gamma \in [30,50]$ keV, however, even drastic parameter modifications do not lead to any asymmetry change: the modeled asymmetry remains constant in the scan.
The absolute values of count rate and T_γ are significantly underestimated by the modeling. The former is at least partly due to the high imposed radial transport and the latter could be ascribed to uncertainties in the density and electric field at the absorption location, which can have a significant impact on the spectrum (cf Fig. 5.13).

RF scattering Regarding the transport, stochastic scattering of the RF waves in the outer region of the plasma (by density fluctuations, e.g. in the form of density blobs) could have an effect on the difference in the profile width that is comparable to that of increased diffusion, but without high losses of suprathermal electrons and energy. This could also explain the more modest discrepancy for

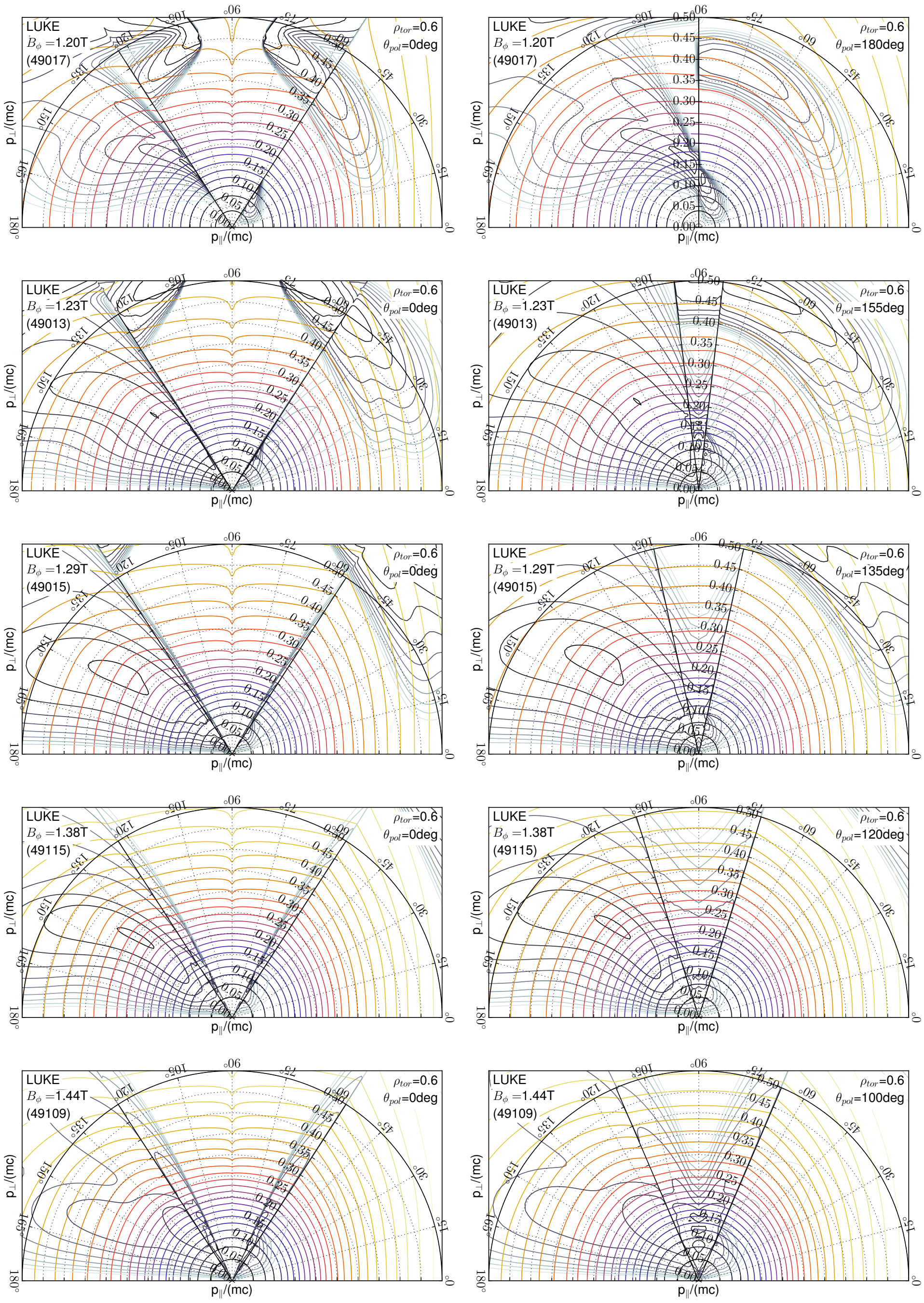

Figure 5.29: Modeled e.d.f. (color) and RF resonance (gray) in phase space at the RF absorption peak for varying poloidal angle of absorption position (B_ϕ increasing from top to bottom, absorption from HFS to LFS) from LUKE; showing the e.d.f. at minimum magnetic field (LFS, left) and at the absorption location (right).

the HFS heated discharges: the resonance layer is parallel to the flux surface in that case, and scattering hardly widens the radial absorption.
Even though the modeling of such scattering is not available in CQL3D, it can be emulated by perturbing the launch point and direction of the RF waves before starting the ray tracing by a randomly distributed deviation. This results in a widening of the beam that is equivalent to the effect of scattering in real space when τ_c is longer than the time scale of the fluctuations [162]. Indeed, perturbing the launch of the 60 TORAY rays by a uniformly distributed deviation with maximal values of ±4 cm in vertical direction (z) and ±8 deg in poloidal injection angle (θ) (Fig. 5.26) reproduces in large part the experimental observation in the normalized profiles (Fig. 5.27): the asymmetry dependence on the poloidal angle of the absorption location is clearly visible and monotonic as in the experiment. Similar results are obtained with LUKE where the scattering is emulated by a beam broadening to 300 % (Fig. 5.28). The agreement is much better than can be achieved with transport alone, where LUKE achieves partial agreement and CQL3D sees no change in the asymmetry for any transport parameters.
Nonetheless, even with scattering the modeling cannot reproduce the `absolute` count rate values of the experiments, being one to two orders of magnitude higher than the calculation of the synthetic diagnostics. As discussed later (Sec. 6.2.1), this discrepancy is often observed for far off-axis heating and may be resolved by an anomalous suprathermal particle pinch.

E.d.f. in phase space The modeled e.d.f. at the absorption location shows the theoretically expected behavior of different heating of trapped and passing particles (Fig. 5.29). Furthermore, the CD efficiency is also increased at low B_ϕ when only passing particles are heated.

Further experiments

A second series of experiments were performed with HXRS camera 7 additionally in place (scenario P2). To increase the HXR statistics and avoid problems with the far off-axis deposition modeling the scan was performed at a more central radius of $\rho_{\mathrm{tor}} = 0.38$ ($B_\phi = 1.28$ T in the base discharge). This solves indeed the modeling problem and the experiments are well reproduced, including the absolute HXR count rates. However, the heating is too central and therefore the change in poloidal asymmetry too small to be measurable.

5.3.4 V-X scan

To study the effect of RF scattering further, the V-X scan was carried out. The $B_\phi = 1.28$ T discharge of the poloidal angle scan was chosen to be repeated with the wave traces crossing close to the plasma center and forming an X shape in the poloidal plane, whereas the original shape resembles a rotated V (Fig. 5.30). Ray-tracing and F-P modeling predicts a much broader deposition profile in this X case, simply due to the longer wave path through the plasma, crossing its high density center and thus undergoing more refraction.
In the experiment, no such broadening is observed, and the experimental count

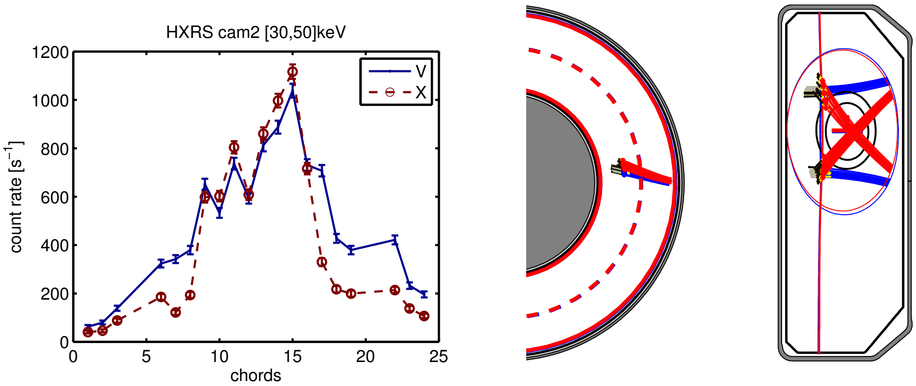

Figure 5.30: Poloidal asymmetry for V (blue) and X (red) RF injection geometry. Left: HXRS camera 2 measurement; right: ray tracing (Toray): top view and poloidal cross section, the absorption location is indicated in yellow.

rates in the interval [30, 50] keV practically do not change from V to X (Fig. 5.30), while modeling predicts an absolute difference of one order of magnitude (lower in the X case). By applying emulated scattering only in the V case (which is anyway difficult to justify), the discrepancies with experiment are reduced, but there is still no good agreement.

5.3.5 Scan of $n_\parallel$

ECRH acts more on the electrons at the trapped-passing boundary than ECCD, where the resonance moves towards electrons with higher $v_\parallel$ for increasing $n_\parallel$. This difference should also appear in the poloidal HXR emission asymmetry, because electrons close to the trapped-passing boundary are more affected by the magnetic field increase from LFS to HFS; their $v_\parallel$ get strongly reduced. This effect was investigated by a series of 4 shots with ψ taking values in $\{-20, 0, 10, 20\}$ deg, where the 10 deg co-ECCD discharge is the base discharge of scenario P1.
The experiment shows that the asymmetry is indeed significantly increased for pure ECRH and still a bit higher for low $n_\parallel$ than for high $n_\parallel$ (Fig. 5.31). The sign of $\psi = \pm 20$ deg plays, however, no significant role in the poloidal asymmetry.
The simulations match the experiments better than for the poloidal angle scan but again differences in the codes appear: the narrower emission profile in the pure ECRH case is better captured by LUKE, whereas CQL3D predicts that it is even broader than in the ECCD cases. Some discrepancies, such as the one order of magnitude reduced absolute HXR emission in these far off-axis heated discharges, are also observed in this scan.

5.3.6 Current scan

An increase of the plasma current results in steeper inclination of the magnetic field lines. To drive higher current, V_{loop} (E_ϕ) is increased. A two-point current scan was carried out, using reference scenario P2 as the high-current point and performing a similar discharge with reduced $I_p = 220$ kA.

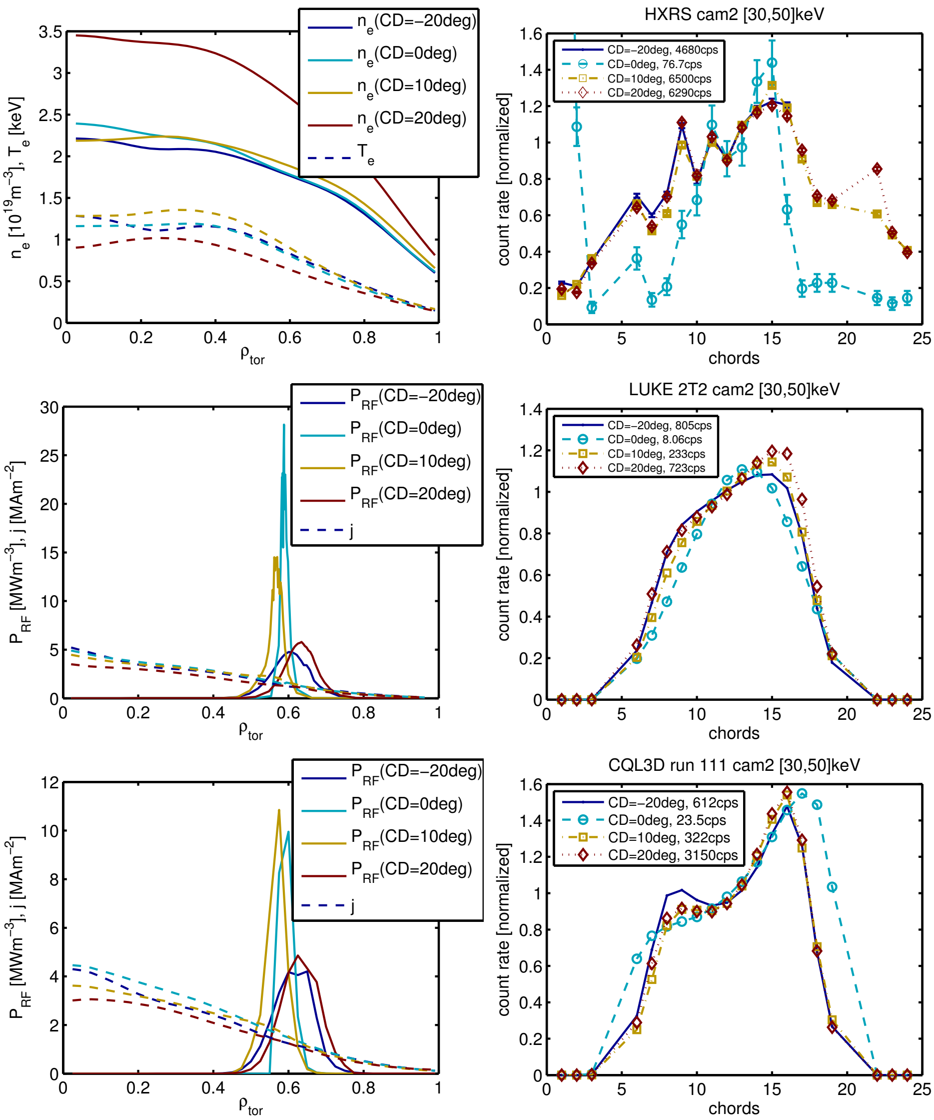

Figure 5.31: Experimental and modeled poloidal asymmetry $n_\parallel$ scan (toroidal injection angles −20, 0, 10 and 20 deg). On the left: radial plasma profiles followed by the radial RF power deposition and current profiles from LUKE and CQL3D. On the right: HXRS camera 2 measurement compared to LUKE and CQL3D synthetic HXR diagnostic. The normalization factor in cps is indicated in the legend.

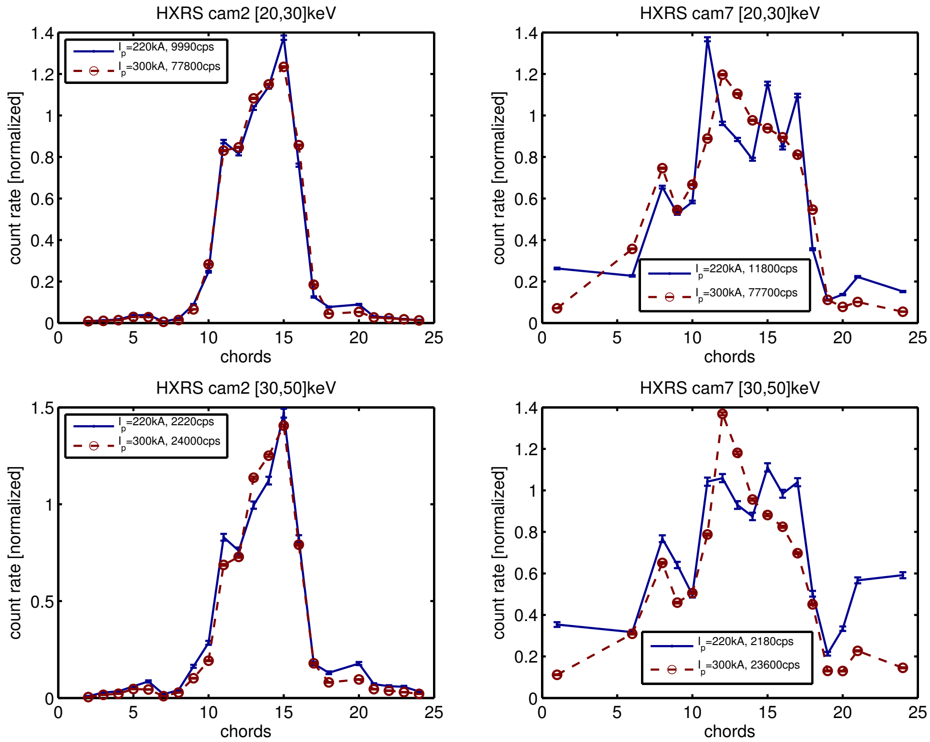

Figure 5.32: Poloidal asymmetry I_p scan. Experimental data of the upper HXRS camera 2 (left) and the lower HXRS camera 7 (right) in energy bins $[20,30]$ keV (top) and $[30,50]$ keV (bottom). The numbering of the chords starts, for camera 7 as for camera 2, with 1 on the LFS and ends with 24 on the HFS.

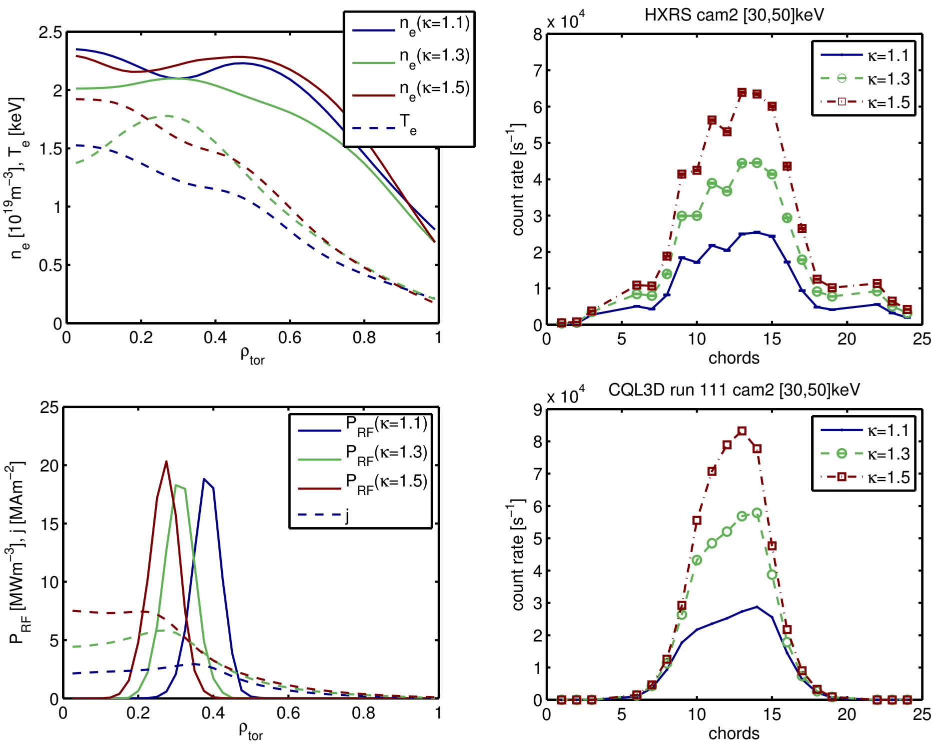

Figure 5.33: Poloidal asymmetry elongation scan: n_e, T_e profiles (top left), RF absorption and current drive profiles from CQL3D (bottom left), HXRS camera 2 measurement in $[30,50]$ keV (top right) and synthetic diagnostic result from CQL3D with $\chi_{se} = 1\,\mathrm{m^2s^{-1}}$ (bottom right).

In the new discharge the HXR emission (Fig. 5.32) is lower by one order of magnitude due the the reduced ohmic heating. Nonetheless the statistics are sufficient and the slight dependence of poloidal asymmetry on I_p through magnetic field line inclination can be glimpsed.
The measurements of camera 7 underline the importance of the magnetic field line helicity as compared to phase space effects. Due to the opposing positions of the upper and lower cameras w.r.t. the plasma they see the same phase space effects while the helicity effect is inverted. Note however that - even ignoring phase space effects - the effect of inverting the helicity effect is not a simple inversion of signal between the two cameras, owing to LFS-HFS asymmetries (see also Fig. 5.21). These asymmetries can be due to a shape that is not simply elliptical or, even for a purely elliptical plasma, to the Shafranov shift. However, an inversion of the direction of the asymmetry can be expected in most cases. Here, since the poloidal asymmetry is indeed nearly reversed, it follows that the helicity effect dominates in the measured HXR emission.

5.3.7 Elongation scan

The main reason why the plasma elongation (κ) could have an influence on the poloidal asymmetry is a modification of the field line inclination, which should

however by quite small. To change only the elongation in the scan (scenario P1b), the radial electron and current densities were kept constant by adjusting the line-integrated n_e and I_p references linearly with κ. Obviously, the measured HXR emission is also increased due to the longer integration path in the plasma.
No significant change in the asymmetry of the measurement is observed (Fig. 5.33), confirming that the influence of κ is marginal at best. The modeling confirms the results, also quantitatively, by using a constant $\chi_{se} = 1\,\mathrm{m^2 s^{-1}}$ profile for the suprathermal electron transport in CQL3D.

5.3.8 Triangularity scan

In contrast to the scans presented so far, poloidal asymmetry change by triangularity (δ) is more difficult to track since the plasma shape is no longer symmetric in the HFS-LFS direction. An appropriate tool to evaluate the obviously changing emission profile on the chords of HXRS camera 2 is GTI, since it can perform independent tomographic inversion on the flux surfaces of the HFS and LFS halves of the plasma. This accounts for the integration length change in the individual flux surfaces due to shape modification.
In the set of 5 (scenario P1b) discharges B_ϕ was slightly adjusted according to the Shafranov shift such that the HFS resonance layer was at the same radial location for all discharges. When δ is varied from -0.4 to 0.4, the mean of the inverted emission (Fig. 5.34) moves by 0.06 in ρ_{pol} (1.5 cm) towards the HFS, mainly due to the apparent poloidal asymmetry increase. The modeling results reproduce not only the asymmetry change, but also match well the profile shape and the absolute count rate.

5.4 Implications and conclusions

The toroidal and poloidal HXR emission experiments and their analysis in conjunction with modeling give more answers than expected beforehand, but also raise some new questions. While the main focus of the study is on quantifying e.d.f. anisotropies and phase space dynamics in ECRH and ECCD, original results are also obtained regarding RF scattering and suprathermal electron transport.
The predicted toroidal HXR emission asymmetry is experimentally confirmed for co-ECCD and cnt-ECCD. The increase of $T_{e,2}$ with $n_\parallel$ is also clearly demonstrated and quantified. Especially at large $n_\parallel$ and low density the interplay of EC- and E_ϕ-driven electron acceleration is difficult to reproduce with modeling and also reveals differences in the F-P codes. CQL3D generally underestimates the E_ϕ contribution while LUKE comes close to the experimental values. Furthermore, sawtooth oscillations, which are not considered in the modeling, can have also a significant impact.
Magnetic field reversal experiments and the use of a top and a bottom HXRS camera quantify the relative impact of magnetic field line helicity on the poloidal asymmetry at $E_\gamma = 50\,\mathrm{keV}$ to up to a tenth of the B_ϕ/I_p change.
In the poloidal RF deposition angle scan the opening of the passing particle cone towards HFS as the main phase space effect turns out to contribute less to the poloidal asymmetry change than RF scattering. The F-P simulations with em-

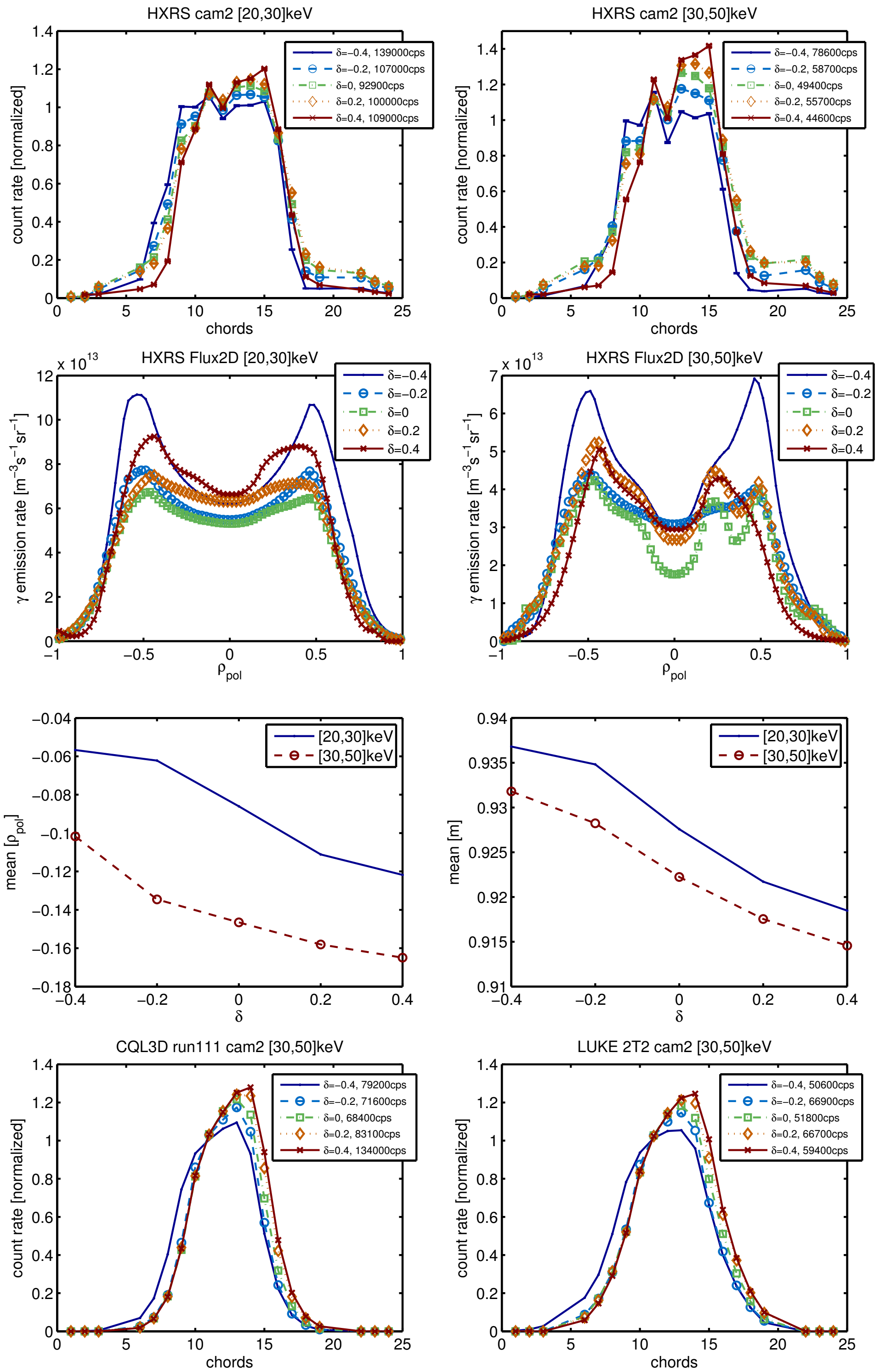

Figure 5.34: Poloidal asymmetry triangularity scan: raw experimental data for [20,30] and [30,50] keV; below: tomographic inversions on HFS (neg. ρ_{pol}) and LFS flux surfaces (pos. ρ_{pol}); below: mean emission position vs δ, left in ρ_{pol}, right in m); bottom: CQL3D $\chi_{se} = 1\,\text{m}^2\text{s}^{-1}$ left, LUKE $\chi_{se} = 2\,\text{m}^2\text{s}^{-1}$ right, for the [30,50] keV range. The normalization factor in cps is indicated in the legend.

ulated scattering on edge density fluctuations explain the experimental dependence of asymmetry on the poloidal deposition angle. This dependence cannot be reproduced by assuming suprathermal electron diffusion alone. Although transport is still used at a reduced level, the series of experiments demonstrate for the first time in EC-heated tokamak plasmas that the effect of RF scattering is important and can be separated from transport, also in normalized HXR emission profiles; although a significant discrepancy in absolute count rate remains.
The following V-X scan cannot be reproduced by modeling: the HXRS measurement hardly changes, in contrast to modeling that predicts large differences. An explanation may be provided by anomalous particle pinch (Sec. 6.2.1).
Further scans of $n_\parallel$, I_p, κ and δ confirm the generally good agreement of experiment and modeling and do not uncover any additional unexpected phenomena.

Chapter 6

ECRH/CD and suprathermal electron dynamics

The dynamics of the ECRH/CD created suprathermal electron distribution are not yet fully understood. There remain open questions, especially concerning transport and quasi-linear (QL) effects, as pointed out in the motivation of Sec. 1.6, which are addressed in the following.

6.1 Suprathermal electron diffusion

6.1.1 Revisitation of HXRC study

A previous study of spatial suprathermal electron transport during ECCD in TCV using HXRC measurements reported broadened radial HXR emission profiles and therefore also a radially broader suprathermal electron distribution compared to the RF power deposition profile calculated with ray-tracing. This broadening can also explain the experimentally observed current drive efficiency, which is significantly lower than predicted in the absence of transport. Fokker-Planck simulations using CQL3D were able to reproduce the broadened HXR emission profile shape and CD efficiency by assuming a suprathermal electron diffusion coefficient (χ_{se}) of about $1\,m^2/s$, depending on the specific plasma parameters. [163, 3, 124]
One of the shortcomings of the assumed radial transport was the finding that the HXR count-rate predicted by the synthetic diagnostic of CQL3D was significantly lower than the HXRC measurement. Since the shielding of the HXRC is insufficient against radiation in the MeV range and the diagnostic lacks a blind detector, bremsstrahlung emission from runaways could provide an alternative explanation for the increased experimental count rates and the observed broad HXR profiles. However, the location of the HXRC camera, pointed vertically at some distance from the plasma, tends to reduce the likelihood of significant runaway radiation.
In order to analyze the role of runaways, and possibly exclude a significant contribution to the HXR measurement, the main discharges of the previous study were repeated with the 3 HXRS cameras in place. Here, camera 7 is of great impor-

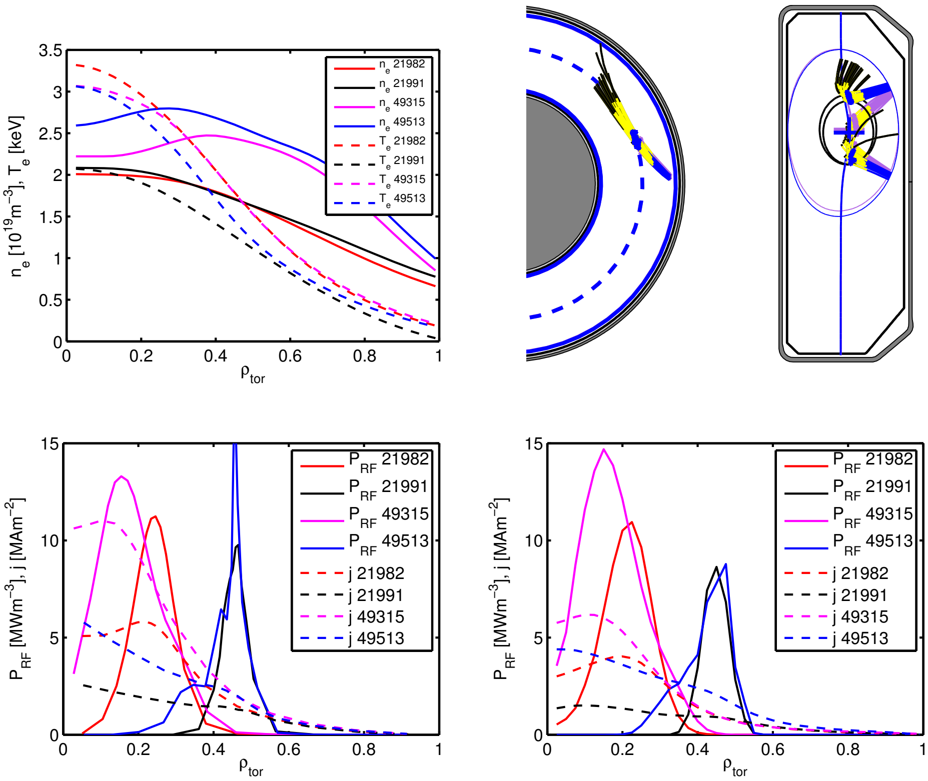

Figure 6.1: Radial plasma profiles (top left) and radial RF power deposition and current profiles from LUKE (bottom left) and CQL3D (bottom right) for TCV discharges 21982 and 21991 (with HXRC) compared to 49315 and 49513 (HXRS). The ray tracing (TORAY, top right) shows 49315 (magenta) and 49513 (blue), repeating 21982 and 21991, respectively.

tance, since its lower numbered channels' $(4-11)$ LoS form essentially the same fan as the HXRC $(7-17)$. In addition, the full coverage and increased resolution of the HXRS system should enable a more detailed characterization of the radial transport.

Experimental results

The original discharges 21982 and 21991 form, together with discharge 22003, a scan of the radial deposition location of co-ECCD RF power. The first two discharges of this scenario D were repeated in 49315 and 49513, with the RF deposition at $\rho_{\rm tor} = 0.15$ and $\rho_{\rm tor} = 0.45$, respectively. The far off-axis heated discharge 22003 could not be repeated because safety detectors have been installed on the vacuum windows in the meantime. Due to the very low absorption, these detectors are hit by the EC waves and trigger security interlock cuts of the gyrotrons. In any case, only the repeated central and mid-radius heated discharges provide high RF absorption and HXR statistics.
The electron density is, due to limited control, somewhat higher than in the original discharges, while the RF deposition is well matched (Fig. 6.1). In the original

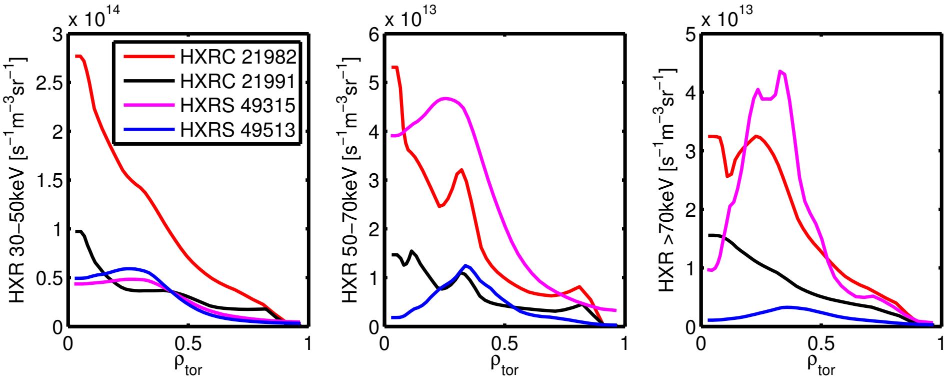

Figure 6.2: Radial HXR emission profiles from GTI (Flux1D discretization, 3 energy bins) for TCV 21982 and 21991 (HXRC) compared to 49315 and 49513 (HXRS).

discharges 1.2 MW was injected by 5 X2 launchers, while 4 X2 gyrotrons with a total power of 1.8 MW were used in the repetitions. As expected, these imperfect matches lead to quantitative differences. Nonetheless, the main results are reproduced. In all discharges, the radial HXR emission profiles obtained with GTI (Fig. 6.2) are much broader than the modeled RF absorption (Fig. 6.1, bottom), indicating substantial radial suprathermal electron transport. Importantly, the HXRS' blind detector signals clearly exclude the presence of significant radiation from runaways.

Comparison to modeling

Modeling is required to estimate the radial suprathermal electron diffusion coefficient from the experimental data. The modeling provides also a quantitative comparison of the old and new discharges with their slightly different plasma parameters (Fig 6.3).
LUKE captures the shape of the HXRC and HXRS measurement well for a range of transport parameters and the total plasma current matches the experiment. For a quite central value in this range, $\chi_{se} = 1\,\mathrm{m^2s^{-1}}$, LUKE also reproduces the absolute count rate quite accurately. The mismatch for discharge 49513 indicates that the transport is slightly increased in this plasma.
As in the previous study [3], CQL3D underestimates the HXR emission by a factor of two to three, while the shape of the HXR emission profile is well matched for $\chi_{se} = 0.5\,\mathrm{m^2s^{-1}}$. Except for 21991, where the current drive is generally underestimated by CQL3D, I_p is also well reproduced for this value of χ_{se}.

6.2 ECCD scans to study transport and CD efficiency

As an extension of the revisited HXRC suprathermal electron study a series of discharges were performed to scan further off-axis deposition locations and the effect of $n_\parallel$ on the current drive.

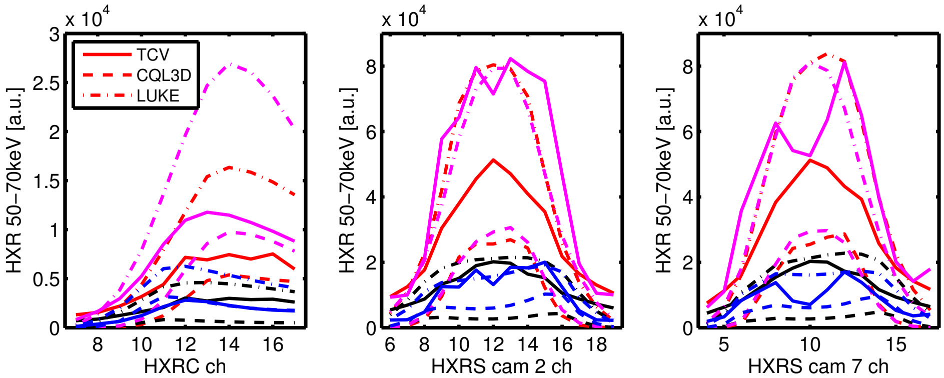

Figure 6.3: Experimental and modeled HXR data of discharges 21982 (red), 21991 (black), 49315 (magenta) and 49513 (blue) for the HXRC and the HXRS cameras 2 and 7. For 21982 and 21991, the HXRC measurement is shown directly (left), while the HXRS channels (cam 2 middle and cam 7 right) are mapped from the radial emission profile (from GTI, Fig. 6.2), since HXRS was not available in these discharges. For 49315 and 49513, the HXRS measurement is shown directly (cam 2 middle and cam 7 right), whereas the unavailable HXRC data is reconstructed from the tomographic inversion of the HXRS data (Fig. 6.2). The radial suprathermal electron transport is set to $\chi_{se} = 1\,\mathrm{m^2 s^{-1}}$ in LUKE and $\chi_{se} = 0.5\,\mathrm{m^2 s^{-1}}$ in CQL3D.

6.2.1 Deposition location scan

In a discharge of scenario T, the radial deposition location as calculated by CQL3D was varied from $\rho_{\mathrm{tor}} = 0.7$ to $\rho_{\mathrm{tor}} = 0.45$ in 4 steps (Fig. 6.4). The RF power was kept at 1 MW and the toroidal injection angle remained at 18 deg ± 2 deg.
This scan should enable the analysis of suprathermal electron (diffusive) transport in comparison to possible RF power deposition broadening by scattering, as proposed for the far off-axis heated poloidal angle scan discharges (Sec. 5.3.3, 5.3.4). Due to the co-ECCD component, the match in current drive efficiency can be used as an additional constraint, as in the HXRC study.

HXRS measurement

Although the absorption location from ray-tracing as computed by TORAY and C3PO is far off-axis, the measured HXR emission is peaked in the plasma center. There is no additional measurable peak at the deposition location. The absolute emission increases significantly (by more than an order of magnitude at E_γ = 20 keV) from the deposition at $\rho_{\mathrm{tor}} = 0.7$ to the most central one at $\rho_{\mathrm{tor}} = 0.45$. That the heating is more efficient for more central deposition is also reflected in the T_e profiles measured with TS, where $T_{e,0}$ increases from 1.1 keV to 1.6 keV.
In any case, the suprathermal tail remains quite cold and small as compared to central RF deposition: count rates above 50 keV are insignificant; $T_{e,2}$ increases from a value close to T_e to about 4 keV, with the radial profile being essentially flat (Fig. 6.4).
The experiment demonstrates that the suprathermal electron distribution is cen-

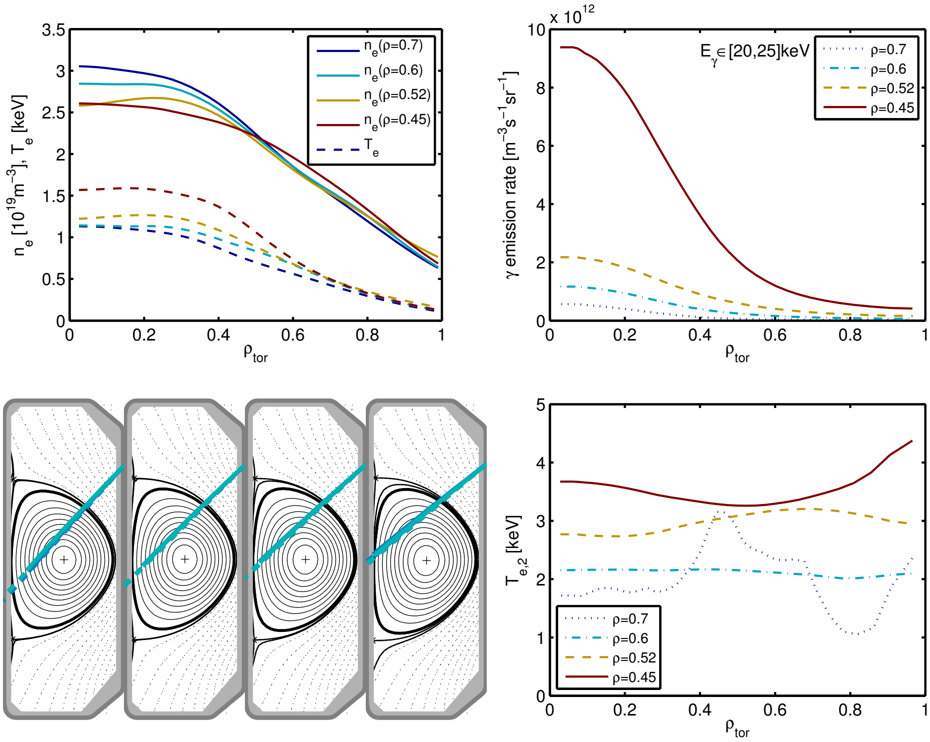

Figure 6.4: ECCD radial deposition location scan: top left: n_e, T_e profiles; bottom left: equilibrium and RF launch direction in the poloidal plane; top right: radial HXR emission profiles at [20, 25] keV from GTI; bottom right: radial $T_{e,2}$ profiles, calculated from GTI HXRS profiles; large error bars for $\rho_{tor} > 0.7$ due to low statistics.

trally peaked and therefore either strong radially inward transport or wave deviations leading to some central deposition have to be in play.

Comparison to modeling

As previously, F-P modeling is the chosen tool to determine suprathermal electron transport and RF scattering by matching the experimental observations. It turns out that the measurement cannot be reproduced and therefore the physics processes involved go beyond the modeling capabilities.
Anomalous suprathermal electron diffusion at reasonable values as inferred in other experiments still result in a very broad and off-axis peaked HXR profile while the predicted count rates are more than an order of magnitude lower than the measurement. A further increase of the diffusive transport leads first to a narrowing of the HXR emission profile in the more central deposition cases, but this lets the absolute counts fall to an order of one, below the HXRS noise level. So diffusive transport only can definitely not explain the experimental facts.
The scattering at density fluctuations in the plasma edge are, as for the far off-axis heated poloidal asymmetry scans, emulated by artificial beam broadening. This broadens the RF deposition and leads indeed to a higher HXR emission from the center. However, the absolute count rates remain too low and the quite narrow central peaking is also not reproduced.
Combining diffusive transport and scattering does not really decrease the disagreement to the experimental data: the issues of an overly broad emission profile, especially in the $\rho_{\mathrm{tor}} \geq 0.6$ cases, and of a low absolute count rate persist.

Further considerations

A possible effect that is not considered in the modeling is a combination of scattering and reflection. If a part of the beam is scattered and can partially traverse the plasma (at low n_e, where it is not fully absorbed), this remaining wave can be reflected off the tiles on the central column, re-enter the plasma and possibly deposit its power in the center. This seems to be a reasonable possibility for the deposition at $\rho_{\mathrm{tor}} = 0.7$, where the absorption lies at only 75% and slightly upward scattered beam trajectories hit the center after a reflection. In the two central deposition cases unrealistically large scattering would be required for significant unabsorbed power in the first pass and to reflect it to the plasma center. This also means that the correlation in the scan, much higher emission at more central deposition, would not be recovered.
Another possible mechanism is the anomalous particle pinch, which is necessary to explain the central peaking of n_e profiles in the absence of sources in the plasma center [164]. A similar approach was able to explain novel aspects in the physics of ITBs in TCV [165]. A study of this mechanism is outside the scope of this thesis.

6.2.2 Scan of $n_\parallel$

A series of 4 discharges of scenario T were performed to study the effect of $n_\parallel$ on the radial suprathermal electron profiles and on the EC-driven current. While

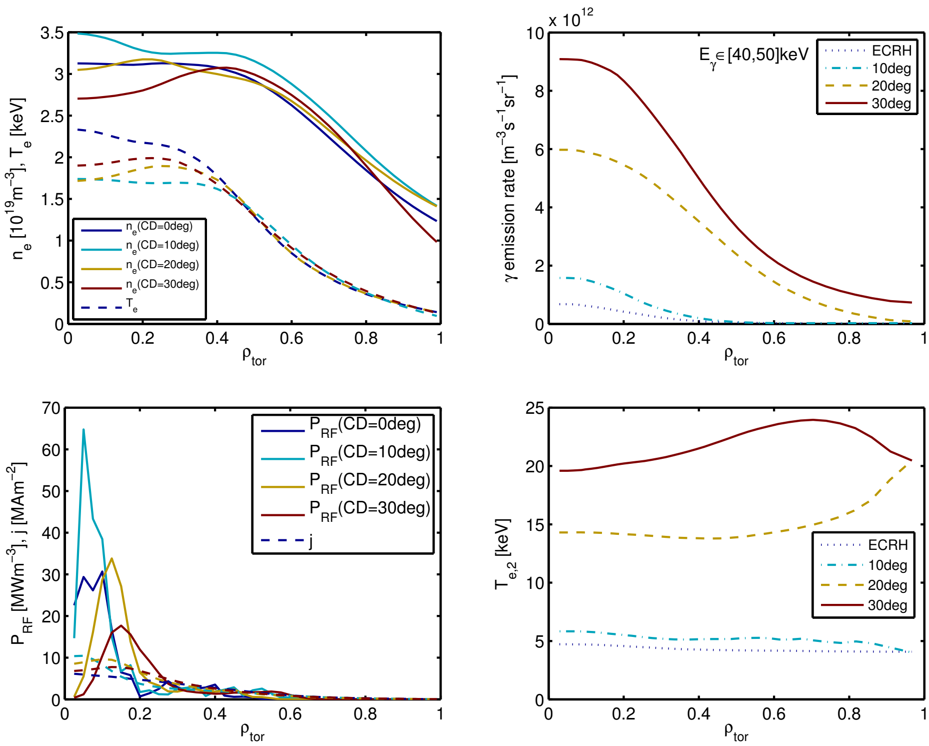

Figure 6.5: ECCD $n_\parallel$ scan experiment: top left: n_e, T_e profiles; bottom left: RF absorption and current drive profiles from CQL3D; top right: radial HXR emission profiles at $[40, 50]$ keV from GTI; bottom right: radial $T_{e,2}$ profiles, calculated from GTI HXRS profiles.

keeping the central deposition of 2 MW at $\rho_{\text{tor}} \le 0.2$, ψ was stepped through $\{0, 10, 20, 30\}$ deg; in the last case however, owing to mechanical problems, the 4 launchers reached only 22, 24, 25 and 28 deg instead of the full 30 deg. The density profile is flat up to $\rho_{\text{tor}} = 0.5$ at a value of $n_{e,0} = 3.2 \cdot 10^{19}\,\text{m}^{-3}$ (Fig. 6.5); I_p is kept at 270 kA by controlling V_{loop}, taking values of 0.694 V, 0.69 V, 0.67 V and 0.65 V from ECRH to full ECCD.

HXRS measurement

Due to the central deposition, the centrally peaked measured HXRS profiles are no surprise. With increasing $n_\parallel$ the emission increases by about one order of magnitude (at $E_\gamma = 40\,\text{keV}$) while the profile broadens overall by $10-20\,\%$ of ρ_{tor} (Fig. 6.5). As in the deposition location scan, the $T_{e,2}$ profile is essentially flat. While $T_{e,2}$ remains nearly unchanged for small $n_\parallel$ ($\psi \le 10$ deg), it increases significantly with $n_\parallel$ for $\psi \ge 10$ deg, as similarly observed in the $n_\parallel$ scans of the HXR emission asymmetry studies (Sec. 5.2.4, 5.3.5).

Comparison to modeling

Similar to already presented results with central RF deposition, the HXR emission can be well reproduced by F-P modeling. The increased HXR emission peaking of the more central and more localized deposition for lower $n_\parallel$ is well matched, both in LUKE and CQL3D (Fig. 6.6). The absolute count rates agree reasonably well for $\psi \ge 20$ deg if a comparably high suprathermal electron diffusion of $\chi_{se} = 4\,\text{m}^2\text{s}^{-1}$ is assumed. The HXR emission at pure ECRH and low CD component, however, is significantly underestimated and cannot be recovered by switching off the transport (kept at a standard value of $\chi_{se} = 1\,\text{m}^2\text{s}^{-1}$ for these 2 specific cases).
LUKE agrees within 20 kA to the experimental plasma current. CQL3D overestimates I_p in general, even in the pure ECRH case, with values of $340\,\text{kA} \pm 30\,\text{kA}$.

6.3 ECRH/CD response and quasilinear effects

The plasma response to the sudden application of high power ECCD was studied in a series of discharges using very short RF pulses and leaving the plasma enough time in between these pulses to reach its unperturbed state again. Concretely, 182 duty cycles of 11 ms with 1.7 MW ECRH blips of about 2 ms (exact time trace in Fig. 6.7) deposited in the plasma center (Fig. 6.8) were performed in a scenario P plasma at full field. The experiment was repeated with both HXRS camera 5 positions: horizontal for co-/cnt-I_p-view and vertical for full 2D tomography.
In the discharge with co-/cnt-I_p problems with the density control led to a density approximately about 30 % too high and therefore the plasma remains quite cold. Still, the injected RF power leads to a significant increase in HXR emission (Fig. 6.7). The rise is linear, so no QL effects can be measured in these conditions. The same holds for T_γ, which rises from 2.5 keV to 3.5 keV.
In the repeated discharge with 3-camera tomographic measurement the density was well controlled and T_e is higher. By consequence, the suprathermal electron

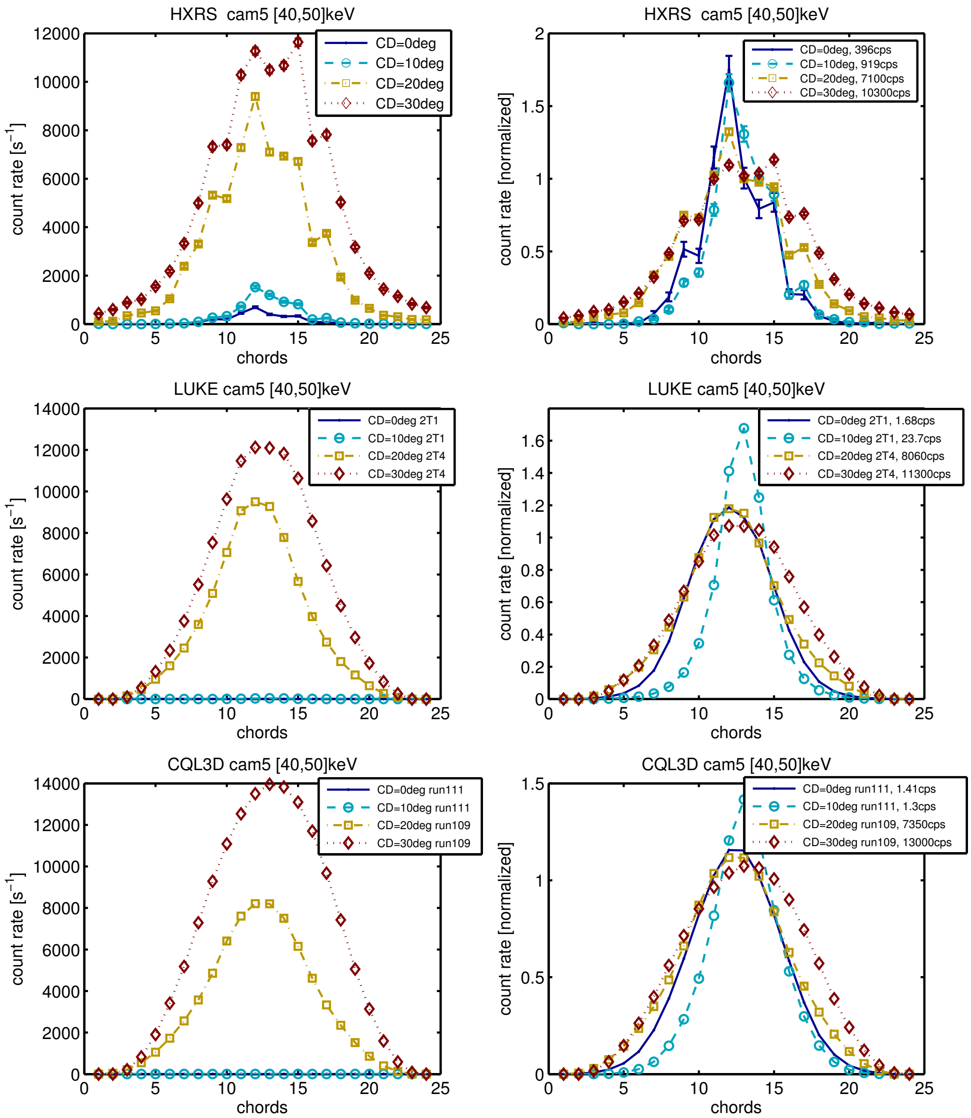

Figure 6.6: ECCD $n_\parallel$ scan, comparison of modeling and experiment: HXRS measured (top), LUKE (middle) and CQL3D (bottom) modeled emission on the chords of HXRS camera 5. Left: absolute values; right: normalized profiles, the normalization factor in cps is indicated in the legend. $\chi_{se} = 1\,\mathrm{m^2s^{-1}}$ for 0 deg and 10 deg, $\chi_{se} = 4\,\mathrm{m^2s^{-1}}$ for 20 deg and 30 deg CD.

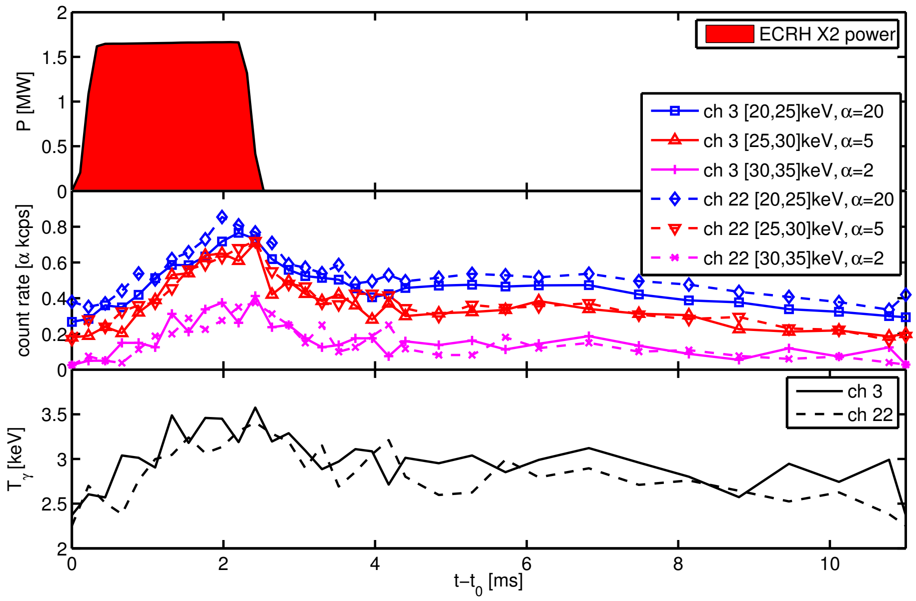

Figure 6.7: HXR emission ECCD response in co- and cnt-I_p directions, conditionally averaged over 182 duty cycles of 11 ms; top: ECRH power; middle: HXRS measurement in co-view ch 3 and cnt-view ch 22, the count rates are scales by α, which depends on the energy bin to facilitate the comparison of the relative signal evolution; bottom: T_γ on ch 3 and ch 22.

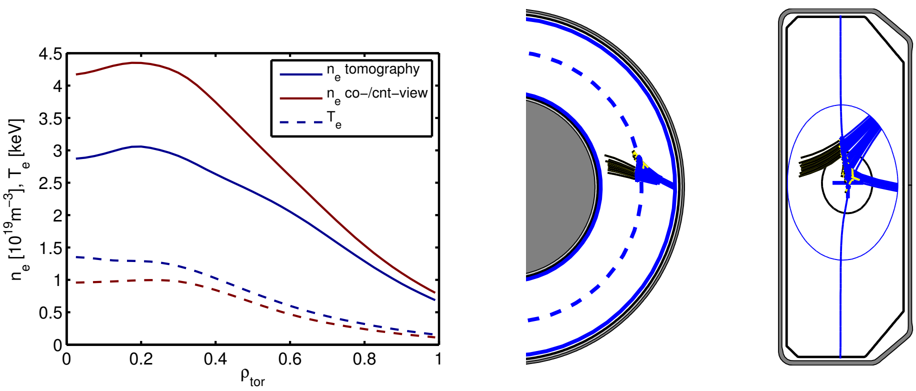

Figure 6.8: Radial plasma profiles for both ECCD response discharges (left) and ray tracing (TORAY) for the tomography discharge (right).

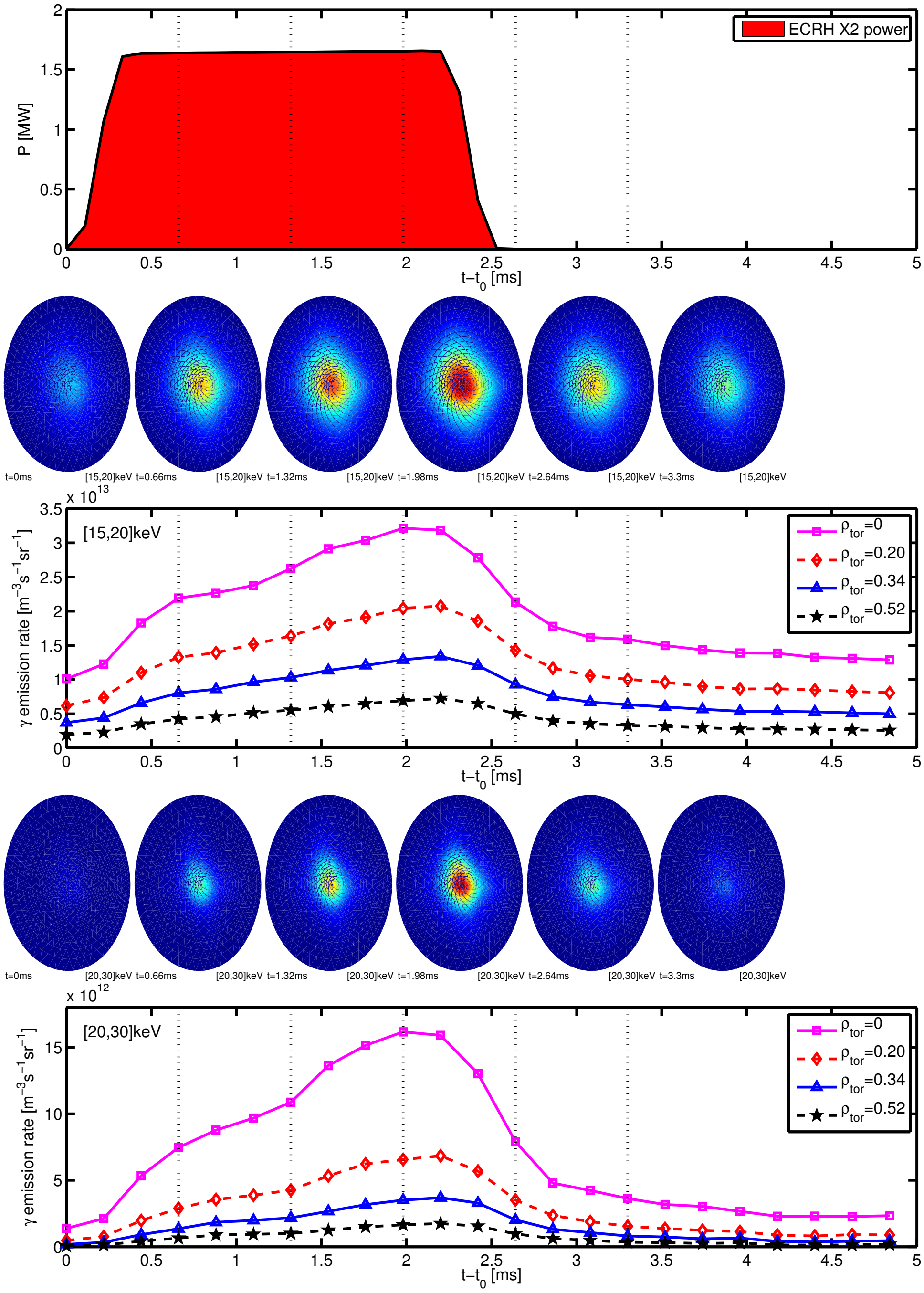

Figure 6.9: HXR emission ECCD response conditionally averaged over 182 duty cycles of 11 ms (only first 5 ms displayed): ECRH power (top); GTI HXRS in poloidal plane at the time steps indicated in the time trace, where the emission at 4 radial positions is shown: for low HXR energy (middle) and higher HXR energy (bottom).

fraction and energy is increased and $T_{e,2}$ rises from 2.5 keV to 5 keV. This also improves the HXR statistics such that a tomographic inversion can be performed up to HXR energies of 30 keV (Fig. 6.9). Again, the rise is essentially linear and no QL effects are observed. The 2D emission profiles indicate that the suprathermal part of the e.d.f. is also well aligned to the flux surfaces and extends radially during the heating phase. When the heating stops, the HXR emission decays with a time constant of 0.7 ms.

6.4 Conclusions

The revisitation of a previous suprathermal electron study with the new diagnostic capabilities confirmed the result that suprathermal electron diffusion can explain the broadening of the HXR emission profiles in TCV. Additionally, the presence of runaways that could invalidate the measurement was excluded. The EC-driven current is also well reproduced by the F-P modeling, including a scan of $n_\parallel$ for central co-ECCD.

However, the experimental observations in far off-axis heated plasmas cannot be explained by such transport or RF scattering and require additional effects that go beyond the model implemented in the F-P codes. Adding an anomalous suprathermal particle pinch may provide an explanation.

Investigating QL effects by short (2 ms) high power (2 MW) ECCD pulses, the response of the e.d.f. is found to be essentially linear.

Chapter 7

Interaction between suprathermal electrons and MHD modes

In the plasma center, a significant fraction of the e.d.f. can be suprathermal and may interact with MHD modes at the same location, most often internal $m/n = 1/1$ internal kink modes. This chapter reports studies of the transport of suprathermal electrons by such perturbations of the equilibrium. In the case of MHD events such as sawtooth crashes (Sec. 7.1) this includes the acceleration of electrons due to magnetic reconnection. Even more challenging is the investigation of reciprocal mode excitation by suprathermal electrons: the effect of suprathermal electron pressure will be addressed in Sec. 7.2 and resonant interaction, yielding electron fishbones, is discussed in Ch. 8.

7.1 Suprathermal electron dynamics during sawtooth crashes

The dynamics of the e.d.f. and especially suprathermal electrons during sawtooth crashes are studied in EC-heated low confinement mode (L-mode) plasmas in TCV. ECRH/CD is neither used for sawtooth triggering nor to stabilize sawteeth, such as to produce extremely long or large sawteeth (monster sawteeth). The sawtooth period is about $3-4$ ms and the crash amplitude is about $20-30$ % in the SXR signal and in the bulk electron temperature relative to the peak before the crash. It turns out that two main regimes, primarily depending on n_e and V_{loop}, can be distinguished.
At low density, at the limit to a fully runaway discharge, HXR bursts in the MeV-range are observed immediately after each sawtooth crash.
At high density, the temporal variation of the HXR emission, and partially of $T_{e,2}$, mimic those of the SXR and thermal bulk temperature.
The characteristics of these two regimes are presented below, followed by the even more interesting dynamics occurring in the transition region in between.

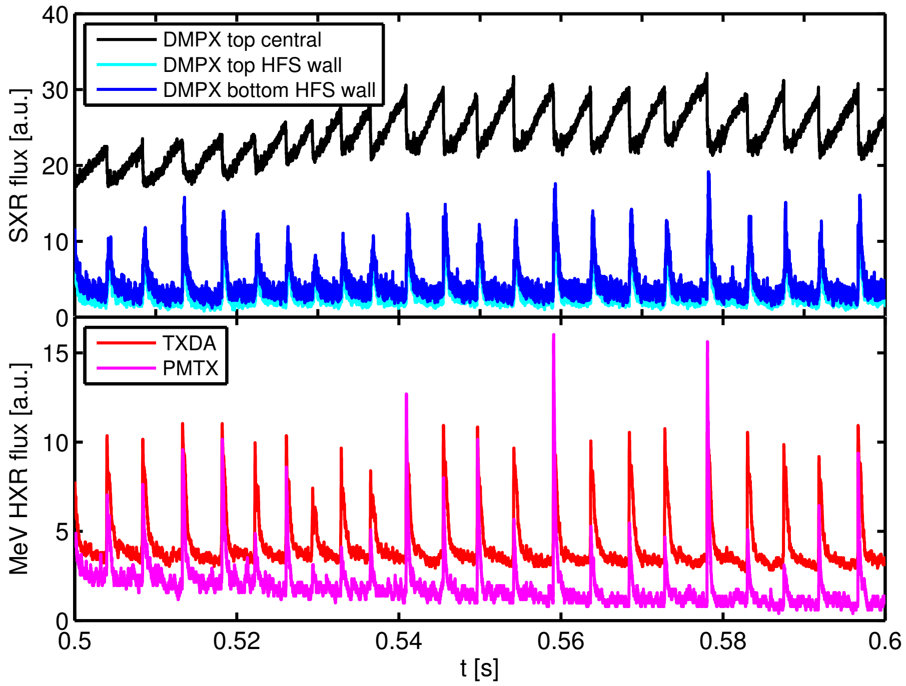

Figure 7.1: SXR DMPX signal and MeV HXR bursts (TXDA, PMTX) at sawtooth crashes in the low n_e TCV discharge 43039 ($P_{\mathrm{RF}} = 641\,\mathrm{kW}$, $n_{\mathrm{e,avg}} \approx 1.2 \cdot 10^{19}\,\mathrm{m}^{-3}$).

7.1.1 HXR bursts at low density

At low electron density, typically $n_e \approx 1 \cdot 10^{19}\,\mathrm{m}^{-3}$, HXR bursts are observed by the TXDA and PMTX diagnostics (Fig. 7.1). In order to be detected by the PMTX their energy has to lie in the MeV-range. The shielding of the TXDA is insufficient for such energetic photons. Furthermore, a series of experiments with the TXDA tangentially observing different locations in the plasma, and in co- and counter-current direction, do not show any dependence of the measurement on either the location or the direction. This means that not even a distinguishable fraction of the TXDA signal comes from collimated radiation.

While the PMTX observes significant radiation outside of the bursts only in an initial phase of the discharge where it is fully runaway, the TXDA still collects reduced, but definitely non-zero radiation, attributed to a lowered, but persisting runaway electron population.

Also the blind HXRS detectors, especially in the lateral camera, see a finite number of high-energy photons in between the sawtooth crashes, while their signal is entirely saturated during the MeV γ bursts coinciding with the crash (Fig. 7.2). Therefore, the HXRS can detect these bursts and their duration, but cannot deliver any additional information such as emission location, photon flux or time evolution.

The DMPX has a low detection efficiency (η) at high $E_\gamma > 30\,\mathrm{keV}$ and due to its position in a bottom port it does not lie in the main emission cone of high energy and runaway electrons. The top DMPX camera signal is therefore hardly affected by the bursty emission, and the central chords observe the typical sawtooth cycle.

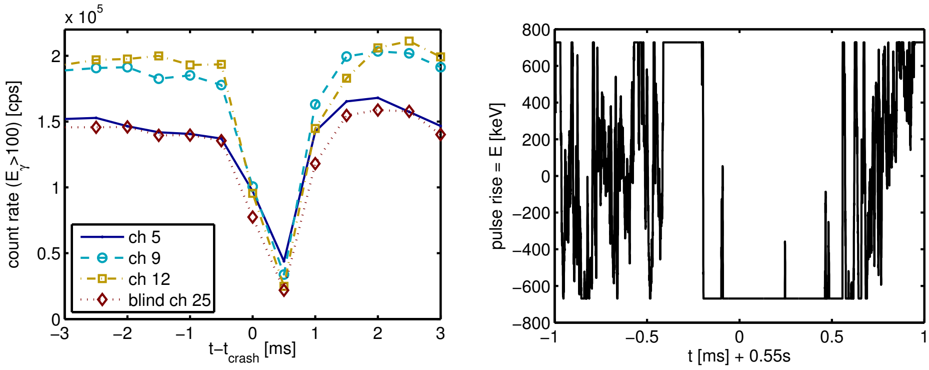

Figure 7.2: HXRS data during the MeV HXR bursts: the computed count rate for the blind detector (ch 25 in camera 5) and 3 more channels show the same time evolution (left). The signal is corrupted especially at the sawtooth crash, where it decreases due to the full saturation of the raw signal, exemplified by the raw data of the blind detector around the burst at 0.55 s (right).

The bottom DMPX camera has a higher low energy threshold due to its thicker filter and therefore a relatively increased η at higher energy. It observes the bursts at the sawtooth crashes on all channels, especially on the channel looking at the HFS limiter. On this outermost HFS LoS, also the top DMPX camera observes the bursts. Tomographic inversion shows that the signal comes mainly from the limiter, while there is a gap with no significant signal between the edge and the emission hill in the region between sawtooth mixing and inversion radii that originates from the bulk plasma expelled from the hot core by the sawtooth crash.
This indicates that high energy electrons hit the wall right after the sawtooth crash. A possible explanation is that electrons are accelerated due to magnetic reconnection during the sawtooth crash. A part of them is also transported to the HFS wall explaining the increased radiation from there, while also a significant part of the high-energy bremsstrahlung emission comes from the plasma. The alternative explanation is that the few persisting runaway electrons that are present in the plasma core emit little bremsstrahlung radiation due to their low collisionality there. During the sawtooth crash they are transported to the limiting wall, where they collide with the thick target.
Without spatial resolution or additional diagnostics (e.g. synchrotron radiation measurements of runaway electrons), the relative importance of these two effects cannot be quantified.

7.1.2 Dynamics at high density

The situation is quite different in higher electron density discharges, typically at $n_e \approx 3 \cdot 10^{19}\,\mathrm{m}^{-3}$ and above (in absolute terms of TCV medium and high density, but among the highest densities of discharges presented in this thesis): The temperature of the suprathermal tail is usually quite low, and so are the HXRS count rates above $E_\gamma \gtrsim 40\,\mathrm{keV}$; the presence of runaway electrons in particular can be excluded. In these discharges, the time evolution of the HXR and SXR emission

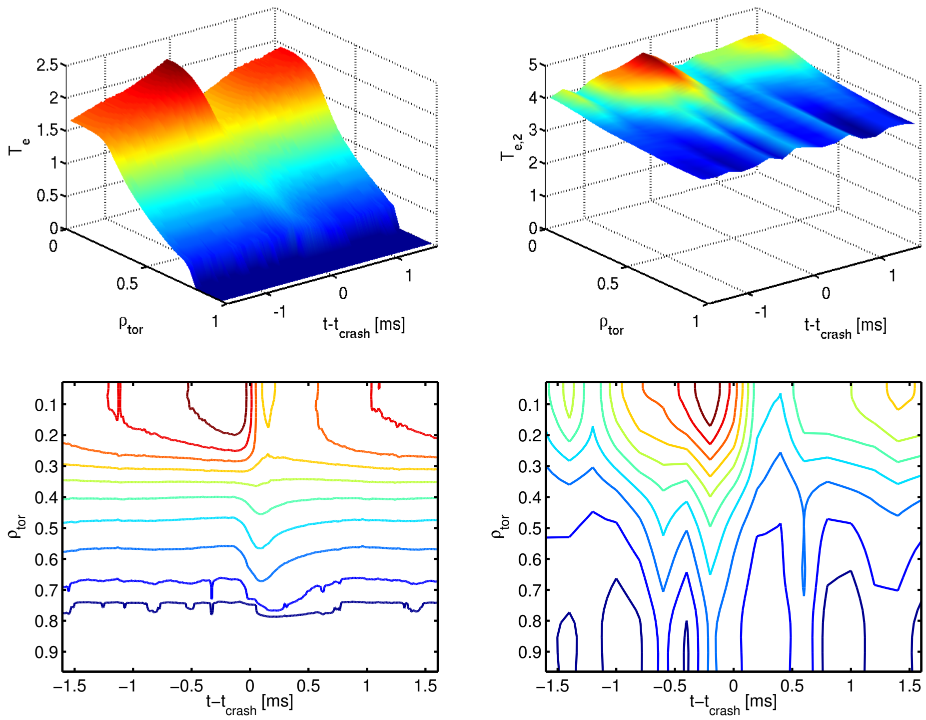

Figure 7.3: Bulk (left) and suprathermal electron temperature profile (right) at sawtooth crashes in the high density TCV discharge 43185 ($P_{\mathrm{RF}} = 946\,\mathrm{kW}$, $n_{\mathrm{e},0} \approx 2.8 \cdot 10^{19}\,\mathrm{m}^{-3}$). First, the DMPX and HXRS data is conditionally averaged and inverted by GTI. T_e is then obtained from the ratio of the radial SXR emission profiles (top divided by bottom DMPX camera and calibrated w.r.t. TS). The HXRS data is available in more than two different energy bins, so $T_{e,2}$ is the result of a linear fit to the logarithmic slope of the spectrum.

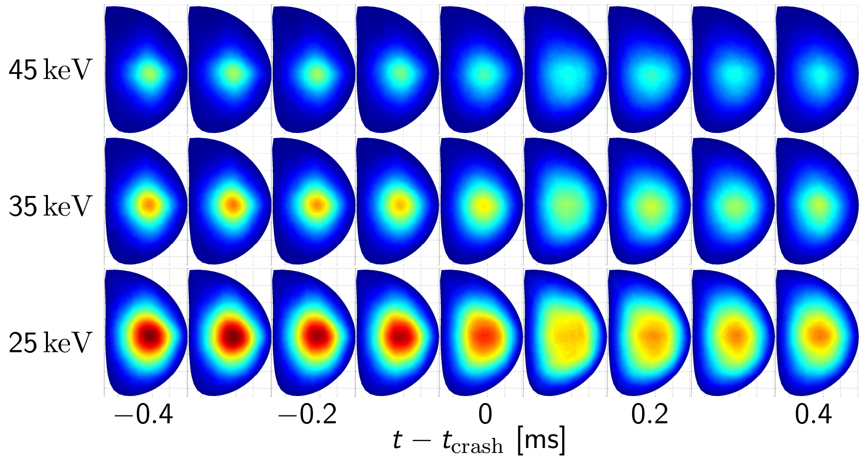

Figure 7.4: Evolution of the 2D HXR emission profile at different photon energies during a sawtooth crash in scenario S, obtained with GTI from conditionally averaged HXRS data of cameras 2 and 5.

is very similar during a sawtooth cycle. The slow rise of the central emission is followed by a sudden drop at the crash; then the rise starts again. The same behavior is also observed in the deduced temperatures for the bulk (T_e) and the suprathermal tail ($T_{e,2}$) (Fig. 7.3). The only apparent difference is that the relative temperature variation of the suprathermal tail is much lower than that of the bulk plasma, while the signal drop in the HXRS and DMPX bottom channels is comparable; i.e. the suprathermal electron loss does not depend significantly on energy in the observed range.
While in the SXR and T_e profiles a central flattening and radial broadening is observed, the suprathermal tail is reduced everywhere, and neither $T_{e,2}$ nor the density of suprathermal electrons increases outside the inversion radius. This also means that no bulk acceleration of electrons due to magnetic reconnection at the $q = 1$ surface can be inferred from HXRS data. Nonetheless, acceleration of electrons at thermal energies and/or at a lower rate as compared to the loss is not excluded.

7.1.3 Suprathermal electron transport and reheating

Since the sawtooth crash dynamics of suprathermal electrons for low and high density differ so significantly, there has to be a transition, either abrupt or via one or more intermediate regimes. It turns out that the transition window is quite narrow, but the intermediate regime can still be studied.
At low density but with significant current drive (scenario S), i.e. low V_{loop}, a high energy suprathermal tail is built up. The blind detector of the upper HXRS camera 2 sees no radiation, so the measurement of the camera is collimated. The lateral camera 5 is slightly perturbed by a low level of uncollimated HXR but can still be used in the lower energy bins.
The result of the 2D tomographic inversion in the plasma center shows that the behavior there is similar to the higher density case with greatly increased supra-

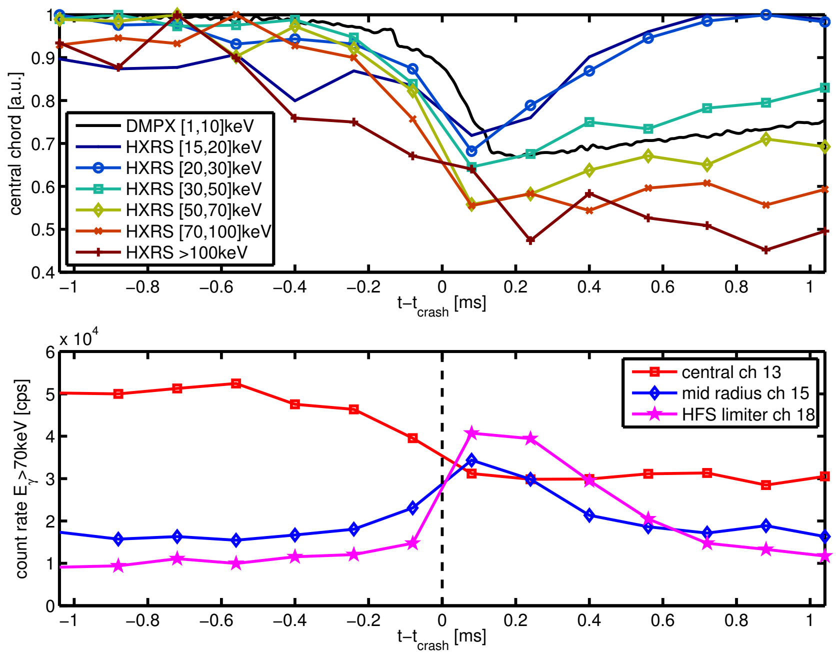

Figure 7.5: Evolution of the HXRS central chord measurement at different energies compared to the SXR evolution (top) and evolution of high energy HXR measurement from central, mid-radius and HFS limiter position (bottom) during a sawtooth crash in scenario S, obtained from conditional averaging.

thermal electron temperature and density; additionally, a broadening of the emission profile is observed (Fig. 7.4). The emission drop in the plasma core is observed by the DMPX and HXRS central chords in different energy bins (Fig. 7.5), that show essentially the same evolution during the crash. After the crash, the low-energy HXR emission rises more rapidly than the SXR and high-energy HXR signals. This indicates that the suprathermal tail is built up rapidly at low energy and then grows to higher energy more slowly on the timescale of the T_e rise.
The chords of camera 2 that observe the HFS limiter register only a very low signal in the inter-crash phase. Right after the crash, however, the emission at high energies ($\gg 50\,$keV) shows a burst with similar evolution as the bursts in the low density case, but at lower, still measurable energies, and collimated. The comparison to the central and a mid-radius chord (Fig. 7.5) shows that while the high energy HXR emission decreases in the center during the crash it already increases at mid-radius; 0.1 ms later, in the middle of the crash, the emission from the limiter increases much more quickly. The bottom of the central emission coincides with the top of the mid-radius and edge emission peak.

In summary, the intermediate regime exhibits some characteristics of the low and high-density cases. The central suprathermal electron distribution is significantly affected by sawtooth crashes throughout all energies observed, up to $\gtrsim 100\,$keV. The suprathermals are rather transported radially outwards than accelerated in the reconnection layer; ultimately, a large fraction of the fast electrons hits the limiter and emits energetic HXR bursts.

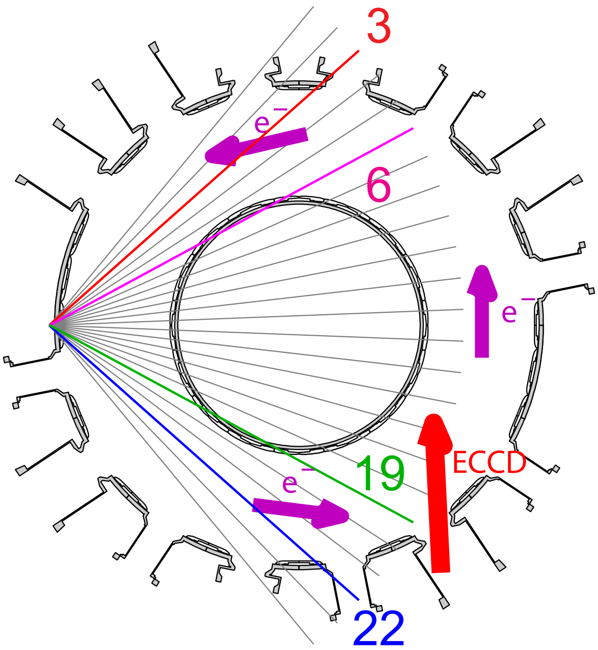

Figure 7.6: Top view of TCV with the chords of HXRS camera 5 in horizontal position for toroidal coverage during sawtooth crash experiments: chords 3 and 22 observe the plasma center, whereas chords 6 and 19 see the limiter (central column tiles); the chord coloring corresponds to Figs. 7.7 and 7.8.

7.1.4 Acceleration of (suprathermal) electrons

To investigate possible forward electron acceleration during the sawtooth crash at the high electron energies involved, tangential observation of the HXR emission is more efficient. Since a contribution from acceleration could not be distinguished from perpendicular observation (Sec. 7.1.3) parallel emission data is even essential. With the HXRS camera 5 in horizontal position (Fig. 7.6), such measurements are done in the co- and cnt-ECCD angle scan discharges of scenario T (Sec. 5.2.4). There, a change in MHD and sawtooth activity (longer period, larger crash amplitude) causes a density drop in the second phase of the discharge that puts it into the right parameter range for the transitional regime. The HXRS can resolve the dynamics with 0.1 ms resolution, as shown in Fig. 7.7 for co-ECCD and Fig. 7.8 for cnt-ECCD, due to conditional averaging w.r.t. the crash time. The about 400 sawtooth crashes are detected by the DMPX and the reference time is put at the middle of the drop. It turns out that in the resulting HXRS signal the middle of the crash appears 0.1 ms earlier.

Sawtooth crash impact

In both cases, the impact of the sawtooth crash is severe: the parallel HXR emission from the plasma center in the lower energy range (20−50 keV) drops to about one fourth within about 0.2 ms. At higher energies (≈ 75 keV), it falls only to a

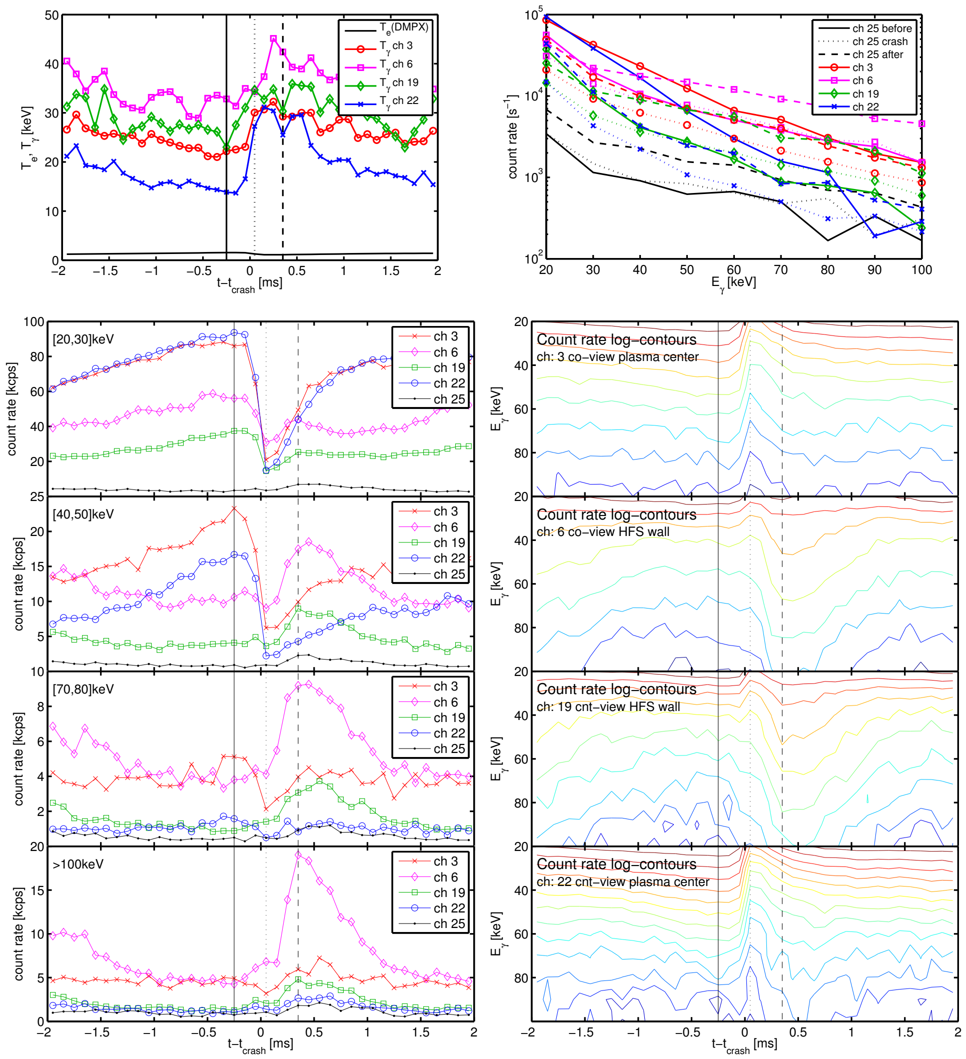

Figure 7.7: Time evolution of the HXR signal in the tangential chords 3 (co-I_p view on plasma center), 6 (co-view on HFS wall), 19 (counter-I_p view on HFS wall), 22 (cnt-view on plasma center) and 25 (blind detector; background) in the co-ECCD discharge 43205 (scenario T).
Top left: time evolution of the photon temperature (T_γ) compared to the bulk temperature (T_e) from DMPX; vertical lines indicate the time points for the top right plot: HXRS spectrum on the chords before, at, and after the sawtooth crash (-0.25, 0.05, 0.35 ms w.r.t. t_{crash}); bottom left: count rate evolution in selected energy bins for the 5 HXRS channels; bottom right: spectral evolution for the 4 HXRS channels (without background ch 25).

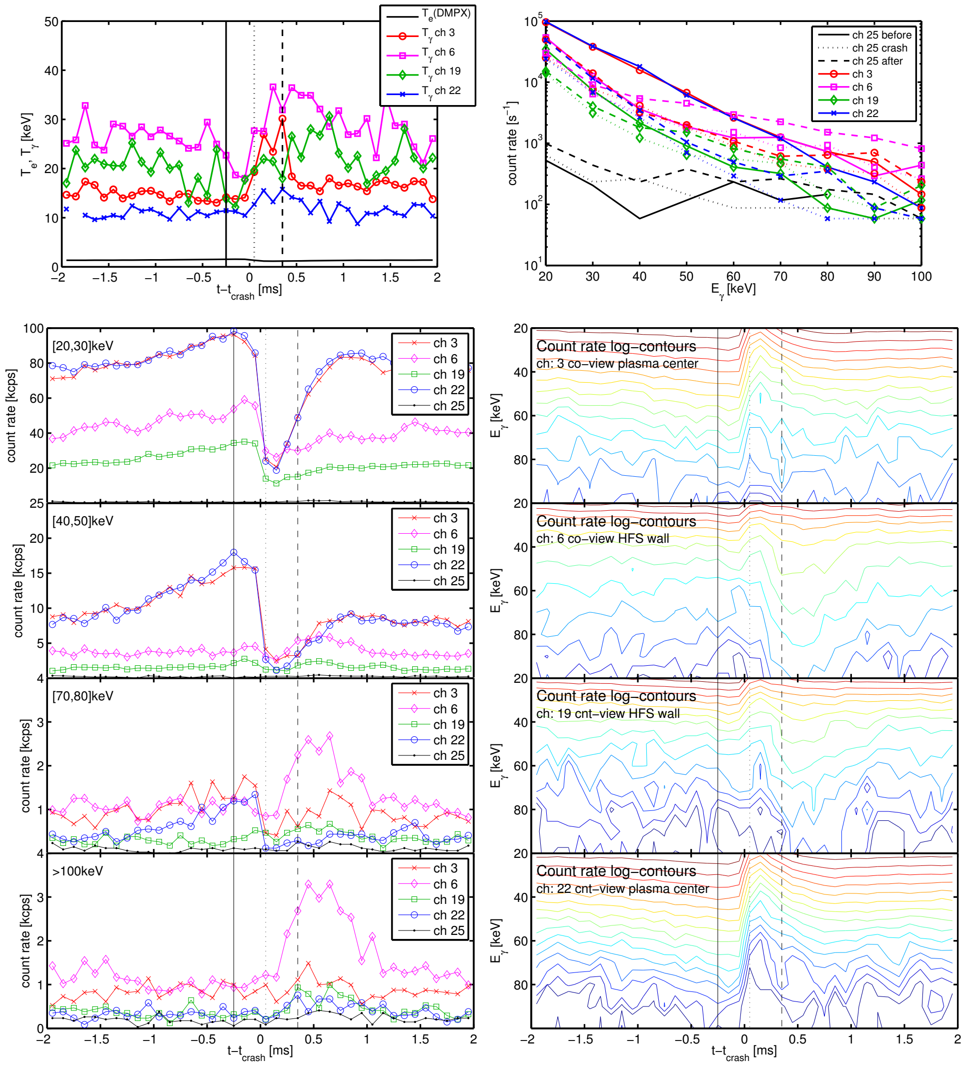

Figure 7.8: Time evolution of the HXR signal in the tangential chords 3 (co-I_p view on plasma center), 6 (co-view on HFS wall), 19 (counter-I_p view on HFS wall), 22 (cnt-view on plasma center) and 25 (blind detector; background) in the cnt-ECCD discharge 43206 (scenario T).
Top left: time evolution of the photon temperature (T_γ) compared to the bulk temperature (T_e) from DMPX; vertical lines indicate the time points for the top right plot: HXRS spectrum on the chords before, at, and after the sawtooth crash (-0.25, 0.05, 0.35 ms w.r.t. t_{crash}); bottom left: count rate evolution in selected energy bins for the 5 HXRS channels; bottom right: spectral evolution for the 4 HXRS channels (without background ch 25).

half. Energies above 100 keV are even less affected, which is also reflected in the increase of T_γ during the crash. The lower statistics prevent a precise quantification at such high energy. Results on LHCD-created suprathermal tails at higher energy in giant sawteeth [166] suggest that electrons with relativistic $v_\parallel$ are hardly affected by sawtooth crashes. Due to larger $v_\perp$ in the case of ECCD, neoclassical effects play a larger role than in the case of LHCD and may explain why suprathermal electron loss is still observed at energies around 100 keV on TCV. Also there are very significant differences, e.g. shaping, between the TCV and Tore Supra [167] scenarios, prohibiting a quantitative comparison.
The signal on the chords observing the HFS wall nearly tangentially and crossing the plasma center at an angle of about 45 deg drops also significantly at the crash in the low energy range (20 − 30 keV), but hardly changes for $E_\gamma > 40$ keV. Interestingly, the relative drop depends, for all channel pairs, neither on the viewing nor on the current drive direction. This indicates a general suprathermal electron loss, probably depending on (parallel) momentum, during the sawtooth crash; in this phase, no signs of particle acceleration can be found in the HXR emission.

Post-crash dynamics

Immediately after the crash the HXRS measurement suggests more complex dynamics. In the co-ECCD case the forward emission at $E_\gamma > 40$ keV rises about twice as fast (0.4 ms) as the backward emission (0.8 ms) to a more than doubled emission. For cnt-ECCD this reheating is nearly equally fast in both directions (0.6 ms).
The co-view chord observing the HFS wall sees a quickly (0.2 ms) rising HXR burst at high energy, subsequently decaying with a time constant of about 0.6 ms. It is more intense for co-ECCD, where it is also observed by the cnt-view chord, at lower amplitude and energy.
There are only two intermediate chords and they do not cover the mid-radius position whose emission in scenario S clearly indicates transport. But the time scales agree, the transport to the limiter occurs within 0.2 ms, i.e. at $\gtrsim 1.2\,{}^{km}/_{s}$, corresponding to $\chi_{se} \gtrsim 200\,\mathrm{m^2 s^{-1}}$. The slight time shift in energy hints that it may be on the slower side for electrons with higher $v_\parallel$.
In contrast to the crash phase, now particle acceleration also seems to play a role: the emission above 100 keV rises beyond the pre-crash value in the chords observing the plasma center. Due to the low statistics, however, the acceleration cannot be quantified, but one observes that the accelerated particles are also quickly lost.

7.2 Suprathermal electron interaction with the bursty mode

In TCV EC-heated plasmas an internal $m/n = 1/1$ kink mode that occurs in bursts in between sawtooth crashes is often observed and closely connected to suprathermal electron dynamics.

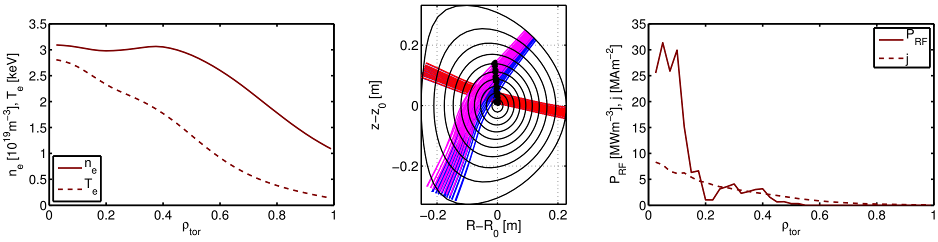

Figure 7.9: n_e and T_e profiles (left), ray-tracing (middle), RF absorption and current profiles (right) in the bursty mode scenario T (43618, pure ECRH).

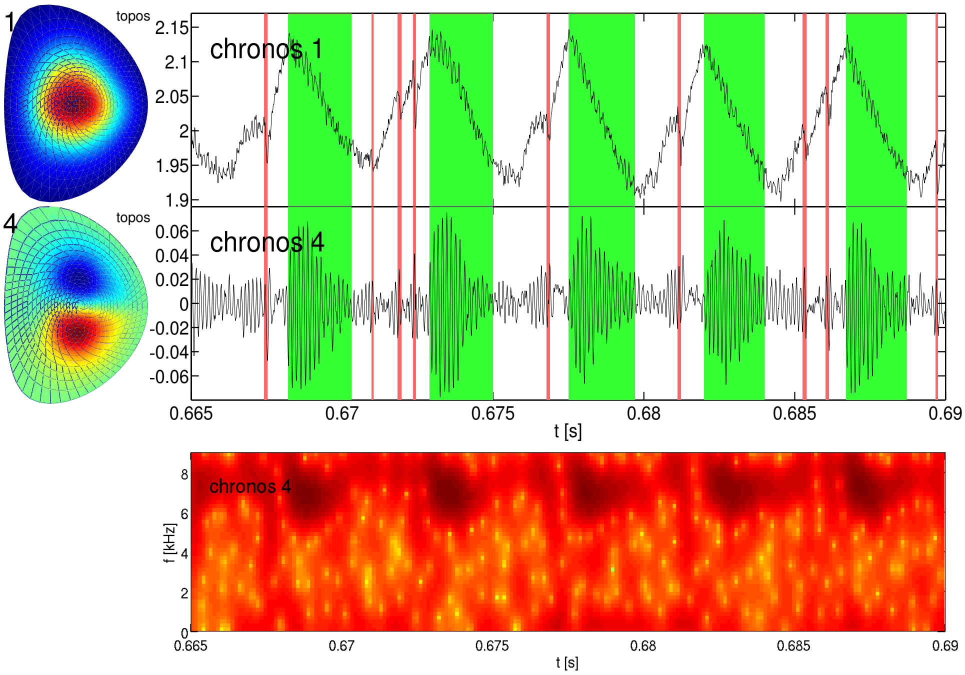

Figure 7.10: Evolution of the bursty mode in scenario T with pure ECRH: the main SXR emission is shown in topos and chronos 1 (top), and the $m = 1$ mode is represented by the topos-chronos pair 4 (middle). The red and green areas indicate sawtooth crashes and mode bursts, respectively. The spectrogram of chronos 4 (bottom) shows the frequency evolution of the mode.

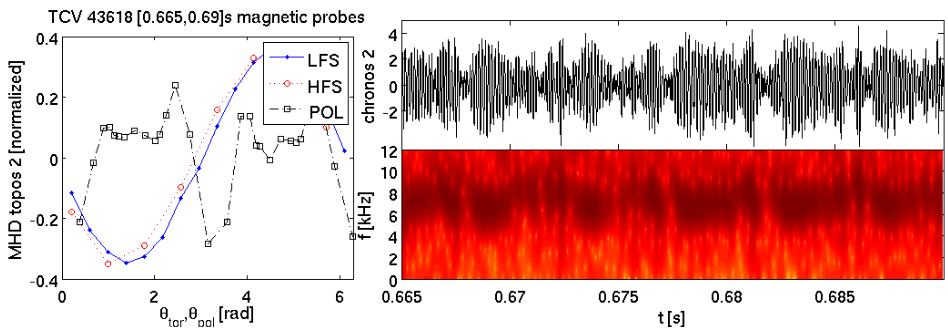

Figure 7.11: Bursty mode evolution in the SVD of the Mirnov coil (magnetic probe) arrays in scenario T.

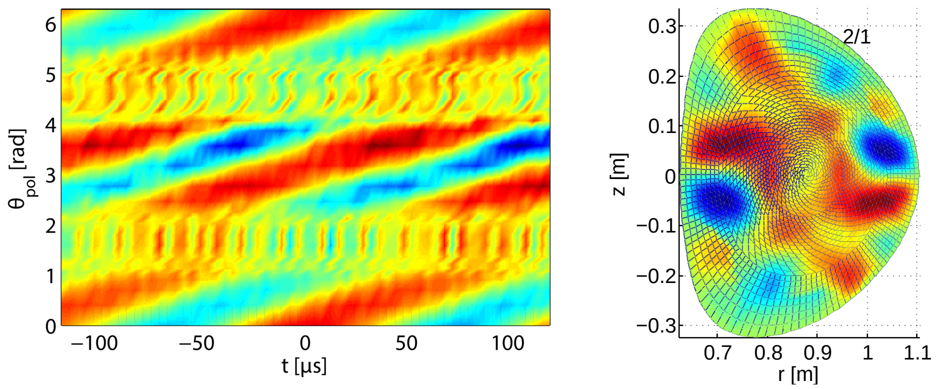

Figure 7.12: The evolution of one bursty mode period in scenario T on the poloidal Mirnov coil array (left), obtained with conditional averaging at time points from peak detection in SVD chronos from GTI XTOMO, shows the $m = 2$ component.
The subtraction of $m = 1$ from the GTI XTOMO SVD topos (right) reveals this $m = 2$ component also in the SXR data.

7.2.1 Bursty mode dynamics overview

The mode and its interaction with suprathermal electrons was first studied in scenario T with pure ECRH (Fig. 7.9) and low $n_{\parallel}$ ECCD. An optimized ECCD deposition profile in scenario D (Fig. 7.13) increases the mode amplitude.

Scenario T

In the triangular plasma scenario T, central ECRH is applied with some additional off-axis heating (Fig. 7.9). During the heating phase mode bursts are observed on the SXR (XTOMO) and MHD spectrograms.
The evolution of the mode (Fig. 7.10) is related to sawtooth crashes, but it is neither a pre- nor a post-cursor. In the phases between the bursts of ≈ 2 ms length, one or more sawtooth crashes are observed. A first sawtooth crash occurs $1-2$ ms after the mode burst vanishes; if it happens rather early more sawteeth can follow before the next burst phase, while a rather late sawtooth has more impact and is not followed by others before the mode recurs. After a single late sawtooth or the last sawtooth of a series, the central SXR emission rises to a value that is significantly higher than the top of the sawtooth cycle. During this rise, which lasts for less than 1 ms, no mode activity is observed in the SXR signal.
At a certain point, the $m/n = 1/1$ mode is destabilized and grows within one or two oscillations ($f \approx 7$ kHz) to its maximal amplitude. Its impact on confinement is traced in the now decreasing central SXR emission. The amplitude of the mode hardly changes in the first half of the burst (after its sudden rise), before it decreases, while the mode frequency remains constant for the entire burst duration (Fig. 7.10).

On the Mirnov coil arrays (Fig. 7.11), the SVD of the toroidal arrays observes a toroidal mode number $n = 1$, as expected for the $m = 1$ mode. The poloidal

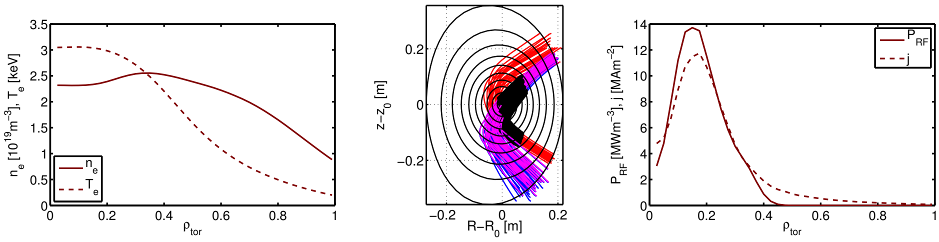

Figure 7.13: n_e and T_e profiles (left), ray-tracing (middle), RF absorption and current profiles (right) in the bursty mode scenario D (49315, co-ECCD).

array, however, shows two peaks, therefore $m = 2$. While the frequency is equal, the time evolution also differs significantly from the XTOMO (SXR) observation: the $m/n = 2/1$ mode persists and its amplitude varies irregularly, not in periodic self-similar bursts.

Nevertheless, the two modes are closely related. Since the mode frequency is the same, one can perform conditional averaging of the poloidal Mirnov coil array based on the GTI XTOMO SVD chronos (Fig. 7.12). It shows again the observation of $m = 2$ by the poloidal probes and also means that the modes (or mode components) are in phase, even over multiple bursts.

To eliminate the dominant modes in each of the two diagnostics, we make use of the principle that a rotation of a poloidal signal by $\Delta\theta_{\text{pol}} = \pi$ (half a turn) keeps the even m components unchanged, while the odd components are inverted. The sum of the poloidal Mirnov array and its rotation therefore removes the main $m = 2$ feature. Still, no $m = 1$ component is revealed: very likely its magnetic perturbation is well shielded due to the very central location of the mode. In contrast, the difference of the GTI XTOMO SVD topos to its half a turn rotated counterpart eliminates the $m = 1$ component and unfolds the further off-axis $m = 2$ mode structure. Its SXR amplitude is clearly weaker due to the generally lower emission at its location as compared to the central $m = 1$ structure.

Scenario D

In scenario D, with co-ECCD located close to the $q = 1$ surface (Fig. 7.13), the bursty mode occurs again (Fig. 7.14). It shows essentially the same time evolution and spatial structure, and the frequency is only slightly shifted upwards. However, the amplitude of the mode is greatly increased, leading to a drop of central SXR emission (confinement) of about 15 %. Also, the (absolute and relative) signal drop in the preceding sawtooth crashes is reduced.

7.2.2 Suprathermal electron dynamics during bursts

The central $m/n = 1/1$ component of the bursty mode has a significant effect on the e.d.f. in the thermal range that appears in the SXR emission. The effect on the suprathermal tail of the high RF power deposited in the plasma core is studied with the HXRS diagnostic. Conditional averaging over $\gg 2000$ mode oscillations (4565 in the scenario T discharge) is performed to achieve sufficient time resolution. The reference times are obtained from the peaks in the first chronos of

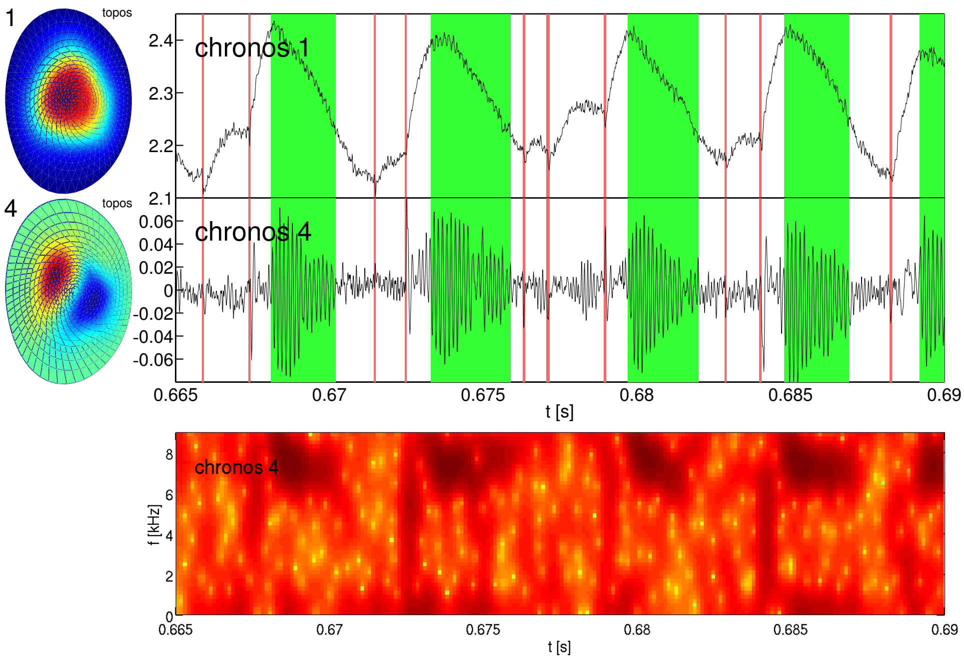

Figure 7.14: Evolution of the bursty mode in scenario D with slightly off-axis ECCD: the main SXR emission is shown in topos and chronos 1 (top), and the $m = 1$ mode is represented by the topos-chronos pair 4 (middle). The red and green areas indicate sawtooth crashes and mode bursts, respectively. The spectrogram of chronos 4 (bottom) shows the frequency evolution of the mode.

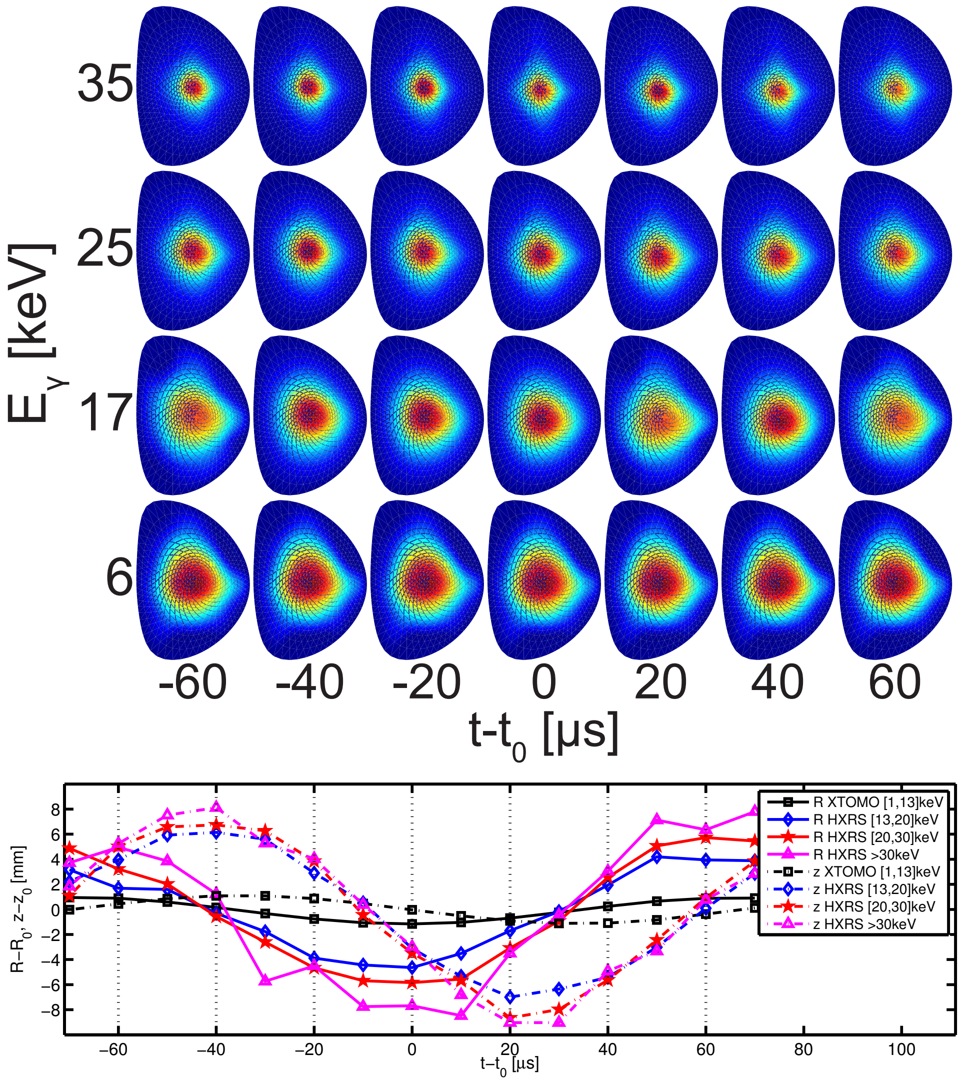

Figure 7.15: Tomographic inversion of X-ray emission in the poloidal plane in 4 energy bins at several times in a mode period and the evolution of the emission center (1st moment) in R and z direction during a mode period.

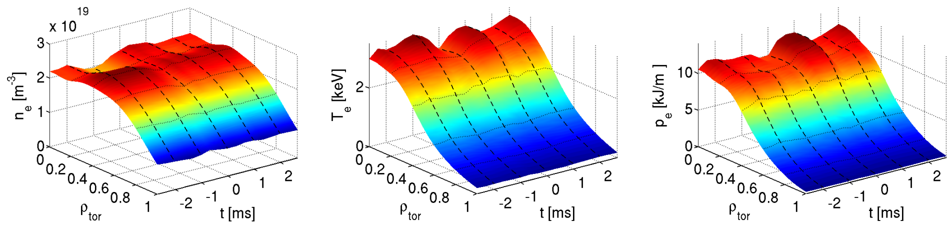

Figure 7.16: The evolution of n_e (left), T_e (middle) and p_e (right) measured by TS, conditionally averaged w.r.t. the start of the p_e rise ($t = 0$) after the last mode-preceding sawtooth crash ($t \approx 0.4\,\text{ms}$); the mode burst occurs in $t = [0.2, 1.3]\,\text{ms}$.

the SVD corresponding to the frequency band filtered tomographically inverted XTOMO data, which is available at a sampling rate of 100 kHz. Due to the large number of reference times, the HXRS statistics increase by a factor of more than 1000, such that the same time resolution as the XTOMO (10 μs) is attained.
Since non-axisymmetric structures in the plasma (the bursty mode) are slower than such a high time resolution, the assumption of toroidal axisymmetry in the X-ray emission breaks down. This causes no difficulties for XTOMO, whose cameras are located in the same sector (#11) of the machine. The HXRS cameras 2 and 7, however, are located in sector 4, while camera 5 was installed in sector 9. Therefore, a standard tomographic inversion does not give correct results, since the cameras observe the non-axisymmetric structures at different toroidal locations. Fortunately, the toroidal mode number $n = 1$ and the helicity, rotation direction and frequency of the mode are known. Using this information, the difference in toroidal angle ($\Delta\phi$) corresponds to a time shift

$$\Delta t = \sigma \frac{n\Delta\phi}{2\pi f}, \tag{7.1}$$

where f is the mode frequency (f_{mode}) and $\sigma \in \{\pm 1\}$ is a sign depending on helicity and rotation direction. In the present case, Δt is applied on the raw data time traces of the individual HXRS cameras depending on their position w.r.t. sector 11 (XTOMO). Conditional averaging of this time-shifted HXRS data reproduces the HXR emission of $n = 0$ and $n = 1@f_{\text{mode}}$ structures as if the HXRS cameras were all located in the XTOMO sector. Therefore, standard tomographic inversion of this modified data produces a correct result.
As shown in Fig. 7.15 for scenario T, the radial excursion of the first moment of the HXR emission pattern in the poloidal plane is much larger than in the SXR range, both exhibiting the $m/n = 1/1$ structure; an $m = 2$ component is not observed. The excursion in the HXR range increases further with photon energy (E_γ).
In summary, the suprathermal electron population is significantly affected by the mode, and this is more pronounced at higher energies.

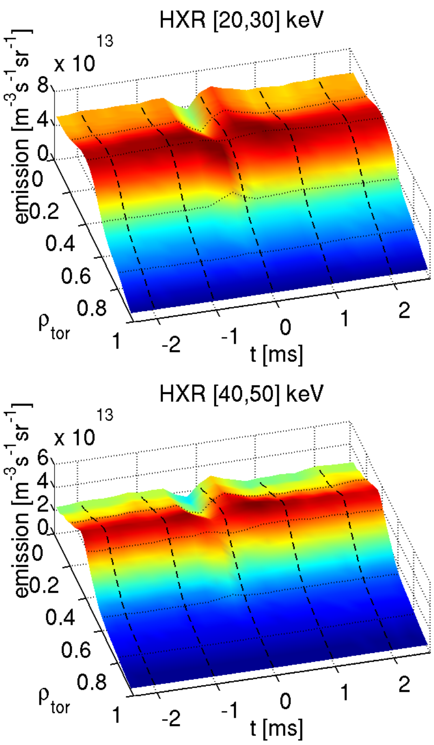

Figure 7.17: The evolution of radial HXR emission profiles in different energy bins (top left and right and bottom left) and the deduced $T_{e,2}$ profile (bottom right), obtained from HXRS measurements by conditional averaging w.r.t. the start of the p_e rise ($t = 0$) after the last mode-preceding sawtooth crash ($t \approx 0.4\,\mathrm{ms}$); the mode burst occurs in $t = [0.2, 2.2]\,\mathrm{ms}$.

7.2.3 Mode excitation

To study the stability and excitation of the bursty mode, the phase after the last preceding sawtooth crash is crucial. Therefore, we put $t = 0$ in the middle of this phase, corresponding to the start of the electron pressure (p_e) rise. Conditional averaging (and shifting) w.r.t. this reference times delivers n_e, T_e and subsequently p_e profiles from TS at a sub-ms time-scale (Fig. 7.16). The time evolution of these profiles is additionally verified by a cross-check with tomographic inversion of FIR and DMPX data. The same conditional averaging is performed on the HXRS data in order to derive an estimate of the corresponding suprathermal electron pressure (p_{se}) profile (Fig. 7.17). In conjunction with the typical q profile evolution during sawtooth cycles, the bursty mode excitation and evolution can be explained as follows.

The last burst-preceding sawtooth crash flattens the central q profile and increases q_{min}. Suprathermal electrons are, as generally observed for sawtooth crashes, ejected from their slightly off-axis peaked location at the $q = 1$ surface. Meanwhile, $T_{e,2}$ and the thermal profiles do not change significantly.

After the expulsion of some of the suprathermal electrons, the suprathermal electron population grows rapidly and broadly in the whole plasma center, up to $\rho_{\mathrm{tor}} \approx 0.35$. As already observed for sawteeth in the intermediate regime (Sec. 7.1.3), the suprathermal electron pressure rises more rapidly than its thermal counterpart during a phase in which the q profile is still flat in the center. While the insufficient T_e and the elevated q_{min} prolong the stability against a sawtooth crash, the suprathermal electrons, aided by the flat central $q \approx 1$, already destabilize the bursty mode. The importance of strong coupling to the present $m = 2$ component under these q profile conditions may also play a major role in the excitation of the $m = 1$ burst [168, 169].

Due to its impact on confinement, the mode then reduces $T_{e,0}$ and prevents sawtooth crashes during its whole duration. Since the mode mainly drags the suprathermal electrons around, rather than ejecting them from its habitat, the mode persist. Ultimately, due to diffusion of the I_p profile, the central q drops again, reducing the mode drive and therefore its amplitude.

After the mode has diminished, q_{min} - by then significantly reduced - and the adequate present p_e destabilize a sawtooth crash. Especially crashes with small amplitude seem to be insufficient to produce the conditions required for a destabilization of the bursty mode, e.g. regarding the rise and flattening in q (possibly incomplete reconnection). Hence, they can be followed by one or more sawteeth, eventually re-establishing the bursty mode destabilization.

7.3 Conclusions

The suprathermal electron dynamics during the sawtooth cycle are dominated by the impact of the sawtooth crash. Depending on n_e (E_D/E_ϕ), a low and a higher density regime can be distinguished. The intermediate regime can be efficiently studied with the HXRS and exhibits characteristics of both limits. As in the high density case, the suprathermal electrons show a similar behavior as the thermal electrons, the slow rise in between crashes is followed by a fast loss of electrons

during the crash. This is observable up to energies of 100 keV and the outward transport decreases only marginally with energy in this range.
As in the low density case, high energy electrons are transported to the limiter and emit bursts of thick-target bremsstrahlung radiation.
Immediately after the crash, the lower energy part of the suprathermal tail is reheated faster than the thermal and higher energy e.d.f.. Electron acceleration by magnetic reconnection cannot be explicitly observed, but it is conceivable that some electrons are accelerated to runaway energies and undergo such a low number of collisions in the plasma that only their bremsstrahlung emission from the limiting wall can be measured.

The bursty mode is an internal $m/n = 1/1$ kink mode coupled to a $m/n = 2/1$ mode and connected to sawtooth crashes. It has a significant impact on overall confinement and drags the suprathermal electrons around, with a higher radial excursion of the first moment than the thermal electrons. Its excitation can be explained by the coupling to the persistent $m = 2$ component under the flat $q \approx 1$ profile condition after a sawtooth crash. Furthermore, the destabilization of the mode seems to be connected to the faster reheating of the suprathermal electron distribution at the mode location as compared to the thermal e.d.f.. Also, this probably stabilizes the sawtooth until the appearing mode burst reduces confinement and therefore then lowers the sawtooth-destabilizing p_e.

Chapter 8

Electron fishbone studies

Electron fishbones are, as introduced in Sec. 1.5.2, an MHD instability in the plasma center, typically $m/n = 1/1$, that is non-resonant (does not require $q = 1$) and is excited by the resonant interaction with drift-reversed suprathermal electrons. A complete characterization and theoretical description of this mode, which was discovered only recently [47] but may have significant impact on the understanding of ion fishbone instabilities in future fusion reactors, is still missing.

For such a step forward, an experimental study using flexible high power density electron heating and current drive for current and pressure profile tailoring, combined with high-resolution suprathermal electron diagnostics, is required to put the pieces together.

TCV features such a high performance ECRH/CD system and also unprecedented suprathermal electron measurement capabilities (mainly HXRS). In addition, it provides a set of additional state of the art diagnostics, including XTOMO, DMPX, magnetic probes and also ECE diagnostics. The lack of q-profile measurements is the most significant shortcoming. This drawback, however, can be overcome by using sawteeth as an indicator of the presence and location of a $q = 1$ surface. Experiments at TCV may therefore contribute significantly to the understanding of the fishbone excitation process and the influence of fishbones on the suprathermal electron distribution.

8.1 Design of the experiment

The search for the electron fishbone was performed along three paths, partly in parallel. First, experiments were based on past discharges in which bursty $m/n = 1/1$ modes had been observed, optimizing them towards electron fishbone conditions. Then, another type of (much older) TCV discharges where fishbone-like signals appeared on the magnetic probes, but at too low resolution to draw any solid conclusions, were repeated in order to investigate the same plasma with improved diagnostic capabilities. In parallel, two scenarios based on theoretical predictions and experiments on other machines were conducted: one used negative triangularity plasmas at low elongation and the other was based on circular plasma discharges.

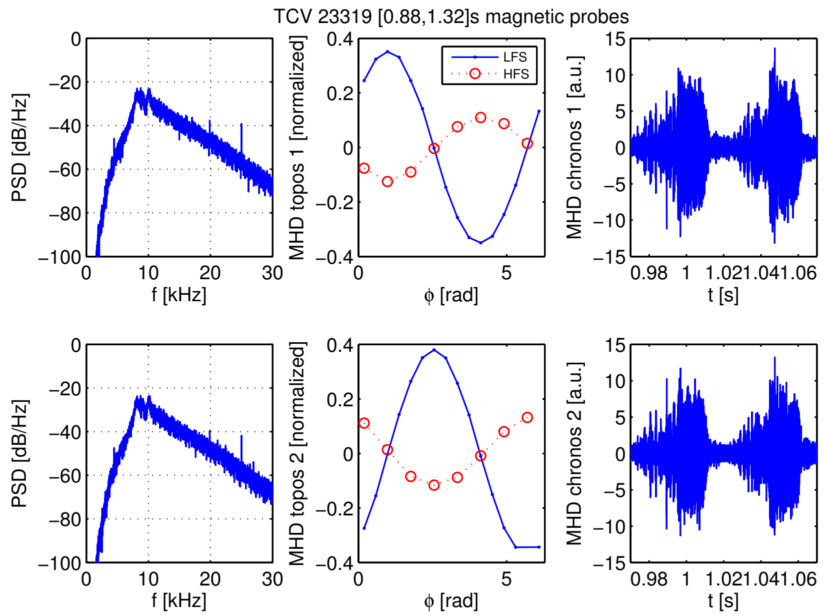

Figure 8.1: MHD observation of the magnetic probe arrays in TCV discharge 23319: power spectral density of the chronos (left), topos (middle) and chronos (right) of the first two topos-chronos pairs of the LFS array SVD (blue). The least-squares fitted topos (w.r.t. the LFS chronos) of the HFS array are also shown (middle, red).

8.1.1 Bursty mode observations

In several TCV discharges a bursty $m/n = 1/1$ mode was observed together with a correlated $m/n = 2/1$ mode at the same frequency (Sec. 7.2, [79]). In these observations sawteeth are present. Although the bursty behavior is reminiscent of electron fishbones, the bursty mode frequency stays constant throughout its entire evolution. This is in contrast to the frequency chirping of electron fishbones that is observed in other tokamak experiments and predicted by theory (Sec. 1.5.2). Nonetheless, there may be some connection between these two bursting $m/n = 1/1$ instabilities. In order to investigate this, the bursty mode discharges are modified according to electron fishbone theory: B_ϕ is reduced for off-axis ECRH on the HFS and I_p is reduced and ramped such that $q_{\min}$ crosses 1 from above.

8.1.2 Observations in historic TCV discharges

As discussed above, one approach to fishbone experiment design was to check the whole TCV database for past discharges with signatures of electron fishbones. First, a pre-selection using the Alma database was made for shots with a line-averaged electron density $(n_{e,\text{l.avg.}}) \lesssim 2.5 \cdot 10^{19}\,\text{m}^{-3}$, $q_{\min} \approx 1$, low normalized internal inductance (l_i) (corresponding to a broad current profile) and X2 heating off-axis on the HFS ($B_\phi < 1.4\,\text{T}$). Then, the MHDxSVD snapshots of these discharges were browsed to capture signatures that resemble those expected for

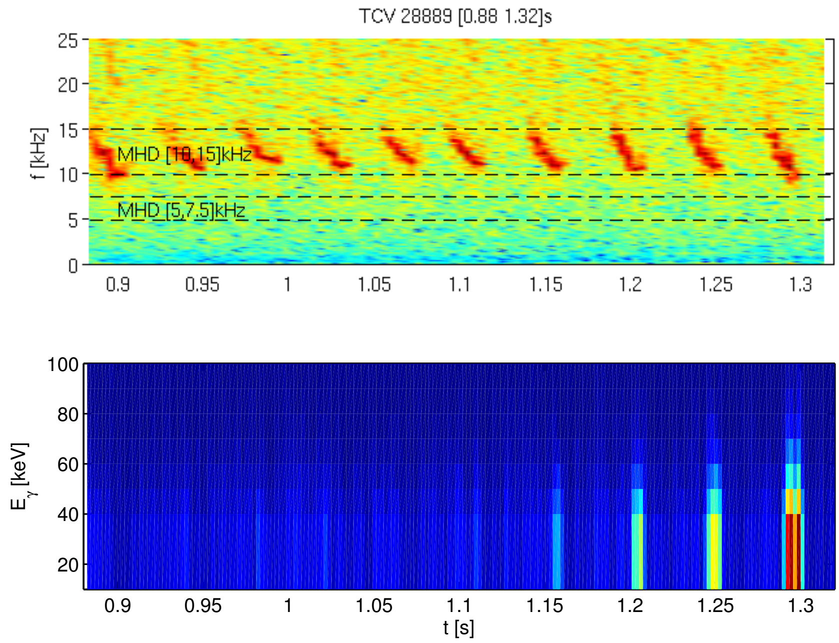

Figure 8.2: MHD spectrogram of a LFS magnetic probe (upper) and the correlated HXR observations of the HXRC (lower plot) in TCV discharge 28889.

electron fishbones according to observations on other tokamaks and theory. Here, also the criterion of frequency chirping was included, excluding the bursty mode discharges of the first approach.

The result of this database scan was that no clear evidence of electron fishbones was found in previous shots. However, in the two similar discharges 23319 (Fig. 8.1) and 28889 (Fig. 8.2) regular bursts of frequency chirping $n = 1$ modes were present, as observed by the toroidal magnetic probe arrays. Also, the HXRC detected HXR bursts at the mode termination which may be a sign of interaction of the mode with the suprathermal electron population. Unfortunately, the poloidal array data quality is too poor in these discharges to give conclusive information on the poloidal mode number m. Also, the XTOMO provided only a time resolution of 0.1 ms for these old shots, limiting the SXR mode analysis to 5 kHz. Therefore, a repetition of these shots proved necessary to clarify the observations.

8.1.3 Theory-based scenarios

In an other approach, the most promising scenarios for electron fishbones in TCV were developed from observations on other tokamaks and from theory based on those experiments (Sec. 1.5.2). Two paths, one with a circular shape and another one with low-κ negative-δ shape, were pursued, in order to maximize the population of barely trapped electrons and the depth of their drift reversal. The remaining parameters are similar: X2 heating is localized on the HFS in a co-ECCD configuration, with the minor radius being scanned in B_ϕ steps from shot to shot. This yields the required off-axis peaked pressure profile and a flat or slightly reversed q-profile due to co-ECCD and optional additional central cnt-ECCD.

	43618	48068	48069	48070
t_0 [s]	0.6	1.55	1.85	1.35
duration [s]	>0.5	0.2	0.3	0.2
final burst duration [s]	-	0.05	0.1	0.05
$n_{e,0}$ $\left[10^{19}\mathrm{m}^{-3}\right]$	3.1	6.0	5.3	6.9
$T_{e,0}$ [keV]	2.3	800	840	830
P_{ECRH} [kW]	1820	1300	1300	1300
ECCD inj. angle [deg]	0	0	+20	+20
$B_\phi(R=0.88\,\mathrm{m})$ [T]	-1.44	-1.32	-1.32	-1.32
I_p [kA]	-268	-218	-196	-180
$\frac{dI_p}{dt}$ $\left[\frac{\mathrm{kA}}{\mathrm{s}}\right]$	0	-92	-64	-41
$f_{1/1}$ [kHz]	7.0	$7.7\to6.2$	$8.2\to6.9$	$8.5\to7.4$
ρ_{tor}	0.35	0.2	0.2	0.2

Table 8.1: Main parameters of a series of discharges designed for electron fishbone studies (48068–70) based on the bursty mode scenario (represented by shot 43618). The time refers to a representative point in time during the mode appearance.

The q_{min} is ramped from above one through $q_{\mathrm{min}} = 1$ to below one and back by ramping I_p. The appearance of sawteeth indicates that the safety factor has dropped below one. I_p has to be kept quite low due to the constraints in q and the rather low B_ϕ. The resulting T_e (ohmic preheating) is just sufficient for initial X2 absorption if n_e is comparably low. Such low n_e is also advantageous to increase the fraction of suprathermal electrons, and subsequently the fraction of trapped energetic electrons.
The scenario is, due to this low n_e requirement, closely bounded by the threshold for significant runaway production and the threshold for good initial X2 absorption. The latter is the bigger concern, since X2 waves that are only partially absorbed and can thus escape the plasma may trigger the window protection system and shut down the gyrotrons; however, runaways are an issue for the HXRS and even SXR diagnostics signals (saturation).

8.2 Results

8.2.1 Bursty mode scenarios

As discussed above, a series of discharges based on the bursty mode scenario but modified for electron fishbones were performed. The main changes w.r.t. the bursty mode discharges was the EC resonance position on the HFS (reduced B_ϕ) and a lower, ramped I_p, to cross $q_{\mathrm{min}} = 1$ from above.

Mode observations

In most such discharges, covering different n_e, EC heating location and CD component, no fishbone-like modes are observed. A series of three consecutive dis-

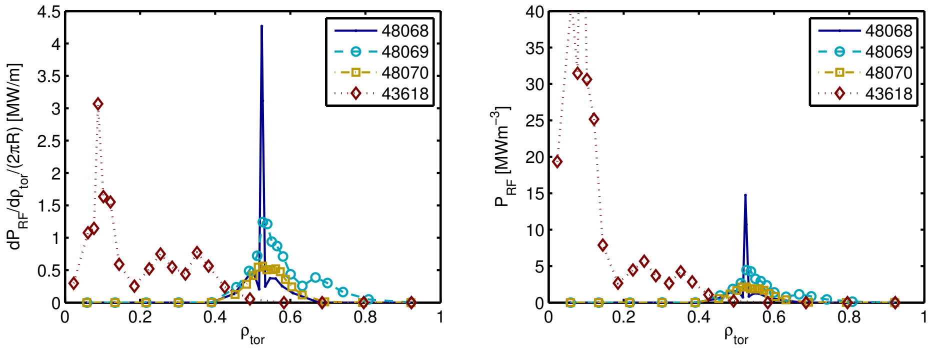

Figure 8.3: ECRH power deposition profiles as computed by LUKE for the shots and times listed in table 8.1; left: radial power per unit length, right: power density.

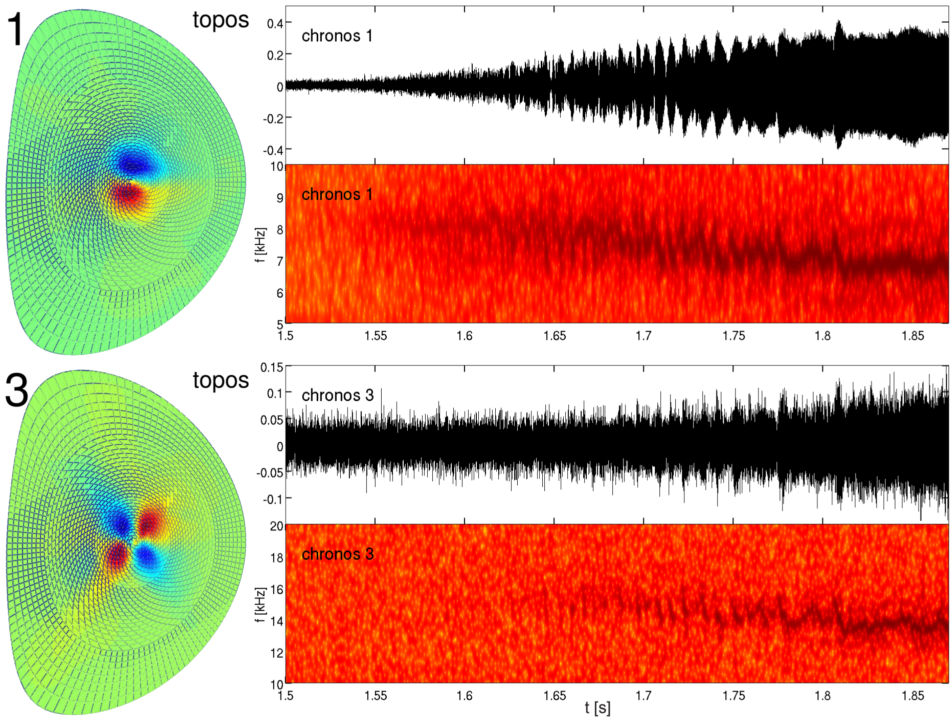

Figure 8.4: Selected XTOMO topos and chronos of TCV discharge 48069 showing the spatial structure in the poloidal plane (left), the time evolution of the amplitude (middle) and the frequency evolution (right) of the bursts. A high-pass filter (2500 Hz) is applied after the tomographic inversion right before the SVD analysis.

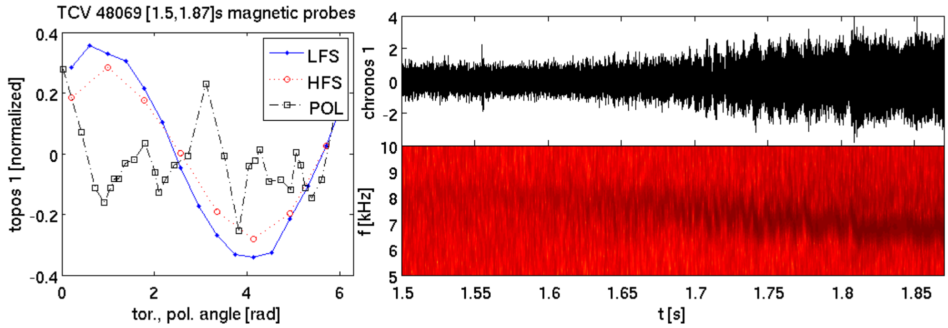

Figure 8.5: The first LFS magnetic probe array topos (left, blue) and chronos (middle) of TCV discharge 48069 show the toroidal mode structure and the time evolution of the amplitude. The spectrogram of the chronos (right) shows the frequency evolution of the bursts. Additionally, the least-square fitted topos of the HFS (red) and the poloidal (black) magnetic probe arrays are shown in the left plot.

charges (48068, 48069, 48070), however, show an interesting $m = 1$ mode that could be a candidate for electron fishbones. It occurs together with a $m = 2$ mode at double frequency, in the current ramp phase just before the first sawtooth appears. The three shots are very similar, with only two significant differences: first, in 48068 pure ECRH (no ECCD) was applied while for the following shots the EC waves were injected at an angle of 20 deg for co-ECCD, in all cases at the same far off-axis radial location ($\rho_{tor} \approx 0.55$) on the HFS (Fig. 8.3). Secondly, from one shot to the other, the current ramp rate ($\frac{dI_p}{dt}$) was reduced in order to decrease q_{min} more slowly and enable a longer phase during which the mode may develop. The time points at the end of this phase (t_0), just before the first sawtooth, are listed in Tab. 8.1, together with the most important plasma parameters.
During this phase, until t_0, I_p and n_e rise at constant rates while T_e drops slowly. Due to the increasing n_e the refraction of the EC waves is enhanced, moving the resonance location slowly radially outwards and decreasing the absorption.
First, weak bursts of $m = 1$ oscillations are registered in SXR measurements (Fig. 8.4). They are correlated to $n = 1$ oscillations in the toroidal magnetic probe array (Fig. 8.5). The bursts become stronger over time and persist for a duration of 0.2-0.3 s (Tab. 8.1). A weaker $m = 2$ multiple at the same radial position ($\rho_{tor} \approx 0.2$) is seen by XTOMO after a delay, but then develops in time in a similar way as the fundamental (Fig. 8.4).

Frequency evolution

The bursts are chirping in nature, with frequency decreasing within the burst; additionally, the mean frequency of the bursts decreases slowly from the first appearance to the last (at t_0). The frequency change within the bursts are electron fishbone like, but the time-space resolution of the SXR diagnostic is not sufficient to determine if the frequency chirping accompanies a radially outward displacement. The slow change of the mean frequency, however, may be attributed to the

evolution of the plasma. This is also consistent with the precession frequency of the barely trapped electrons being proportional to their temperature [55]. Due to the increasing density and the consequently decreasing effectively deposited ECRH power, the temperature of these suprathermal electrons decreases according to Fokker-Planck simulations. An experimental verification of this temperature drop is not possible due to the statistics of the HXRS signal being far too poor.
The last mode appearance is much longer and differs from the previous bursts by having a rather constant frequency (final burst duration, Tab. 8.1). Also, the density rise stops at the final burst appearance, with T_e still dropping or staying at the same level. Later, these n_e and T_e levels remain limited by the sawteeth.

Conclusion

The final conclusion for this path is that the observed mode exhibits some characteristics attributed to electron fishbones, especially its time evolution including the frequency chirping and the appearance in the phase before the first sawtooth. However, the ECRH absorption takes place at $\rho_{\text{tor}} \approx 0.55$ while the mode is observed at $\rho_{\text{tor}} \approx 0.2$. Suprathermal electron transport might explain a spatial link, but the HXRS does not observe a significant suprathermal electron fraction at all. While high transport reduces the HXRS signal in general, negligible HXR emission also clearly means that the number of suprathermal electrons is very small.
Accordingly, the next step was to heat more centrally ($B_\phi = 1.35\,\text{T}$, still off-axis on the HFS, close to the expected mode location), resulting in a significant HXRS signal (suprathermal electron distribution). However, this approach did not reproduce any similar observations and was finally abandoned when the focus was placed on the two other, more promising paths, which are described in the following.

8.2.2 Revisitation of old TCV shots

A successful repetition of discharge 23319 was obtained with discharge 48438, after several optimization steps. The plasma and auxiliary heating parameters were closely matched (Fig. 8.6). The only significant difference, which however should not change the physics, is that both B_ϕ and I_p directions are reversed.
In the replica shot the historic observations (Sec. 8.1.2) were not reproduced.
Nonetheless, the experience gained during the scenario development, in combination with the results obtained in the previous chapters of this thesis, suggests an alternative explanation for the original observations.

Alternative explanation

First, in the bursty mode discharges the $m/n = 1/1$ mode is only observed by SXR, HXR and ECE diagnostics, but not by the magnetic probes that observe only the peripheral modes such as $m/n = 3/2$ and $m/n = 2/1$. Although the nature of electron fishbones is different from the bursty mode, both their radial location and

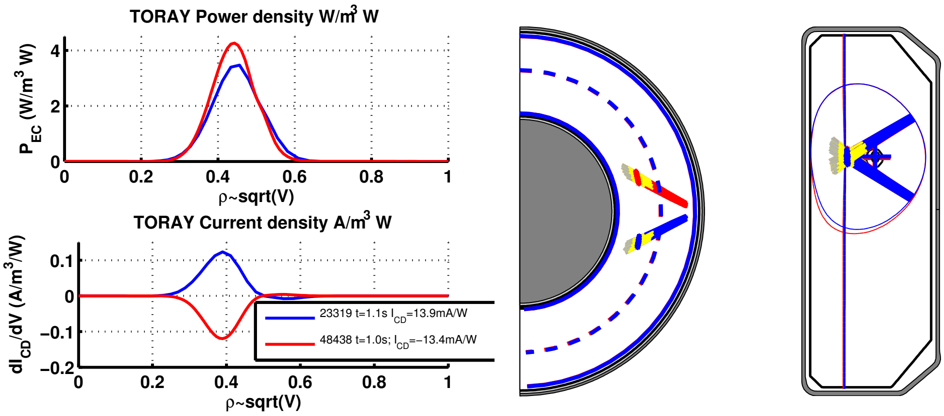

Figure 8.6: Comparison of TCV discharge 23319 (blue) to its repetition 48438 (red) showing the equilibria (right) and TORAY power absorption (top left) and ECCD computations (bottom left). Both I_p and B_ϕ are reversed, while their absolute values and all other plasma parameters are well matched.

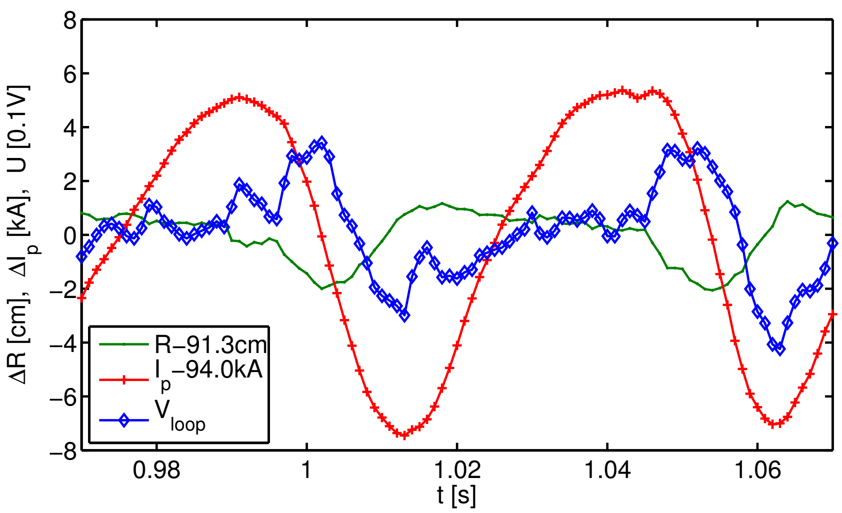

Figure 8.7: Radial oscillation of the magnetic axis position (R, green), I_p (red) and V_{loop} (blue) in TCV discharge 23319.

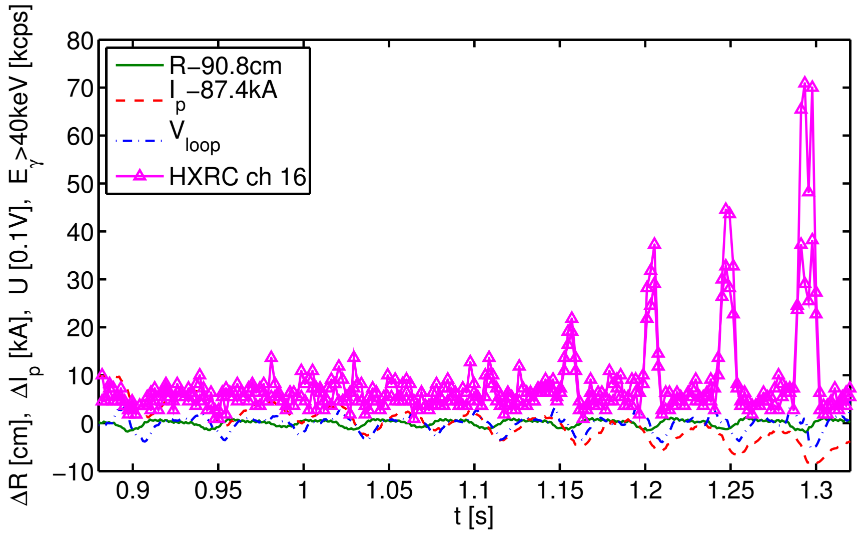

Figure 8.8: Radial oscillation of the magnetic axis position (R, green), I_p (red) and V_{loop} (blue) in TCV discharge 28889. The HXR bursts observed on HXRC chord 16 (magenta) occur when the plasma moves to the HFS wall.

magnetic field perturbation should be comparable. Therefore, it is unlikely that electron fishbones could be observed at all on the magnetic probes in TCV. The $n = 1$ mode signal in shots 23319 and 28889, however, is very clear in the LFS and HFS magnetic probe arrays, and, apart from the chirping, it corresponds well to standard $m/n = 2/1$ mode observations.

The chirping is explained by a slow ($\approx 20\,$Hz) oscillation of the radial plasma position due to a resonance in the feedback control loop. The old shots (23319 and 28889) were carried out in the fully non-inductive mode and at low density which both makes them more prone to such an oscillation. This affects the whole plasma significantly, as can be seen in the I_p and V_{loop} oscillations (Fig. 8.7). By contrast, shot 48438 was partly inductive and thus more stable radially.

The low density in the discharges leads to a significant runaway population, experimentally verified in 48438 by the signal of the blind HXRS detectors being at the same high level (and partially saturated) as all other HXRS detectors. This level of bremsstrahlung radiation remains rather constant in the replica shot. The radial oscillations in the old shots, however, lead to strong bursts in the HXRC signal when the plasma, and the runaways therein, touch the HFS limiting wall (Fig. 8.8). Consequently, the observed HXR bursts are not related to suprathermal electron - mode interaction, rather they originate in runaway electron transport towards the first wall due to bulk plasma movement.

Furthermore, this prompt radial displacement coincides with the mode termination and may be assumed to be responsible for that too.

Conclusion

In summary, the revisitation of the old shots was successful in the sense that the observations can be explained consistently by large radial plasma oscillations

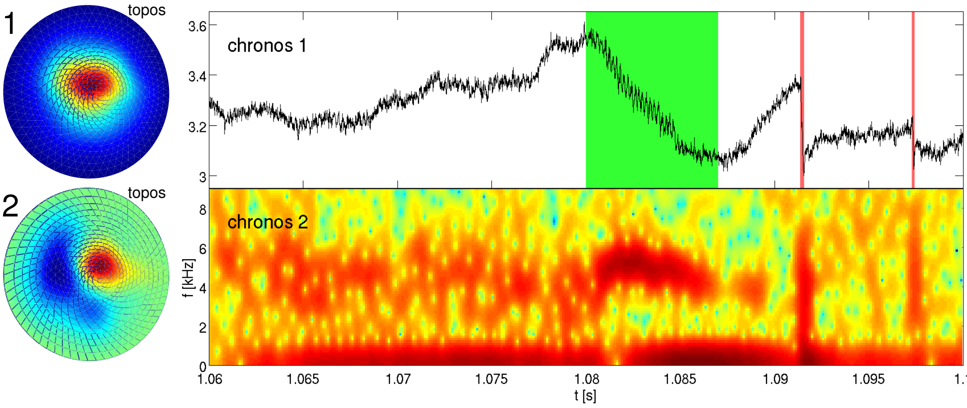

Figure 8.9: The first two XTOMO topos and chronos of TCV discharge 48440 showing the spatial structure in the poloidal plane (left), the time evolution of the amplitude in chronos 1 (top) and the frequency evolution in chronos 2 (bottom). The first chronos represents the background SXR emission profile and the second chronos the fishbone-like burst. The time interval of the burst appearance is indicated by a green area and the first two sawtooth crashes are highlighted by red areas in the first chronos plot.

and a $m/n = 2/1$ mode being affected by them. In the replica shot, well stabilized in the radial direction, there is no indication of electron fishbones.

8.2.3 Theory-based scenarios

Abandonment of negative triangularity scenario

The theory-inspired circular plasma scenarios exhibit the most striking observation of electron fishbone-like modes on TCV, whereas the parallel path of negative δ plasmas was also abandoned, for several reasons. The main problem was the small plasma volume, especially on the HFS. This made it practically impossible to absorb all injected ECRH power there, and triggered security interlock cuts of the gyrotrons by safety detectors on the vacuum windows hit by the EC waves. Also, the SXR diagnostics, essential for the detection of electron fishbone features, could not resolve the small plasma volume in a satisfactory way and were disturbed by strong spiky noise on several channels in this scenario. Therefore the focus was placed on the circular scenario instead.

Circular plasma scenario

First observation A repeat with a slower I_p ramp and better controlled, constant n_e ($n_{e,0} = 2\cdot 10^{19}\,\mathrm{m}^{-3}$) succeeds in TCV discharge 48440. On the XTOMO, a single fishbone-like burst, a $m/n = 1/1$ mode chirping down in frequency, appears at $t = 1.08\,\mathrm{s}$ when $q_{\min} \approx 1$, just before the first sawtooth (Fig. 8.9). It is also observed by the LFS ECE system, but not by the magnetic probes. The LUKE simulation shows a significant fraction of barely trapped (and passing) energetic electrons close to the mode location. Due to the low density, the HXRS measurement is polluted

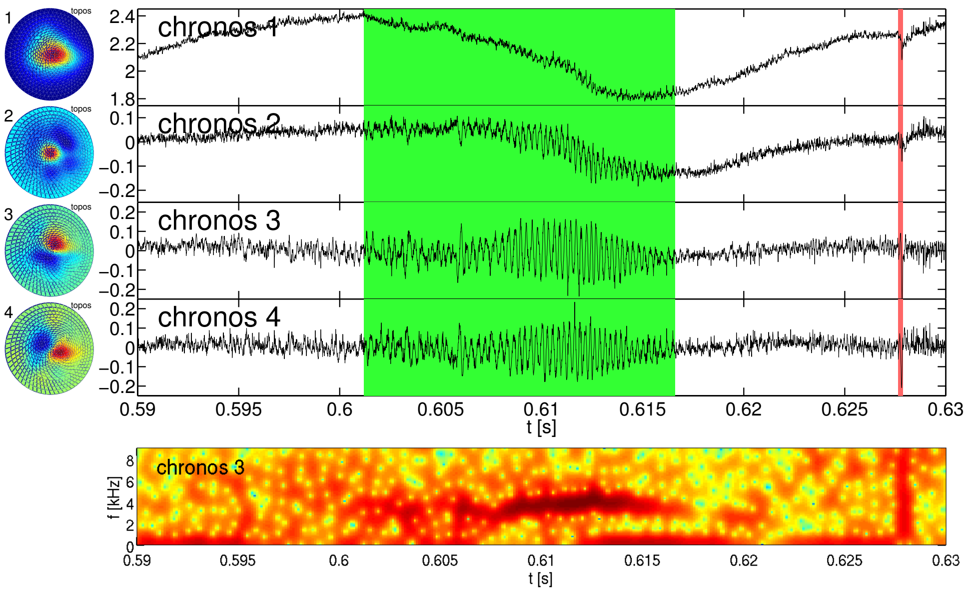

Figure 8.10: The first four XTOMO topos and chronos of TCV discharge 48442 showing the spatial structure in the poloidal plane (left), the time evolution of the amplitude (upper 4 plots) and the frequency evolution on the example of chronos 3 (bottom, same for chronos 4). The first chronos represents the background SXR emission profile and the pair of chronos 3 and 4 the fishbone-like burst. The time interval of the burst appearance is highlighted in green and the first sawteeth crash in red.

by radiation from runaway electrons and cannot be used to obtain experimental information on suprathermal electrons.

Optimization In order to prolong the phase when the mode appears, 48440 was repeated at a constant $I_p = 164\,\mathrm{kA}$. In this discharge, 48442, a similar burst appears on the XTOMO (Fig. 8.10) and LFS-ECE, also just before the first sawtooth, when q_{min} drops below 1. Although the total current remains constant, q_{min} decreases due to the q-profile evolution. So the burst is not significantly longer than before. Again, it is not repeated, as had been observed on other tokamaks. The LUKE simulation and the HXRS give also essentially the same result as in 48440.
In contrast to 48440, the frequency of the mode chirps upwards, which is unusual for electron fishbones.

Interpretation The oscillation in both experiments is very similar, except for the direction of the frequency chirping. Experimental observations on other tokamaks and theory tell us that electron fishbones chirp down in frequency because they are moving radially outwards and the temperature of the mode-driving electrons decreases.
In 48440 and 48442, however, the XTOMO shows that the radial extent of the mode shrinks slightly, by a few percent of ρ_{pol}. Since the Fokker-Planck simulation does not take any direct effects of the mode into account and there is no usable HXRS data, the evolution of the barely trapped (and passing) suprathermal electron population remains unclear. To be consistent with electron fishbone theory and observations on other tokamaks, the temperature of this population has to decrease in 48440, overcompensating the radial displacement, and increase in 48442. If the mode is not an electron fishbone, the differing frequency chirping direction could be explained by the different I_p and q-profile evolution.

Further experiments

Based on the very promising discharges 48440 and 48442, further discharges were performed in a later experimental session, aiming at lengthening the phase $q_{\mathrm{min}} \gtrapprox 1$ by slowly decreasing I_p. In theory, this should result in longer or even multiple bursts. Additionally, discharges with increased n_e were performed to prevent the generation of runaway electrons and obtain a useful HXRS measurement. However, none of these discharges showed any evidence of modes similar to those of 48440 and 48442. Moreover, even a straight repetition of 48442 in discharge 48717 could not reproduce the fishbone-like mode, although all plasma parameters were well matched.
This hints that the discharge conditions are such that the mode is only marginally unstable. Therefore, a few more experiments based on 48440 were planned, but with modified heating and current profile tailoring, aimed at finding a more unstable point in parameter space. Due to the limited number of shots at the end of the 2013 campaign it was not possible to conduct all planned experiments and the ones that were performed did not contribute further fishbone-like observations.

8.3 Conclusions

The three paths pursued in the electron fishbone study presented give mixed results.
In the shots based on the bursty mode scenario the expected frequency chirping is observed, but considerations such as the small suprathermal electron population and the gap between the heating and mode location suggest a different excitation mechanism for the observed $m/n = 1/1$ mode.
The revisitation of old shots with regular frequency-chirping bursts led to the finding that a large radial plasma oscillation was responsible for both the mode and HXR burst observations.
The theory-based scenario, finally, originated good candidates for electron fishbones. Lack of experimental data (HXRS polluted by runaways) and reproducibility prevent a definitive conclusion on the nature of the observed mode. Further investigation was limited by experimental time, but is to be continued in future campaigns at TCV.

Chapter 9

Conclusions

The main goals of this thesis were to characterize the (suprathermal) electron distribution in ECRH and ECCD and the interaction of suprathermal electrons with MHD instabilities. The phase space dynamics and open questions in the physics of ECRH/CD were addressed by dedicated experiments in TCV, which are analyzed primarily by HXR measurements and in conjunction with Fokker-Planck modeling. The analysis of suprathermal electron interaction with MHD instabilities focused on several categories of the $m/n = 1/1$ internal kink mode.

Tools

A set of advanced tools were required to perform these studies, and their development and implementation constitutes an important part of this thesis work. The first 3 cameras of the HXRS system were calibrated and installed on the tokamak. The system is unique in several respects:

- First HXR tomography with more than 2 cameras.
- First HXR tomography for non-circular plasmas.
- First HXR tomography and poloidal HXR asymmetry measurements of
  - EC-heated plasmas.
  - plasmas with non-circular poloidal cross section.
- First HXR spectrometer with toroidal coverage in both directions.
- Digital acquisition and pulse processing, enabling
  - optimal time, space and energy resolution.
  - coherent and conditional averaging for greatly increased resolution.
- Bulk W shielding and collimator, and blind detectors to ensure collimation.

An extensive study of digital pulse processing algorithms at high count rates was carried out in order to apply the optimal solution. Rather than implementing a single algorithm and highlighting its advantages over other algorithms described

in the literature, a broad and objective approach was chosen and a general benchmarking tool was implemented. This enabled the complete comparative analysis of all eligible algorithms from literature and original techniques, resulting in the choice of an optimal FIR filter and dynamic threshold detection [2].
The capabilities of this unique HXR diagnostic were enhanced by progressive data analysis methods and tools, inter alia conditional averaging and tomographic inversion. The latter was implemented in the modern GTI code, including advanced post-processing features such as SVD, which proved to be practical for MHD mode analysis. Further X-ray diagnostics were reactivated and/or improved. For modeling, the well-supported LUKE and the established CQL3D F-P codes were applied in parallel, with the attendant benefit of providing the first extensive benchmarking of these two codes. The interfaces to TCV data were newly implemented or refurbished, including the integration of the HXRS specifications into the synthetic HXR diagnostics. As for the diagnostics, flexible data analysis and visualization software was engineered.

Physics of ECRH/CD and suprathermal electron dynamics

With the well-equipped toolbox described above, the phase space dynamics in ECRH and ECCD were tackled by investigating toroidal and poloidal HXR emission asymmetries in well-thought-out dedicated experiments on TCV. The theory-predicted asymmetries in the forward and backward directions of I_p were experimentally confirmed for the first time, for co-ECCD and cnt-ECCD, scanning a large range of $n_\parallel$. While in general there is a good agreement of experimental data with modeling results, anomalous effects in the suprathermal tail that occur in some discharges at low density can be reproduced with the Fokker-Planck codes by an equivalent E_ϕ modification.
The impact of the magnetic field line helicity on the poloidal asymmetry was quantified by magnetic field reversal to up to a tenth of the change in B_ϕ/I_p at $E_\gamma = 50\,\mathrm{keV}$. With the effect separated, the phase space effects, mainly the opening of the passing particle cone towards HFS, were investigated. In the poloidal RF deposition location angle scan the asymmetry change due to this effect was found to be minor as compared to RF scattering. With this series of experiments, the effects of RF scattering and anomalous suprathermal electron diffusion (on the observed HXR emission broadening) were clearly separated for the first time, although discrepancies in absolute count rate remain. This result is of potentially great importance for NTM control, the main application of ECCD in present and future tokamak experiments, where the required highly localized current drive may be significantly disturbed by RF scattering at density fluctuations in the edge of the plasma [162]. Further experiments on poloidal HXR emission asymmetry, comprising scans of $n_\parallel$, I_p, κ and δ, confirm the generally good agreement of experiment and modeling.
Significant discrepancies still remain in the case of far off-axis RF deposition, because the attributed anomalous suprathermal particle pinch lies beyond the scope of the modeling capabilities. An analysis of QL effects showed linear HXR emission response to ECCD blips.

The result of a previous study, that suprathermal electron diffusion can explain the observed broad HXR emission profiles, was confirmed by revisiting the scenario with the improved diagnostic capabilities; in addition, the presence of runaway electrons that could invalidate the measurement was excluded. Furthermore, the current drive efficiency is modeled correctly by LUKE at the same transport parameters that reproduce the experimental HXRS data for $n_{\parallel}$ ranging from ECRH to maximal CD, whereas CQL3D estimates the total current wrongly in several cases.

Interaction of suprathermal electrons with MHD instabilities

The suprathermal electron dynamics related to sawteeth are dominated by the impact of the crash. The dynamics in low and higher density regimes are somewhat different, and can be studied efficiently in the intermediate regime providing energetic suprathermal tails and good HXR statistics. As in the higher density case, where the suprathermals mimic the behavior of the thermal electrons, a large fraction of fast electrons is lost due to the impact of the crash. This is observable with spatial resolution up to energies of 100 keV and only marginally decreases with energy. As in the low density case, highly energetic electrons are transported to the limiter (first wall) and emit bursts of thick target bremsstrahlung in the MeV range immediately after the crash. Electron acceleration by magnetic reconnection is not explicitly observed.
The effective reheating of the suprathermal tail in its lower energy region seems to play also an important role in the destabilization of the bursty mode, an $m/n = 1/1$ internal kink mode, in connection with coupling to a $m = 2$ component under the flat $q_{\mathrm{min}} \approx 1$ profile conditions provided by a preceding sawtooth crash. The mode has a significant impact on confinement, with the SXR emission being reduced by up to 15 % during the burst evolution.
The excitation of the electron fishbone instability proved more difficult than expected and was generally unreliable. Nonetheless, the obtained preliminary results are a promising starting point for further studies.

Main results and achievements

- Sophisticated tools were implemented and used for experiment design and data analysis, in order to investigate unexplored physical processes individually.
- Anomalous effects in the interplay of inductive and EC-driven electron acceleration at low density were quantified by an equivalent E_ϕ modification.
- Through a poloidal RF deposition location angle scan, the effects of RF scattering and anomalous suprathermal electron transport on the HXR profile shape were separated and characterized for the first time.
- Previous results [3] on anomalous suprathermal electron diffusion and current drive efficiency were reproduced with increased confidence arising from enhanced diagnostic specifications.
- The suprathermal electron dynamics during sawtooth crashes were analyzed in greater detail and especially time resolution than previous studies. The dynamics were found to be transport-dominated and forward acceleration cannot explicitly be observed.
- In low density discharges the suprathermal electron loss during sawtooth crashes was also found to cause energetic electron showers onto the limiter.
- Coupled bursts alternating with sawtooth crashes (CAS), the bursty mode, were characterized for the first time, giving new insight in mode coupling and the interaction of MHD instabilities with suprathermal electrons.
- The first observations of electron fishbones on TCV were made.

Appendix A

Electron distribution function

A.1 Basics

An electron distribution function (e.d.f.) is a function

$$\begin{aligned} f \in \left(L^1 \cap L^2\right) : \mathbb{R}^3 \times B &\to \mathbb{R}^+ \\ \left(\mathbf{r}, \boldsymbol{\beta}\right) &\mapsto f\left(\mathbf{r}, \boldsymbol{\beta}\right) \end{aligned} \tag{A.1}$$

with the space coordinate $\mathbf{r} \in \mathbb{R}^3$ and the velocity $\boldsymbol{\beta}$ with respect to the speed of light

$$\boldsymbol{\beta} := \mathbf{v}/c \in B, \tag{A.2}$$

where B is defined as the unit ball in $\mathbb{R}^3$

$$B := \left\{\boldsymbol{\beta} \in \mathbb{R}^3 | \beta := \|\boldsymbol{\beta}\| < 1\right\}. \tag{A.3}$$

The above definition defines a steady-state e.d.f. or the e.d.f. for one point in time. It is clear that, in general, this function may additionally be time-dependent. By integrating in velocity space the electron density is obtained:

$$n_e(\mathbf{r}) = \int_B f\left(\mathbf{r}, \boldsymbol{\beta}\right) d^3\beta. \tag{A.4}$$

If the variable in velocity space is renormalized, for instance to 1 m/s instead of the speed of light (c), the distribution function has to be renormalized accordingly, such that (A.4) is fulfilled correspondingly.

In a tokamak it is usually assumed that the e.d.f. and subsequently the electron density is constant on flux surfaces, which reduces the space coordinate to one dimension

$$f\left(\rho_\psi, \boldsymbol{\beta}\right) := f\left(\mathbf{r}, \boldsymbol{\beta}\right)|_{\psi(\mathbf{r})=\rho_\psi^2} \tag{A.5}$$

This is justified by the transit- and bounce-times τ_{t}, τ_{b} being much smaller than the time scale we are interested in (collision time scale τ_{c} or greater). Since the gyro motion takes place on an even shorter time scale ${\omega_c}^{-1}$ it can be further assumed that f is independent of the direction of the component of $\boldsymbol{\beta}$ perpendicular to the magnetic field lines to reduce the configuration space dimension to three:

$$f\left(\rho_\psi, \boldsymbol{\beta}\right) = f\left(\rho_\psi, \beta_\parallel, \beta_\perp\right). \tag{A.6}$$

A.2 Analytic distribution functions

A.2.1 Maxwellian electron distribution

For a plasma in or close to equilibrium a Maxwellian is a good approximation and we can define an electron temperature (T_e). So for each point in space we get

$$f\left(\mathbf{r},\boldsymbol{\beta}\right) = f_{T_e}\left(\mathbf{r},\boldsymbol{\beta}\right) = n_e\left(\mathbf{r}\right)\left(\frac{mc^2}{2\pi kT_e}\right)^{3/2}\exp\left(-\frac{mc^2\beta^2}{2kT_e}\right) \tag{A.7}$$

for a plasma of electron temperature T_e in the non-relativistic case $kT_e \ll mc^2$. This case is usually valid in tokamaks where $kT_e \lesssim 50\,\mathrm{keV} \ll 511\,\mathrm{keV} = mc^2$.
For relativistic temperatures $kT_e \gtrsim mc^2$ the Maxwell-Jüttner distribution [60, 61] should be used. With γ we can write this distribution function as

$$f\left(\mathbf{r},\gamma\right) = n_e\left(\mathbf{r}\right)\frac{\gamma^2\beta mc^2}{kT_eK_2\left(\frac{mc^2}{kT_e}\right)}\exp\left(-\frac{\gamma mc^2}{kT_e}\right) \tag{A.8}$$

where K_2 is the modified Bessel function of the second kind.
As a function of normalized momentum (p/mc) (A.8) reads

$$f\left(\mathbf{r},\frac{p}{mc}\right) = n_e\left(\mathbf{r}\right)\frac{mc^2}{4\pi kT_eK_2\left(\frac{mc^2}{kT_e}\right)}\exp\left(-\frac{mc^2}{kT_e}\sqrt{1+\left(\frac{p}{mc}\right)^2}\right) \tag{A.9}$$

A.2.2 Bi-Maxwellian and Kappa distributions

If the e.d.f. is non-Maxwellian, but the deviation from the Maxwellian is mainly characterized by a suprathermal electron distribution / tail it can often be well approximated by using the sum of two Maxwellian distributions. Such a Bi-Maxwellian is defined as

$$f\left(\mathbf{r},\boldsymbol{\beta}\right) = f_{T_e}\left(\mathbf{r},\boldsymbol{\beta}\right) + f_{T_{e,2}}\left(\mathbf{r},\boldsymbol{\beta}\right), \tag{A.10}$$

where T_e is the bulk and $T_{e,2}$ the suprathermal electron temperature.
If the suprathermal tail shows a power law decrease one can use the Kappa distribution [170]

$$f^\kappa\left(\mathbf{r},\boldsymbol{\beta}\right) = n_e\left(\mathbf{r}\right)\left(\frac{mc^2}{\pi\left(2\kappa-3\right)kT_e}\right)^{3/2}\frac{\Gamma\left(\kappa+1\right)}{\Gamma\left(\kappa-1/2\right)}\left(1+\frac{mc^2\beta^2}{\left(2\kappa-3\right)kT_e}\right)^{-\left(\kappa+1\right)} \tag{A.11}$$

or equivalently

$$f^\kappa\left(\mathbf{r},\boldsymbol{\beta}\right) = n_e\left(\mathbf{r}\right)\left(\frac{c^2}{\pi\kappa w_\kappa^2}\right)^{3/2}\frac{\Gamma\left(\kappa+1\right)}{\Gamma\left(\kappa-1/2\right)}\left(1+\frac{c^2\beta^2}{\kappa w_\kappa^2}\right)^{-\left(\kappa+1\right)} \tag{A.12}$$

where

$$w_\kappa := \sqrt{\left(2-\frac{3}{\kappa}\right)\frac{kT_e}{m}} \tag{A.13}$$

is the thermal velocity, T_e the equivalent temperature and Γ the Gamma function. Obviously the parameter κ has to be larger than the critical value $\kappa_c = 3/2$. In the

limit $\kappa \to \infty$ the Kappa distribution degenerates into a Maxwellian.
In the case of an anisotropic e.d.f. a Bi-Kappa distribution can be defined starting from (A.12) yielding

$$f^{\kappa}\left(\mathbf{r}, \beta_{\parallel}, \beta_{\perp}\right) = n_e\left(\mathbf{r}\right)\left(\frac{c^2}{\pi\kappa}\right)^{3/2} \frac{1}{w_{\perp}^2 w_{\parallel}} \frac{\Gamma\left(\kappa+1\right)}{\Gamma\left(\kappa-1/2\right)} \left(1 + \frac{c^2\beta_{\parallel}^2}{\kappa w_{\parallel}^2} + \frac{c^2\beta_{\perp}^2}{\kappa w_{\perp}^2}\right)^{-(\kappa+1)} \tag{A.14}$$

with a parallel and perpendicular temperature $T_{\parallel}$ and $T_{\perp}$.
Additional to Bi-Maxwellian and (Bi-)Kappa distributions arbitrary sums of Maxwellian and/or Kappa distributions may be used to approximate the e.d.f. even better. However, with the number of functions the number of fitting parameters increases as well and may lead to badly conditioned fitting.

Appendix B

Bremsstrahlung

During Coulomb collisions the involved charged particles are accelerated and therefore photons are emitted. This radiation is called bremsstrahlung, German for braking radiation, since the incident particles lose kinetic energy at expense of the emitted photons.
Electron-nucleus bremsstrahlung is the most important bremsstrahlung process in physics and also in plasma physics. It is an inevitable and significant energy loss mechanism in MCF plasmas. For high energy electrons and low atomic number (Z) also electron-electron bremsstrahlung contributes significantly and has to be taken into account.

B.1 Scattering geometry

The general scattering geometry (Fig. B.1) can be simplified in the electron-nucleus case by assuming the nucleus at rest: $\mathbf{p}_2 = \mathbf{p}_2' = \mathbf{0}$, being a good approximation until the GeV range [73]. The reaction plane $[x, z]$ is spanned by the incoming incident (first) electron momentum $\mathbf{p} = \mathbf{p}_1$ and the outgoing photon $\mathbf{k}$ in z direction at an angle θ. The outgoing incident (first) electron momentum $\mathbf{p}' = \mathbf{p}_1'$ has an azimuth angle ϕ w.r.t. the reaction plane. In Cartesian coordinates the vectors read

$$\mathbf{p} = p \begin{pmatrix} \sin\theta \\ 0 \\ \cos\theta \end{pmatrix} \tag{B.1}$$

$$\mathbf{p}' = p' \begin{pmatrix} \sin\theta' \cos\phi \\ \sin\theta' \sin\phi \\ \cos\theta' \end{pmatrix} \tag{B.2}$$

$$\mathbf{k} = k \begin{pmatrix} 0 \\ 0 \\ 1 \end{pmatrix} \tag{B.3}$$

with $p = \|\mathbf{p}\|$, $p' = \|\mathbf{p}'\|$ and $k = \|\mathbf{k}\|$. With the corresponding kinetic energies $E = E_1$ and $E' = E_1'$ of the incident (first) electron, its incoming and outgoing velocities in units of c are $\beta = p/E$ and $\beta' = p'/E'$, respectively.

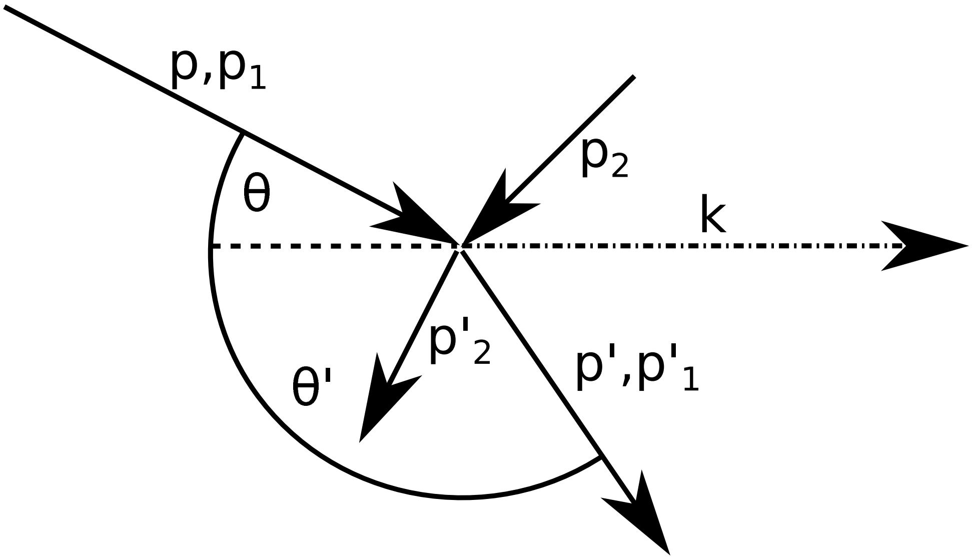

Figure B.1: Bremsstrahlung scattering geometry: photon $\mathbf{k}$ in z direction, incoming ($\mathbf{p} = \mathbf{p}_1$, angle θ) and outgoing ($\mathbf{p}' = \mathbf{p}_1'$, angles θ and (not shown) ϕ) incident electron and target: incoming ($\mathbf{p}_2$) and outgoing ($\mathbf{p}_2'$) second electron or nucleus (assumed at rest, $\mathbf{p}_2 = \mathbf{p}_2' = \mathbf{0}$).

In the case of electron-electron scattering the incoming and outgoing momenta of the second (target) electron ($\mathbf{p}_2$ and $\mathbf{p}_2'$) have to be included too.

B.2 Electron-nucleus bremsstrahlung

The differential cross section for electron-nucleus bremsstrahlung in Born approximation is given by the Bethe-Heitler formula [171]. The Born approximation is valid only if the de Broglie wavelength of the electron is large as compared to the size of the Coulomb field

$$\beta, \beta' \gg \alpha Z \tag{B.4}$$

with the fine-structure constant (α). The Elwert factor (F_E) [172]

$$F_E = \frac{a'}{a} \frac{1 - e^{-2\pi a}}{1 - e^{-2\pi a'}}, \tag{B.5}$$

where

$$a = \frac{\alpha Z}{\beta} = \alpha Z \frac{E}{p}, \tag{B.6}$$

$$a' = \frac{\alpha Z}{\beta'} = \alpha Z \frac{E'}{p'} \tag{B.7}$$

allows to take the Coulomb correction approximately into account, resulting in the following expression for the (triply) differential electron-nucleus bremsstrahlung cross section [73]

$$\begin{aligned}\frac{d^3\sigma_{B,en}}{dk d\Omega_k d\Omega_{p'}} = F_E \frac{\alpha Z^2 r_e^2}{4\pi^2 k q^4} \frac{p'}{p} \Bigg\{ & \left(4E'^2 - q^2\right) \frac{p^2 \sin^2\theta}{\left(E - p\cos\theta\right)^2} \\ & + \left(4E^2 - q^2\right) \frac{p'^2 \sin^2\theta'}{\left(E' - p'\cos\theta'\right)^2} \\ & - \left(4EE' - q^2 + 2k^2\right) \frac{2pp' \sin\theta \sin\theta' \cos\phi}{\left(E - p\cos\theta\right)\left(E' - p'\cos\theta'\right)} \\ & + 2k^2 \frac{p^2 \sin^2\theta + p'^2 \sin^2\theta'}{\left(E - p\cos\theta\right)\left(E' - p'\cos\theta'\right)} \Bigg\}\end{aligned} \tag{B.8}$$

with the classical electron radius (r_e) and

$$\begin{aligned} q^2 = 2k & \left[\left(E - p\cos\theta\right) - \left(E' - p'\cos\theta'\right)\right] \\ & + 2\left[EE' - pp'\left(\sin\theta\sin\theta' + \sin\theta\sin\theta'\cos\phi\right) - 1\right]. \end{aligned} \tag{B.9}$$

B.2.1 Integrated cross section

In lots of applications, including bremsstrahlung emission from plasmas, the direction of the outgoing electron is not observed. To describe this process, one integrates over the outgoing electron angle, yielding the double differential cross section w.r.t. photon energy and angle [173, 174] with Coulomb correction

$$\begin{aligned}\frac{d^2\sigma_{B,en}}{dk d\Omega_k} = F_E \frac{\alpha Z^2 r_e^2}{4\pi k} \frac{p'}{p} \Bigg\{ & \frac{4\sin^2\theta\left(2E^2+1\right)}{p^2\Delta^4} - \frac{5E^2 + 2EE' + 3}{p^2\Delta^2} - \frac{p^2 - k^2}{Q^2\Delta^2} + \frac{2E'}{p^2\Delta} \\ + \frac{L}{pp'} \Bigg[& \frac{2E\sin^2\theta\left(3k - p^2E'\right)}{p^2\Delta^4} + \frac{2E^2\left(E^2 + E'^2\right) - 7E^2 + 3EE' + E'^2 + 1}{p^2\Delta^2} \\ & + \frac{k\left(E^2 + EE' - 1\right)}{p^2\Delta} \Bigg] - \frac{2\epsilon}{p'\Delta} + \frac{\epsilon_Q}{p'Q}\left[\frac{2}{\Delta^2} - \frac{3k}{\Delta} - \frac{k\left(p^2 - k^2\right)}{Q^2\Delta^2}\right] \Bigg\}\end{aligned} \tag{B.10}$$

with

$$\Delta = E - p\cos\theta, \tag{B.11}$$

$$Q^2 = p^2 + k^2 - 2pk\cos\theta, \tag{B.12}$$

$$L = \ln\frac{EE' - 1 + pp'}{EE' - 1 - pp'}, \tag{B.13}$$

$$\epsilon = \ln\frac{E' + p'}{E' - p'}, \tag{B.14}$$

$$\epsilon_Q = \ln\frac{Q + p'}{Q - p'}. \tag{B.15}$$

In the limit of no nucleus recoil, the energy and momentum of the outgoing electron (E', $\mathbf{p}'$) follow directly from the conservation of energy and momentum, respectively:

$$E' = E - h\nu, \tag{B.16}$$

$$\mathbf{p}' = \mathbf{p} - \mathbf{k}. \tag{B.17}$$

B.3 Electron-electron bremsstrahlung

Since the electric dipole moment of two electrons is zero, electric quadrupole radiation is emitted by the non-relativistic collision of two electrons. Hence, it is very low as compared to the electric dipole radiation from electron-nucleus collisions in the non-relativistic case. In plasmas, its contribution is only important for $T_e > 20\,\mathrm{keV}$ or suprathermal electron populations in this energy range. [175]
Due to the non-negligible recoil of the target electron and exchange effects eight Feynman diagrams contribute to the matrix element [175]. Therefore, the differential electron-electron bremsstrahlung cross section is much more complicated than the Bethe-Heitler formula (B.8) and reads [73]

$$\frac{d^3\sigma_{B,ee}}{dk\,d\Omega_k\,d\Omega_{p_1'}} = F_{ee}\frac{\alpha r_e^2}{\pi^2}\frac{k}{R\sqrt{(p_1 p_2)^2 - 1}}\sum_{\nu=1}^{2} p_{\mathbf{k}\nu}'^2 A\left(p_{\mathbf{k}\nu}'\right) \tag{B.18}$$

with $p'_{\mathbf{k}1}$ and $p'_{\mathbf{k}2}$ being the outgoing electron momenta for fixed photon momentum $\mathbf{k}$. The expression for the squared matrix element (A) (averaged over incoming electron spins and outgoing electron spins and photon polarization) is lengthy and can be found in appendix B of [73]. It can be easily evaluated numerically.
The electron-electron bremsstrahlung Coulomb correction factor (F_{ee}), defined as

$$F_{ee} = \frac{a'_{ee}}{a_{ee}}\frac{e^{2\pi a_{ee}} - 1}{e^{2\pi a'_{ee}} - 1}, \tag{B.19}$$

with

$$a_{ee} = \frac{\alpha}{\beta_{12}}, \tag{B.20}$$

$$a'_{ee} = \frac{\alpha}{\beta'_{12}}, \tag{B.21}$$

$$\beta_{12} = \frac{\sqrt{(p_1 p_2)^2 - 1}}{p_1 p_2}, \tag{B.22}$$

$$\beta'_{12} = \frac{\sqrt{(p'_1 p'_2)^2 - 1}}{p'_1 p'_2} \tag{B.23}$$

is the counterpart of F_E [73].

B.4 Thick-target bremsstrahlung

For thick-target bremsstrahlung (e.g. from a graphite or W tile), first of all additional corrections are required in the cross section of the elementary process.

Most importantly the atomic screening [73] in electron-nucleus, but also the effect of bound target electrons [176] in electron-electron collisions, have to be taken into account.
Moreover, thick target refers usually to cases where scattering and energy loss of electrons traversing the target have significant influence on the bremsstrahlung emission. Additionally, especially at low energies, absorption of emitted bremsstrahlung in the thick target itself plays an important role. Therefore, good analytical expressions are only available for the relativistic case, while those for lower energies are quite limited. [174]
Using computers, thick-target bremsstrahlung can be easily calculated for arbitrary materials and geometries (e.g. supplied by computer-aided design (CAD) drawings) using Monte Carlo simulations, for instance EGSnrc [177].

Appendix C

Units, coordinate systems and transformations

Here units, coordinate systems and conventions used in the different tools are presented together with transformations in between them.

C.1 Units

C.1.1 General

CQL3D, TORAY and GENRAY

The CQL3D code and related codes such as TORAY and GENRAY use cgs units and angles are specified in degrees (deg). Internally, also normalized units are used. In the netCDF result file every variable comes with its units.

C.1.2 X-ray flux and count rates

HXRC and HXRS

The MATLAB functions `hxrc_getcbn` and `hxrs_getcbn` are used to read the measured data from the MDS+ database. They return the chord brightness (`cbn`) in the specified energy intervals and at the requested time resolution in cps.

GTI

In GTI, one can either use a direct inversion of the raw data from the HXRC and HXRS measurement in cps, where in the case of the HXRC the variation of G is taken into account. Additionally, it is possible to include the Be window, filters and the étendue (G), which is required if any of these variables is not equal for all selected chords. In this latter case the output is the local photon emission rate of the specified energy interval in $\mathrm{m}^{-3}\mathrm{s}^{-1}\mathrm{sr}^{-1}$.

LUKE

The synthetic FEB diagnostic of LUKE, R5-X2, takes into account the detection efficiency of the HXRC and HXRS systems and returns directly the count rates in the requested energy intervals (provided in keV) in cps.

CQL3D

The CQL3D synthetic X-ray diagnostic results are given in terms of energy flux (variable `eflux`) in units of $\frac{\mathrm{erg}}{\mathrm{cm^2\,s\,sr\,eV}}$. For comparison to HXRC and HXRS measurements (count rate cbn in an energy interval $[E_1, E_2]$) in cps, the following conversion factor applies

$$\mathtt{cbn}_{[E_1,E_2]} = \mathtt{eflux}_{[E_1,E_2]} \frac{\mathrm{erg}}{\mathrm{eV}} \frac{\Delta E}{\overline{E_\gamma}} \frac{\mathrm{m}^2}{\mathrm{cm}^2} G \tag{C.1}$$

with the length of the energy interval

$$\Delta E = (E_2 - E_1) \tag{C.2}$$

and the average photon energy ($\overline{E_\gamma}$), both in keV; and G in $\mathrm{m^2 sr}$. The term

$$\frac{\mathrm{erg}}{\mathrm{eV}} \frac{\mathrm{m}^2}{\mathrm{cm}^2} \approx 6.24 \cdot 10^{15} \tag{C.3}$$

accounts for the conversion in energy and area units. For a HXRS channel and an energy interval of length 10 keV, one gets simply

$$\mathtt{cbn}_{[E_0,E_0+10\,\mathrm{keV}]} \approx 2.75 \cdot 10^8 \frac{\mathtt{eflux}_{[E_0,E_0+10\,\mathrm{keV}]}}{\overline{E_{\gamma 0}}}. \tag{C.4}$$

The detector efficiency is not integrated in the CQL3D synthetic diagnostic output. It can be easily taken into account, which was done for all the data in this thesis.

C.2 Coordinate systems and angle definitions

C.2.1 Coordinate conventions

TCV

TCV is subdivided into 16 sectors that are numbered in the trigonometric positive direction (counter-clockwise) seen from the top. For the cylindrical (R, ϕ, z), toroidal (r, θ, ϕ) and Cartesian (x, y, z) coordinate systems, the following conventions apply [103]:

- R is parallel to the equatorial plane, positive towards the outside of TCV and $R = 0$ on the TCV vertical axis
- r is in the poloidal plane, positive towards the outside of the plasma and $r = 0$ on the plasma magnetic axis.

- ϕ is positive counter-clockwise (trigonometric positive direction) seen from the top; $\phi = 0$ halfway between sectors 16 and 1.
- θ is positive clockwise (trigonometric negative direction) seen in ϕ direction (with the TCV vertical axis on the left); $\theta = 0$ on the HFS radius.
- z is the TCV vertical axis, positive upwards and $z = 0$ on the equatorial plane.
- x and y are in R direction at $\phi = 0$ and $\phi = \pi/2$, respectively.

B_ϕ and I_p are positive when they are in positive ϕ direction.
An overview of tokamak coordinate conventions can be found in [178].

Psi-toolbox

Psi-toolbox uses (R, z, ϕ) coordinates, corresponding to the standard TCV coordinate convention (Sec. 2.1.1) with swapped ϕ and z [179]. The system is therefore left-handed.

LUKE

LUKE uses (R, Z, ϕ) coordinates, where R and ϕ correspond to the standard TCV coordinate convention (Sec. 2.1.1), but Z is defined inversely: $Z = -z$ [82]. The system is right-handed.
In the toroidal coordinate system (r, θ, ϕ) r and toroidal angle (ϕ) are defined as in the standard TCV coordinate convention (Sec. 2.1.1). However, θ is in trigonometric positive direction (negative clockwise) seen in ϕ direction (with the TCV vertical axis on the left); $\theta = 0$ on the LFS radius.

CQL3D and TORAY

In CQL3D, coordinates x_{CQL} and z_{CQL} are defined such that

$$x_{\mathrm{CQL}} = 100R\frac{\mathrm{cm}}{\mathrm{m}} \tag{C.5}$$

$$z_{\mathrm{CQL}} = 100\,(z - z_0)\,\frac{\mathrm{cm}}{\mathrm{m}} \tag{C.6}$$

with R and z in standard TCV coordinates (Sec. 2.1.1), shifted by the vertical position of the magnetic axis (z_0) and transformed from m to cm. Due to axisymmetry, the 3$^{\mathrm{rd}}$ dimension is neglected. The same holds for the related TORAY code.

FPCDF

In the FPCDF, the real space coordinate system in the poloidal plane is $(\rho_{\mathrm{tor}}, \theta)$, with ρ_{tor} and θ defined as for LUKE (trigonometric positive direction; $\theta = 0$ on the LFS radius).

C.2.2 Phase space coordinates

LUKE

LUKE uses the non-spherical coordinates (p, ξ, φ) defined in $\mathbb{R}^+ \times [-1, 1] \times [0, 2\pi[$, related to (p_x, p_y, p_z), with p_z along the field line, by [82]

$$p = \sqrt{p_x^2 + p_y^2 + p_z^2} \tag{C.7}$$

$$\xi = \frac{p_z}{\sqrt{p_x^2 + p_y^2 + p_z^2}} \tag{C.8}$$

$$\varphi = \arctan\left(\frac{p_y}{p_z}\right) + \pi H(-p_x) \tag{C.9}$$

with the Heaviside function (H).
The momentum p is, as n_e and T_e, normalized to reference values. The reference momentum (p_{ref}) depends on the reference T_e ($T_{e,\text{ref}}$) and is defined by [161]

$$p_{\text{ref}} = \sqrt{m_e T_{e,\text{ref}}} \tag{C.10}$$

The relative perpendicular component ξ is relates to θ simply via

$$\xi = \cos\theta \tag{C.11}$$

and the angle φ is not important since it is removed from the equations and quantities by averaging over the gyro-motion.
Internally, the variables representing the normalized momentum and the relative perpendicular component are named `pn` and `mhu`, respectively.

CQL3D

CQL3D uses spherical coordinates (u, θ, φ) with u being the velocity times γ in normalized units and θ being the pitch angle.
Internally, u and θ are named `x` and `y`, respectively. The reference velocity for u, `vnorm` in cm/s, is also the boundary of the simulation domain and can be set with the parameter `enorm`, the corresponding energy, in keV.

FPCDF

In FPCDF, spherical coordinates were chosen too, namely $\left(\frac{p}{mc}, \theta, \varphi\right)$. The momentum is normalized to electron mass (m_e) and c, φ is not explicitly defined since unused.

C.2.3 Diagnostic chords and launcher angle definitions

TCV

The toroidal viewing angle (ψ) and toroidal injection angle (ψ) need to be specified for diagnostic chord and wave launch directions, when they do not lie in the poloidal plane. This additional angle ψ is defined by the required rotation in trigonometric positive direction in order to move the chord into the poloidal plane. Its definition corresponds to the one of `tvd` in Psi-toolbox.

Psi-toolbox

In Psi-toolbox, the diagnostic reference point is given by (R_0, z_0, ϕ_0). From this starting point of the diagnostic chord, its direction is given by angles `pvd` and `tvd` with the following definitions [179]

- `pvd` is the poloidal viewing angle, measured between the horizontal plane (constant z) and the chord, positive if the chord is pointing above the plane (z direction); in radians.
- `tvd` is the toroidal viewing angle, measured between the vertical plane $[R, z]$ and the vertical plane containing the chord itself, positive if the chord is looking in the direction of increasing toroidal angle and zero if it looks at the machine axis ($R = 0$). This means positive clockwise (trigonometric negative direction) seen from the top. `tvd` is also measured in radians.

Here, the diagnostic chord direction is specified from the detector, the way it is looking.

LUKE

In LUKE, the reference point for a chord of the R5-X2 synthetic X-ray diagnostic is specified by $(R_{\text{hxr}}, Z_{\text{hxr}})$, and by $(R_{\text{L}}, Z_{\text{L}}, \phi_{\text{L}})$ for the launch point of C3PO. Here, $Z_{\ldots}$ is in standard z coordinates, the transformation to the LUKE coordinates $Z = -z$ is only performed internally.
The direction is then given (for R5-X2 and C3PO) by angles α and β, defined as

- α is the toroidal viewing angle, measured between the vertical plane $[R, z]$ and the vertical plane containing the chord itself, in right-hand sense w.r.t. the z-axis (trigonometic positive direction seen from the top). It starts with zero in the outwards direction and is given in radians, so $\alpha = \pi$ when looking at the machine axis ($R = 0$).
- β is the poloidal viewing angle, measured from the z-axis; in radians.

The variables are called α_{hxr}, β_{hxr} and α_{L}, β_{L}, respectively.
In contrast to Psi-toolbox and CQL3D, the vector has to point in the direction in which the photons are moving. While this is the same for the launch direction, the diagnostic chord direction (e.g. in R5-X2) is inverted, pointing towards the detector.
In addition to these definitions the I_p and B_ϕ directions in LUKE are both reversed w.r.t. the TCV convention. Therefore, the above definition of α_{hxr} has to be multiplied by

$$\frac{\operatorname{sign}\left(I_{p,\text{LUKE}}\right)}{\operatorname{sign}\left(I_{p,\text{TCV}}\right)} = -1 \tag{C.12}$$

to capture the physics correctly. In contrast to that, the launcher angle α_{L} remains unchanged since here the factor that keeps the physics unchanged is

$$\frac{\operatorname{sign}\left(I_{p,\text{LUKE}}\right)\operatorname{sign}\left(B_{\phi,\text{LUKE}}\right)}{\operatorname{sign}\left(I_{p,\text{TCV}}\right)\operatorname{sign}\left(B_{\phi,\text{TCV}}\right)} = 1. \tag{C.13}$$

CQL3D and TORAY

In CQL3D, the reference point for the synthetic X-ray (sxr) diagnostic is specified by x_{sxr} and z_{sxr}. The direction of the chord is then given by angles `thet1` (θ_1) and `thet2` (θ_2), defined as

- θ_1 is the poloidal viewing angle, measured from the z-axis, in deg.
- θ_2 is the toroidal viewing angle, measured between the vertical plane $[x, z]$ and the vertical plane containing the chord itself, in right-hand sense w.r.t. the z-axis (trigonometic positive direction seen from the top). It starts with zero in the outwards direction and is also given in deg, so $\theta_2 = 180$ when looking at the machine axis.

Hence, the angle definition of CQL3D is in principle the same as in LUKE, with θ_1 corresponding to β and θ_2 to α. However, one has to be aware of the different units and the direction. Additionally, since I_p and B_ϕ are set to their absolute values in TORAY and subsequently also CQL3D, θ_2 has to be multiplied by $\mathrm{sign}\left(I_{p,\mathrm{TCV}}\right)$ to capture the physics correctly. For a correct observation of the X-ray emission in the poloidal plane, the z position and the angles θ_1 need to be mirrored upside down.

C.3 Transformations

The presented conventions are summarized in an overview table (Tab. C.1).

TCV, base	Psi-toolbox	LUKE: C3PO	LUKE: R5-X2	CQL3D: sxr
R	R	R	R	$x_{\mathrm{CQL}} = x_{\mathrm{sxr}} = 100 R \frac{\mathrm{cm}}{\mathrm{m}}$
ϕ	z	$Z = -z$	$Z = -z$	$\begin{cases} z_{\mathrm{CQL}} = 100\,(z - z_0)\,\frac{\mathrm{cm}}{\mathrm{m}} \\ z_{\mathrm{sxr}} = \mathrm{sign}\left(B_\phi\right) z_{\mathrm{CQL}} \end{cases}$
z	ϕ	ϕ	ϕ	-
ψ	$\mathtt{tvd} = \psi$	$\alpha_{\mathrm{L}} = \pi - \psi$	$\alpha_{\mathrm{hxr}} = \psi$	$\theta_2 = \mathrm{sign}\left(I_p\right) \alpha_{\mathrm{L}}$
θ	$\mathtt{pvd} = \theta$	$\beta_{\mathrm{L}} = \frac{\pi}{2} - \theta$	$\beta_{\mathrm{hxr}} = \theta - \frac{\pi}{2}$	$\theta_1 = \begin{cases} \beta_{\mathrm{L}}, & B_\phi > 0 \\ \pi - \beta_{\mathrm{L}}, & B_\phi < 0 \end{cases}$
B_ϕ	B_ϕ	$-B_\phi$	$-B_\phi$	$\left\lvert B_\phi \right\rvert$
I_p	I_p	$-I_p$	$-I_p$	$\left\lvert I_p \right\rvert$
V_{loop}	V_{loop}	$-V_{\mathrm{loop}}$	$-V_{\mathrm{loop}}$	$\mathrm{sign}\left(I_p\right) V_{\mathrm{loop}}$

Table C.1: Transformations in between the used conventions. Angles in the ψ and θ rows are, if necessary, further mapped such that those in the ψ row lie in $(-\pi, \pi]$ and those in the θ row lie in $\left[-\frac{\pi}{2}, \frac{\pi}{2}\right]$ for θ, pvd and $[0, \pi]$ for β, θ_1, respectively. Eventually, the CQL3D angles θ_1, θ_2 have to be transformed from radians to degrees.

List of Figures

List of Tables

Acronyms

Al aluminum. 51

Ar argon. 35

A squared matrix element. 184

B_0 minimum magnetic field. 86, 87

B_ϕ toroidal magnetic field. 8, 28, 84, 94, 106–108, 110, 114, 116, 118, 123, 160–162, 165, 174, 189, 191–193

B_θ poloidal magnetic field. 8, 31

Be beryllium. 34–36, 38, 39, 49, 187

CH_4 methane. 35

$CdTe$ cadmium-telluride. i, iii, vii, 21, 37, 38, 49, 53, 54

E_D Dreicer field. 19, 99, 100, 106, 156

E_F Fermi energy. 3

E_γ photon energy. 116, 123, 130, 134, 140, 141, 148, 154, 174

E_ϕ toroidal electric field. 84, 92, 96, 99–101, 106, 119, 123, 156, 174, 176

$E_{Coul.}$ Coulomb energy. 3

E energy. 17, 86, 188

F_E Elwert factor. 46, 182, 184

F_{ee} electron-electron bremsstrahlung Coulomb correction factor. 184

Fe iron. 51

G étendue. 45, 49, 53, 187, 188

HgI_2 mercury(II) iodide. 53

H Heaviside function. 190

I_p plasma current. 8, 27, 28, 31, 37, 92, 94, 100, 106–108, 110, 119, 122, 123, 125, 129, 134, 156, 160, 162, 164, 165, 167, 168, 170, 174, 189, 191–193

Kr krypton. 35

L_i internal inductance. 160, 205

N_D Debye number. 4

P_{RF} RF power. 130

Q amplification factor. 1, 2

R major radius. 9, 25, 27

T_γ photon temperature. 92, 99, 106, 114, 116, 134, 148

T_e electron temperature. 17, 18, 20, 27, 32–36, 44, 84, 86, 89, 103, 106, 130, 134, 139, 143, 144, 156, 162, 164, 165, 178, 184, 190, 202

T_i ion temperature. 27, 89

$T_{e,0}$ central electron temperature. 36, 130, 156, 162

$T_{e,2}$ suprathermal electron temperature. 18, 123, 130, 134, 138, 139, 143, 156, 178

$T_{e,\mathrm{ref}}$ reference T_e. 190

T temperature. 1, 2, 11

V_{loop} loop voltage. 31, 94, 99, 101, 119, 134, 139, 143, 167, 193

W tungsten. 34, 38, 49, 173, 184

Xe xenon. 35

Z_i ion charge. 3

Z_{eff} effective ion charge. 33, 34, 84, 89, 106

Zr zirconium. 39

Z atomic number. 181

$\Delta\phi$ difference in toroidal angle. 154

Δt time shift. 154

Δ Shafranov shift. 10

Λ plasma parameter. 4

Ψ relative magnetic field. 86

α fine-structure constant. 182

α alpha particle. 17

$\bar{g}_\nu$ Gaunt factor. 33

$\bar{g}_n$ Gaunt factor. 33

$\bar{g}_{ff}$ free-free Gaunt factor. 33

β normalized pressure factor. 7

χ_e electron heat diffusion coefficient. 84

χ_i first ionization potential. 33

χ_{se} suprathermal electron diffusion coefficient. 83, 99, 100, 107, 116, 123, 127, 129, 134, 135, 148

δ triangularity. 10, 27, 28, 106, 123, 125, 161, 168, 174

ϵ aspect ratio. 9, 25, 27

η detection efficiency. 140, 141

η resistivity. 6, 11

$\frac{dI_p}{dt}$ current ramp rate. 164

γ gamma ray. 54, 140

γ relativistic factor. 13, 178, 190

κ elongation. 10, 27, 28, 33, 110, 122, 123, 125, 161, 174

λ_D Debye length. 3

$\ln\Lambda$ Coulomb logarithm. 4, 83

$\mathbf{B}$ magnetic field. 4, 6, 7, 9, 10, 13, 20, 21, 23, 86, 89, 205

$\mathbf{E}$ electric field. 5–7, 19, 99–101

$\mathbf{J}$ current. 6, 10

$\mathbf{k}$ wave vector. 13, 181

$\mathbf{p}$ momentum. 148

$\mathbf{v}$ velocity. 6

$\mathscr{C}$ collision operator. 22

$\mathscr{E}$ electric field operator. 22

$\mathscr{H}$ synchrotron radiation operator. 22

$\mathscr{Q}^{\mathrm{RF}}$ quasilinear RF diffusion operator. 22

$\mathscr{S}$ source and sink term. 22

$\mathscr{T}$ transport operator. 22

μ magnetic moment. 5, 86

${}^{\delta B}/_{B}$ ripple amplitude. 10

${}^{p}/_{mc}$ normalized momentum. 178

ν_p plasma frequency. 3

ν_{ei} electron-ion collision frequency. 19

ν_e electron collision frequency. 96

ν collision frequency. 5, 19, 96, 204

ω_c cyclotron frequency. 4, 5, 177

ω_p plasma frequency. 4, 11

ω_{ce} electron cyclotron frequency. 11, 20, 28, 30

$\overline{E_\gamma}$ average photon energy. 188

ϕ toroidal angle. 189, 191

ψ_{pol} poloidal flux. 10

ψ_{tor} toroidal flux. 10

ψ stream function. 10

ψ toroidal injection angle. 101, 103, 106, 110, 114, 119, 130, 134, 190

ψ toroidal viewing angle. 190, 191

ρ_{pol} poloidal flux surface label. 10, 45, 123, 170

ρ_{tor} toroidal flux surface label. 10, 110, 114, 116, 118, 128, 130–132, 134, 156, 162, 164, 165, 189

ρ_{vol} volume-based flux surface label. 10

ρ density. 6

σ_j singular value. 42

σ standard deviation. 56

τ_{E} energy confinement time. 1, 7

τ_{b} bounce time. 13, 22, 23, 177

τ_{c} collision time. 22, 118, 177

τ_{dt} collisional detrapping time. 13, 22

τ_{d} drift time. 5

τ_e electric field acceleration time. 22

τ_ql quasilinear diffusion time. 22

τ_t transit time. 22, 23, 177

θ_0 pitch angle at minimum magnetic field. 86

θ_1 `thet1`. 192

θ_2 `thet2`. 192

θ_tp trapped-passing boundary. 5, 7, 13, 83, 87, 89, 110, 119

θ angle of the wave vector to the magnetic field. 19, 20

θ pitch angle. 5, 7, 86, 89, 190, 205

θ poloidal injection angle. 118

θ poloidal angle. 45, 110, 116, 189

deg degree. 187, 192

ζ squareness. 10

^2D deuterium. 1, 2

^3T tritium. 1, 2

^{241}Am americium-241. 54–56

^{55}Fe iron-55. 39

a minor radius. 9, 25, 27

c speed of light. 177, 181, 190

f_mode mode frequency. 154

f_{T_e} Maxwellian. 18

l_i normalized internal inductance. 160

m_e electron mass. 190

$n_\parallel$ parallel propagation component. 13, 92, 94, 101, 103, 106, 119, 123, 125, 129, 132, 134, 138, 150, 174, 175

n_e electron density. 2, 17, 19, 27, 28, 31–34, 44, 45, 84, 86, 94, 106, 114, 123, 128, 132, 139–141, 156, 162, 164, 165, 168, 170, 190

n_i ion density. 3

$n_{e,0}$ central electron density. 106, 110, 134, 162

$n_{e,\mathrm{l.avg.}}$ line-averaged electron density. 160

n density. 1

p_{ref} reference momentum. 190

p_e electron pressure. 156, 157, 206

p_{se} suprathermal electron pressure. 156

p pressure. 6, 156, 206

q_{min} minimal q. 16, 156, 160, 162, 164, 168, 170, 175

q safety factor. ii, iv, viii, 9, 16, 107, 143, 156, 157, 161, 162, 170, 206

r_L Larmor radius. 4, 5

r_e classical electron radius. 183

s magnetic shear. 9

v_{ref} reference velocity. 84

$v_{\parallel}$ parallel velocity. 4, 5, 13, 92, 100, 119, 148

$v_{\perp}$ perpendicular velocity. 4, 5, 13, 92, 106, 110, 148

`lac` CRPP linux analysis cluster. 213, *Glossary:* `lac`

1D one-dimensional. 21, 22, 44, 45, 86

2D two-dimensional. 21, 22, 41, 44, 45, 86, 134, 138, 143

3D three-dimensional. 22, 23, 86, 214

7D seven-dimensional. 22

ADC analog to digital converter. 49, 54, 57, 58

AXUV absolute extreme ultraviolet bolometer cameras. 45

Bi-Maxwellian sum of two Maxwellians. 18, 22, 178, 179

BOLO foil bolometers. 45

CAD computer-aided design. 185

CAS coupled bursts alternating with sawtooth crashes. 176

CC cross-correlation. 58, 59, 68, 74, 75, 80, 81

CD current drive. i–iv, vii, viii, 13, 14, 17, 18, 22, 24, 25, 27, 30, 44, 87, 92, 96, 118, 127, 129, 134, 139, 148, 159, 162, 173–176

chronos v_j. 42, 43, 151

CIS change-in-sign. 59–61, 74, 75, 78–81

CLI command-line interface. 85

cnt-ECCD counter-current ECCD. 92, 94, 96, 99–101, 106, 123, 145, 148, 161, 174

co-ECCD co-current ECCD. 92, 94, 96, 99, 101, 103, 106, 110, 114, 119, 123, 128, 130, 138, 145, 148, 151, 161, 164, 174

cps counts per second. 37, 187, 188

CPU central processing unit. 80, 87, 213

CR capacitor-resistor. 58, 61, 62

CRPP Centre de Recherches en Physique des Plasmas. 25, 44, 47, 235, 236

CS central solenoid. 26

CW continuous wave. 31

CZT cadmium zinc telluride. 53

DDJ Diagnosticien du jour. 236

DDL double delay line. 58, 59, 64, 65, 78

DEMO demonstration reactor. 1, *Glossary:* DEMO

DKE drift kinetic equation. 214

DMPX duplex multiwire proportional X-ray counter. 35, 44, 45, 140, 141, 143–145, 156, 159

DNBI diagnostic neutral beam injector. 30

DSP digital signal processor. 57

dyn. thres. dynamic threshold. 59, 60

e.d.f. electron distribution function. i, ii, 14, 16–23, 46, 83, 86, 87, 89, 92, 96, 99–101, 103, 107, 110, 118, 123, 138, 139, 151, 157, 177–179, 214

e.g. for example. 28, 84, 106, 116, 141, 148, 156, 184, 185, 191

EC electron cyclotron. ii, 13, 14, 18, 23, 30, 92, 106, 107, 123, 125, 128, 132, 138, 139, 148, 162, 164, 168, 173, 176

ECCD electron cyclotron current drive. i, iii, vii, 11, 12, 16, 18, 27–29, 38, 92, 94, 96, 101, 119, 123, 127, 134, 138, 148, 150, 162, 164, 173, 174, 207

ECE electron cyclotron emission. 19–23, 46, 159, 165, 168, 170, 213, 214

ECRH electron cyclotron resonant heating. i–iv, vii, viii, 11, 12, 14–16, 18, 22, 24, 25, 27–30, 41, 44, 87, 92, 107, 108, 119, 123, 127, 134, 139, 150, 159, 160, 164, 165, 168, 173–175

ELM edge localized mode. 14, 27

EPFL École Polytechnique Fédérale de Lausanne. 25, 47

eval. evaluation. 59

F-P Fokker-Planck. i, iii, vii, 25, 83, 87, 118, 123, 127, 132, 134, 138, 173, 174

FastCam fast visible camera. 45

FEB fast electron bremsstrahlung. 46, 188

FEM finite element method. 45

FIR finite impulse response. 58, 62–68, 71, 74, 75, 78, 80, 174

FIR far infrared interferometer. 31, 33, 44, 45, 156

FPGA field programmable gate array. 54, 71, 80

FTU Frascati Tokamak Upgrade. 16

Full-HD full high definition. 44

FWHM full width at half maximum. 56

GTI general tomographic inversion. i, iii, vii, 32, 35, 36, 44, 45, 110, 123, 129, 151, 174, 187

GUI graphical user interface. 47, 85, 87, 88

HD high definition. 44, 208

HDD hard disk drive. 54

HFS high field side. 11, 16, 20, 31, 35, 43, 45, 49, 89, 92, 107, 108, 110, 114, 116, 118, 119, 121–123, 141, 144, 148, 160–162, 164, 165, 167, 168, 174, 189

HPC high-performance computing. 47, 84, 86

HV high voltage. 35

HXR hard X-ray. i, ii, 16, 19, 21–24, 28, 34, 37, 38, 44, 46, 84, 86, 89, 92, 96, 99–101, 103, 106–108, 110, 114, 118, 119, 122, 123, 125, 127–130, 132, 134, 138–141, 143–145, 148, 154, 161, 165, 167, 171, 173–176

HXRC hard X-ray camera. 38, 44, 45, 62, 127–130, 161, 167, 187, 188

HXRS hard X-ray tomographic spectrometer. i–iv, vii, viii, 24, 25, 37–39, 44, 45, 47, 53, 54, 57, 58, 61, 69, 71, 72, 75, 78–81, 89, 103, 107, 108, 110, 114, 116, 118, 123, 125, 127–129, 132, 134, 140, 141, 143–145, 148, 151, 154, 156, 159, 162, 165, 167, 168, 170, 171, 173–175, 187, 188, 213, 235

i.d.f. ion distribution function. 89

i.e. that is. 92, 143, 148

I/O input/output. 58

ICF inertial confinement fusion. 2

ICRH ion cyclotron resonant heating. 11, 30

IIR infinite impulse response. 58, 61, 62, 74, 78

ITB internal transport barrier. 12, 27, 132

JET Joint European Torus. 1, 8, 15

L-mode low confinement mode. 139

LCFS last closed flux surface. 10, 45

LFS low field side. 16, 20, 21, 23, 29–31, 35–38, 43, 45, 92, 108, 110, 114, 119, 121–123, 167, 168, 170, 189

LH lower hybrid. 11, 18

LHCD lower hybrid current drive. 11, 15, 16, 18, 22, 30, 148

LMS least (mean) squares. 58, 59, 67, 68, 74, 75, 80, 81

LoS line of sight. 21, 23, 33, 34, 36, 37, 39, 44, 45, 49, 51, 53, 92, 128, 141

LS least (mean) squares. 43, 46

MA moving average. 59, 64, 65

Maxwellian Maxwell-Boltzmann distribution. 13, 17, 18, 20, 22, 33, 83, 89, 178, 179, 205, 206

MCF magnetic confinement fusion. 2, 7, 8, 11, 27, 181, 215

MFI minimum Fisher information. 44, 46

MHD magnetohydrodynamics. i–iv, vii, viii, 6, 10, 12, 14, 15, 18, 24, 31, 34, 41, 44, 106, 139, 145, 150, 159, 173, 174, 176, 235

MOU matching optics unit. 28, 30, 107

MPI message passing interface. 214

MPX multiwire proportional X-ray counter. 35

MST medium-size tokamak. 27

mult. cond. multiple condition. 59

NBH neutral beam heating. 11, 15–17, 22

NBI neutral beam injector. 30

NTM neoclassical tearing mode. 14, 15, 34, 35, 46, 174

O-mode ordinary mode. 11, 28, 210

O1 1st harmonic O-mode. 11

O2 2nd harmonic O-mode. 11, 30

OOP object oriented programming. 46

OS operating system. 87

PC personal computer. 54, 213

PCB printed circuit board. 53

PD pulse detection. 58, 59

PDJ Physicien du jour. 236

PET positron emission tomography. 70

PF poloidal field. 8, 26, 27

PHA pulse height analysis. 56–59, 68, 71

PHAV vertical pulse height analyser. 25, 39, 56, 213

PLC programmable logic controller. 25

PMTX photomultiplier tube for hard-X rays. 39, 140

PNG portable network graphics. 43, 44

PSD pulse-shape discriminator. 59, 60, 64, 74, 75, 78–81

QL quasi-linear. ii, iv, 24, 86, 127, 134, 138, 174

r.h.s. right hand side. 2, 19, 22

RAM random-access memory. 87

RC resistor-capacitor. 58, 61, 62

RF radio frequency. i, viii, 13, 18, 22, 28, 86, 94, 96, 99, 103, 110, 114, 116, 118, 123, 125, 127–130, 132, 134, 138, 151, 174, 176, 202

RFP reversed field pinch. 7

RMS root mean square. 54

S/N signal-to-noise. 33, 43

SAW surface acoustic wave. 62

SCD Système de Contrôle Distribué. 27, 30, *Glossary:* SCD

SCSI small computer system interface. 49, 211

SCSI-2 second generation small computer system interface. 49, 53

SDD silicon drift detector. 21, 39

SDL single delay line. 58, 59, 63–65

SDLC synchronous data link control. 213

Si silicon. 36

SOL scrape-off layer. 10

SVD singular value decomposition. 41–43, 46, 150, 151, 154, 174

SVM support vector machine. 58

SXR soft X-ray. 33–35, 44, 89, 139, 141, 143, 144, 150, 151, 154, 161, 162, 164, 165, 168, 175

sxr synthetic X-ray. 192, 193

TCV Tokamak à Configuration Variable. i, ii, iv, vii, viii, 3, 15, 21, 25–35, 37–39, 43–47, 49, 53, 62, 69, 78, 86, 87, 89, 100, 101, 103, 108, 127, 132, 138, 139, 141, 148, 159, 160, 167, 168, 171, 173, 174, 176, 188, 189, 191, 193, 213–215, 236

TF toroidal field. 8, 26

thres. threshold. 59

topos u_j. 42, 43, 151

Trpz trapezoidal. 59, 64, 65, 75, 78, 80

TS Thomson scattering. 32, 45, 103, 130, 156

TXDA tangential X-Ray detector array. 25, 38, 140

w.r.t. with respect to. 56, 89, 107, 122, 145, 154, 156, 162, 181, 183, 191, 192

X-mode extraordinary mode. 11, 28, 30, 212

X1 1st harmonic X-mode. 11

X2 2nd harmonic X-mode. 11, 20, 30, 38, 92, 110, 114, 129, 160–162

X3 3rd harmonic X-mode. 11, 29, 30, 38, 99

XML extensible markup language. 44, 84

XTe soft X-ray electron temperature. 36

XTePro XTe profiles. 25, 36, 45

XTOMO soft X-ray tomography. 34, 44, 45, 150, 151, 154, 159, 161, 164, 168, 170

Glossary

ξ number of available holes in the ion's lowest unfilled shell. 33

Alma database The Alma database contains a set of of representative plasma parameters for every TCV discharge at predefined times. It is created using the MDB software and implemented as a table of the TCV "logbook" MySQL database [84]. 160

BITBUS an open and non-proprietary fieldbus based on standard technologies like RS-485 and synchronous data link control (SDLC). It is a simple to use Master-Slave communication system. As an international standard and it is also known as IEEE-1118. 49, 53, 54

BLAS the Basic Linear Algebra Subprograms are very efficient low level implementations of basic linear algebra (matrix) operations. 215

C a general-purpose imperative programming language. 57

C3PO the ray tracing code used by LUKE [82, 132]. 46, 87, 116, 130, 191, 193, 214

CPU time the amount of time for which a CPU was used to process instructions of a program. 87

CQL3D a relativistic collisional/quasilinear 3D bounce-averaged Fokker-Planck solver, coupled with the TORAY ray tracing code and several synthetic diagnostics (e.g. X-ray bremsstrahlung and GENRAY for ECE) [133, 83]. i, iii, vii, 24, 25, 46, 47, 83, 84, 86, 87, 94, 96, 99–101, 103, 106, 107, 116, 118, 119, 123, 127, 129, 130, 134, 174, 175, 187–193, 214, 235

`crpppc271` the PHAV acquisition PC, hosting a FAST ComTec MCA-3 multichannel analyzer; it is also used for the HXRS calibration. 39

`crpppc82` the server hosting the HXRS database and also providing most of the software available on the CRPP linux analysis cluster (`lac`) machines. 54, 57

DEMO a planned nuclear fusion reactor to demonstrate the feasibility of a commercial fusion power plant. 1

EGSnrc the electron gamma shower (EGS) of the Canadian national research council (NRC) is a Monte Carlo simulation software modeling the passage of electrons and photons through matter, including all sorts of interaction [177]. 185

Fortran an imperative programming language especially suited for numeric computation and scientific computing. 46, 215

FPCDF the Fokker-Planck common data format (FPCDF) is a python module with a set of classes for 3D e.d.f. data from LUKE and CQL3D for direct comparison of the results and further analysis. 25, 86, 87, 189, 190

GENRAY a general ray tracing code for 3D plasmas providing synthetic ECE spectra from CQL3D results. 46, 187, 213

ilôt French for isle, is the name for instrument cabinets in the TCV hall. There are 4 ilôts around TCV (SE, SO, NO and NE for South-East, South-West, North-East and North-West) with separate grounding and an ilôt in the basement (ilôt Langmuir) at the tokamak ground potential. 39

ITER international tokamak experiment under construction in Cadarache, France; latin word for “the way”, formerly also acronym for international thermonuclear experimental reactor. 1, 3, 8

LAPACK the Linear Algebra Package is a standard software library for numerical linear algebra; ScaLAPACK implements a subset of LAPACK for distributed memory parallel computers. 215

LEMO a push-pull connector by LEMO company (Écublens, Switzerland) commonly used in instrumentation for physics experiments. 53

LIUQE the equilibrium reconstruction code used at TCV; its name is the backward spelling of “equil”. 45

LUKE a fully relativistic 3D bounce-averaged Fokker-Planck solver (formerly drift kinetic equation (DKE)), coupled with the C3PO ray tracing code and the R5-X2 X-ray bremsstrahlung calculator [82, 132]. i, iii, vii, 24, 25, 46, 47, 83–87, 94, 96, 99, 100, 103, 106, 116, 118, 119, 123, 129, 134, 168, 170, 174, 175, 188–193, 213–215, 235

MATLAB a multi-paradigm numerical computing environment and programming language. 47, 56, 87, 187

MDS+ MDSplus (MDS for minimum data set) is a set of software tools for data acquisition and storage and a methodology for management of complex scientific data [180]. 39, 44, 57, 84, 86, 187

mpi4py a Python implementation of the message passing interface (MPI). 57

MUMPS the MUltifrontal Massively Parallel sparse direct Solver is a software library for the solution of large sparse systems, implemented in Fortran; for dense matrix computations BLAS and ScaLAPACK are used. 87

Nd:YAG Neodymium-doped yttrium aluminium garnet $Nd : Y_3Al_5O_12$ (Nd:YAG) is a crystal that is used as a lasing medium for solid-state lasers [181]. 32

netCDF network common data form is a machine-independent binary data format for exchange of array-based scientific data. 46, 187

`pgplot` a graphics subroutine library mostly written in Fortran. 46

Psi-toolbox a partially object-oriented toolbox for describing flux surfaces, diagnostic chords and other quantities in different coordinate systems of a tokamak [179]. 189–191, 193

Python a general-purpose high-level programming language. 44, 47, 56, 57, 84, 86, 214

R5-X2 a synthetic X-ray bremsstrahlung diagnostic for LUKE [82, 132]. 46, 47, 188, 191, 193, 214

SCD The Système de Contrôle Distribué is the distributed digital real-time control system of TCV. 212

tokamak The most researched and successful MCF device type; russian acronym translating to toroidal chamber with magnetic coils. i, ii, iv, 7, 8, 25, 33, 125, 173

TORAY the ray tracing code that is used most at TCV. 46, 84, 116, 118, 130, 187, 189, 192, 213, 235

Vsystem a collection of comprehensive, real-time, networked process control software tools by Vista Control Systems used at TCV. 25, 53

Index

Bibliography

[1] S. Gnesin, S. Coda, J. Decker, and Y. Peysson. Suprathermal electron studies in the TCV tokamak: Design of a tomographic hard-x-ray spectrometer. *Review of Scientific Instruments*, 79(10):10F504, 2008.

[2] J. Kamleitner, S. Coda, S. Gnesin, and Ph. Marmillod. Comparative analysis of digital pulse processing methods at high count rates. *Nuclear Instruments and Methods in Physics Research Section A: Accelerators, Spectrometers, Detectors and Associated Equipment*, 736(0):88–98, 2014.

[3] S. Coda, S. Alberti, P. Blanchard, T. P. Goodman, M. A. Henderson, P. Nikkola, Y. Peysson, and O. Sauter. Electron cyclotron current drive and suprathermal electron dynamics in the TCV tokamak. *Nuclear Fusion*, 43(11):1361, 2003.

[4] M. Kikuchi, K. Lackner, and M. Q. Tran, editors. *Fusion physics*. International atomic energy agency, Vienna International Centre, PO Box 100, A-1400 Vienna, Austria, 2012.

[5] J. P. Freidberg. *Plasma physics and fusion energy*. Cambridge University Press, Cambridge, 2007.

[6] M. Keilhacker, A. Gibson, C. Gormezano, P. J. Lomas, P. R. Thomas, M. L. Watkins, P. Andrew, B. Balet, D. Borba, C.D. Challis, I. Coffey, G. A. Cottrell, H. P. L. De Esch, N. Deliyanakis, A. Fasoli, C. W. Gowers, H. Y. Guo, G. T. A. Huysmans, T. T. C. Jones, W. Kerner, R. W. T. König, M. J. Loughlin, A. Maas, F. B. Marcus, M. F. F. Nave, F. G. Rimini, G. J. Sadler, S. E. Sharapov, G. Sips, P. Smeulders, F. X. Söldner, A. Taroni, B. J. D. Tubbing, M. G. von Hellermann, D. J. Ward, and JET Team. High fusion performance from deuterium-tritium plasmas in JET. *Nuclear Fusion*, 39(2):209, 1999.

[7] J. D. Lawson. Some Criteria for a Power Producing Thermonuclear Reactor. *Proceedings of the Physical Society. Section B*, 70(1):6, 1957.

[8] J. Wesson. *Tokamaks*. Oxford University Press, 4th edition, October 2011.

[9] J. Schweinzer. Physikalische Grundlagen des Kernfusionsreaktors, 2009.

[10] J. P. Freidberg. *Ideal Magnetohydrodynamics*. Plenum Press, 1987.

[11] The ASDEX Upgrade Team. ASDEX Upgrade Intranet: Documentation: Machine: Pictures, Description and Details:AUG.

[12] O. Sauter, M. A. Henderson, F. Hofmann, T. Goodman, S. Alberti, C. Angioni, K. Appert, R. Behn, P. Blanchard, P. Bosshard, R. Chavan, S. Coda, B. P. Duval, D. Fasel, A. Favre, I. Furno, P. Gorgerat, J.-P. Hogge, P.-F. Isoz, B. Joye, P. Lavanchy, J. B. Lister, X. Llobet, J.-C. Magnin, P. Mandrin, A. Manini, B. Marlétaz, Ph. Marmillod, Y. Martin, J.-M. Mayor, A. A. Martynov, J. Mlynar, J.-M. Moret, C. Nieswand, P. Nikkola, P. Paris, A. Perez, Z. A. Pietrzyk, R. A. Pitts, A. Pochelon, G. Pochon, A. Refke, H. Reimerdes, J. Rommers, E. Scavino, G. Tonetti, M. Q. Tran, F. Troyon, and H. Weisen. Steady-State Fully Noninductive Current Driven by Electron Cyclotron Waves in a Magnetically Confined Plasma. *Phys. Rev. Lett.*, 84:3322–3325, Apr 2000.

[13] O. Sauter, T. P. Goodman, S. Coda, M. Henderson, F. Hofmann, J.-P. Hogge, Y. Peysson, Z. A. Pietrzyk, R. Pitts, H. Reimerdes, and H. Weisen. Sustained fully non-inductive scenarios using pressure and current profile control with {ECCD}. *Fusion Engineering and Design*, 53(1–4):289–299, 2001.

[14] O. Sauter, C. Angioni, S. Coda, P. Gomez, T. P. Goodman, M. A. Henderson, F. Hofmann, J.-P. Hogge, J.-M. Moret, P. Nikkola, Z. A. Pietrzyk, H. Weisen, S. Alberti, K. Appert, J. Bakos, R. Behn, P. Blanchard, P. Bosshard, R. Chavan, I. Condrea, A. Degeling, B. P. Duval, D. Fasel, J.-Y. Favez, A. Favre, I. Furno, R. R. Kayruthdinov, P. Lavanchy, J. B. Lister, X. Llobet, V. E. Lukash, P. Gorgerat, P.-F. Isoz, B. Joye, J.-C. Magnin, A. Manini, B. Marlétaz, Ph. Marmillod, Y. R. Martin, A. Martynov, J.-M. Mayor, E. Minardi, J. Mlynar, P. J. Paris, A. Perez, Y. Peysson, V. Piffl, R. A. Pitts, A. Pochelon, H. Reimerdes, J. H. Rommers, E. Scavino, A. Sushkov, G. Tonetti, M. Q. Tran, and A. Zabolotsky. Steady-state fully noninductive operation with electron cyclotron current drive and current profile control in the tokamak à configuration variable (TCV). *Physics of Plasmas (1994-present)*, 8(5):2199–2207, 2001.

[15] J. I. Paley, F. Felici, S. Coda, T. P. Goodman, F. Piras, and the TCV Team. Real time control of the sawtooth period using EC launchers. *Plasma Physics and Controlled Fusion*, 51(5):055010, 2009.

[16] F. Felici, J. X. Rossel, G. Canal, S. Coda, B. P. Duval, T. P. Goodman, Y. Martin, J.-M. Moret, O. Sauter, D. Testa, and The TCV Team. Real-time control of multiple MHD instabilities on TCV by ECRH/ECCD. *EPJ Web of Conferences*, 32:02005, 2012.

[17] M. F. F. Nave, T. Johnson, L.-G. Eriksson, K. Crombé, C. Giroud, M.-L. Mayoral, J. Ongena, A. Salmi, T. Tala, and M. Tsalas. Influence of Magnetic Field Ripple on the Intrinsic Rotation of Tokamak Plasmas. *Phys. Rev. Lett.*, 105:105005, Sep 2010.

[18] F. Wagner, A. Becoulet, R. Budny, V. Erckmann, D. Farina, G. Giruzzi, Y. Kamada, A. Kaye, F. Koechl, K. Lackner, N. Marushchenko, M. Murakami, T. Oikawa, V. Parail, J.M. Park, G. Ramponi, O. Sauter, D. Stork, P.R. Thomas, Q.M. Tran, D. Ward, H. Zohm, and C. Zucca. On the heating mix of ITER. *Plasma Physics and Controlled Fusion*, 52(12):124044, 2010.

[19] R. Prater. Heating and current drive by electron cyclotron waves. *Physics of Plasmas*, 11(5):2349–2376, 2004.

[20] T. P. Goodman and TCV the team. Experience in integrated control of the multi-megawatt electron cyclotron heating system on the TCV tokamak: the first decade. *Nuclear Fusion*, 48(5):054011, 2008.

[21] R. Prater, H. J. Grunloh, C. P. Moeller, J. L. Doane, R. A. Olstad, M. A. Makowski, and R. W. Harvey. A design study for the ECH launcher for ITER. In Tony Donné and Toon Verhoeven, editors, *Proceedings ot the Tenth Joint Workshop on Electron Cyclotron Emission and Electron Cyclotron Heating*, pages 531–540, 1997.

[22] T. P. Goodman, S. M. Ahmed, S. Alberti, Y. Andrèbe, C. Angioni, K. Appert, G. Arnoux, R. Behn, P. Blanchard, P. Bosshard, Y. Camenen, R. Chavan, S. Coda, I. Condrea, A. Degeling, B. P. Duval, P. Etienne, D. Fasel, A. Fasoli, J.-Y. Favez, I. Furno, M. Henderson, F. Hofmann, J.-P. Hogge, J. Horacek, P. Isoz, B. Joye, A. Karpushov, I. Klimanov, P. Lavanchy, J. B. Lister, X. Llobet, J.-C. Magnin, A. Manini, B. Marlétaz, Ph. Marmillod, Y. Martin, A. Martynov, J.-M. Mayor, J. Mlynar, J.-M. Moret, E. Nelson-Melby, P. Nikkola, P. J. Paris, A. Perez, Y. Peysson, R. A. Pitts, A. Pochelon, L. Porte, D. Raju, H. Reimerdes, O. Sauter, A. Scarabosio, E. Scavino, S. H. Seo, U. Siravo, A. Sushkov, G. Tonetti, M. Q. Tran, H. Weisen, M. Wischmeier, A. Zabolotsky, and G. Zhuang. An overview of results from the TCV tokamak. *Nuclear Fusion*, 43(12):1619, 2003.

[23] S. Coda, E. Asp, E. Fable, T. P. Goodman, O. Sauter, V. S. Udintsev, R. Behn, M. A. Henderson, A. Marinoni, G. P. Turri, C. Zucca, and TCV the team. The physics of electron internal transport barriers in the TCV tokamak. *Nuclear Fusion*, 47(7):714, 2007.

[24] G. P. Canal, B. P. Duval, F. Felici, T. P. Goodman, J. P. Graves, A. Pochelon, H. Reimerdes, O. Sauter, D. Testa, and TCV the Team. Fast seeding of NTMs by sawtooth crashes in TCV and their preemption using ECRH. *Nuclear Fusion*, 53(11):113026, 2013.

[25] T. Ohkawa. Steady state operation of tokamaks by rf heating. *General Atomics Report*, GA-A13847, 1976.

[26] N. J. Fisch and A. H. Boozer. Creating an Asymmetric Plasma Resistivity with Waves. *Phys. Rev. Lett.*, 45:720–722, Sep 1980.

[27] B.B. Kadomtsev. Disruptive instability in tokamaks. *Sov. J. Plasma Phys.*, 1:389–91, 1975.

[28] L. Chen, R. B. White, and M. N. Rosenbluth. Excitation of Internal Kink Modes by Trapped Energetic Beam Ions. *Phys. Rev. Lett.*, 52:1122–1125, Mar 1984.

[29] B.B. Kadomtsev. *Tokamak Plasma: A Complex Physical System.* IOP, Bristol, 1992.

[30] D. Biskamp. *Nonlinear Magnetohydrodynamics.* Cambridge University Press, Cambridge, 1993.

[31] Russell M. Kulsrud. Magnetic reconnection in a magnetohydrodynamic plasma. *Physics of Plasmas*, 5(5):1599–1606, 1998.

[32] R. M. Kulsrud. Magnetic reconnection: Sweet-Parker versus Petschek. *Earth Planets Space*, 53(6):417–422, 2001.

[33] F. Porcelli, D. Borgogno, F. Califano, D. Grasso, M. Ottaviani, and F. Pegoraro. Recent advances in collisionless magnetic reconnection. *Plasma Physics and Controlled Fusion*, 44(12B):B389, 2002.

[34] J. Birn. *Reconnection of Magnetic Fields.* Cambridge University Press, Cambridge, 2007.

[35] P. V. Savrukhin. Generation of Suprathermal Electrons during Magnetic Reconnection at the Sawtooth Crash and Disruption Instability in the T-10 Tokamak. *Phys. Rev. Lett.*, 86(14):3036–3039, Apr 2001.

[36] I. Klimanov, A. Fasoli, T. P. Goodman, and the TCV team. Generation of suprathermal electrons during sawtooth crashes in a tokamak plasma. *Plasma Physics and Controlled Fusion*, 49(3):L1, 2007.

[37] E. Priest and T. Forbes. *Magnetic Reconnection: MHD Theory and Applications.* Cambridge University Press, Cambridge, 2000.

[38] J. F. Drake, M. A. Shay, W. Thongthai, and M. Swisdak. Production of Energetic Electrons during Magnetic Reconnection. *Phys. Rev. Lett.*, 94(9):095001, Mar 2005.

[39] G. M. Webb, W. I. Axford, and T. Terasawa. On the drift mechanism for energetic charged particles at shocks. *The Astrophysical Journal*, 270:537–553, July 1983.

[40] N. Shimada, T. Terasawa, and J. Jokipii. Stochastic particle acceleration by a pair of slow shocks. *J. Geophys. Res.*, 102(A10):22301–22310, October 1997.

[41] S. Tsuneta and T. Naito. Fermi Acceleration at the Fast Shock in a Solar Flare and the Impulsive Loop-Top Hard X-Ray Source. *The Astrophysical Journal Letters*, 495(1):L67, 1998.

[42] K. McGuire, R. Goldston, M. Bell, M. Bitter, K. Bol, K. Brau, D. Buchenauer, T. Crowley, S. Davis, F. Dylla, H. Eubank, H. Fishman, R. Fonck, B. Grek, R. Grimm, R. Hawryluk, H. Hsuan, R. Hulse, R. Izzo, R. Kaita, S. Kaye, H. Kugel, D. Johnson, J. Manickam, D. Manos, D. Mansfield, E. Mazzucato, R. McCann, D. McCune, D. Monticello, R. Motley, D. Mueller, K. Oasa, M. Okabayashi, K. Owens, W. Park, M. Reusch, N. Sauthoff, G. Schmidt, S. Sesnic, J. Strachan, C. Surko, R. Slusher, H. Takahashi, F. Tenney, P. Thomas, H. Towner, J. Valley, and R. White. Study of High-Beta Magnetohydrodynamic Modes and Fast-Ion Losses in PDX. *Phys. Rev. Lett.*, 50:891–895, Mar 1983.

[43] M. F. F. Nave, D. J. Campbell, E. Joffrin, F. B. Marcus, G. Sadler, P. Smeulders, and K. Thomsen. Fishbone activity in JET. *Nuclear Fusion*, 31(4):697, 1991.

[44] W. Chen, X. T. Ding, Y. Liu, Q. W. Yang, X. Q. Ji, M. Isobe, G. L. Yuan, Y. P. Zhang, Y. Zhou, X. Y. Song, Y. B. Dong, W. Li, J. Zhou, G. J. Lei, J. Y. Cao, W. Deng, X. M. Song, X. R. Duan, and HL-2A Team. Features of ion and electron fishbone instabilities on HL-2A. *Nuclear Fusion*, 50(8):084008, 2010.

[45] C. Perez von Thun, A. Salmi, A. Perona, S. E. Sharapov, S. D. Pinches, S. Popovichev, S. Conroy, V. G. Kiptily, M. Brix, M. Cecconello, T. Johnson, and JET-EFDA Contributors. Study of fast-ion transport induced by fishbones on JET. *Nuclear Fusion*, 52(9):094010, 2012.

[46] B. Coppi and F. Porcelli. Theoretical Model of Fishbone Oscillations in Magnetically Confined Plasmas. *Phys. Rev. Lett.*, 57:2272–2275, Nov 1986.

[47] K. L. Wong, M. S. Chu, T. C. Luce, C. C. Petty, P. A. Politzer, R. Prater, L. Chen, R. W. Harvey, M. E. Austin, L. C. Johnson, R. J. La Haye, and R. T. Snider. Internal Kink Instability during Off-Axis Electron Cyclotron Current Drive in the DIII-D Tokamak. *Phys. Rev. Lett.*, 85:996–999, Jul 2000.

[48] X. T. Ding, Y. Liu, G. C. Guo, E. Y. Wang, K. L. Wong, L. W. Yan, J. Q. Dong, J. Y. Cao, Y. Zhou, J. Rao, Y. Yuan, H. Xia, Y. Liu, and the HL-1M group. Observation of internal kink instability purely driven by suprathermal electrons in the HL-1M tokamak. *Nuclear Fusion*, 42(5):491, 2002.

[49] R. Cesario, L. Panaccione, M. Marinucci, P. Smeulders, A. Botrugno, G. Calabro, C. Castaldo, A. Romano, V. Pericoli, A. A. Tuccillo, and F. Zonca. Fishbone-like internal kink instability driven by supra-thermal electrons on FTU generated by lower hybrid radiofrequency power. IAEA, 2008.

[50] W. Chen, X. T. Ding, Y. Liu, G. L. Yuan, Y. P. Zhang, Y. B. Dong, X. Y. Song, J. Zhou, X. M. Song, W. Deng, Q. W. Yang, X. Q. Ji, X. R. Duan, Y. Liu, and the HL-2A Team. Destabilization of the internal kink mode by energetic electrons on the HL-2A tokamak. *Nuclear Fusion*, 49(7):075022, 2009.

[51] A. Macor, M. Goniche, J. F. Artaud, J. Decker, D. Elbeze, X. Garbet, G. Giruzzi, G. T. Hoang, P. Maget, D. Mazon, D. Molina, C. Nguyen, Y. Peysson, R. Sabot, and J. L. Ségui. Redistribution of Suprathermal Electrons due to Fishbone Frequency Jumps. *Phys. Rev. Lett.*, 102:155005, Apr 2009.

[52] F. Zonca, P. Buratti, A. Cardinali, L. Chen, J.-Q. Dong, Y.-X. Long, A. V. Milovanov, F. Romanelli, P. Smeulders, L. Wang, Z.-T. Wang, C. Castaldo, R. Cesario, E. Giovannozzi, M. Marinucci, and V. P. Ridolfini. Electron fishbones: theory and experimental evidence. *Nuclear Fusion*, 47(11):1588, 2007.

[53] Z. O. Guimarães Filho, S. Benkadda, D. Elbeze, A. Botrugno, P. Buratti, G. Calabrò, J. Decker, N. Dubuit, X. Garbet, P. Maget, A. Merle, G. Pucella, R. Sabot, A. A. Tuccillo, and F. Zonca. Electron fishbones in FTU and Tore Supra tokamaks. *Nuclear Fusion*, 52(9):094009, 2012.

[54] A. Merle, J. Decker, X. Garbet, R. Sabot, Z. O. Guimarães Filho, and T. Nicolas. Stability of the electron-driven fishbone mode. *Physics of Plasmas*, 19(7):072504, 2012.

[55] J. P. Graves. Toroidal drift precession and wave–particle interaction in shaped tokamaks with finite beta and neoclassical equilibrium effects. *Plasma Physics and Controlled Fusion*, 55(7):074009, 2013.

[56] Y. P. Zhang, Y. Liu, X. Y. Song, G. L. Yuan, W. Chen, X. Q. Ji, X. T. Ding, J. W. Yang, J. Zhou, X. Li, Q. W. Yang, X. R. Duan, C. H. Pan, and Y. Liu. Measurements of the fast electron bremsstrahlung emission during electron cyclotron resonance heating in the HL-2A tokamak. *Review of Scientific Instruments*, 81(10):103501, 2010.

[57] L. Delgado-Aparicio, S. Shiraiwa, L. Sugiyama, R. Parker, S. G. Baek, R. Mumgaard, R. Granetz, I. Faust, S. Scott, D. A. Gates, N. Gorelenkov, N. Bertelli, M. Bitter, C. Gao, M. Greenwald, K. Hill, A. Hubbard, J. Hughes, J. Irby, E. Marmar, O. Meneghini, N. Pablant, P. Phillips, J. E. Rice, W. Rowan, J. Walk, Wallace G., R. Wilson, S. Wolfe, and S. Wukitch. Study of suprathermal electron dynamics by energy-resolved tomography of hard X-ray emission on the TCV tokamak. *Europhysics Conference Abstracts*, 37D:P1.159, July 2013.

[58] G. Vlad, S. Briguglio, G. Fogaccia, F. Zonca, V. Fusco, and X. Wang. Electron fishbone simulations in tokamak equilibria using XHMGC. *Nuclear Fusion*, 53(8):083008, 2013.

[59] S. Sangaroon, M. Cecconello, M. Weiszflog, S. Conroy, G. Ericsson, I. Wodniak, D. Keeling, M. R. Turnyanskiy, and MAST team. Conceptual design of a neutron camera upgrade for MAST Upgrade. *Europhysics Conference Abstracts*, 37D:P5.124, July 2013.

[60] F. Jüttner. Das Maxwellsche Gesetz der Geschwindigkeitsverteilung in der Relativtheorie. *Annalen der Physik*, 339:856, 1911.

[61] S. R. De Groot, W. A. van Leeuwen, and Ch. G. van Weert. *Relativistic kinetic theory*. North-Holland, Amsterdam, 1980.

[62] J. Kamleitner, S. Gnesin, S. Coda, Ph. Marmillod, and J. Decker. A new hard x-ray spectrometer for suprathermal electron studies in TCV. *Europhysics Conference Abstracts*, 36F:P1.010, 2012.

[63] H. Dreicer. Electron and Ion Runaway in a Fully Ionized Gas. I. *Phys. Rev.*, 115:238–249, Jul 1959.

[64] H. Dreicer. Electron and Ion Runaway in a Fully Ionized Gas. II. *Phys. Rev.*, 117(2):329–342, Jan 1960.

[65] R. M. Kulsrud, Y.-C. Sun, N. K. Winsor, and H. A. Fallon. Runaway Electrons in a Plasma. *Phys. Rev. Lett.*, 31:690–693, Sep 1973.

[66] J. C. Wiley, D.-I. Choi, and W. Horton. Simulations of the runaway electron distributions. *Physics of Fluids (1958-1988)*, 23(11):2193–2203, 1980.

[67] P. V. Savrukhin. Effect of the magnetohydrodynamic modes on generation of the nonthermal electrons in high density tokamak plasma. *Physics of Plasmas*, 9(8):3421–3428, 2002.

[68] S. Coda. Diagnostic techniques for measuring suprathermal electron dynamics in plasmas (invited). *Review of Scientific Instruments*, 79(10):10F501, 2008.

[69] I. H. Hutchinson. *Principles of plasma diagnostics*. Cambridge University Press, Cambridge, 1987.

[70] T. P. Goodman, V. S. Udintsev, F. Felici, C. Zucca, and C. Schlatter. Co- and Counter – viewing oblique ECE measurements during ECH and ECCD on the TCV tokamak. *Europhysics Conference Abstracts*, 31F:P2.147, July 2007.

[71] W. Nakel. The elementary process of bremsstrahlung . *Physics Reports*, 243(6):317–353, 1994.

[72] S. von Goeler, S. Jones, R. Kaita, S. Bernabei, W. Davis, H. Fishman, G. Gettelfinger, D. Ignat, F. Paoletti, G. Petravich, F. Rimini, P. Roney, J. Stevens, and W. Stodiek. Camera for imaging hard x rays from suprathermal electrons during lower hybrid current drive on PBX-M. *Review of Scientific Instruments*, 65(5):1621–1630, 1994.

[73] E. Haug and W. Nakel. *The Elementary Process of Bremsstrahlung*. World Scientific Publishing Co. Pte. Ltd., 5 Toh Tuck Link, Singapore 596224, 2004.

[74] Z. Y. Chen, B. N. Wan, S. Y. Lin, Y. J. Shi, L. Q. Hu, X. Z. Gong, H. Lin, and M. Asif. Measurement of the runaway electrons in the HT-7 tokamak. *Review of Scientific Instruments*, 77(1):–, 2006.

[75] J. S. Belapure. *Non-thermal electron populations in microwave heated plasmas investigated with X-ray detectors*. PhD thesis, Technische Universität München, April 2013.

[76] Y. Peysson and F. Imbeaux. Tomography of the fast electron bremsstrahlung emission during lower hybrid current drive on TORE SUPRA. *Review of Scientific Instruments*, 70(10):3987–4007, 1999.

[77] P. V. Savrukhin and I. Klimanov. Tangential x-ray imaging system for analysis of the small-scale modes in the T-10 tokamak. *Review of Scientific Instruments*, 72(3):1668–1671, 2001.

[78] T. I. Madeira, A. P. Rodrigues, C. A. F. Varandas, P. Amorim, and B. P. Duval. Real-time signal analysis on the TCV PHA diagnostic. *Review of Scientific Instruments*, 74(3):2004–2006, 2003.

[79] J. Kamleitner, S. Coda, J. Decker, J. P. Graves, and S. Gnesin. Study of suprathermal electron dynamics by energy-resolved tomography of hard X-ray emission on the TCV tokamak. *Europhysics Conference Abstracts*, 37D:P5.127, July 2013.

[80] M. Anton, H. Weisen, M. J. Dutch, W. von der Linden, F. Buhlmann, R. Chavan, B. Marlétaz, Ph. Marmillod, and P. Paris. X-ray tomography on the TCV tokamak. *Plasma Physics and Controlled Fusion*, 38(11):1849, 1996.

[81] J. Stevens, S. Von Goeler, S. Bernabei, M. Bitter, T. K. Chu, P. Efthimion, N. Fisch, W. Hooke, J. Hosea, F. Jobes, C. Karney, E. Meservey, R. Motley, and G. Taylor. Modelling of the electron distribution based on bremsstrahlung emission during lower-hybrid current drive on PLT. *Nuclear Fusion*, 25(11):1529, 1985.

[82] J. Decker and Y. Peysson. LUKE: A fast numerical solver for the 3-D relativistic bounce-averaged electron Drift Kinetic Equation. Technical report, Euratom-CEA, April 2007.

[83] R. W. Harvey and M. G. McCoy. The CQL3D Fokker-Planck Code. Technical report, General Atomics, February 2011.

[84] TCV the team. CRPP intranet.

[85] F. Hofmann, J. B. Lister, W. Anton, S. Barry, R. Behn, S. Bernel, G. Besson, F. Buhlmann, R. Chavan, M. Corboz, M. J. Dutch, B. P. Duval, D. Fasel, A. Favre, S. Franke, A. Heym, A. Hirt, C. Hollenstein, P. Isoz, B. Joye, X. Llobet, J. C. Magnin, B. Marletaz, Ph. Marmillod, Y. Martin, J. M. Mayor, J.-M. Moret, C. Nieswand, P. J. Paris, A. Perez, Z. A. Pietrzyk, R. A. Pitts, A. Pochelon, R. Rage, O. Sauter, G. Tonetti, M. Q. Tran, F. Troyon, D. J. Ward, and H. Weisen. Creation and control of variably shaped plasmas in TCV. *Plasma Physics and Controlled Fusion*, 36(12B):B277, 1994.

[86] S. Coda. Progress and scientific results in the TCV tokamak. *Nuclear Fusion*, 51(9):094017, 2011.

[87] S. Coda and TCV for the Team. Overview of recent and current research on the TCV tokamak. *Nuclear Fusion*, 53(10):104011, 2013.

[88] J. I. Paley, S. Coda, B. P. Duval, F. Felici, and J.-M. Moret. Architecture and commissioning of the TCV distributed feedback control system. In *Real Time Conference (RT), 2010 17th IEEE-NPSS*, pages 1–6, may 2010.

[89] F. Piras, S. Coda, B. P. Duval, B. Labit, J. Marki, S. Y. Medvedev, J.-M. Moret, A. Pitzschke, and O. Sauter. "Snowflake" H Mode in a Tokamak Plasma. *Phys. Rev. Lett.*, 105(15):155003, Oct 2010.

[90] C. Zucca, O. Sauter, E. Asp, S. Coda, E. Fable, T. P. Goodman, and M. A. Henderson. Current density evolution in electron internal transport barrier discharges in TCV. *Plasma Physics and Controlled Fusion*, 51(1):015002, 2009.

[91] L. Federspiel. *Rotation and Impurity Studies in the presence of MHD activity and Internal Transport Barriers on TCV*. PhD thesis, EPFL, Lausanne, 2014.

[92] F. Felici, T. P. Goodman, O. Sauter, G. Canal, S. Coda, B. P. Duval, J. X. Rossel, and TCV the Team. Integrated real-time control of MHD instabilities using multi-beam ECRH/ECCD systems on TCV. *Nuclear Fusion*, 52(7):074001, 2012.

[93] J.X. Rossel, J.-M. Moret, S. Coda, O. Sauter, T.P. Goodman, F. Felici, D. Testa, Y. Martin, and TCV the Team. Edge-localized mode control by electron cyclotron waves in a tokamak plasma. *Nuclear Fusion*, 52(3):032004, 2012.

[94] F. Felici, J. X. Rossel, B. P. Duval, S. Coda, T. P. Goodman, Y. Martin, J.-M. Moret, O. Sauter, and TCV the Team. Real-time control of the period of individual ELMs by EC power on TCV. *Nuclear Fusion*, 53(11):113018, 2013.

[95] J. B. Lister, F. Hofmann, J.-M. Moret, F. Bühlmann, M. J. Dutch, D. Fasel, A. Favre, P.-F. Isoz, B. Marletaz, Ph. Marmillod, Y. Martin, A. Perez, and D. J. Ward. The Control of Tokamak Configuration Variable Plasmas. *Fusion Science and Technology*, 32(3):321–373, 1997.

[96] H. Anand, J.-M. Moret, S. Coda, and H. B. Le. Development of plasma shape control using real-time equilibrium reconstruction on TCV. *Europhysics Conference Abstracts*, 37D:P2.157, July 2013.

[97] W. A. J. Vijvers, F. Felici, H. B. Le, B. P. Duval, S. Coda, and the TCV team. Non-linear digital real-time density control in the TCV tokamak. *Europhysics Conference Abstracts*, 36F:P1.066, 2012.

[98] F. Hofmann, M. J. Dutch, J.-M. Moret, et al. Plasma shape control in TCV using MGAMS. *Europhysics Conference Abstracts*, 19C:II–101, July 1995.

[99] M. Thumm. MW gyrotron development for fusion plasma applications. *Plasma Physics and Controlled Fusion*, 45(12A):A143, 2003.

[100] A. N. Karpushov, Y. Andrebe, B. P. Duval, and A. Bortolon. The diagnostic neutral beam injector with arc-discharge plasma source on the {TCV} Tokamak. *Fusion Engineering and Design*, 84(2–6):993–997, 2009. Proceeding of the 25th Symposium on Fusion Technology (SOFT-25).

[101] A. N. Karpushov, B. P. Duval, R. Chavan, E. Fable, J.-M. Mayor, O. Sauter, and H. Weisen. A scoping study of the application of neutral beam heating on the TCV tokamak. *Fusion Engineering and Design*, 86(6–8):868–871, 2011. Proceedings of the 26th Symposium of Fusion Technology (SOFT-26).

[102] A. Fasoli, S. Alberti, R. Chavan, B. P. Duval, A. Karpushov, Y. Martin, O. Sauter, M. Toussaint, H. Weisen, and TCV the Team. An upgraded TCV for tokamak physics in view of ITER and DEMO. *Europhysics Conference Abstracts*, 37D:P2.104, July 2013.

[103] J.-M. Moret, F. Buhlmann, D. Fasel, F. Hofmann, and G. Tonetti. Magnetic measurements on the TCV Tokamak. *Review of Scientific Instruments*, 69(6):2333–2348, 1998.

[104] S. Barry, Ch. Nieswand, and S. L. Prunty. Far-infrared polarimetry on the TCV tokamak. *Proceedings of the 8th International Symposium on Laser-aided Plasma Diagnostics*, pages 313–318, 1997.

[105] J. Kamleitner. General tomographic inversion at TCV. Technical report, CRPP, EPFL, 2011.

[106] R. Behn. Private communication.

[107] R. Behn, J. H. Rommers, R. A. Pitts, Z. A. Pietrzyk, R. Chavan, and B. Marletaz. A Thomson scattering diagnostic for measurements in the divertor region of TCV. *Review of Scientific Instruments*, 70(1):768–771, 1999.

[108] G. Zhuang, R. Behn, I. Klimanov, P. Nikkola, and O. Sauter. Influence of non-Maxwellian velocity distributions during ECRH and ECCD on electron temperature measurements by Thomson scattering. *Plasma Physics and Controlled Fusion*, 47(9):1539, 2005.

[109] J. Kamleitner. Thomson scattering under the condition of non-thermal electron velocity distributions. Technical report, CRPP, EPFL, September 2012.

[110] S. von Goeler. Soft X-Ray Measurements. In E. Sindoni and C. Wharton, editors, *Diagnostic for fusion experiments*, pages 79–110. Pergamon Press, September 1978.

[111] I. Furno. *Fast transient transport phenomena measured by soft x-ray emission in TCV tokamak plasmas.* PhD thesis, EPFL, Lausanne, 2001.

[112] M. Anton, M. J. Dutch, and H. Weisen. Relative calibration of photodiodes in the soft-x-ray spectral range. *Review of Scientific Instruments*, 66(7):3762–3769, 1995.

[113] W. J. Veigele. Photon cross sections from 0.1 keV to 1 MeV for elements Z = 1 to Z = 94. *Atomic Data and Nuclear Data Tables*, 5(1):51–111, 1973.

[114] N. N. Greenwood and A. Earnshaw. *Chemie der Elemente.* Wiley, 1st edition, 1988.

[115] J. F. Shackelford and W. Alexander, editors. *CRC Materials Science and Engineering Handbook.* CRC Press, 3rd edition, 2000.

[116] A. Sushkov, V. Andreev, Y. Camenen, A. Pochelon, I. Klimanov, A. Scarabosio, and H. Weisen. High-resolution multiwire proportional soft x-ray diagnostic measurements on TCV. *Review of Scientific Instruments*, 79(2):023506, 2008.

[117] I. Furno, H. Weisen, J. Mlynar, R. A. Pitts, X. Llobet, Ph. Marmillod, and G. P. Pochon. Fast bolometric measurements on the TCV tokamak. *Review of Scientific Instruments*, 70(12):4552–4556, 1999.

[118] P. Blanchard, S. Alberti, S. Coda, H. Weisen, P. Nikkola, and I. Klimanov. High field side measurements of non-thermal electron cyclotron emission on TCV plasmas with ECH and ECCD. *Plasma Physics and Controlled Fusion*, 44(10):2231, 2002.

[119] I. Klimanov, L. Porte, S. Alberti, P. Blanchard, A. Fasoli, and T. P. Goodman. Electron cyclotron emission spectrometry on the Tokamak à Configuration Variable. *Review of Scientific Instruments*, 76(9):093504, 2005.

[120] V. Vuille, L. Porte, S. Brunner, S. Coda, A. Fasoli, Z. Huang, C. A. de Meijere, G. Merlo, and L. Vermare. Investigation of turbulence and zonal flows for different shapes and scenarios in TCV using correlation ECE. *Europhysics Conference Abstracts*, 37D:P2.176, July 2013.

[121] S. Gnesin. *Electron Cyclotron Heating and Suprathermal Electron Dynamics in the TCV Tokamak*. PhD thesis, EPFL, 2011.

[122] Y. Peysson, S. Coda, and F. Imbeaux. Hard X-ray CdTe tomography of tokamak fusion plasmas. *Nuclear Instruments and Methods in Physics Research Section A: Accelerators, Spectrometers, Detectors and Associated Equipment*, 458(1-2):269–274, 2001. Proc. 11th Inbt. Workshop on Room Temperature Semiconductor X- and Gamma-Ray Detectors and Associated Electronics.

[123] S. Coda, Y. Peysson, T. P. Goodman, M. A. Henderson, J.-P. Hogge, X. Llobet, B. Marlétaz, Z. A. Pietrzyk, A. Pochelon, G. Pochon, O. Sauter, and H. Weisen. Measurements of Hard X-Ray Emission Profiles in the TCV Tokamak during Electron Cyclotron Heating and Current Drive. *Europhysics Conference Abstracts*, 23J:1097–1100, 1999.

[124] P. Nikkola, O. Sauter, R. Behn, S. Coda, I. Condrea, T. P. Goodman, M. A. Henderson, R. W. Harvey, and the TCV team. Modelling of the electron cyclotron current drive experiments in the TCV tokamak. *Nuclear Fusion*, 43(11):1343, 2003.

[125] S. Coda, Y. Peysson, S. Alberti, T. P. Goodman, M. A. Henderson, P. Nikkola, and O. Sauter. Suprathermal X-ray Emissivity with 2nd and 3rd Harmonic Electron Cyclotron Heating in the TCV Tokamak. *Europhysics Conference Abstracts*, 25A:301–304, 2001.

[126] S. Gnesin, J. Decker, S. Coda, T. P. Goodman, Y. Peysson, and D. Mazon. 3rd harmonic electron cyclotron resonant heating absorption enhancement by 2nd harmonic heating at the same frequency in a tokamak. *Plasma Physics and Controlled Fusion*, 54(3):035002, 2012.

[127] D. Block, I. Teliban, F. Greiner, and A. Piel. Prospects and limitations of conditional averaging. *Physica Scripta*, 2006(T122):25, 2006.

[128] A. A. Townsend. The fully developed turbulent wake of a circular cylinder. *Australian Journal of Scientific Research*, 2:451–468, 1949.

[129] P.Y. Chou. On velocity correlations and the solutions of the equations of turbulent fluctuation. *Quarterly of applied mathematics*, 3:38–54, 1945.

[130] D. Praetorius. Numerische Mathematik, 2004.

[131] X. Wu. An Efficient Antialiasing Technique. *SIGGRAPH Comput. Graph.*, 25(4):143–152, July 1991.

[132] Y. Peysson and J. Decker. Fast electron bremsstrahlung in axisymmetric magnetic configuration. *Physics of Plasmas*, 15(9):092509, 2008.

[133] R. W. Harvey and M. G. McCoy. The CQL3D Code. In *Proc. IAEA TCM on Advances in Sim. and Modeling of Thermonuclear Plasmas*, pages 489–526, Vienna, 1992. IAEA.

[134] R. Prater, D. Farina, Yu. Gribov, R. W. Harvey, A. K. Ram, Y.-R. Lin-Liu, E. Poli, A. P. Smirnov, F. Volpe, E. Westerhof, A. Zvonkov, and the ITPA Steady State Operation Topical Group. Benchmarking of codes for electron cyclotron heating and electron cyclotron current drive under ITER conditions. *Nuclear Fusion*, 48(3):035006, 2008.

[135] M. S. Basunia. Nuclear Data Sheets for A = 237. *Nuclear Data Sheets*, 107(8):2323–2422, 2006.

[136] J. B. Simões and C. M. B. A. Correia. Pulse processing architectures. *Nuclear Instruments and Methods in Physics Research Section A: Accelerators, Spectrometers, Detectors and Associated Equipment*, 422(1–3):405–410, 1999.

[137] J. M. R. Cardoso, J. B. Simões, and C. M. B. A. Correia. A mixed analog-digital pulse spectrometer. *Nuclear Instruments and Methods in Physics Research Section A: Accelerators, Spectrometers, Detectors and Associated Equipment*, 422(1–3):400–404, 1999.

[138] M. Mutterer, W. H. Trzaska, G. P. Tyurin, A. V. Evsenin, J. von Kalben, J. Kemmer, M. Kapusta, V. G. Lyapin, and S. V. Khlebnikov. Breakthrough in pulse-shape based particle identification with silicon detectors. *Nuclear Science, IEEE Transactions on*, 47(3):756–759, jun 2000.

[139] D. M. Scates and J. K. Hartwell. A comparison of the high count-rate performance of three commercially available digital signal processors. *Applied Radiation and Isotopes*, 63(4):465–473, 2005.

[140] H. Seta, M. S. Tashiro, Y. Terada, Y. Shimoda, K. Onda, Y. Ishisaki, M. Tsujimoto, T. Hagihara, Y. Takei, K. Mitsuda, K. R. Boyce, and A. E. Szymkowiak. Development of a Digital Signal Processing System for the X-ray Microcalorimeter onboard ASTRO-H. *AIP Conference Proceedings*, 1185(1):278–281, 2009.

[141] Shiping Li, Xiufeng Xu, Hongrui Cao, Guoliang Yuan, Qingwei Yang, and Zejie Yin. A real-time n/γ digital pulse shape discriminator based on FPGA. *Applied Radiation and Isotopes*, 72(0):30–34, 2013.

[142] K. Vetter, A. Kuhn, M. A. Deleplanque, I. Y. Lee, F. S. Stephens, G. J. Schmid, D. Beckedahl, J. J. Blair, R. M. Clark, M. Cromaz, R. M. Diamond, P. Fallon, G. J. Lane, J. E. Kammeraad, A. O. Macchiavelli, and C. E. Svensson. Three-dimensional position sensitivity in two-dimensionally segmented HP-Ge detectors. *Nuclear Instruments and Methods in Physics Research Section A: Accelerators, Spectrometers, Detectors and Associated Equipment*, 452(1–2):223–238, 2000.

[143] T. Tada, K. Hitomi, T. Tanaka, Y. Wu, S.-Y. Kim, H. Yamazaki, and K. Ishii. Digital pulse processing and electronic noise analysis for improving energy resolutions in planar TlBr detectors. *Nuclear Instruments and Methods in Physics Research Section A: Accelerators, Spectrometers, Detectors and Associated Equipment*, 638(1):92–95, 2011.

[144] S. H. Byun and H. Peng. Radiation & Radioisotope Methodology. http://www.science.mcmaster.ca/medphys/courses/166-med-phys-4r06.html, 2012.

[145] M. Nakhostin. Recursive Algorithms for Real-Time Digital Pulse Shaping. *Nuclear Science, IEEE Transactions on*, 58(5):2378–2381, oct. 2011.

[146] V. T. Jordanov. Exponential signal synthesis in digital pulse processing. *Nuclear Instruments and Methods in Physics Research Section A: Accelerators, Spectrometers, Detectors and Associated Equipment*, 670(0):18–24, 2012.

[147] A. Pullia, A. Geraci, and G. Ripamonti. Quasi-optimum γ and X spectroscopy based on real-time digital techniques. *Nuclear Instruments and Methods in Physics Research Section A: Accelerators, Spectrometers, Detectors and Associated Equipment*, 439(2–3):378–384, 2000.

[148] Y. Takenaka, A. Uritani, K. Inoue, H. Sakai, and C. Mori. Novel pulse-shape-analysis method by using similarity. *Applied Radiation and Isotopes*, 49(9–11):1219–1223, 1998.

[149] M. Faisal, R. T. Schiffer, M. Flaska, S. A. Pozzi, and D. D. Wentzloff. A correlation-based pulse detection technique for gamma-ray/neutron detectors. *Nuclear Instruments and Methods in Physics Research Section A: Accelerators, Spectrometers, Detectors and Associated Equipment*, 652(1):479–482, 2011.

[150] K. R. Boyce, M. D. Audley, R. G. Baker, J. J. Dumonthier, R. Fujimoto, K. C. Gendreau, Y. Ishisaki, R. L. Kelley, C. K. Stahle, A. E. Szymkowiak, and G. E. Winkert. Design and performance of the ASTRO-E/XRS signal processing system. *Proc. SPIE*, 3765:741–750, 1999.

[151] H. Sakai, Y. Takenaka, A. Uritani, K. Inoue, and C. Mori. Improvement of energy spectrum characteristics of CdZnTe semiconductor detector by means

of digital waveform processing with neural network algorithm. *Nuclear Instruments and Methods in Physics Research Section A: Accelerators, Spectrometers, Detectors and Associated Equipment*, 400(2–3):401–408, 1997.

[152] M. van Berkel, G. Witvoet, M. R. de Baar, P. W. J. M. Nuij, H. G. ter Morsche, and M. Steinbuch. Real-time wavelet detection of crashes in limit cycles of non-stationary fusion plasmas. *Fusion Engineering and Design*, 86(12):2908–2919, 2011.

[153] J. Gomez, I. Melgar, and J. Seijas. Upgrading Pulse Detection with Time Shift Properties Using Wavelets and Support Vector Machines. *Proceedings of the World Automation Congress (WAC-04)*, June 2004.

[154] C. J. C. Burges. A Tutorial on Support Vector Machines for Pattern Recognition. *Data Mining and Knowledge Discovery*, 2(2):121–167, 1998.

[155] V. Radeka. Trapezoidal filtering of signals from large germanium detectors at high rates. *Nuclear Instruments and Methods*, 99(3):525–539, 1972.

[156] J. Canny. A Computational Approach to Edge Detection. *Pattern Analysis and Machine Intelligence, IEEE Transactions on*, PAMI-8(6):679–698, nov. 1986.

[157] S. Riboldi, A. Geraci, R. Abbiati, E. Gatti, and G. Ripamonti. A new method for LMS synthesis of optimum finite impulse response (FIR) filters with arbitrary time and frequency constraints and noises. In *Nuclear Science Symposium Conference Record, 2002 IEEE*, volume 1, pages 198–202 vol.1, nov. 2002.

[158] B. Joly, G. Montarou, J. Lecoq, G. Bohner, M. Crouau, M. Brossard, and P.-E. Vert. An Optimal Filter Based Algorithm for PET Detectors With Digital Sampling Front-End. *Nuclear Science, IEEE Transactions on*, 57(1):63–70, feb. 2010.

[159] A. Pullia and S. Riboldi. Time-domain Simulation of electronic noises. *Nuclear Science, IEEE Transactions on*, 51(4):1817–1823, 2004.

[160] R. W. Harvey, K. D. Marx, and M. G. McCoy. Non-linear Fokker-Planck studies of RF current drive efficiency. *Nuclear Fusion*, 21(2):153, 1981.

[161] I. P. Shkarofsky and M. M. Shoucri. Modelling of lower hybrid current drive in the presence of spatial radial diffusion. *Nuclear Fusion*, 37(4):539, 1997.

[162] J. Decker, Y. Peysson, and S. Coda. Effect of density fluctuations on ECCD in ITER and TCV. *EPJ Web of Conferences*, 32:01016, 2012.

[163] R. W. Harvey, O. Sauter, R. Prater, and P. Nikkola. Radial Transport and Electron-Cyclotron-Current Drive in the TCV and DIII-D Tokamaks. *Phys. Rev. Lett.*, 88:205001, May 2002.

[164] G. Becker and O. Kardaun. Anomalous particle pinch and scaling of v in / D based on transport analysis and multiple regression. *Nuclear Fusion*, 47(1):33, 2007.

[165] E. Fable, O. Sauter, S. Coda, T. P. Goodman, M. A. Henderson, H. Weisen, A. Zabolotsky, C. Zucca, and The TCV team. Inward thermodiffusive particle pinch in electron internal transport barriers in TCV. *Plasma Physics and Controlled Fusion*, 48(9):1271, 2006.

[166] F. Imbeaux and Y. Peysson. Dynamics of Fast Electrons Driven by the Lower Hybrid Wave in Giant Sawtoothing Plasmas. *Phys. Rev. Lett.*, 84:2873–2876, Mar 2000.

[167] B. Saoutic, M. Chatelier, and C. De Michelis. Tore Supra: Toward Steady State in a Superconducting Tokamak. *Fusion Science and Technology*, 56(3):1079–1091, October 2009.

[168] D. Brunetti, J. P. Graves, W. A. Cooper, and C. Wahlberg. Fast growing resistive two fluid instabilities in hybrid-like tokamak configuration. *Plasma Physics and Controlled Fusion*, 56(7):075025, 2014.

[169] D. Brunetti, J. P. Graves, F. D. Halpern, J.-F. Luciani, H. Lütjens, and W. A. Cooper. Extended MHD simulations of infernal mode dynamics and coupling to tearing modes. *Plasma Physics and Controlled Fusion*. accepted for publication.

[170] V. Pierrard and M. Lazar. Kappa Distributions: Theory and Applications in Space Plasmas. *Solar Physics*, 267:153–174, 2010. 10.1007/s11207-010-9640-2.

[171] H. Bethe and W. Heitler. On the Stopping of Fast Particles and on the Creation of Positive Electrons. *Proceedings of the Royal Society of London. Series A, Containing Papers of a Mathematical and Physical Character*, 146(856):83–112, 1934.

[172] G. Elwert. Verschärfte Berechnung von Intensität und Polarisation im kontinuierlichen Röntgenspektrum. *Annalen der Physik*, 34(5):178–208, 1939.

[173] F. Sauter. Über die Bremsstrahlung schneller Elektronen. *Annalen der Physik*, 20(5):404, 1934.

[174] H. W. Koch and J. W. Motz. Bremsstrahlung Cross-Section Formulas and Related Data. *Rev. Mod. Phys.*, 31:920–955, Oct 1959.

[175] E. Haug. Electron–electron and electron–positron bremsstrahlung . *Radiation Physics and Chemistry*, 75(10):1330–1345, 2006. Bremsstrahlung: Theory and Experiment.

[176] E. Haug and M. Keppler. Bremsstrahlung in the field of bound electrons. *Journal of Physics B: Atomic and Molecular Physics*, 17(10):2075, 1984.

[177] I. Kawrakow. Accurate condensed history Monte Carlo simulation of electron transport. I. EGSnrc, the new EGS4 version. *Medical Physics*, 27(3):485–498, 2000.

[178] O. Sauter and S.Yu. Medvedev. Tokamak coordinate conventions: COCOS. *Computer Physics Communications*, 184(2):293–302, 2013.

[179] J.-M. Moret. A software package to manipulate space dependencies and geometry in magnetic confinement fusion. *Review of Scientific Instruments*, 76(7):073507, 2005.

[180] mdsplus.org.

[181] W. Koechner. *Solid-state laser engineering*, volume 1 of *Springer series in optical sciences*. Springer, 6 edition, 2006.

[182] J. Kamleitner, S. Coda, and J. Decker. Suprathermal electron dynamics and hard X-ray tomography in TCV. In *56th Annual Meeting of the APS Division of Plasma Physics*, volume 49, page TP8.43, 2014.

Acknowledgment

First of all and most importantly, I want to thank my supervisor Stefano for his guidance and help throughout my PhD studies at CRPP. Stefano, I was, and will always be impressed by your broad and deep knowledge in the field and your passion for your work. I am grateful that you let me a lot of freedom and responsibility in my work but also paid attention that I stayed on track. Although you have great responsibility and a large of amount of work in the lab you were always there when I needed advice. Grazie mille, Stefano!

Je voudrais remercier l'équipe de mon bureau comme elle était quand j'arrivais au CRPP. Loïc, Silvano, Andreas et Théo, vous m'avez appris la vie au labo et aidé beaucoup à améloirer mon français. Je me sentais vraiment bienvenu en Suisse! Merci Loïc pour l'aide en physique et français et les discussions intéressentes; gracie mille Silvano, tu m'as appris la physique des X durs et qu'il ne faut jamais être stressé!
My office mates for the most time of my PhD, Falk, Gustavo, Himank and Zhouji made the working time really enjoyable and also helped me whenever there was a problem. It was great fun to be in “our” office :) Danke Falk, für all die coolen Sachen die wir gemeinsam unternommen und organisiert haben! Thank you Gustavo, for your great physics knowledge answering lots of questions and your Brasilian savoir-vivre! Thanks Himank, for your help with English and Zhouji, sorry for using your desk from time to time and thanks for answering the questions none else would know an answer for.
To my new office mates, thank you Matteo and Jéremy, for ensuring me that the life in our office will never get boring.

Un grand merci à Silvano, Philippe et Guy pour le travail en équipe sur le projet HXRS. Aussi à tous les techniciens, sans lesquels mon travail n'aurait pas été possible. Espécialement Pascal, Omar, Claude et Steve pour l'aide avec la mise en place des caméras et Xavier, P.-F., Minh et Pierre pour l'aide à la côté informatique.
Thank you Basil, I've learned so much from you, and I even think some of it can be very useful ;)
Merci Joan, que tu m'as aidé si beaucoup avec les simulations LUKE et aussi à comprendre la physique des électrons rapides!
Thank you Jon, for your great help in MHD and the electron fishbone mission; and for reading this whole document!
Merci Olivier! Ton aide avec TORAY et CQL3D était très importante et ta compréhension des plasmas tokamaks est indispensable pour tout le labo!
Danke Holger, auch wenn sich unsere Arbeitsthemen nicht so recht überschnit-

ten haben warst du doch oft eine große Hilfe!

For the operation of TCV, being essential for this thesis, I want to express my gratitude to the PDJs Stefano, Wouter, Basil, Roland, Duccio and Jean-Marc, the pilotes P.-F., Alexander Karpushov, Ugo, Frédéric and Yanis and the gyrotron operators Miguel, François, Tim and Laurie. Thank you for running the machine from the early morning until the late evening!
Since good measurements are equally important, I want to thank also the DDJs for doing all the autogains by hand and running up and down to switch the cables for the magnetic probes.

Thanks to the whole group of PhDs at the CRPP; you made the lab life so much easier and we had so much fun together! I'm glad that I could find so many good friends among you. Thank you, Fabio, for sharing the flat and having a great time in Lausanne.
Merci to all my Swiss friends, or rather, to all my friends living in Switzerland. For the time we spent in the mountains, at the lake or on the bike, always seeking for new destinations; and for the unforgettable parties!
Danke to all my Austrian friends, supporting me from about 900 km away. Ein ganz spezieller Dank gilt allen, die mich hier in Lausanne besucht haben um die Schweiz gemeinsam zu entdecken! Danke Sarah für den unvergesslichen Urlaub in Kenia, und Anna, danke für deine Gastfreundschaft in Nairobi!
I cannot tell how much I want to thank you, Margit! Dafür, dass du in den letzten zweieinhalb Jahren immer für mich da warst, obwohl wir doch so weit voneinander entfernt lebten. Danke für Alles!
Last but not least I want to thank my family! Danke, Mama und Papa, Oma und Opa, dass ihr mich immer unterstützt habt, schon von klein auf, aber auch in meiner Entscheidung in die Schweiz zu gehen. Es war sicher nicht immer leicht dass ich so weit weg war, da war es auch toll, dass ihr mich so oft besucht habt! Danke, lieber Stefan und Bernhard, dass wir trotz der Distanz noch so vieles gemeinsam unternommen haben! Ich freue mich schon wieder auf Österreich :)

Publications and contributions

Refereed journal articles

J. Kamleitner, S. Coda, S. Gnesin, Ph. Marmillod. Comparative analysis of digital pulse processing methods at high count rates. *Nuclear Instruments and Methods in Physics Research Section A: Accelerators, Spectrometers, Detectors and Associated Equipment*, **736** (2014) 88-98 [2]

J. Kamleitner, S. Coda, J. Decker, J. P. Graves, the TCV team. Suprathermal electron dynamics and MHD instabilities in a tokamak. Submitted to *Plasma Physics and Controlled Fusion*

Conference proceedings

J. Kamleitner, S. Gnesin, S. Coda, Ph. Marmillod, J. Decker. A new hard X-ray spectrometer for suprathermal electron studies in TCV. Europhysics Conference Abstracts **36F** (2012) P1.010 [62]

J. Kamleitner, S. Coda, J. Decker, J. P. Graves, S. Gnesin. Study of suprathermal electron dynamics by energy-resolved tomography of hard X-ray emission on the TCV tokamak. Europhysics Conference Abstracts **37D** (2013) P5.127 [79]

J. Kamleitner, S. Coda, J. Decker. Suprathermal electron dynamics and hard X-ray tomography in TCV. 56th Annual Meeting of the APS Division of Plasma Physics. Bulletin of the American Physical Society **49** (2014) TP8.43 [182]

Curriculum vitae of DI DI Josef Kamleitner

born on January 24, 1984 in St. Pölten, Nationality: Austria
Addr.: avenue de Sévery 7, CH-1004 Lausanne, Switzerland
Tel.: +41 78 67 07 232
E-Mail: josef.kamleitner@alumni.tuwien.ac.at

fluent in German, English & French

Driving license: A, B, C, E

School
Service

1990/91 - 1993/94: Grillparzer VS, St. Pölten
1994/95 - 2001/02: BRG St. Pölten, Matura with excellent success
Sept. 2002 - Apr. 2003: military service in Austria

From Oct. 2003: 123 positive exams (of 123), 512.6 ECTS points
June 25, 2009 **DI (Master) in Technical Physics**
Thesis "Neutral Na beam plasma edge diagnostic at ASDEX Upgrade";
supervisor: Univ.-Prof. F. Aumayr, Institut für Allgemeine Physik (IAP), TU Wien
& Dr. E. Wolfrum, Max-Planck-Institut für Plasmaphysik (IPP) in Garching, DE
June 24, 2010 **DI (Master) in Technical Mathematics** "Auszeichnung"
"Numerical methods in quantum propagation"; supervisor: Univ.-Doz.
Dr. O. Koch, Insitut für Analysis und Scientific Computing (ASC), TU Wien

ÉCOLE POLYTECHNIQUE FÉDÉRALE DE LAUSANNE

Nov 1, 2010 - Feb. 27, 2015: **Dissertation** (PhD) in physics
"Suprathermal electron studies in Tokamak plasmas by means of
diagnostic measurements and modeling"; supervisor: MER Dr. Stefano Coda,
Centre de Recherches de Physique des Plasmas (CRPP),
École Polytechnique Fédérale de Lausanne (EPFL, rank 19 Shanghai '14)

Summer schools & talks

2 Summer schools (2008, 2010), CECAM-workshop 2010
Talks at the SPS/APS meeting 2011, Fusenet PhD-event 2012
3 conferences (poster) with publications: EPS 2012, 2013, APS 2014
Invited talk 19^{th} Workshop on MHD Stability Control, Auburn AL, 2014

Public.

J. Kamleitner et al., Nucl. Instr. Meth. Phys. Res. A 736 (2014) 88-98
J. Kamleitner et al., submitted to Plasma Phys. Controlled Fusion

Skills

organizational skills, responsibitily, high performance & learning capacity
Extraordinary *problem solving competence* in technical questions
Expert in numerical methods: FEM, tomography, Monte-Carlo, etc.
Excellent *programming skills* in C, C++, Matlab, Python, Java, Fortran,
MPI, Shell script, C#; OOP; experience in PLC, Labview, bus systems;
Linux, Subversion; Windows & Office; MDSplus, OpenVMS

Jobs

May 2 - June 13, 2003: practical training in the RLH garage St. Pölten
Aug. 27 - Sept. 27, 2007: working student at IPP in Garching, DE
WS 2007/08, 08/09 & 09/10: tutor for numerical mathematics at ASC
Nov. 2010 - Jan. 2015: assistant-doctorant (physics) at EPFL

Varia

Hobbies: race bike, hiking, climbing, playing football, rowing, reading

2001 & 2002: 1^{st} (in NÖ) & 3^{rd} (AT) "cangaroo" mathematics competition
Since 2002 member of the voluntarian fire brigade St. P. - Pummersdorf
2005-2007 leader of the rural youth St. Pölten, organization of events
2007: 1^{st} place in the Lower Austrian Ploughing competition
2010: 4^{th} place in the speakers competition of the rural youth Austria
2012-2014: organization of the monthly PhD seminar at CRPP